Design and Analysis of Thorium-fueled Reduced Moderation Boiling Water Reactors

By

Phillip Michael Gorman

A dissertation submitted in partial satisfaction of the requirements for the degree of

Doctor of Philosophy

in

Engineering – Nuclear Engineering

in the

Graduate Division

of the

University of California, Berkeley

Committee in charge:

Professor Ehud Greenspan, Chair
Professor Massimiliano Fratoni
Professor Jasmina Vujic
Professor Ralph Greif

Fall 2016

Design and Analysis of Thorium-fueled Reduced Moderation Boiling Water Reactors

By

Phillip Michael Gorman

Abstract

Design and Analysis of Thorium-fueled Reduced Moderation Boiling Water Reactors

By

Phillip Michael Gorman

Doctor of Philosophy in Engineering – Nuclear Engineering

University of California, Berkeley

Professor Ehud Greenspan, Chair

The Resource-renewable Boiling Water Reactors (RBWRs) are a set of light water reactors (LWRs) proposed by Hitachi which use a triangular lattice and high void fraction to incinerate fuel with an epithermal spectrum, which is highly atypical of LWRs. The RBWRs operate on a closed fuel cycle, which is impossible with a typical thermal spectrum reactor, in order to accomplish missions normally reserved for sodium fast reactors (SFRs) – either fuel self-sufficiency or waste incineration. The RBWRs also axially segregate the fuel into alternating fissile "seed" regions and fertile "blanket" regions in order to enhance breeding and leakage probability upon coolant voiding.

This dissertation focuses on thorium design variants of the RBWR: the self-sufficient RBWR-SS and the RBWR-TR, which consumes reprocessed transuranic (TRU) waste from PWR used nuclear fuel. These designs were based off of the Hitachi-designed RBWR-AC and the RBWR-TB2, respectively, which use depleted uranium (DU) as the primary fertile fuel. The DU-fueled RBWRs use a pair of axially segregated seed sections in order to achieve a negative void coefficient; however, several concerns were raised with this multi-seed approach, including difficulty with controlling the reactor and unacceptably high axial power peaking. Since thorium-uranium fuel tends to have much more negative void feedback than uranium-plutonium fuels, the thorium RBWRs were designed to use a single elongated seed to avoid these issues.

A series of parametric studies were performed in order to find the design space for the thorium RBWRs, and optimize the designs while meeting the required safety constraints. The RBWR-SS was optimized to maximize the discharge burnup, while the RBWR-TR was optimized to maximize the TRU transmutation rate. These parametric studies were performed on an assembly level model using the MocDown simulator, which calculates an equilibrium fuel composition with a specified reprocessing scheme. A full core model was then created for each design, using the Serpent/PARCS 3-D core simulator, and the full core performance was assessed.

The RBWR-SS benefited from a harder spectrum than the RBWR-TR; a hard spectrum promotes breeding and increases the discharge burnup, but reduces the TRU transmutation rate. This led the RBWR-SS to have a very tight lattice, which has a lot of experimental uncertainty in the thermal hydraulic correlations. Two different RBWR-SS designs were created assuming

different thermal hydraulic assumptions: the RBWR-SSH used the same assumptions as Hitachi used for the RBWR-AC, while the RBWR-SSM used more conservative correlations recommended by collaborators at MIT. However, the void feedback of the pure Th-fed system was too strongly negative, even with a single elongated seed. Therefore, instead of using just thorium, the self-sustaining designs were fed with a mix of between 30% and 50% DU and the rest thorium in order to keep the void feedback as close to zero as possible. This was not necessary for the RBWR-TR, as the external TRU feed fulfilled a similar role.

Unfortunately, it was found that the RBWR-SSM could not sustain a critical cycle without either significantly downgrading the power or supplying an external feed of fissile material. While the RBWR-SSH and the RBWR-TR could reach similar burnups and transmutation rates to their DU-fueled counterparts as designed by Hitachi, the thorium designs were unable to simultaneously have negative void feedback and sufficient shutdown margin to shut down the core. The multi-seed approach of the Hitachi designs allowed their reactors to have much lower magnitudes of Doppler feedback than the single-seed designs, which helps them to have sufficient shutdown margin. It is expected that thorium-fueled RBWRs designed to have multiple seeds would permit adequate shutdown margin, although care would need to be taken in order to avoid running into the same issues as the DU fueled RBWRs. Alternatively, it may be possible to increase the amount of boron in the control blades by changing the assembly and core design.

Nonetheless, the uncertainties in the multiplication factor due to nuclear data and void fraction uncertainty were assessed for the RBWR-SSH and the RBWR-TR, as well as for the RBWR-TB2. In addition, the uncertainty associated with the change in reactor states (such as the reactivity insertion in flooding the core) due to nuclear data uncertainties was quantified. The thorium RBWRs have much larger uncertainty of their DU-fueled counterparts as designed by Hitachi, as the fission cross section of ^{233}U has very large uncertainty in the epithermal energy range. The uncertainty in the multiplication factor at reference conditions was about 1350 pcm for the RBWR-SSH, while it was about 900 pcm for the RBWR-TR. The uncertainty in the void coefficient of reactivity for both reactors is between 8 and 10 pcm/% void, which is on the same order of magnitude as the full core value.

Finally, since sharp linear heat rate spikes were observed in the RBWR-TB2 simulation, the RBWR-TB2 unit cell was simulated using a much finer mesh than is possible using deterministic codes. It was found that the thermal neutrons reflecting back from the reflectors and the blankets were causing extreme spikes in the power density near the axial boundaries of the seeds, which were artificially smoothed out when using coarser meshes. It is anticipated that these spikes will cause melting in both seeds in the RBWR-TB2, unless design changes – such as reducing the enrichment level near the axial boundaries of the seeds – are made.

Table of Contents

List of Acronyms

∞-norm	Absolute value of the maximum difference between iterations
α	Void fraction
ε	Convergence criterion
η	Fuel reproduction factor; the number of fast neutrons produced by fission per neutron absorbed in fuel
σ	Microscopic cross section or standard deviation, depending on context
Σ	Macroscopic cross section
ABR	Advanced burner reactor, a sodium-cooled fast reactor designed to burn UNF from PWRs
ABWR	Advanced BWR
BOC/BOEC	Beginning of (equilibrium) cycle
BOL	Beginning of fuel life; fresh fuel.
BU	burnup
BWR	Boiling water reactor
CPR	Critical power ratio
CR	Conversion ratio
CZP	Cold zero power; shutdown conditions.
DU	Depleted uranium
EOC/EOEC	End of (equilibrium) cycle
EOL	End of fuel life; at the time of fuel discharge
FCE&S	Fuel Cycle Evaluation & Screening Campaign, conducted by the US DOE. [1]
FTCR	Fuel temperature coefficient of reactivity
FIMA	Fissions per initial metal atom; a measurement of burnup.
H-CISE	A critical power correlation for use with the RBWRs which was modified from the CISE-4 correlation for BWRs; it predicts higher CPRs than the MFP-CISE correlation or the M-CISE correlation. The recommended MCPR limit for this correlation is 1.3.
H/HM	Hydrogen to heavy metal ratio.
HFP	Hot full power; normal operating conditions.
HM	Heavy metals (actinides)
LHGR	Linear heat generation rate.
LPG	Liao, Parlos, and Griffith void fraction correlation; specific for tight lattice bundles.
M-CISE	A critical power correlation for use with the RBWRs which was modified from the CISE-4 correlation for BWRs
MCPR	Minimum critical power ratio
N	Number density
NPP	Nuclear Power Plant
pcm	percent milli or “milli-percent”; 10E-5
RBWR	Resource-renewable BWR
RBWR-AC	DU-fueled fuel-self-sustaining RBWR designed by Hitachi
RBWR-TB2	TRU-burning RBWR fed with a mix of DU and LWR UNF designed by Hitachi
RBWR-SS	Fuel self-sufficient RBWR primarily fueled by Th, with some DU for reactivity feedback control
RBWR-TR	TRU-burning RBWR fed with a mix of LWR UNF and Th

RELAP	RELAP5, a USA safety analysis code which uses the Chexal-Lellouche void fraction correlation. This correlation is referred to as the RELAP void correlation within this document.
SDM	Shutdown margin; the amount of reactivity by which a reactor is shut down.
SFR	Sodium-cooled fast reactor
T/H	Thermal hydraulic
TRF	Transfertile (TRU + TRTh)
TRTh	Transthorium
TRU	Transuranium
UNF	Used nuclear fuel
VCR	Void coefficient of reactivity

Acknowledgements

I'd like to thank many people who helped make his dissertation possible.

First and foremost, I'd like to thank my lovely wife, Hannah Reese, for sticking with me and supporting me throughout all of this, even when she's had her own research to deal with.

My advisors, especially Dr. Ehud Greenspan, for all of his guidance and encouragement. Even when he's in Israel, he manages to stay incredibly involved in all of the neutronics research at UCB. The rest of the advisors in the neutronics group – Dr. Max Fratoni, Dr. Rachel Slaybaugh, and Dr. Jasmina Vujic – were also great resources. It's nice to have a weekly meeting with up to four professors; if you have a problem, at least one of them will be able to point you in the right direction.

My family, for always being there for me.

My colleagues in the neutronics research group, especially Jeff Seifried for his mentorship when I was beginning grad school; George Zhang for being a friendly and reliable colleague whenever I needed a hand; Manuele Aufiero for his help with OpenFOAM and GPT and everything related to Serpent; Kelly Rowland for her help with the clusters; Sandra Bogetic for her help with the RBWR projects; and really just about everyone else. The entire group was a pleasure to work with.

All of the other faculty and staff in the Nuclear Engineering department, but most especially Kirsten Wimple-Hall and Sara Harmon.

My collaborators from University of Michigan, especially Andrew Hall.

My collaborators from MIT, especially Koroush Shirvan and Alex Mieloszyk.

The DOE NEUP program: This work is based upon work supported under a Department of Energy Nuclear Energy University Programs/Integrated University Programs Graduate Fellowship. Any opinions, findings, conclusions or recommendations expressed in this publication are those of the author(s) and do not necessarily reflect the views of the Department of Energy Office of Nuclear Energy. Boilerplate acknowledgement and disclaimer aside, the DOE NEUP helps so much nuclear research get off the ground.

St. Joseph the Worker Catholic Church in Berkeley – it's a beautiful church with beautiful people.

Everyone else I've met and helped me at the many conferences I went to. Reactor physics is a small field, and it's amazing to get to know everyone who's working on similar things from all over the world.

1. Introduction

Light water reactors (LWRs) are the industry standard nuclear power plant (NPP) due in large part to the vast operating experience accumulated with them. In 2013, nuclear energy provided about 5% of the world's energy usage and 13% of the world's electricity [2]; the vast majority of this is through LWRs. However, standard LWRs operate on a once-through fuel cycle that requires fuel enrichment; in the end, only 0.6% of the mined uranium is fissioned [3].

Currently, the inefficiency of how LWRs burn uranium is not much of an economic issue, since the cost of uranium is very low. However, if nuclear power is expanded significantly, then amount of uranium resources could become limiting. Additionally, if the resource utilization is increased, then the volume of waste per unit of energy generated is reduced, which is useful since the United States has not yet designated a final storage repository for nuclear fuel.

Conventionally, closing the fuel cycle has been envisioned by using fast-spectrum sodium cooled fast reactors (SFRs) with continuous recycling [4], [5]. The hard spectrum enhances breeding, which enables fuel to be recycled without limit. However, there is relatively little operating experience with these types of reactors; only three commercial SFRs (Superphénix, BN-600, and BN-800) have been built and operated. This leads to large uncertainty in the capital cost of SFRs, which is generally the most expensive part of an NPP.

It is desired to close the nuclear fuel cycle using conventional LWR technology in order to benefit from the wealth of operational experience and to minimize the necessary research and development. This dissertation focuses on closing the nuclear fuel cycle using LWR technology, particularly hard-spectrum boiling water reactors (BWRs).

1.1. History of the RBWR Project and the Motivation for Thorium

Hitachi recently proposed the use of hard spectrum resource-renewable BWRs (RBWRs) in order to close the nuclear fuel cycle [6], [7]. A hard spectrum is achieved in the RBWR cores through the use of a triangular lattice pitch, a low pitch to diameter ratio, and a high average void fraction in order to reduce the amount of coolant within the fuel assembly. The very high fissile content in the seed also contributes to spectrum hardening. The RBWR cores would use axially layered fissile "seed" and fertile "blanket" regions within the fuel pins in order to ensure negative void feedback. As the coolant boils and the spectrum hardens, more neutrons will leak into the blanket, which would drive down the reactivity. In addition, the leakage effect is enhanced by an atypical upper reflector design, in which extra B_4C is included with the pins in order to reduce reflection more than the positive reactivity feedback due to the effect of spectrum hardening on η. A typical assembly is shown in Figure 1.1, and the design parameters are compared against an ABWR in Table 1.1.

Three different depleted uranium fueled designs were proposed: the RBWR-AC, which is fuel self-sufficient, the RBWR-TB, which operates on a phaseout fuel cycle, and the RBWR-TB2, which burns its own fuel in addition to reprocessed transuranics (TRU) from LWR used nuclear fuel (UNF). The RBWR-TB and RBWR-TB2 are both TRU burning reactors with a conversion ratio (CR) of about 0.5, but in the RBWR-TB2, the extra fuel comes from reprocessed LWR

TRU, whereas for the RBWR-TB, the extra fuel is provided by other RBWR-TB units. This is shown schematically in Figure 1.2.

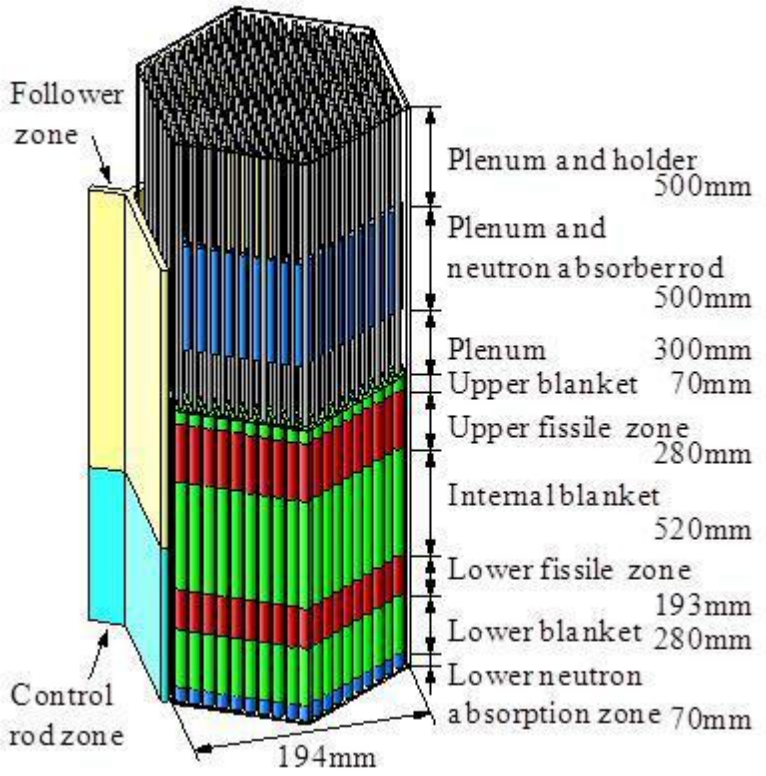

Figure 1.1. Assembly configuration of the RBWR-AC bundle [7].

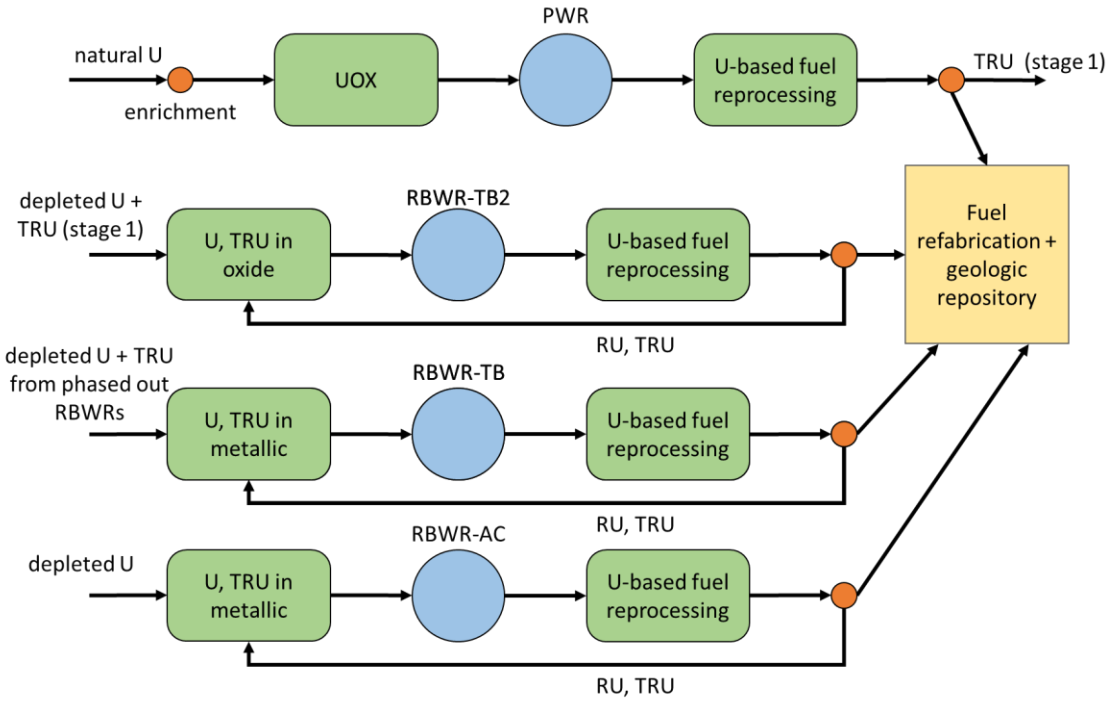

Figure 1.2. Fuel cycle scheme for the RBWR-AC, RBWR-TB, and RBWR-TB2.

Table 1.1. Comparison of the RBWR-AC and RBWR-TB2 design parameters against the ABWR [7], [8]

Parameter	ABWR	RBWR-AC	RBWR-TB2
Thermal power (MWt)	3926	3926	3926
Electric power (MWe)	1356	1356	1356
RPV Diameter (m)	7.1	7.1	7.1
Core Pressure (MPa)	7.2	7.2	7.2
Number of fuel bundles	871	720	720
Assembly pitch (cm)	15.5	19.9	19.9
Control rod type	Cruciform	Y-shaped	Y-shaped
Fuel rod height (cm)	335.5	134.3	102.5
Fuel rod diameter (mm)	10.26	10.1	7.2
Fuel rod pitch (mm)	12.95	11.4	9.4
Coolant mass Flow Rate (t/h)	5.2E+04	2.6E+04	2.4E+04

Hitachi found that the RBWR designs could achieve their design objectives, while maintaining an acceptable discharge burnup and safety margins. However, an independent EPRI evaluation conducted by the University of Michigan, MIT, and UCB found significant uncertainty in several key characteristics, including the void coefficient of reactivity, minimum critical power ratio (MCPR), and neutronic coupling between the two seed regions [9]. Although these issues were addressed in subsequent studies, further issues are discussed in Chapter 5.

Most of these issues stem from the use of two short seed regions, which is necessary in a U/Pu system in order to assure negative void feedback. It was proposed in 2011 that the use of

thorium as the fertile fuel would inherently have negative feedback, and thus eliminate the need for using multiple short seed regions and improve the safety performance of the reactors. Two major physics phenomena lead to the Th/^{233}U fuel cycle providing more negative feedback compared to the ^{238}U/Pu cycle: first, the neutron reproduction factor (η) increases more rapidly in ^{239}Pu than in ^{233}U and begins increasing from a lower energy, as shown in Figure 1.4. Additionally, thorium has a higher threshold energy for fission, as shown in Figure 1.3. As the neutron spectrum hardens, the number of fast fissions would increase more in a U/Pu system than in Th/U system. Both of these features of the Th/U fuel cycle reduce the positive feedback from spectral hardening, which reduces the need to increase leakage in order to maintain negative void feedback. This permits a single long fissile region to be used, which would significantly reduce the peak linear heat generation rate (LHGR) and improve the MCPR.

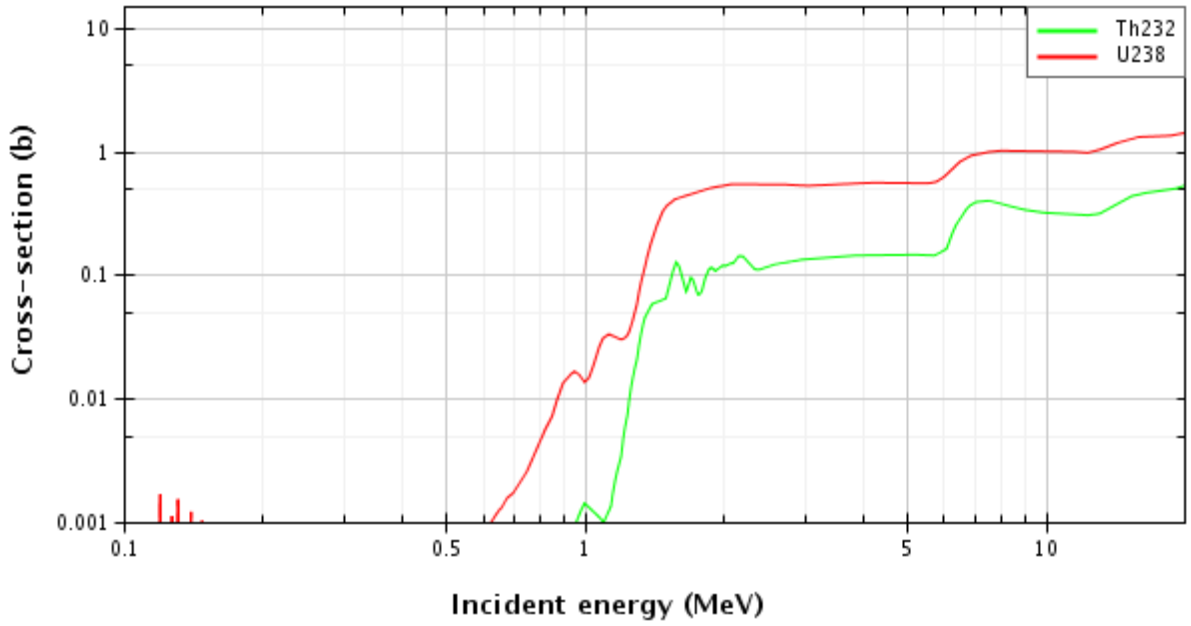

Figure 1.3. Fission cross section for ^{232}Th and ^{238}U near their threshold values. These cross sections were retrieved from the JANIS database [10] for the ENDF/B-VII.1 cross section library.

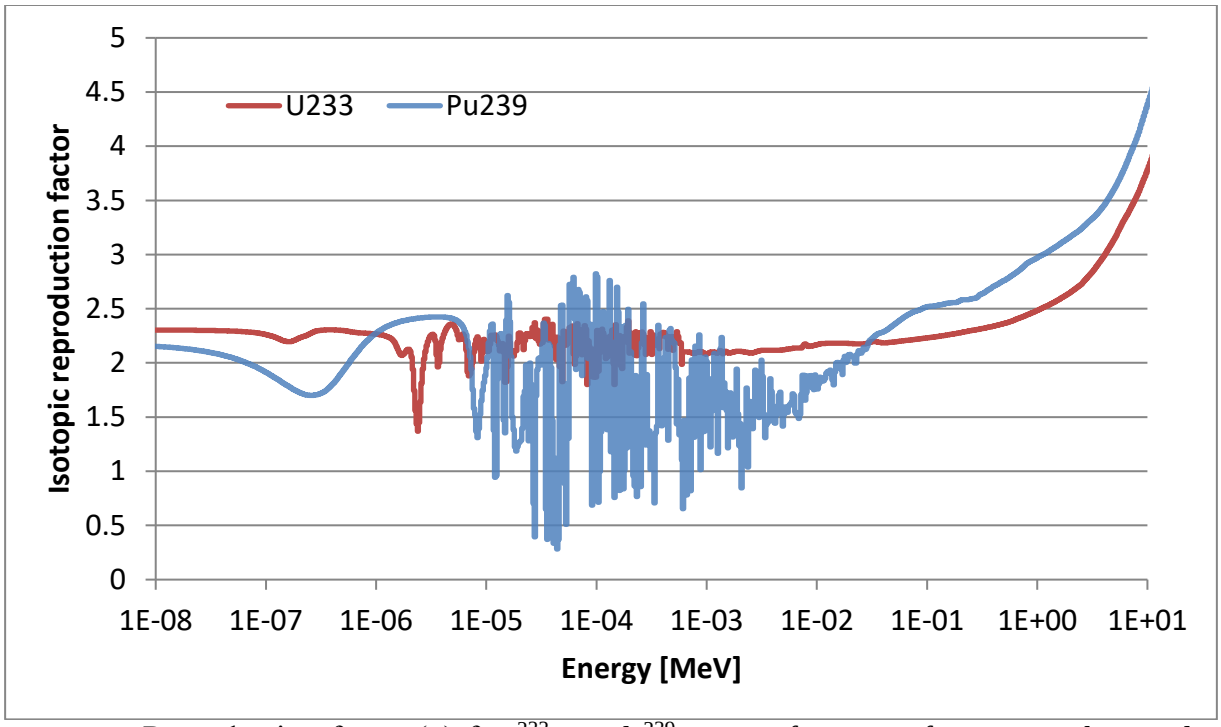

Figure 1.4. Reproduction factor (η) for ^{233}U and ^{239}Pu as a function of energy. These values were calculated using 1000 equal-lethargy bins in an MCNP5 simulation of the RBWRs; due to the fine energy resolution, this figure should be approximately simulation-independent.

1.2. Fundamental Physics Concepts

1.2.1. Flux Spectra and the Closed Fuel Cycle

Before discussing the physics of closed fuel cycles, it is important to identify the key fissile isotopes. The only naturally occurring fissile isotope is ^{235}U, and the only naturally occurring fertile isotopes are ^{232}Th and ^{238}U. U-233 may be bred from ^{232}Th after thorium absorbs a neutron and decays to ^{233}Pa and then to ^{233}U, while ^{239}Pu may be bred from ^{238}U through a similar process (^{238}U + ^{1}n → ^{239}U → ^{239}Np → ^{239}Pu). Pa-233 has a half-life of 27 days, while the half-life of ^{239}Np is one-tenth of that.

Other than the fissile isotopes produced directly through breeding in naturally-occurring fertile isotopes, ^{232}U, ^{241}Pu, ^{242}Am, ^{243}Cm, and ^{245}Cm are also fissile and are produced through irradiation and decay. Of these, ^{241}Pu is the only one which can accumulate in quantities that are significant to the neutronics. U-232 and ^{243}Cm are generally produced through (n,2n) reactions, which have a relatively low cross section. Am-242 is usually created when ^{241}Pu decays to ^{241}Am and absorbs another neutron; since ^{241}Pu has a half-life of 14.2 years, ^{242}Am is generally only produced when Pu-rich fuel is recycled. Therefore, if ^{241}Pu captures a neutron rather than fissioning, then it will likely need to absorb 3 additional neutrons in order to become fissile again (^{242}Pu to ^{245}Cm). Therefore, the vast majority of fissions will occur in ^{233}U, ^{235}U, ^{239}Pu, and ^{241}Pu. Higher actinides will still fission, but their η value will be much lower than those of fissile isotopes, and it will increase significantly with harder spectra.

A typical LWR operates on an open cycle using a thermal spectrum because the large thermal fission cross section of fissile isotopes helps minimize the required enrichment. There is not sufficient exposure to accumulate actinides heavier than Pu. However, if it is desired to operate on a closed fuel cycle, then a thermal spectrum is not sufficient, as the heavier actinides reduce the reactivity. If the reactor is designed to have a conversion ratio lower than unity, more fissile material can be loaded in to improve the reactivity (generally, reprocessed TRU from LWR waste), but too much accumulation of these higher actinides leads to positive void feedback. The impact of these actinides on the void feedback is discussed further in Section 1.2.3.

These issues are not so problematic for fast reactors. The non-fissile actinides have a threshold fission energy, so a fast spectrum is much better at incinerating these isotopes. Additionally, the η of fissile isotopes is generally higher in a fast energy range, which increases the infinite multiplication factor (k_∞) relative to a thermal spectrum. Lastly, the absorption cross section of fission products is reduced significantly more than that of actinides in the fast spectrum, leading to less parasitic absorption. However, this is counterbalanced by the fact that fast reactors have more leakage due to the larger neutron path length. In a multi-recycling system, hardening the spectrum has a net effect of increasing the achievable burnup if everything else is held equal; however, a higher enrichment is needed to sustain criticality.

In a burner reactor (where the objective is to have a conversion ratio lower than unity), the need to have a low conversion ratio is balanced by the need to have an economically acceptable cycle length. Typically in sodium fast reactors which function as burners, lowering the conversion ratio is achieved by increasing the TRU enrichment [4], [11], but that is not feasible for a LWR due to the necessity to have negative void feedback.

When using light water as a coolant, it is not feasible to achieve as hard of a spectrum as in an SFR, since hydrogen is a very effective moderator. However, the RBWRs manage to achieve an epithermal spectrum by using a triangular lattice pitch and a high exit void fraction to reduce the hydrogen to heavy metal ratio (H/HM), and by using a very high TRU concentration in the seed regions. Representative flux spectra are shown in Figure 1.5, while the spectra of neutrons which induce fission are shown in Figure 1.6 and tabulated in Table 1.2. The water density distribution is compared in Figure 1.7. Both the RBWR-SSH and the RBWR-TR are intermediate spectrum reactors, since more than half of their fissions are induced by neutrons between 1 eV and 0.1 MeV; the resonance region is much more important than in fast reactors or in thermal reactors. The fast region is also much more important than in a normal LWR, as well.

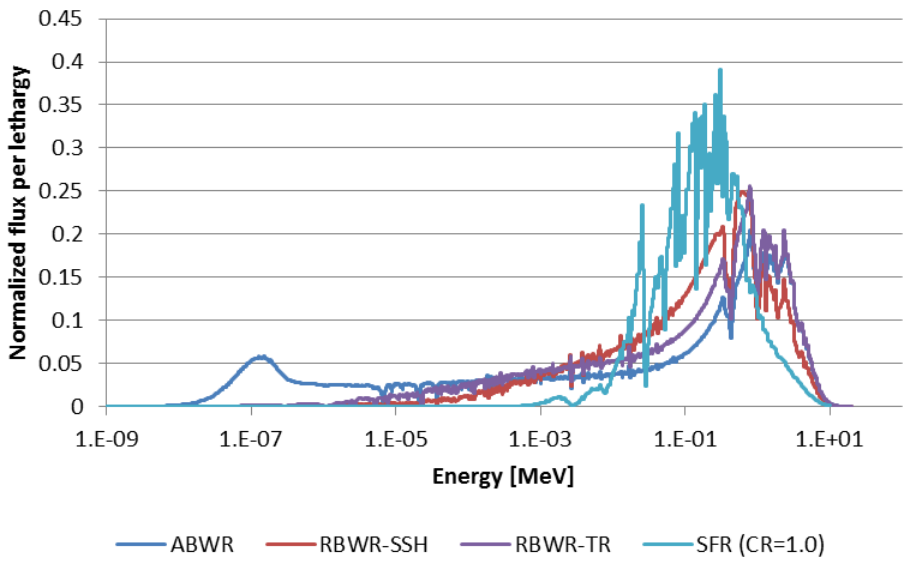

Figure 1.5. Flux of neutrons in the RBWR reactors compared against a thermal reactor (ABWR) and a fast reactor (SFR).

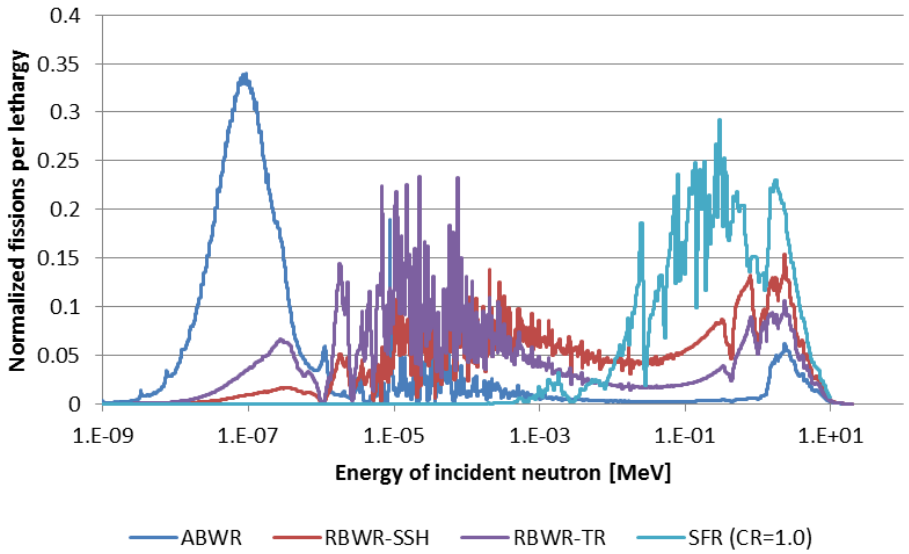

Figure 1.6. Spectrum of neutrons inducing fission in the RBWR reactors compared against a thermal reactor (ABWR) and a fast reactor (SFR).

Table 1.2. Fissions induced by thermal, epithermal, and fast neutrons in each reactor.

Energy range	ABWR	RBWR-TR	RBWR-SSH	SFR (CR=1.0)
< 1 eV	79.3%	13.4%	3.7%	0.0%
1 eV - 0.1 MeV	13.7%	64.5%	60.8%	28.3%
> 0.1 MeV	7.0%	22.1%	35.6%	71.7%

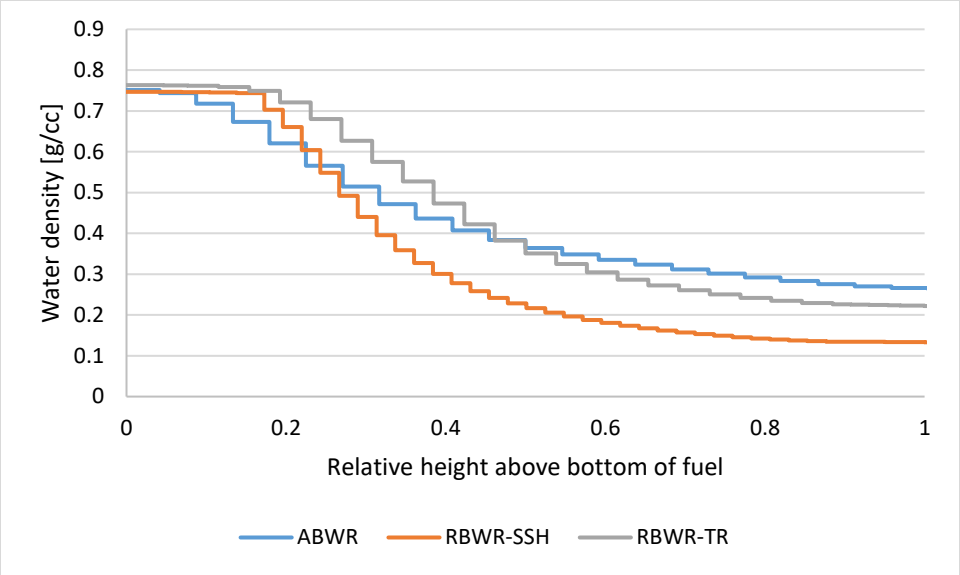

Figure 1.7. Water density comparison between the ABWR, RBWR-SSH, and RBWR-TR.

1.2.2. Thermal Hydraulics

1.2.2.1. Critical heat flux

Like a typical BWR, the RBWRs operate in an annular film boiling regime. As the water boils, the bubbles detach from the rod surface and coalesce into a vapor channel in the center of the flow channel, while the liquid water remains attached to the rod surface. Further up the flow channel, bubble formation is suppressed, and instead the vapor evaporates off of the liquid film's surface. As liquid film thickness decreases, the rod surface temperature reduces, since there is less thermal resistance between the rod surface and the bulk coolant (whose temperature is essentially fixed at the saturation temperature). However, if the liquid film thickness is ever completely depleted, then the heat transfer coefficient plummets since the vapor is much less effective at transferring heat, which causes the wall temperature to spike. This usually leads to fuel failure, and is referred to as dryout [12]. The different flow regimes and heat transfer regimes process are shown pictorially in Figure 1.8.

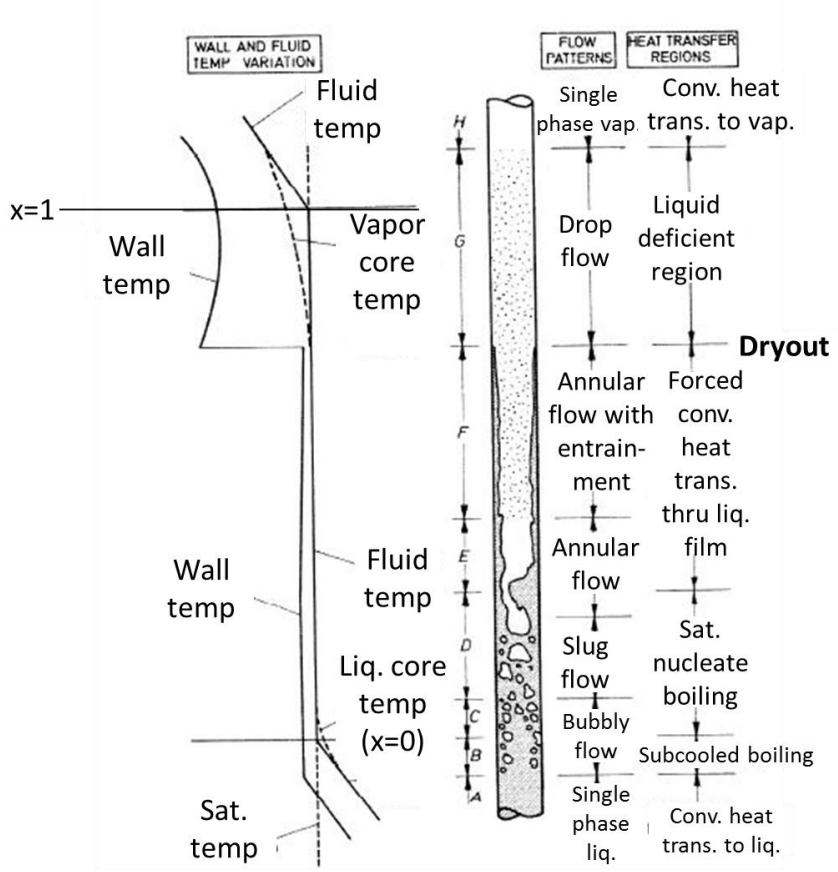

Figure 1.8. Annular flow development with a constant heat flux. Figure adapted from [13] with modifications to improve legibility.

For predicting critical heat flux in standard BWRs, the boiling length approach used by the CISE-4 correlation is a reasonable representation which is easy to use, as it does not require subchannel analysis or pin peaking factors [14]. The general form of the CISE-4 correlation is reproduced below from [12]:

$$x_{cr} = \frac{D_e}{D_h}\left(\frac{aL_b(z)}{L_b(z)+b}\right)$$

$$a = a\left(G, P/P_c\right)$$

$$b = b\left(G, P/P_c, D_e\right)$$

where L_b is the boiling length (defined as the length from the onset of boiling to the point of critical heat flux), D_e is the hydraulic diameter in meters, D_h is the heated diameter in meters, G is the coolant mass flux in kg/m^{2}s, P is the pressure, and P_c is the critical pressure. The empirical constants *a* and *b* vary in different implementations of the correlation. In this approach, the critical quality (x_{cr}) is found for every location along the fuel pin, which is used to calculate the critical power which is necessary to initiate dryout at each point. The critical power ratio (CPR)

is then the ratio of the critical power to the actual power, and the minimum critical power ratio (MCPR) is the minimum CPR in the fuel assembly. The MCPR should always remain above 1, and higher values indicate more margin against dryout. Typically in BWRs, the MCPR is 1.3 or higher in steady state operation in order to provide margin for uncertainty and transients [14]. As discussed in Section 2.4, the RBWR cores feature a very tight lattice which is outside the range of applicability of most correlations.

In general, increasing the boiling length benefits the MCPR, although it has a gradually smaller effect as the length is increased. Similarly, using smaller diameter fuel increases the surface area to volume ratio of the fuel, which improves the MCPR. Reducing the mass flux increases the critical quality, as it reduces the liquid droplets which are entrained in the vapor area, but if the total coolant flow rate is reduced with the mass flux, then the actual quality increases more than the critical quality. In other words, there is a benefit from using a larger flow area. The coolant velocity contributes to reducing the thickness of the liquid film due to shear action of the film [12]; since the velocity is $v = \dot{m}/(\rho A)$, increasing the flow area reduces the velocity and increases the margin against dryout. Reducing the coolant mass flow rate will not benefit the MCPR since it reduces the coolant quality, which is typically more important than the coolant velocity for determining the MCPR.

Along a fuel assembly, the CPR tends to start off high at the onset of two-phase flow, and gradually drops as the coolant is heated up. In the RBWRs, the MCPR is usually at the exit of the seed, since the blankets have a much lower power density.

1.2.2.2. Void fraction

There are many different approaches with varying complexity to solve two-phase flow problems. For the equilibrium analysis of the RBWRs, the main objective is to calculate the pressure drop and water density distribution in steady state conditions; for this, a 4-equation drift flux model is typically sufficient [12], [14]. In a 4-equation model, conservation equations are defined for the mixture mass, mixture energy, mixture momentum, and vapor mass, while an empirical relationship is used to define the relationship between the different phase velocities. In the drift flux formulation, the void fraction is expressed as

$$\alpha = \frac{1}{C_0\left(1+\frac{1-x}{x}\frac{\rho_v}{\rho_l}\right)+\frac{V_{vj}\rho_v}{xG}}$$

where α is the void fraction, C_0 is an empirical constant to describe the radial nonuniformities, and V_{vj} is the drift velocity (which is the relative velocity of the vapor relative to the mixture average) [12]. C_0 and V_{vj} are both empirically determined.

The transition between flow regimes indicated in Figure 1.8 has significant impact on the prediction of the void fraction. Similarly to the CPR, the tight lattice used in the RBWR bundles significantly increases the empirical uncertainty in the void fraction, as discussed further in Section 2.4.

1.2.2.3. Pressure drop

As the coolant flows through the fuel assemblies and heats up, it loses pressure through frictional losses. The pressure drop for two-phase flows is calculated using the following expression [12]:

$$-\Delta p = \Delta\left(\frac{x^2 G^2}{\rho_v \alpha} + \frac{(1-x)^2 G^2}{\rho_l (1-\alpha)}\right) + \phi_{lo}^2 \frac{f_{lo} L}{D_e}\left(\frac{G^2}{2\rho_l}\right) + \sum K \frac{G^2}{2\rho_l}\Psi + \rho g L \cos\theta$$

where x is the quality, α is the void fraction, ρ is the density, G is the mass flux, L is the flow length, ϕ_{lo}^2 is the two-phase friction multiplier, f_{lo} is the liquid-only friction factor, D_e is the hydraulic diameter, K is the local form loss factor, Ψ is the local two-phase loss multiplier, θ is the angle of the flow, and the subscripts *l* and *v* indicate liquid and vapor phases. The first term is the acceleration term, which is positive if the coolant is heated while changing phase; if the fuel is unheated, then this term is zero. The second term is the friction term and the third is the local loss term, which are both always positive. The last term is the gravity term; although this term is important across an entire loop (especially when considering natural circulation), it is nearly negligible in the core region compared to the other two terms.

Increasing the flow rate increases the pressure drop, but the pressure drop does not quite follow the square of the flow rate; if the area is held constant, then increasing the flow rate reduces the quality, which reduces the two-phase friction multiplier (ϕ_{lo}^2). Increasing the flow area and increasing the hydraulic diameter would strongly reduce the pressure drop. The two-phase friction multiplier is very important; the frictional pressure drop in the single-phase region is nearly negligible, while the frictional pressure drop in the two-phase region is significant.

1.2.3. Reactivity Feedback

As the reactor changes conditions, the multiplication factor may either increase or decrease. In order to maintain safe operation of the reactor, it is essential that the reactor is characterized by negative feedback; that is, any attempts to increase the power will reduce the reactivity.

1.2.3.1. Fuel Temperature Feedback

All isotopes have resonances where the likelihood of interaction is increased. These resonances occur at lower energies and with a higher frequency for heavy isotopes, such as actinides. The width and height of these resonances are temperature dependent; the thermal energy of a nucleus might not be negligible compared to the resonance energy, which causes the width of the resonance to increase with increasing temperature. This phenomenon is referred to as Doppler broadening due to its similarity to the Doppler effect, and is shown graphically in Figure 1.9.

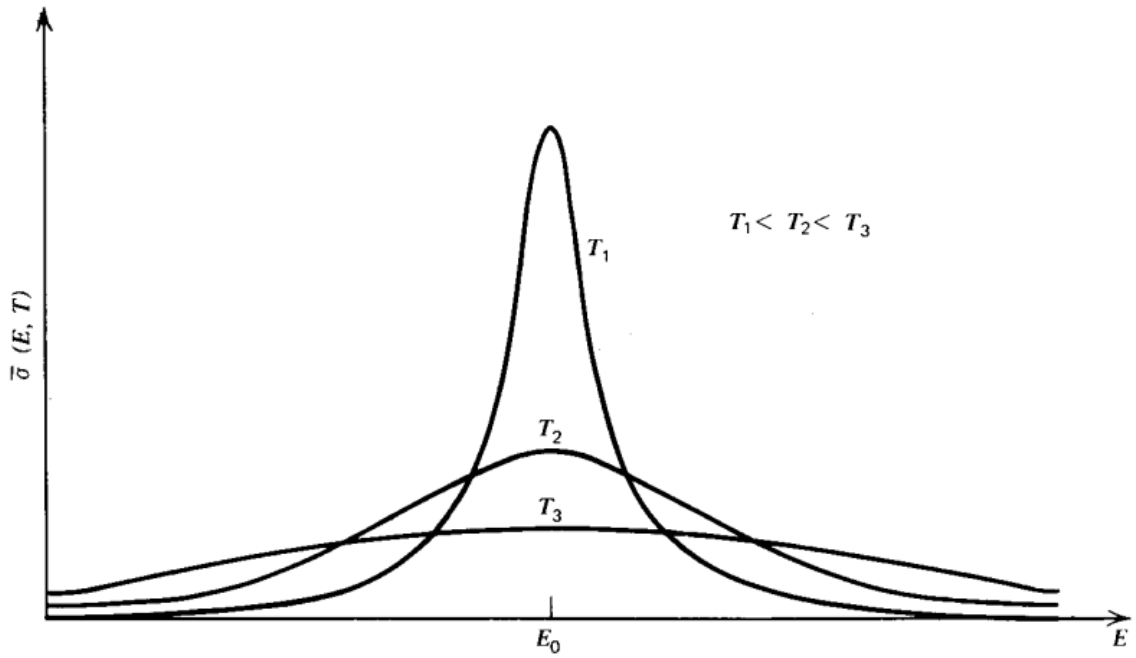

Figure 1.9. Doppler broadening of a cross section, reproduced from [15].

Although the area underneath the resonance is nearly unchanged, increasing the fuel temperature widens the energy range that absorption may occur. This leads to reduced energy self-shielding (in which a resonance peak reduces the flux around that peak) since the peak cross section is reduced, and the overall absorption rate increases. In fuel with a large amount of fertile isotopes, this causes the capture in the fertile material to increase more than the fissions in the fissile fuel, which causes the net reactivity feedback to be negative. If the fuel is mostly fissile, though, then the Doppler effect is nearly zero, since the increase in the likelihood of fissions compensates for the reactivity drop due to enhanced capture. This is the case Hitachi RBWR core designs.

1.2.3.2. Coolant Void Feedback

In a water-cooled system, the coolant functions as a moderator which softens the spectrum. LWRs are designed to be undermoderated so increasing moderation to increases the net reactivity, since thermal neutrons fission readily. If the system is not undermoderated, then the increase in coolant absorption will cause the reactivity to decrease.

In sodium-cooled fast reactors, though, the physics is significantly different. No neutrons reach thermal energies since the sodium is very ineffective at neutron moderation. When the sodium voids, the spectrum will harden slightly, which causes more fast fissions to occur in non-fissile isotopes, increasing the reactivity. Additionally, the neutron reproduction factor (η) of the fuel will slightly increase. This makes a strong positive contribution to the sodium void reactivity feedback. Most sodium fast reactors are designed to be very highly leaking in order to reduce the positive feedback [16]; as the coolant density reduces and the spectrum hardens, the leakage increases, which reduces the reactivity. Nevertheless, the net sodium void worth is positive for most SFRs. It is compensated by the negative feedback due to the Doppler effect, core radial expansion, core axial expansion, and control rod drive expansion so that the power coefficient of reactivity is negative. RBWR cores lack the thermal expansion related negative reactivity

mechanisms, since the coolant (and therefore structural materials) remain at the saturation temperature.

RBWRs function similarly to both SFRs and LWRs. Since the neutron spectrum is significantly harder than that of a typical LWR, the reactivity increase from hardening the spectrum by voiding the coolant is not negligible. The accumulation of higher actinides tends to drive the void coefficient positive, as the fast fission cross section of higher actinides is typically higher than ^{238}U or ^{232}Th and their fission threshold energy tends to be lower. Since the RBWR seed sections are much shorter than typical LWR active fuel, the increased leakage from hardening the spectrum makes it possible to achieve negative coolant void feedback.

1.2.4. Shutdown Margin

It is important for reactor to be able to be shut down at any point in the cycle. There are four major components to the shutdown margin: excess reactivity, fuel temperature reactivity worth, coolant void worth, and control rod worth.

The reactor needs enough reactivity to last an entire cycle; the excess of which is called the excess reactivity. If the reactivity at the beginning of cycle (BOC) is significantly different than the reactivity at the end of cycle (EOC), then it can be difficult to shut down the reactor, as more control rods will be needed to keep the reactor critical at operating conditions and will not be able to overcome the other positive reactivity insertions.

As the fuel cools down, the Doppler feedback provides a positive reactivity insertion, since the temperature coefficient is required to be negative. Similarly, as the reactor is flooded with room temperature water, the reactivity generally increases, unless the coolant void coefficient is strongly positive (which is forbidden in LWRs). If the temperature coefficients are too negative, then it will be impossible to maintain sufficient shutdown margin; in effect, the shutdown margin effectively places limits how negative these coefficients may be.

The control rod worth is the main negative reactivity mechanism when shutting down the core. The shutdown margin is usually reported with the highest worth control rod fully withdrawn, in order to remain in compliance with single failure criteria.

1.3. Previous Thorium RBWR Design Work

Some early scoping studies were performed for the self-sustaining thorium fueled RBWR (RBWR-Th) [17]–[19] before this study, using pure thorium as the feed. These studies concluded that the concept was feasible, and that a negative void coefficient could be achieved while using a single elongated seed. Additionally, it was observed that the void coefficient correlation used by Hitachi tended to overpredict the void fraction, which would overestimate the achievable burnup [18]. This research into self-sustaining designs is extended in Chapter 3 of this dissertation.

Additionally, prior research was performed in the University of Cambridge into thorium fueled low-conversion RBWRs with axially homogeneous, radially heterogeneous assemblies [20]–[22]. The objectives of this research were largely the same as in Chapter 4; however, the methods used are different, and there were a few key differences: firstly, in the Cambridge

studies, pin powers were not considered, while they were considered in the present work; secondly, reprocessing losses were not implemented in the Cambridge work, while they were implemented in this study. As shown in Chapter 4, radially heterogeneous fuels provide significantly peaked power distributions within the assembly, and the reprocessing losses significantly reduce the achievable discharge burnup.

1.4. Scope of Study

This dissertation documents the development of different thorium-based RBWRs and the methods to assess their performance. There are four main chapters.

Chapter 2 describes the methodology that was used to analyze the different cores at different levels. The codes which were used are briefly described, as well as the implementation of these codes. The methodology which was used to arrive at the final designs for Chapters 3 and 4 is also described.

Chapter 3 summarizes the results of the parametric studies which were done to arrive at the final design of the self-sustaining thorium fueled RBWR (the RBWR-SS). It was designed to maximize the discharge burnup when fed only fertile fuel in the seed makeup while still maintaining adequate safety margins. The uncertainties of several neutronics parameters and the fuel cycle impacts are presented for the final design based on an assembly level analysis. The full-core performance is compared against the Hitachi-designed RBWR-AC.

Chapter 4 similarly documents the design of the low-conversion RBWR-TR, and compares its full-core performance against the Hitachi-designed RBWR-TB2. It was designed to maximize the TRU consumption rate while maintaining an adequate cycle length for economic considerations, in addition to the required safety margins. As in the previous chapter, the uncertainties of several neutronics parameters and the fuel cycle impacts of this design are presented, based on an assembly level analysis. In addition, a variant which uses a traditional square lattice instead of the typical RBWR square lattice is documented.

Chapter 5 presents further investigations into the Hitachi-designed RBWR-TB2. This work has not been published prior to this dissertation, but it was performed as part of a contract for Hitachi. Several challenges to the dual-seed approach used by Hitachi are investigated.

In addition to the main text, six appendices are included. Appendix A shows the benchmark between a single assembly in Serpent and PARCS for the RBWR-SSH and the RBWR-TR cores in order to build confidence in the core simulator. Appendix B documents several changes in phenomena between the assembly-level and full core-level models. Appendix C contains a list of the input files used in this dissertation, as well as their location on the Savio cluster. Appendix D contains a small script used to calculate the water density covariance for the RBWR-TB2 for the results of Section 5.3.3; the changes required for it to apply to the other designs are also noted.

2. Methodology

2.1. Necessity for 3-D Cross Section Generation

With the parfait-style RBWR cores, two-dimensional multigroup cross section generation commonly used for deterministic codes is insufficient to accurately simulate the cores. As shown in Section 4 of Reference [23], 2D cross sections lead to a significant overestimation of the k_{eff} and fission rate. When there is an abrupt material change, the spectrum in one region can be significantly different than the spectrum of neutrons leaking from the adjacent region, which invalidates the multigroup cross sections.

For the lattice level calculation used to calculate the equilibrium composition and most of the physics, the issue was circumvented by using MCNP5 for the neutronics (as described in Section 2.5). However, calculating the equilibrium cycle with a full core model is not feasible, since far more histories would be required to achieve converged results, and an inordinate amount of memory would be required to store the material compositions for burnup. Therefore, the Serpent/PARCS/PATHS core simulator was developed for the RBWR projects [23, 24] in order to find the equilibrium full core using axial discontinuity factors to correct the simulation (Section 2.6). In this code suite, Serpent is used for cross section generation using a 3-D assembly unit cell model.

2.2. Design Constraints

In Chapters 3 and 4, new cores are designed, which needed to conform to several constraints, mostly related to the safety of the reactors. They are listed and described below.

1. All transfertile (TRF) material should be recycled. In addition, in Chapter 3, all uranium should also be recycled, since it would not be feasible to isotopically separate the fissile ^{233}U from the fertile ^{238}U. It is assumed that 1.2% of the heavy metals will be lost in recycling and fabrication processes.

2. The core should fit within an ABWR pressure vessel. In practice, this meant using the same number of assemblies and the same assembly dimensions as the Hitachi-designed RBWRs.

3. Provide the full ABWR power in order to keep the design economical and to meet the same demands as the ABWR.

4. Maintain criticality in the equilibrium cycle. The approach to equilibrium was not assessed in this study.

5. Possess negative coefficients of reactivity for fuel temperature, coolant void, and power.

6. Have sufficient shutdown margin to shut down the core at any point in the cycle.

7. Remain compatible with the ABWR pumps. In Chapter 3, this mostly limited the core pressure drop to ≤ 0.3 MPa; in Chapter 4, this also limited the core flow rate to 120% of the ABWR flow rate.

8. Avoid coolant dryout. The implementation of this constraint is discussed in Section 2.4.

9. Operate with a two-phase density wave oscillation decay ratio ≤ 0.7. This was not evaluated in this study for the latest designs; however, if the coolant void coefficients are very close to zero, then this should not be an issue. Additionally, if the exit quality exceeds 40%, then it becomes significantly more difficult to achieve stability.

2.3. Design Variables

A number of design variables were used to meet the constraints. They are listed and described below.

1. The fuel geometry within the assembly was flexible. The design variables included the number of fuel pins, the pin pitch-to-diameter ratio (P/D), and pin diameter, although only two could be changed independently, since the total assembly size was constrained. The ratio of cladding thickness to the pin diameter was held constant.

2. The length and number of axial regions were variable. However, since many of the issues noticed from the Hitachi RBWR design stemmed from the use of multiple seeds (Chapters 1 and 5), it was quickly decided to use only one seed.

3. In Chapter 3, depleted uranium was mixed in with the thorium for the seed makeup stream, while in Chapter 4, recycled PWR TRU was added. In either case, the fraction of the additive (either DU or TRU) in the seed makeup was a variable. The axial blankets always remained pure ThO_2 for the fresh fuel.

4. The coolant mass flow rate was a design variable.

5. The fuel residence time or depletion time was a design variable. However, this variable was effectively determined so that the core was critical at the end of cycle (EOC).

These design variables were selected for their influence on the heavy metal loading, the moderator-to-fuel ratio (H/HM), the axial leakage probability, and flow conditions.

In addition, the void fraction correlation and critical power correlation was considered, but these are not truly design decisions as much as a change of assumptions.

2.4. T/H Correlations

Since the RBWR cores use a tight lattice with a high void fraction in order to achieve their epithermal spectra, they may be outside the range of the standard thermal hydraulic (T/H) correlations. In particular, the results are sensitive to the assumed correlations for the void fraction and the critical power ratio (CPR).

As noted in [14], the standard Chexal-Lellouche void fraction correlation (also known as the RELAP correlation as it is used in the RELAP5 computer code [25]) overpredicts the void fraction in tight lattices. Nonetheless, it has a wide range of validity, and is used as an upper bound for the void fraction prediction for the self-sustaining designs (Chapter 3). The Liao,

Parlos, and Griffith (LPG) correlation is used as a best estimate and a lower bound for the void fraction prediction in the self-sustaining design [14]. For the TRU-burning design (Chapter 4), the P/D is larger, and the hydraulic diameter is more comparable to typical BWRs, so the RELAP correlation is sufficient.

The critical power ratio has similarly large experimental uncertainty in tight lattice bundles [14]. The CISE-4 correlation [12] was adapted for use with these tight light bundles, due to its dependence on bundle average correlations, rather than requiring subchannel analysis [14]. Hitachi developed a proprietary modification to the CISE-4 correlation (H-CISE), which it used for both the self-sustaining RBWR-AC and the low-conversion RBWR-TB2; a minimum CPR (MCPR) of 1.3 was used in both designs, using a margin of 0.1 for uncertainty and 0.2 for transients. Collaborators at MIT found that when compared against data in the open literature, the H-CISE correlation tended to unconservatively overestimate the MCPR in the RBWR rod bundles; therefore, the MIT-modified CISE-4 correlation (M-CISE) was derived from the data available in open literature [14]. Due to the large experimental uncertainty in the open literature, an MCPR limit of 1.5 was recommended, in which the margin for uncertainty was increased from 0.1 to 0.3. Later, another MIT-modified CISE-4 correlation (MFP-CISE) was derived with a smaller uncertainty and a narrower range of applicability in order to use the 1.3 CPR limit [26].

The H-CISE correlation with an MCPR limit of 1.3 was used the "best-case" assumption for all designs. The limits of applicability of the M-CISE and the MFP-CISE correlation are shown in Table 2.1.

Table 2.1. Range of applicability and limits of the MIT-modified CISE correlations.

Paramter	**M-CISE**	**MFP-CISE**
MCPR limit	1.5	1.3
Mass flux [kg/m^2-s]	100 - 2035	500 - 1500
Pressure [MPa]	1.0 - 8.6	6.5 - 7.5
Hydraulic diameter [mm]	2.35 - 7.03	2.8 - 7.5
Heated diameter [mm]	3.56 - 10.95	3.56 - 10.95
Rod diameter [mm]	6.35 - 13	6.35 – 13

Within the assembly-level calculations, the full core MCPR was estimated for the peak assembly by multiplying the power at each axial location by the assumed core radial peaking factor and a 5% overpower factor, while simultaneously reducing the flow rate by 5%. For the full core MCPR calculations, the assembly MCPR was calculated for each assembly with a 5% overpower factor, and the minimum value was reported.

2.5. MocDown

MocDown [27] is a code whose primary use in this dissertation is to find the equilibrium fuel composition for a given design. It was additionally used to find a self-consistent water density distribution for a given time step. As a brief overview, MocDown functions by iteratively executing MCNP [28] for neutron transport and ORIGEN [29] for depletion analysis while recycling the fuel according to a user-defined recycling function. Optionally, it may also iterate between MCNP and a thermal hydraulic solver for a self-consistent water density distribution. The recycling functions used in this dissertation are available in the

`/global/home/groups/co_nuclear/MocDown` directory on the Savio cluster; more details regarding the programming will be available in a forthcoming internal UCB technical report.

As implemented for these studies, the PATHS module [30] was used to calculate the water density distribution, using the power distribution calculated from MCNP. MCNP uses the water density distribution to update the power distribution; MCNP and PATHS are iteratively executed until the p-∞ norm of the water densities is reduced below a user-specified limit. After each burnup step, one-group cross sections for each isotope and one-group fluxes for each cell are passed to ORIGEN2.2, which solves the Batemann equations to find the composition at the next step. Since one ORIGEN run is used per MCNP cell and each of these runs are independent, the ORIGEN runs are executed in parallel. Once the last depletion step is reached, MocDown recycles the fuel according to a user-defined recycling function. The coupling between each module is shown in Figure 2.1.

MocDown uses an accelerated equilibrium search scheme, which is shown in Figure 2.2. After a fully coupled cycle, the cross sections and flux magnitudes as a function of burnup are held constant, and ORIGEN is run stand-alone for several cycles until the compositions reach a pseudo-equilibrium such that the difference in isotopic number density of each isotope in each cell is less than a user-specified isotopic convergence criterion. After converging on this pseudo-equilibrium, another fully coupled cycle is run to update the cross sections. If the difference in cycle-averaged multiplication factor is less than the user-specified k convergence criterion, then the simulation ends.

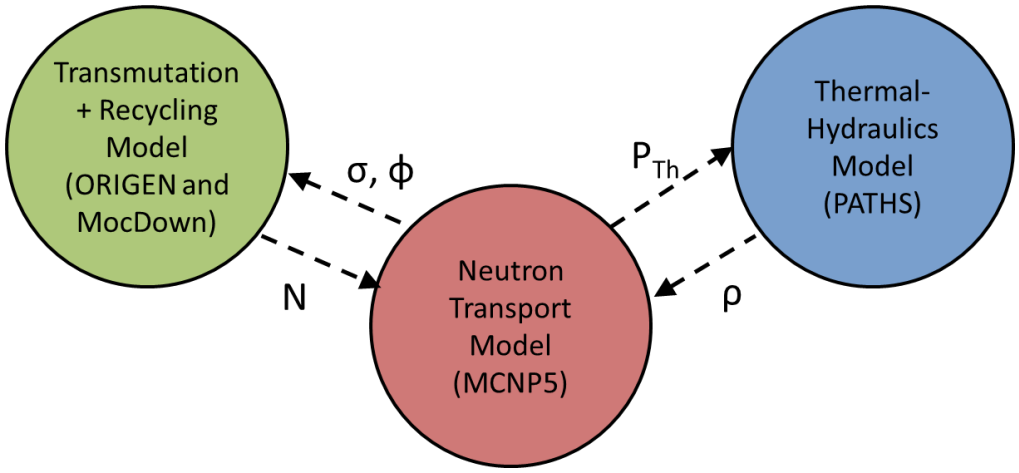

Figure 2.1. Coupling between the different modules within MocDown.

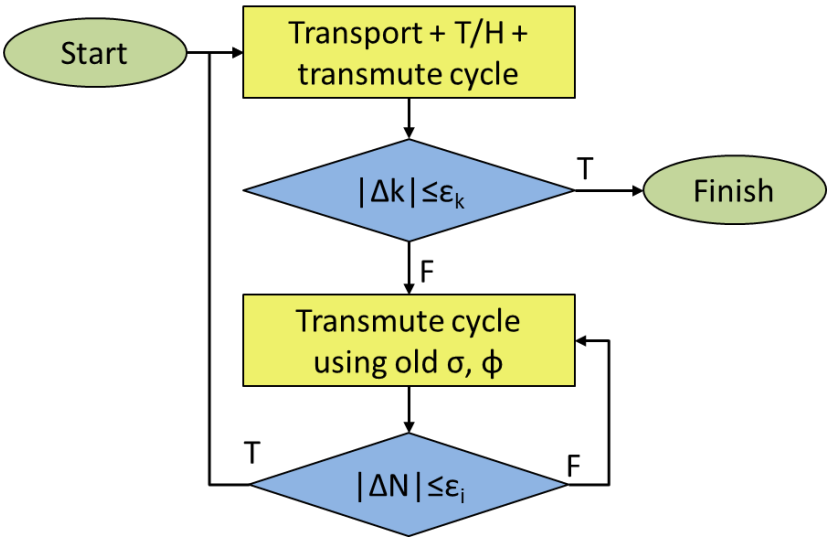

Figure 2.2. Computational flow scheme for MocDown.

2.5.1. MCNP5

MCNP is a Monte Carlo neutron transport code developed by Los Alamos National Laboratory [28]. It can also perform electron and photon transport, but these capabilities were not used in this work. It uses point-wise (continuous energy) cross sections with combinatorial geometry to calculate the eigenvalue for critical systems, and (if requested) can also calculate flux magnitudes, spectra, reaction rates, and leakage rates.

MCNP5.1.60 was used for neutron transport within MocDown. MCNP6 had been released when this work was started; however, it features a bug when rotating hexagonal lattices, which was relevant for this work. It also features a 20% increased run time compared to MCNP5.

For the equilibrium calculations for the RBWR designs, a three-assembly unit cell centered around the control blade was used. The unit cell for each design is shown in each relevant chapter. The geometry was modeled explicitly in order to accurately capture the physics. Average conditions (flow rate, power, control rods) were used at all burnup points; therefore, the control rods were not modelled, since they were never inserted. ENDF/B-VII.0 cross sections [31] were used for all simulations. S(α,β) thermal scattering models were used for water.

2.5.2. PATHS

PATHS [30] is a drift-flux solver within the PARCS [32] code system, used for steady state T/H analysis. It features the LPG and RELAP correlations used for the RBWR. MocDown was modified to run a stand-alone single assembly model using the power distribution from MCNP, and pass resulting the water density distribution to the MCNP input for the next iteration. The pressure as a function of axial location was also read from the PATHS outputs; since the critical power ratio is pressure dependent, the stand-alone model was run again using the conditions for the MCPR calculation (5% overpower including radial peaking and 5% reduced flow) and the pressure was used to calculate the MCPR. The form losses assume that the central orifice scheme is used, which has the lowest pressure drop. The updated executable files and example inputs are available in the `/global/home/groups/co_nuclear/MocDown` directory on the Savio

cluster; more details regarding the programming will be available in a forthcoming internal UCB technical report.

Although the water density distribution is the only parameter used within the neutronics calculation, the pressure drop is also calculated in PATHS. The pressure drop of a single assembly with average conditions does not match the pressure drop in the full core very well, since the radial power peaking and flow distribution will increase the pressure drop; nonetheless, it is useful to assess the changes in pressure drop when design variables are changed.

2.6. Serpent/PARCS Core Simulator

Since modeling a full equilibrium core with fuel shuffling is intractable in a Monte Carlo code due to the large dominance ratio leading to a very long computational time, deterministic codes were used for the full core simulation. Serpent, a Monte Carlo code, was applied to a 3-D assembly unit cell for cross section generation, which is discussed in Section 2.6.1. GenPMAXS (Section 2.6.2) was used to prepare the cross sections, and the PARCS/PATHS code suite (Section 2.6.3) was used model the full core. The computational flow is shown in Figure 2.3.

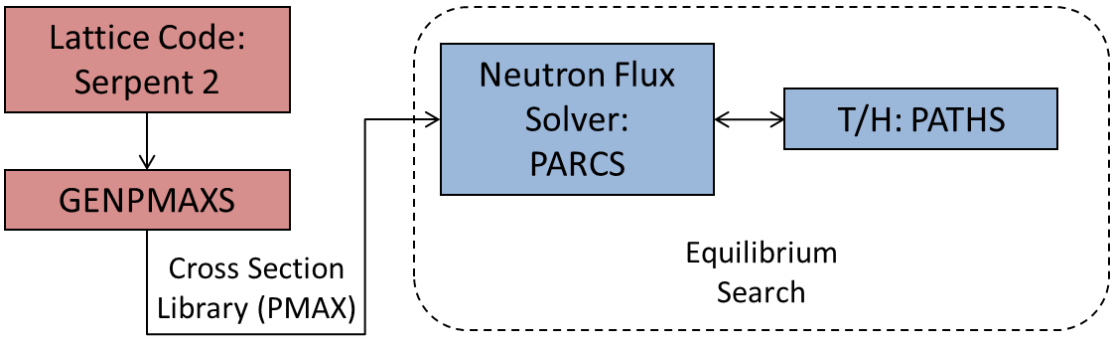

Figure 2.3. Interaction between the different codes in the Serpent/PARCS core simulator.

2.6.1. Serpent and SerpentXS

Serpent [33] is a Monte Carlo code tailored to reactor physics applications which uses a unified energy grid and Woodcock delta-tracking to reduce the computational time relative to traditional ray-tracing codes such as MCNP [28]. It also uses the CRAM method [34] to solve the matrix exponential for burnup analysis.

The continuous energy data libraries in the ENDF format do not use a consistent energy indexing scheme from isotope to isotope. Therefore, when determining the cross sections for a neutron at a particular energy in a region with multiple isotopes, the procedure to look up the cross section value must be repeated for every isotope, which is time consuming. Serpent re-indexes all of the cross sections on a single energy grid, so that the same index may be used to find the cross section at a particular energy for every isotope. This uses much more memory, so it may optionally be disabled.

Additionally, Serpent saves time by using Woodcock delta-tracking in addition to traditional ray tracing. For each neutron history in traditional ray tracing, the distance to the next collision is sampled using the total cross section within the current material. If the distance to the boundary

is shorter than the distance to the collision, then the neutron is moved to the boundary, and the process is repeated. A significant amount of computational time is spent moving the particle to the boundary and determining the material at each interface; Woodcock delta-tracking reduces the time spent tracing each ray by using the largest cross section along the neutron's current flight path, rather than the cross section of the material where the neutron currently is. Since this cross section is the same across the entire flight path, the same flight path is not calculated many times. In order to preserve the "fairness" of the Monte Carlo simulation, each collision may be rejected as a "virtual" collision, with a probability equal to $1-\Sigma_m/\Sigma_M$, where Σ_m is the material cross section where the collision takes place, and Σ_M is the largest cross section along the flight path. This method can increase the computational time spent when there are small amounts of strongly absorbing material present, so Serpent switches between conventional ray tracing and delta-tracking based on the probability of physical collisions occurring.

Unfortunately, delta-tracking precludes the use of a track length-based tally estimate, so Serpent can only use a collision-based estimator. This significantly increases the uncertainty in zones which are optically thin, even if the flux is very high.

Since Serpent was being used to generate cross section libraries for a deterministic code, it was necessary to use the same T/H conditions for each burnup step, regardless of power distribution. A library of cross sections was created for each discrete node, so that PARCS could use the water density, fuel temperature, and control rod insertion depth to interpolate to use appropriate cross sections. A set of four different "histories" were used to deplete the fuel at different conditions, and at each burnup point for each history, twelve instantaneous "branches" were used. This is shown in general in Figure 2.4, while the different conditions used in the simulation of the thorium RBWRs are shown in Table 2.2.

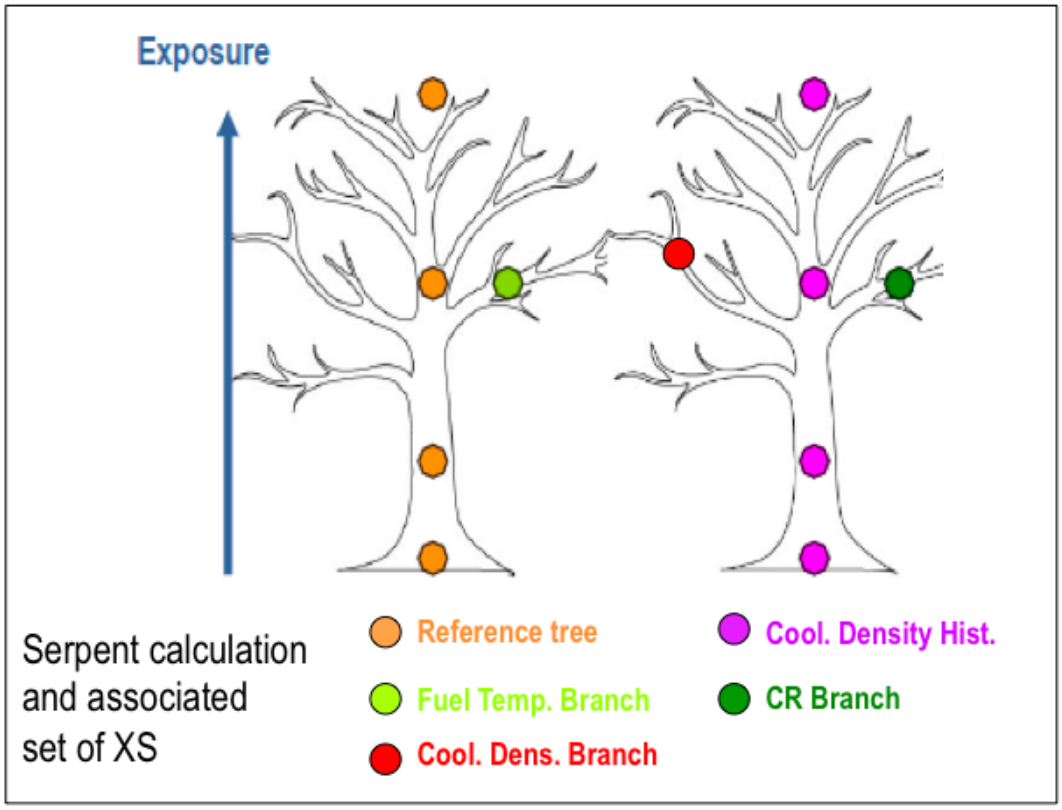

Figure 2.4. The different branch conditions permit interpolation at a burnup point, while the histories allow for interpolation in the change of the cross sections with burnup in difference conditions.

Table 2.2. Branches used in the cross section generation for the thorium RBWRs. The branches marked with a * are used for histories.

Branch Name	Flow Rate (% of average) or density	Fuel Temperature (blanket/seed) [K]	Control rod
Reference*	100% flow	600/900	Withdrawn
Very High Flow*	130% flow	600/900	Withdrawn
High Flow	115% flow	600/900	Withdrawn
Low Flow	85% flow	600/900	Withdrawn
Very Low Flow*	70% flow	600/900	Withdrawn
Flooded	Uniform 1 g/cc	600/900	Withdrawn
Voided	Uniform 0.05 g/cc	600/900	Withdrawn
High Temperature	100% flow	900/1200	Withdrawn
Low Temperature	100% flow	300/600	Withdrawn
Rodded*	100% flow	600/900	Inserted
Cold	Uniform 1 g/cc	Uniform 300	Withdrawn
Shut down	Uniform 1 g/cc	Uniform 300	Inserted

Serpent 2.1.17 was used for cross section generation in every case. Serpent 2 is currently in beta release; nonetheless, the results matched the results from MCNP closely, so it was considered

acceptable to use. SerpentXS [23] was used as a wrapper script in order to autonomously run the different branch cases. The cross sections were radially homogenized over the unit cell.

2.6.2. GenPMAXS

GenPMAXS [35] primarily processes the cross sections from the Serpent output and formats them so that they are readable by PARCS. In addition, it calculates axial discontinuity factors (ZDFs) in order to match the flux profiles from Serpent. In the RBWR cores which feature multiple axial discontinuities, ZDFs are necessary to match the current leaking between different zones, which has significant effects on the multiplication factor. As an example, for the RBWR-TR at BOC, if ZDFs are removed, then the multiplication factor is reduced by 159 pcm. The single-seed variants are much less sensitive to this than the multi-seed designs from Hitachi, and the power distribution is not significantly affected (Figure 2.5).

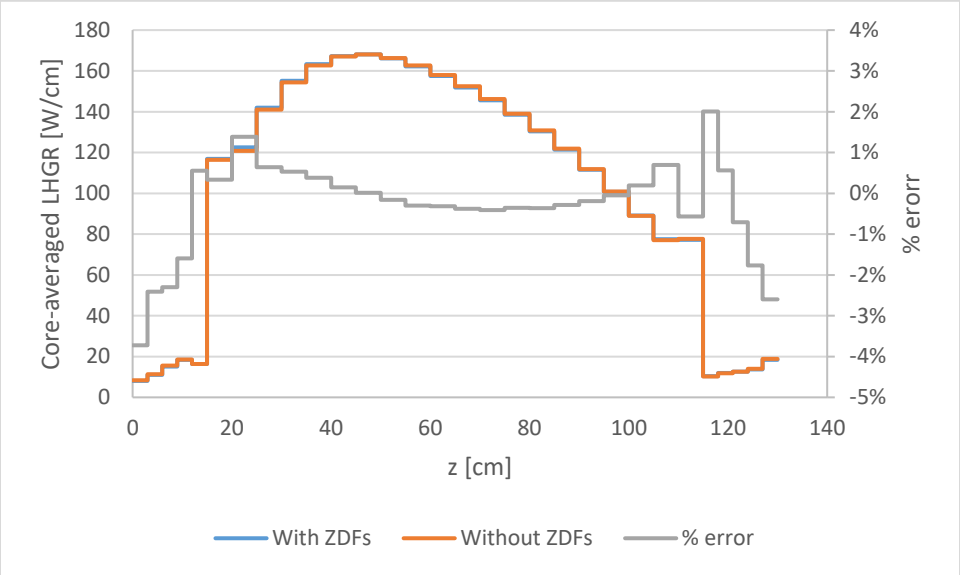

Figure 2.5. Linear heat rate distribution for the RBWR-TR at BOC, with and without ZDFs.

2.6.3. PARCS/PATHS

PARCS [32] is a nodal diffusion code with built-in coupling capabilities with the PATHS [30] drift-flux steady-state thermal hydraulic solver. PARCS was used to find the equilibrium core for each of the designs such that the cores were critical at EOC. It should be noted that "equilibrium" has a different meaning in this context than when used with the MocDown simulation tool; in MocDown, the equilibrium state is reached when the initial fuel composition remains constant between successive cycles. In PARCS, the initial fuel composition is set by the cross sections; however, the composition at the end of each particular assembly is not known, so the PARCS equilibrium core is found when the difference in local burnup is below a specified threshold.

Thermal hydraulic updates were performed at every burnup step, and the equilibrium state was searched for by depleting and shuffling the fuel until the maximum local burnup difference between consecutive EOC states was less than 0.1 GWd/t.

2.7. OpenFOAM Coupling with Serpent 2

The multi-physics open-source toolkit OpenFOAM [36] is a finite-volume C++ library adopted to spatially discretize and numerically solve coupled partial differential equations (PDEs). OpenFOAM has already been successfully coupled with Serpent [37], but never for a BWR. Since OpenFOAM is essentially just a framework and none of the prepackaged solvers were sufficient to analyze a BWR, a new solver was created. The solver receives the power density calculated in Serpent and uses it to calculate the water densities and fuel temperatures, which are used to update the Serpent simulation.

It was desired to use OpenFOAM rather than PATHS for two main reasons. Firstly, many of the correlations within PATHS are hard-coded for UO_2 fuel, while making an OpenFOAM solver would give the flexibility for mixed Pu-U oxide (MOX) or ThO_2 correlations. Secondly, the coupling framework between Serpent and OpenFOAM had already been established.

This OpenFOAM thermal-hydraulic solver was benchmarked against PATHS [30] and reproduced results acceptably, allowing Serpent to be coupled with thermal hydraulic feedback for a BWR. The solver method of solution and benchmark results are documented in this section.

2.7.1. Analytical Models and Correlations

In this work, a new T/H solver was developed using OpenFOAM to be coupled with Serpent aimed to model RBWR cores. In this solver, the water properties are solved using a simple one-dimensional (1D) energy balance in the vertical direction along the fuel. The water properties are calculated from the enthalpy using the IAPWS-IF97 steam tables [38]. The void fraction is calculated using the Chexal-Lellouche void fraction correlation [25] and the Saha-Zuber correlation for subcooled quality [12].

The Chen correlation [12] is used to calculate the two-phase wall heat transfer coefficient. It provides a smooth transition between single phase and boiling heat transfer. The cladding thermal conductivity was retrieved from [39]; it is assumed to be constant at the temperature of the outside surface of the cladding. The gap may be modelled explicitly using a user-specified gap conductance, or it may be omitted if the pellet is assumed in contact with the clad.

The fuel temperature is calculated using a 1D heat conduction equation, assuming no axial heat transfer and azimuthal symmetry:

$$\int_{T(r)}^{T(R_{fuel})} k(T)dT = \frac{q'''\left(R_{fuel}^2 - r^2\right)}{4}$$

The power density is assumed to be constant within the fuel region at a given axial mesh. The fuel conductivity is a function of temperature, and the centerline temperature is calculated iteratively by numerically integrating the conductivity integral – left hand side of above equation. The average fuel temperature was calculated using the Gaussian quadrature and weighting by the volume.

Several different correlations for fuel thermal conductivity were implemented, based on the amount of Pu present in the fuel. For a Pu weight fraction less than 1.5%, equation 6.2 from Reference [40] for pure UO_2 was used. If the Pu weight fraction was between 1.5% and 15%, equation 6.3 from Reference [40] for MOX fuel was used. For greater Pu weight fractions, the recommended correlation for fast reactor grade MOX was used from Reference [41]. Fuel porosity is accounted through a user input, and factored into the thermal conductivity; however, no burnup effects are accounted for. In addition, the fuel thermal conductivity correlation from PATHS was implemented, with a user-specified switch available to use this correlation.

When coupled to Serpent, the fuel axial temperature distribution is applied to every pin uniformly, and the axial water density distribution is the same for every assembly.

2.7.2. Major Assumptions

A number of assumptions and simplifications are used with this solver. Regarding the fluid portion of the solver, only a single channel may be used. It is possible to run the solver once per channel, but a utility to generate a mesh for each channel and run each channel sequentially has not yet been developed. Unlike PATHS [30], a constant pressure model was used. The pressure has a small impact on the water density and the fuel temperature, which is are the only values passed back to Serpent.

Axial conduction through the cladding and the fuel was ignored; this is consistent with the assumptions in the PATHS [30] solver. Most importantly, only a single fuel pin was modeled in the OpenFOAM solver using the average pin flow rate and experiencing the average pin power. The reported centerline temperatures are therefore reported for an "average" pin, rather than the most high-powered pin. Additionally, the average fuel temperatures are volume averaged, and not weighted to get the best estimation for the Doppler coefficient.

2.7.3. Benchmarking Against PATHS

A single assembly model of the RBWR-TB2 was made using the PARCS/PATHS [30, 32] system. A few mistakes and inconsistencies were made in the cross section generation, so these results in this section should not be relied upon; nonetheless, they should be sufficient for benchmarking. The OpenFOAM solver was decoupled from Serpent, and the power distribution was input from the PARCS model. The water enthalpy, water density, average fuel temperature, and centerline fuel temperature at each axial location was compared for fresh fuel. A coarse mesh was used: each seed and the internal blanket were divided into 8 portions, while the upper blanket was divided in half.

The OpenFOAM solver was run twice; once using the PATHS fuel thermal conductivity correlation, and a second time using the fast reactor MOX thermal conductivity [41] for the seed and the ORNL recommended correlation for UOX [40] for the blankets.

Since the water densities and enthalpies are provided at the interfaces between material boundaries, an "upwind" numerical solver was used to match the values at the interfaces. This will cause some small numerical inconsistencies with the fuel temperatures, but since fuel temperature is largely driven by the power distribution and the water temperature is constant after it begins boiling, the differences should be very small.

Figure 2.6 shows the linear heat rate distribution generated from PARCS and input into OpenFOAM. It is a very top-heavy distribution, which is not realistic; nonetheless, it should be acceptable for verifying the solver.

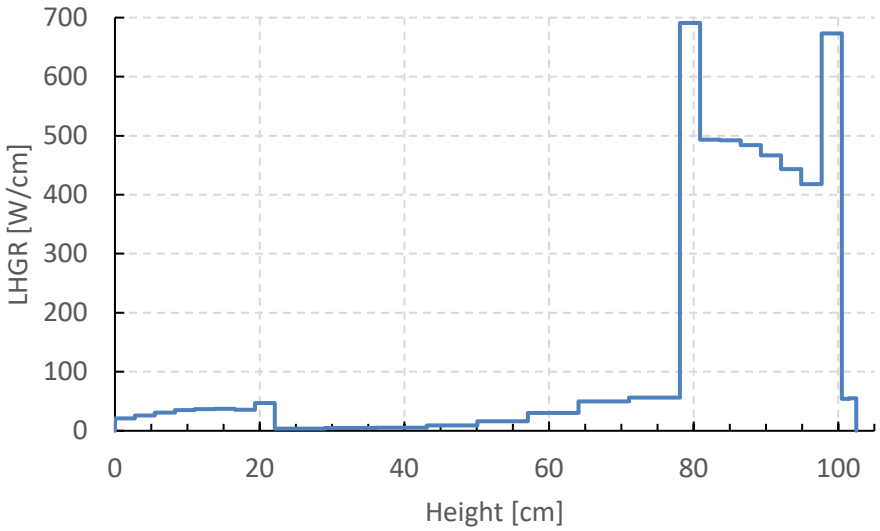

Figure 2.6. Linear Heat Rate Generation (LHGR) profile from PARCS and used in OpenFOAM.

The coolant enthalpy comparison is shown in Figure 2.7, and the coolant water density profile is shown in Figure 2.8. The enthalpy comparison shows that OpenFOAM is calculating the energy balance correctly. The water density distribution is visually very similar, and the differences are likely due to using different steam properties. Since the pressure is identical at the outlet, the comparison shows that ignoring the effects of pressure are not significant.

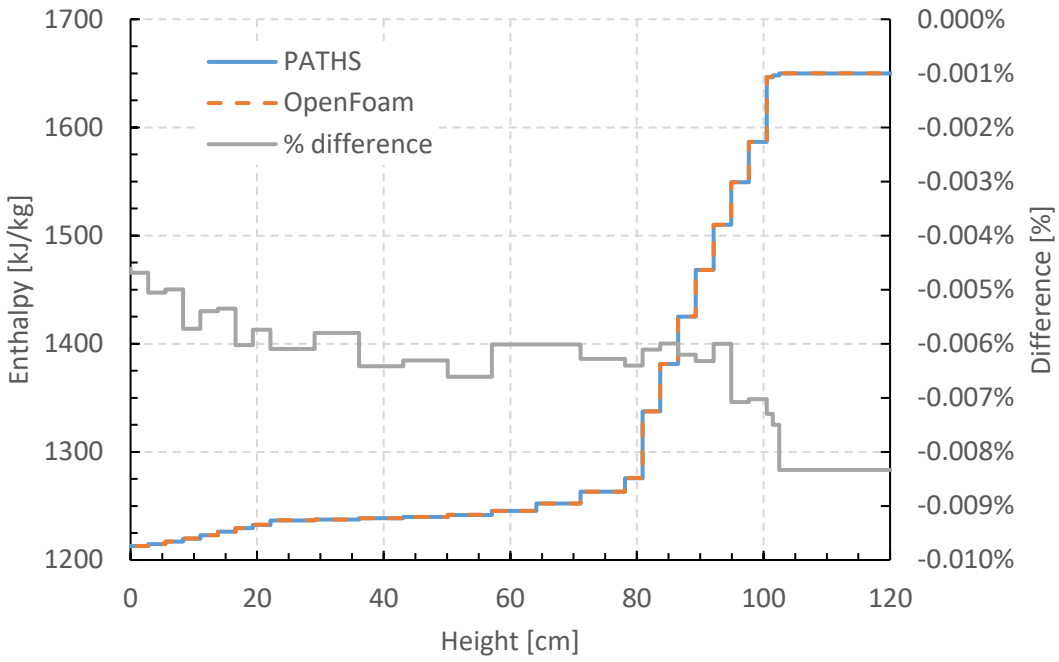

Figure 2.7. Enthalpy comparison between the PATHS and OpenFOAM models.

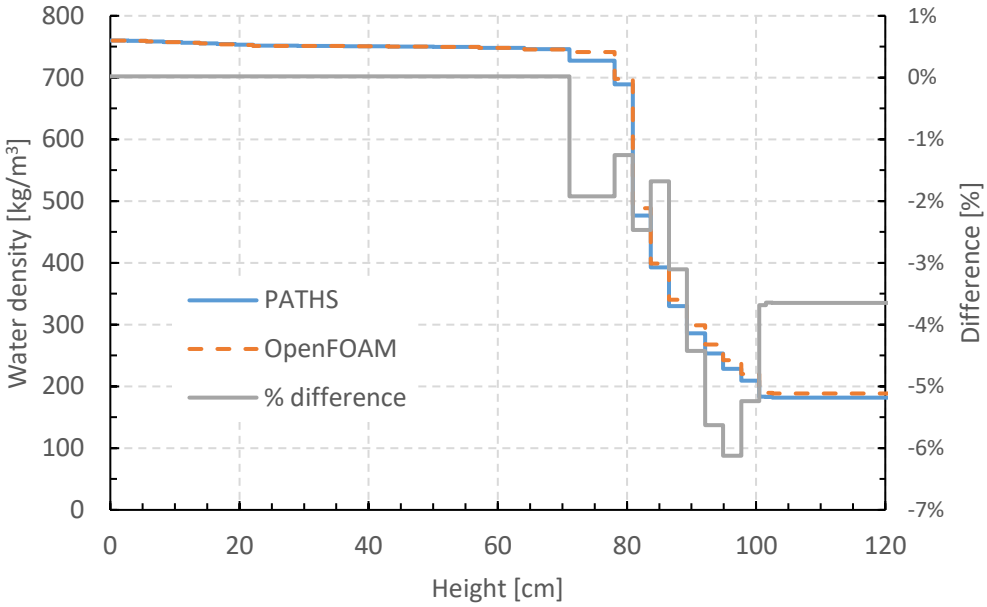

Figure 2.8. Water density comparison between PATHS and OpenFOAM.

Figure 2.9 and Figure 2.10 show the centerline fuel temperature and relative error, while Figure 2.11 and Figure 2.12 show the average fuel temperature and relative error. When using the same thermal conductivity correlation, the centerline fuel temperature is within 5% of the PATHS results for all axial locations; although this is a slightly larger difference than would be preferable in the upper seed, it is clearly smaller than the errors arising from using a more relevant correlation. On the other hand, the average fuel temperatures do not seem to match well

at all. This is due to the OpenFOAM solver using the volume weighted average temperature, while PATHS uses $0.7 \cdot T_{\text{fuel surface}} + 0.3 \cdot T_{\text{fuel center}}$. When the same averaging scheme is employed, the result is acceptable.

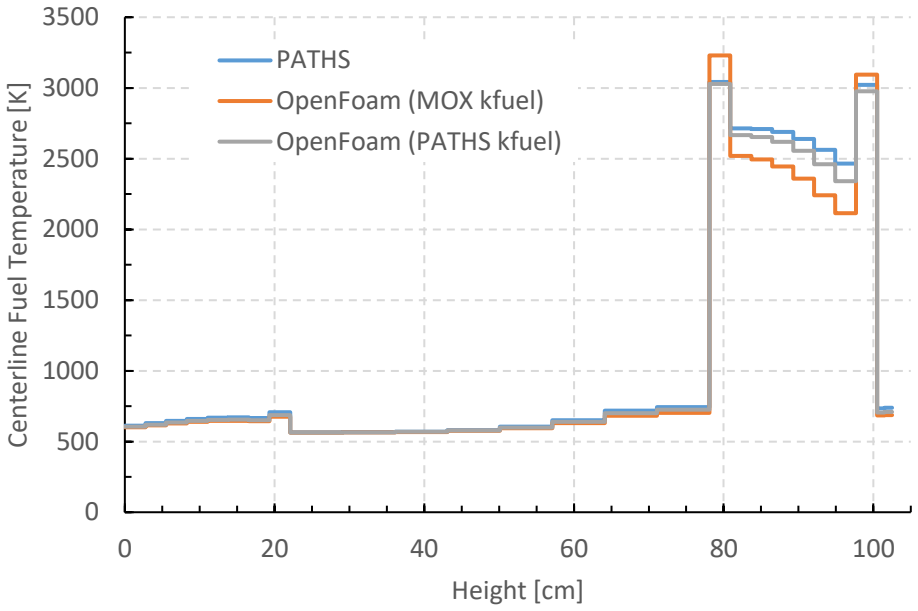

Figure 2.9. Peak fuel temperature using different solvers and fuel thermal conductivity correlations.

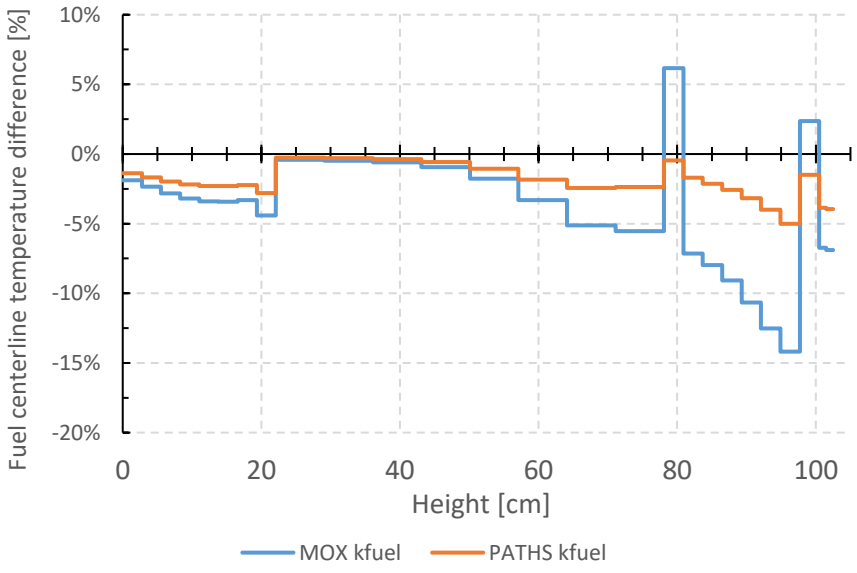

Figure 2.10. Relative error in the centerline fuel temperature of the OpenFOAM solver compared to the PATHS results.

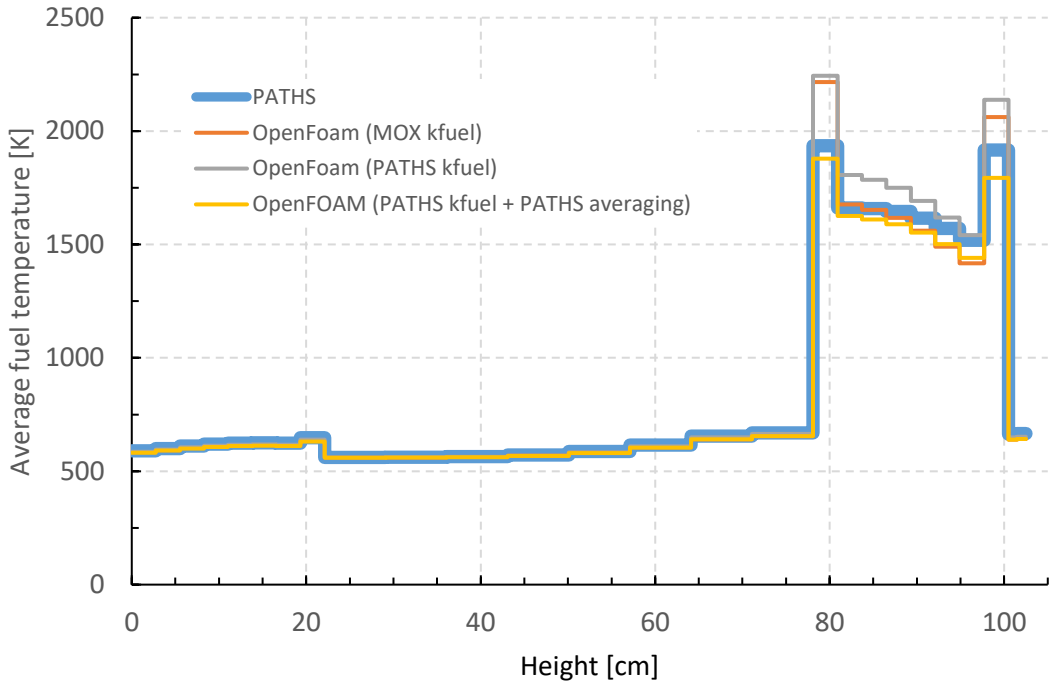

Figure 2.11. Average fuel temperature using different solvers and fuel thermal conductivity correlations.

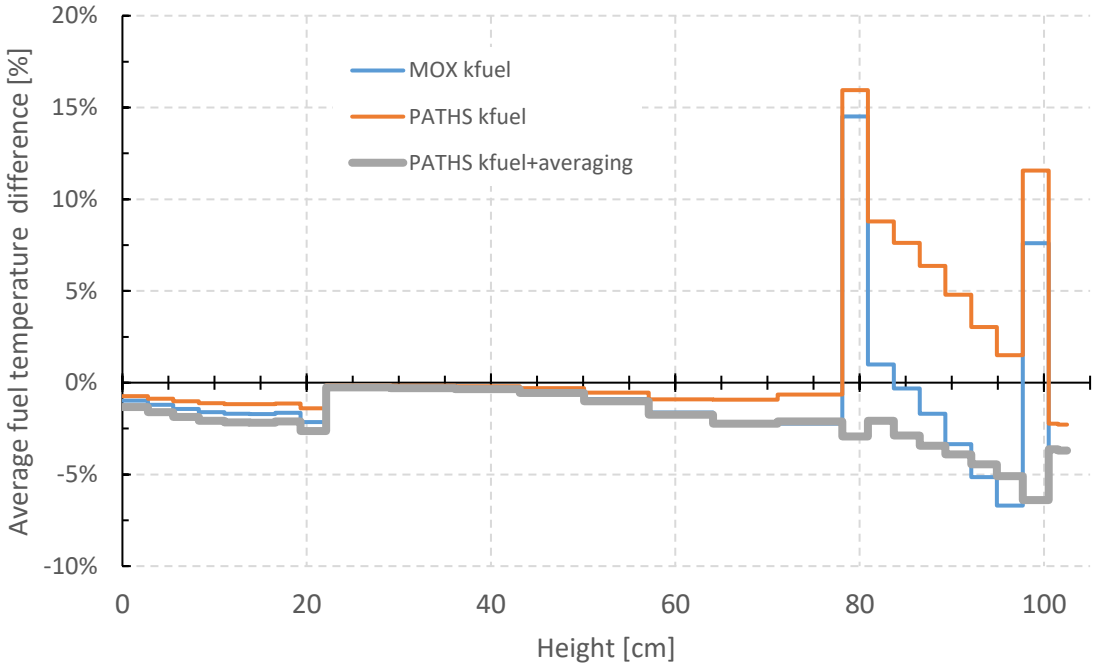

Figure 2.12. Relative error in the average fuel temperature of the OpenFOAM solver compared to the PATHS results.

2.8. Uncertainty Quantification

The ability to calculate the sensitivity of the multiplication factor due to various parameters has recently been investigated using Serpent [42]. This was applied to the RBWR designs as well.

2.8.1. Sensitivity Coefficient Calculation

A modified version of Serpent 2.1.19 was used to calculate the sensitivity of the multiplication factor to the relative changes in the reaction rates of various materials. The modifications to Serpent essentially increase the cross sections of specified isotopes by a fixed percentage, and then reject collisions by the same percentage in order to maintain a fair simulation. These rejected collisions are still tracked, and then propagated using generalized perturbation theory (GPT) to assess their impact on the multiplication factor.

The sensitivity of the multiplication factor to nuclear data was quantified, as well as the sensitivity to local water density changes. The sensitivity to the nuclear data was binned according to the energy binning of the covariance matrices, but no spatial binning was implemented; on the other hand, the sensitivity to the local water density used different axial binning depending on the model. The sensitivity was expressed as the relative change in k per relative change in the independent parameter (for instance, $\underline{S}_{\text{Pu-239, fission}}$ would be the relative change in k per relative change in fission cross section of ^{239}Pu).

2.8.2. Uncertainty Calculation

The variance in the multiplication factor due to uncertainty in nuclear data was calculated as

$$\sigma_i^2 = \sum_{r_1}\sum_{r_2} \underline{S}_{r_2,i} \times \underline{\underline{C}}_{r_1,r_2,i} \times \underline{S}^T_{r_1,i}$$

where i designates the isotope, r_1 and r_2 denote reaction type, $\underline{S}$ is the vector of sensitivity coefficients, and $\underline{\underline{C}}$ is the relative covariance matrix. The variance in the multiplication factor due to uncertainty in the water density distribution was calculated in a similar way, except that there was no summation over different reactions.

These sensitivity coefficients were also used to calculate the uncertainty in the reactivity change between different states (for instance, when voiding the reactor) due to uncertainty in nuclear data. The covariance matrices are independent of reactor configuration, so the uncertainty in the reactivity change is due to differences in the sensitivity. The variance was calculated according to the following equation:

$$\sigma^2_{i,1,2} = \sum_{r_1}\sum_{r_2} \left(\underline{S}_{r_2,i,1} - \underline{S}_{r_2,i,2}\right) \times \underline{\underline{C}}_{r_1,r_2,i} \times \left(\underline{S}_{r_1,i,1} - \underline{S}_{r_1,i,2}\right)^T$$

where the 1 and 2 subscripts indicate the reactor state.

Lastly, the uncertainty from each group for each reaction was calculated using the following relation from [43]:

$$\sigma_{lmn} = \sqrt{s_{lmn}^2 d_{lmn}^2 + \sum_{k}^{Ncorr} Corr_k s_{lmn} d_{lmn} s_k d_k}$$

where the subscripts *l*, *m*, and *n* denote isotope *l*, reaction *m*, and energy group *n*, and *k* is the index for all Ncorr correlated cross sections. *s* denotes the sensitivity coefficient for a particular isotope, reaction, and energy group, while d_k is the element of the covariance matrix between σ_{lmn} and σ_k. This was implemented by the following relation:

$$\sigma_{r_1,i,g}^2 = \sum_{r_2} \underline{S}_{r_2} \times \underline{\underline{C}}_{r_1,r_2,i,g} \times \underline{S}_{r_1}^T$$

where $\underline{\underline{C}}_{r_1,r_2,i,g}$ is the covariance matrix with all elements zeroed out, except for the column corresponding to group g. In other words,

$$\underline{\underline{C}}_{r_1,r_2,g} = \begin{bmatrix} 0 & \cdots & 0 & d_{(r_1,g),(r_2,1)} & 0 & \cdots & 0 \\ & & & d_{(r_1,g),(r_2,2)} & & & \\ & & & \vdots & & & \\ \vdots & \ddots & \vdots & d_{(r_1,g),(r_2,g)} & \vdots & \ddots & \vdots \\ & & & \vdots & & & \\ & & & & & & \\ 0 & \cdots & 0 & d_{(r_1,g),(r_2,G)} & 0 & \cdots & 0 \end{bmatrix}$$

2.8.3. Covariance Matrices for Nuclear Data

The covariance matrices for all isotopes were retrieved from the JANIS [10] database using the ENDF/B-VII.1 cross section library. The covariance matrices were binned into 175 energy groups. All of the actinides which were present in fresh fuel were retrieved. However, the available data is not the same for all isotopes; for instance, ^{239}Pu had the covariance matrices for many "cross terms" (that is, where r_1 and r_2 were not the same), while other isotopes did not.

It was desired to also assess the impact of fission products. However, it was not practical to retrieve the covariance matrices for every fission product isotope; additionally, no data was available for most unstable fission products, including important ones like ^{135}Xe. Therefore, ^{149}Sm and ^{151}Sm were used in order to scope out how important fission products would likely be. These two isotopes were selected due to their large cross section and because they are stable.

2.8.4. Covariance Matrices for Water Density Distribution

The uncertainty in the local water density is very difficult to assess, as it is dependent on the geometry and the local quality; therefore, the covariance matrix would change for every simulation.

Ideally, a covariance matrix would be created by perturbing each of the empirical constants in the void fraction correlation many times by a random amount according to their uncertainty; however, the uncertainty in each of these constants was not feasible to obtain. As a first estimation, the uncertainty of the void fraction as a function of the void fraction based on the Chexal-Lellouche correlation was found based on the uncertainties provided in Table 4 of [44]. The void fraction in each spatial bin was perturbed ten thousand times assuming a normal distribution, and then translated into water densities. The covariance matrix was computed using these ten thousand trials. The script used to generate these covariance matrices is attached as Appendix D.

2.9. Fuel cycle analysis

As part of the project entitled "Technical Evaluation of the Resource-Renewable BWR Design by Hitachi" performed in Japanese fiscal year 2015, the fuel cycle characteristics of the RBWR-TB2 were compared against Argonne National Lab's (ANL) CR=0.73 Advance Burner Reactor (ABR) [4], [11]. This analysis was also extended to the thorium RBWR designs; for the RBWR-SS, the CR=1.0 Advanced Recycling Reactor (ARR) was used as a basis for comparison [4]. Both the ABR and the ARR are sodium fast reactors (SFRs).

2.9.1. Assumptions

The RBWR reactors were all assumed to have a thermal efficiency of 34.5%, while the sodium fast reactors were assumed to have a thermal efficiency of 40%. For this analysis, a 5-year cooling time was assumed between discharge and reprocessing, and it was assumed that 1.2% of all discharged heavy metal is lost in the recycling and fabrication processes. This lost heavy metal mass was assumed to reach the repository with the fission products.

For all burner reactors, a 2-stage system was modeled. Stage 1 consists of PWRs while stage 2 is composed of the burner reactor. An equilibrium state is assumed such that the rate of TRU generation in stage 1 PWRs equals the TRU consumption rate by stage 2 reactors. PWRs rather than ABWRs were considered for this analysis because the recent DOE Fuel Cycle Evaluation & Screening (FCE&S) Campaign used PWRs to represent LWRs [1]; it should not change the conclusions if ABWRs were used instead for the stage 1 reactors, since they are both thermal LWRs. It is assumed that the PWRs are fed with 4.5% ^{235}U enriched UOX fuel that is burned up to 50 MWd/kg followed by a 10-years cooling period before reprocessing. The recovered TRU composition from the PWR is given in Table 2.3.

Table 2.3 Composition of TRU extracted from LWR's UNF discharge at 50 MWd/kg and cooled for 10 years [11].

Isotope	Weight Percent
^{237}Np	4.7%
^{238}Pu	2.2%
^{239}Pu	47.3%
^{240}Pu	22.8%
^{241}Pu	8.4%
^{242}Pu	6.8%
^{241}Am	5.6%
^{243}Am	1.6%
^{244}Cm	0.5%

2.9.2. Comparison Metrics

The comparison metrics are divided into 4 parts: general core and fuel cycle parameters, repository characteristics, proliferation resistance metrics, and fuel cycle costs. An overall technology evaluation similar to the ones provided by the FCE&S Campaign [1] is also performed for the technologies.

The core and fuel cycle performance characteristics compared pertain to the equilibrium cycle and include fuel loading, specific power, power density, peak linear heat generation rate, average discharge burnup, required reprocessing capacity, cycle length, and fuel composition for fresh fuel, discharged fuel, and after 5-years cooling. In addition, for the burner reactors, the support ratio was also calculated. The support ratio is defined as the ratio of electric power generated in stage 1 reactors to the electric power generated in stage 2 reactors. Since it is assumed that the total amount of TRU generated in stage 1 is equal to the total amount consumed in stage 2, this is also equal to the ratio of TRU consumption rate per unit electricity generated in stage 2 to the ratio of TRU production rate per unit electricity generated in stage 1. The self-sustaining designs only have one stage, so the support ratio is undefined for them.

The repository characteristics include radioactivity of the used nuclear fuel and high level waste at short term (10 years) and long term (100,000 years) after fuel discharge, as well as inhalation toxicity and ingestion toxicity at the same time periods. The methodology used to compute these metrics are discussed in Section 2.9.3.

The proliferation related metrics included plutonium throughput, fissile plutonium fraction, ^{238}Pu fraction, specific decay heat, and the number of neutrons spontaneous fissions. These were assessed at the time of reprocessing, after cooling for 5 years.

The fuel cycle costs of the RBWR and SFR designs were quantified accounting for both front-end and back-end activities. The economics of nuclear power plants are usually measured by the levelized electricity cost, which is composed of the capital cost, operation-and-maintenance (O&M) cost, and fuel cycle cost. Due to the large uncertainty in the SFR capital and O&M cost, this analysis focuses on the fuel cycle cost, accounting for both front-end and back-end cost components. Due to the high fissile contents in the discharged fuel, aqueous reprocessing and

low enriched UOX fabrication technology developed for conventional PWR fuel may not be applicable for RBWRs. This study assumes that the RBWR discharged fuel undergoes electro-chemical reprocessing and remote fuel fabrication, as planned for the SFRs based on the experience gained in the EBR-II project in the US. The nominal values reported in [45] and reproduced in Table 2.4 are used for the cost of major activities in the fuel cycle. The costs for innovative technologies are subjected to large uncertainties due to lack of commercial experience. Nevertheless, sensitivity analysis is not performed in this comparison.

Table 2.4. Cost of major fuel cycle activities [45].

Fuel Cycle Activitiy	**Cost**
Natural uranium mining and milling	$60/kgU
Thorium mining and milling	$100/kgTh
Conversion processes	$10/kg(U or Th)
Enrichment	$105/SWU
LWR UO_2 fuel fabrication	$240/kgU
UREX aqueous separation	$1,000/kgHM
Reprocessing - electrochemical & remote fuel fabrication	$5,000/kgHM
SNF conditioning/packaging/disposal	$1100/kgHM
RU conditioning	$93/kgHM
Aqueous HLW conditioning/storage/packaging (FPs+Ln)	$2,000/kgFPs
Geologic repository (HLW FPs+Ln+Tc)	$10,000/kg FPs

Finally, a high-level comparison of the different reactor technologies was conducted using the evaluation criteria developed by the FCE&S campaign [1]. The primary objective on this undertaking was to find whether the fuel cycle of the RBWR-TB2 is as promising as the FCE&S campaign claimed for the SFR fuel cycle. These criteria include nuclear waste management, environmental impact and resource utilization. Each evaluation criterion is composed of several evaluation metrics defined in Appendix A of Reference [1]. The detailed impact factors, like water use for uranium enrichment and radiological dose for fuel reprocessing, are summarized in Appendix C of Reference [1]. To account for uncertainties and differences in calculation approaches, each calculated metric is assigned with a letter score based on a binned approach defined in Appendix D of Reference [1] such that two systems exhibit same performance for that metric if the calculated metric values fall within the same bin range. This method will help to find whether RBWRs can accomplish the missions previously assigned to SFRs and be as attractive as the SFRs.

Within the FCE&S campaign [1], rather than examining each design individually, 40 different evaluation groups (EG) were assessed, grouped based on the physics of each group. One "Analysis Example" for each group was evaluated per EG. Each of the RBWRs are compared against the evaluation groups that accomplish the most similar objective; for the RBWR-SS, this is EG24 and EG28, while for the RBWR-TR and RBWR-TB2, this is EG32.

In order to account for the different thermal efficiency of reactors used in the different fuel cycle options, the FCE&S campaign renormalized the mass flow rate to a uniform thermal efficiency of 33%. Analytical formulas were developed for this re-normalization to modify the mass flow

and power sharing between reactors in different stages of the fuel cycle options. The formulas used are defined in Appendix D of Reference [1]:

$$F_k^n = \frac{\omega_k F_k^o}{\sum_i \omega_i F_i^o}$$

$$M_k^n = \frac{M_k^o}{\sum_i \omega_i F_i^o}$$

where the superscripts of "n" and "o" indicate the new and original thermal efficiencies, respectively, and the subscript "k" and "i" denotes the stage number, F is the power-sharing fraction, M is the mass flow, ω_k is the ratio of the new thermal efficiency to the original thermal efficiency of kth stage ($\frac{\eta_k^n}{\eta_k^o}$), and η_k is the thermal efficiency of stage k reactor.

2.9.3. Computational Methods

One-group cross-sections were generated using MCNP5 [28] for each isotope tracked within MocDown (Section 2.5) for use with ORIGEN2.2 [29]. For the RBWRs, which feature blankets and seeds with vastly different spectra, one cross section for each isotope was used for the seeds and one cross section was used for the blankets. Within ORIGEN2.2, each fuel was burned to the same discharge burnup using a constant flux, accounting for 879 fission products and 128 actinides. The atom densities, radioactivity, and decay heat of the discharged fuel after discharge are calculated at key time points (5 years after discharge, 10 years after discharge, and 100,000 years after discharge) and used to calculate the comparison metrics.

In order to calculate inhalation and ingestion toxicities, 1.2% of the discharged heavy metals and all of the discharged fission products are assumed to be in the waste stream. The values of the activity were weighted by the inhalation and ingestion conversion factor (207 fission products and 91 actinides in [46]). Effective inhalation/ingestion coefficients were applied for a typical adult member of the public with median aerodynamic (1 μm diameter) radionuclides being inhaled into the blood stream via the lungs. The typical values of inhalation/ingestion coefficients are shown in Table 2.5. In general, the alpha-emitters heavy metals tend to contribute more radiation damage than most low atomic mass elements (like FPs) which are mostly beta-emitters. The actinides inhaled through lungs are far more hazardous than ingested via stomach [47].

Table 2.5. Effective inhalation/ingestion coefficients.

Dose Conversion Factor (Sv/Bq)	Inhalation	Ingestion
FPs	1.E-5 ~1.E-4	1.E-7 ~ 1.E-6
Actinide	1.E-10 ~ 1.E-8	1.E-10 ~ 1.E-8

3. RBWR-SS

The RBWR-SS is a self-sustaining design based on the Hitachi RBWR-AC [7, 48], which maintains a fissile inventory ratio of 1. The primary design objective for the RBWR-SS was to maximize the discharge burnup while meeting the constraints in Section 2.2 in order to assure adequate safety margins.

In the design space of the RBWR-AC, the RELAP void fraction correlation tends to overestimate the void fraction, especially when the quality is low [14]. The Liao, Parlos, and Griffith void fraction correlation is a much closer estimate for such tight lattices. Additionally, the data available in the open literature indicates that the Hitachi critical power correlation may not give a conservative bound for the MCPR [26]. Therefore, two different designs for the RBWR-SS are presented in this chapter. The RBWR-SSH maintains a fair comparison against the RBWR-AC by assuming the RELAP void fraction correlation and the H-CISE CPR correlation are valid; an MCPR limit of 1.3 was applied. The RBWR-SSM uses the MIT-recommended correlations (LPG for void fraction, MFP-CISE for CPR with an MCPR limit of 1.3) in order to provide a conservative bound on the performance.

In the early stages of the thorium RBWR research, it was desired to use only thorium as the feed material [17–19]; however, it was quickly observed that it would be impossible to shut down the core due to the strong negative void reactivity feedback [49]. It was found that the most practical way to provide more shutdown margin would be to add depleted uranium (DU) as an additive in order to breed more plutonium and make the void feedback closer to zero. Since only fertile material was charged to the reactor, the fissile inventory ratio was maintained at unity, and it was considered satisfactory. The depleted uranium had additional benefits towards denaturing the fuel, which are described in more detail in Section 3.5.

Section 3.1 describes the models that were used, and additionally shows the results of a few modeling sensitivity studies. Section 3.2 documents the parametric studies that were performed in order to guide the designs. Section 3.3 presents the final RBWR-SS designs and compares their performance against that of the RBWR-AC and an analogous SFR. Section 3.4 calculates the uncertainty in several neutronics phenomena using generalized perturbation theory (GPT), and Section 3.5 analyses the fuel cycle of the RBWR-SS. Section 3.6 summarizes this chapter and draws general conclusions about the RBWR-SS designs.

3.1. Assembly Model

3.1.1. Assembly Model Description

Due to the time investment required to generate cross sections for the full core simulator, most of the design studies were performed on the assembly level using MocDown (Section 2.5) and extrapolating the performance to a full-core level.

In order to save on the computational costs, only two radial enrichment zones were modelled for the equilibrium simulation. The pins closest to the control blade were modelled as pure blanket material, with the same fraction of DU and Th as used in the seed makeup stream. The axial blankets remained pure thorium. The seed was axially segmented into 30 equally sized zones,

while each of the blankets were divided into 5 equal volume zones. The gap in the fuel pin was not explicitly modelled, as it is expected that the fuel will expand to fill the gap after very little exposure time. For the RBWR-SSH, it was assumed that the water in the inter-assembly gap was boiling at the same rate as the rest of the fuel, while for the RBWR-SSM, it was assumed that the inter-assembly gap was liquid density water. A radial slice of the assembly as used in MocDown is shown in Figure 3.1, while the fuel cycle scheme is shown in Figure 3.2.

For the cross section generation, 7 different pin enrichment were used. The reasoning for 7 enrichment groups is justified in Section 3.1.2.

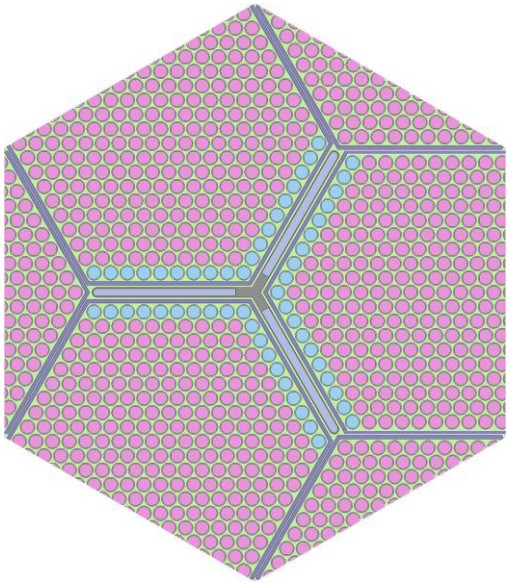

Figure 3.1. X-Y plot of the assembly unit cell model used in the equilibrium analysis. The pin dimensions were left as a design variable.

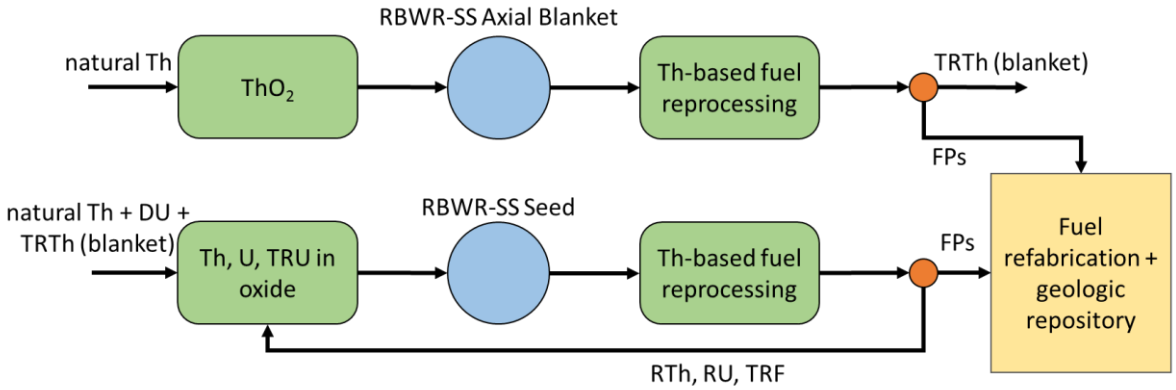

Figure 3.2. Fuel cycle scheme used by the RBWR-SS cores, implemented within MocDown.

3.1.2. Pin Peaking and Enrichment Study

As in typical BWRs, there is extra moderation near the edges of the assembly can, due to the extra bypass flow between the assemblies. This is especially true for the sides near the control

blade. However, unlike a typical BWR, there are no partial length fuel pins, nor are there any water rods, since it is desirable to have as hard of a spectrum as possible.

With a uniform fuel enrichment, the power will peak in the corner with the control blade follower, due to the increased moderation; in order to maximize the discharge burnup, it is also desirable to have most of the fissions produced in the radial center of the assembly where the spectrum is the hardest.

For the assembly power maps shown in Sections 3.1.2.1 through 3.1.2.3, the design metrics are presented in Table 3.1. An equilibrium cycle was found for each enrichment scheme assuming the bypass flow was boiling using the specified depletion length (corresponding to an average discharge burnup of 38.5 GWd/t) regardless of what achievable burnup was actually achievable for each design. After reaching an equilibrium composition, the pin peaking was assessed for a fresh assembly twice (once assuming inlet density coolant bypass, and once assuming boiling bypass flow). An estimation of the achievable burnup was calculated by linearly fitting the multiplication factor with burnup, discarding the first 0.15 GWd/t due to the accumulation of fission products, and finding the burnup which would cause the batch-averaged end of cycle (EOC) multiplication factor equal to 1.02. This was calculated according to the following expression:

$$k_{\text{EOC,full core}} = \frac{5}{\sum_{b=1}^{5}\left(k^{-1}\right)_b}$$

where b signifies the batch. The value 1.02 was chosen as it approximately captures the radial leakage and the different fuel temperature profile in the full core model.

Table 3.1. Design parameters for the assembly enrichment studies.

Parameter	Units	Value
Assembly power	MW_{th}	5.453
Assembly HM mass (BOL)	kg	216.8
Avg TRF/HM at BOL	w/o	11.69%
Seed TRF/HM at BOL	w/o	16.51%
Assembly pitch	cm	19.77
Assembly coolant flow rate	kg/s	10.16
Upper blanket length	cm	20
Seed length	cm	114.3
Lower blanket length	cm	28
Fuel pin OD	cm	1.005
Fuel pin pitch	cm	1.135
Fuel pin P/D	-	1.13
Pins per assembly	-	271
Fraction of seed makeup which is DU	a/o	50
Depletion time	EFPD	1530

3.1.2.1. Sensitivity to Bypass Water Density Assumptions

The pin power distribution for a uniformly enriched assembly is shown in Figure 3.3 and Figure 3.4. The pin peaking factor in Figure 3.3 is smaller than 1.2, but the peak pin power in Figure 3.4 is 1.39 times the average; since the bypass region will likely boil at a slower rate than the coolant within the assembly, it was still desired to seek alternative pin enrichment schemes which would perform better. The achievable discharge burnup was found to be 20.9 GWd/t.

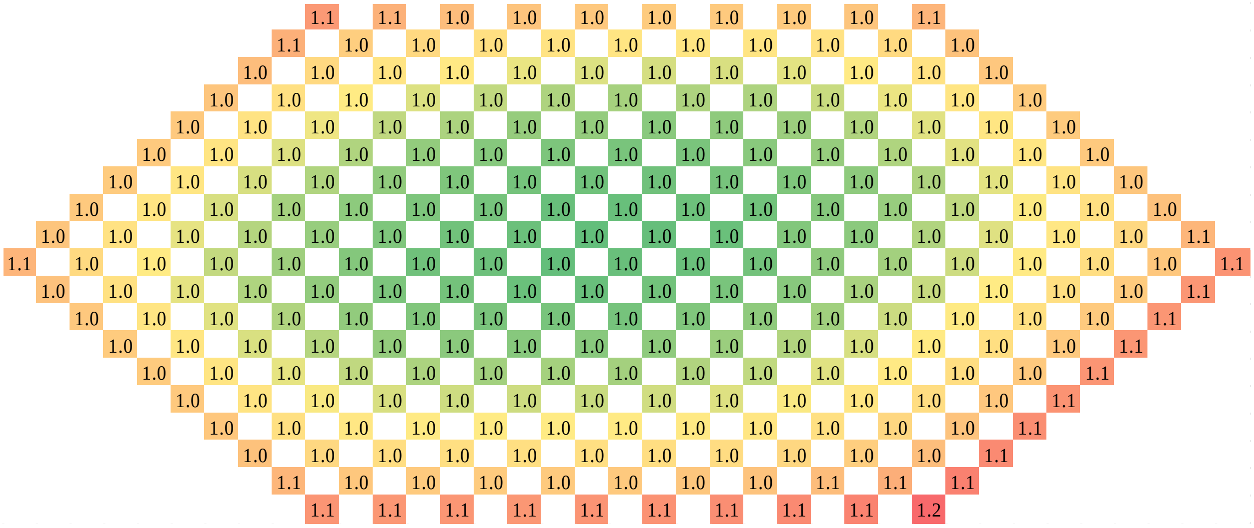

Figure 3.3. Pin power distribution at BOL for a uniformly enriched RBWR-SSH assembly with 271 pins, assuming the water in the bypass region is boiling. The control blade is along the bottom and lower right faces.

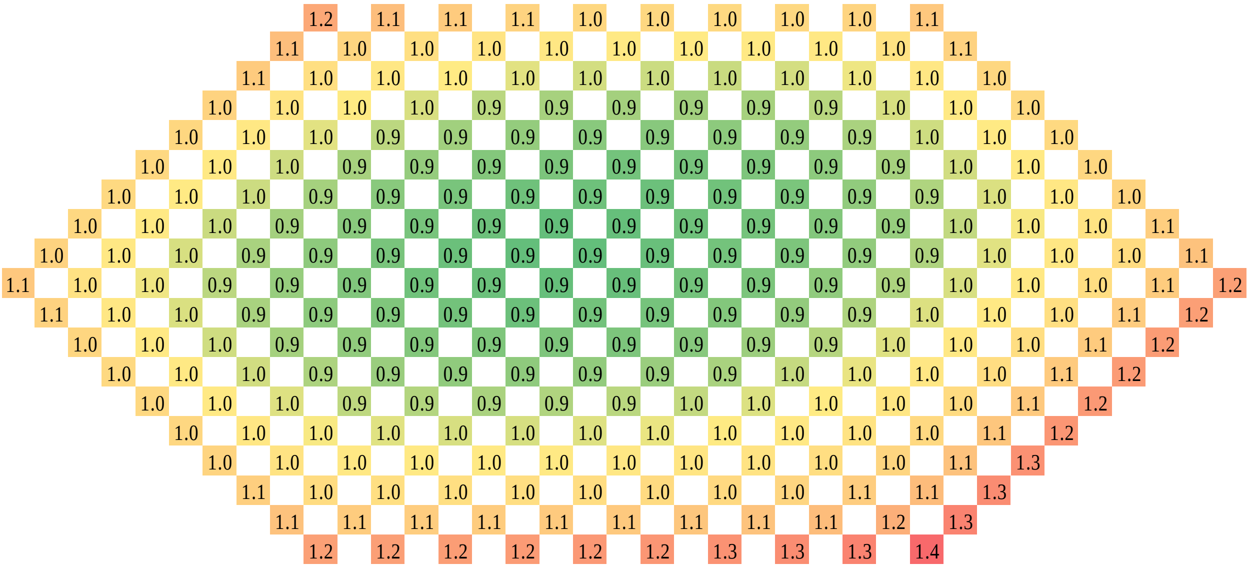

Figure 3.4. Pin power distribution at BOL for a uniformly enriched RBWR-SSH assembly with 271 pins, assuming the water in the bypass region is liquid water. The control blade is along the bottom and lower right faces.

3.1.2.2. Segregated Th/TRTh and DU/TRU pins

Since the fertile fuel will be a mixture of Th and DU, it was decided to examine the performance of using separate Th-^{233}U pins and DU-Pu pins. This would probably help reduce the reprocessing costs since the well-characterized uranium-based reprocessing could be used for the DU-Pu pins. For the final designs, it was found that putting the Th pins in the center of the assembly would help minimize the power peaking; however, it was also found this scheme could only achieve a discharge burnup of 16.6 GWd/t, which is a 20% reduction relative to the uniform enrichment. This is likely due to ^{233}U having a higher η than ^{239}Pu in the more thermal regions, such as near the periphery of the assembly; unfortunately, the Th-^{233}U pins cannot be placed around the periphery for the same reason, as it would have extremely high peak powers. As shown in Section 3.1.2.3, a burnup gain can be achieved using mixed fuel pins while achieving acceptable peak pin powers, so the segregated pin designs were not pursued further.

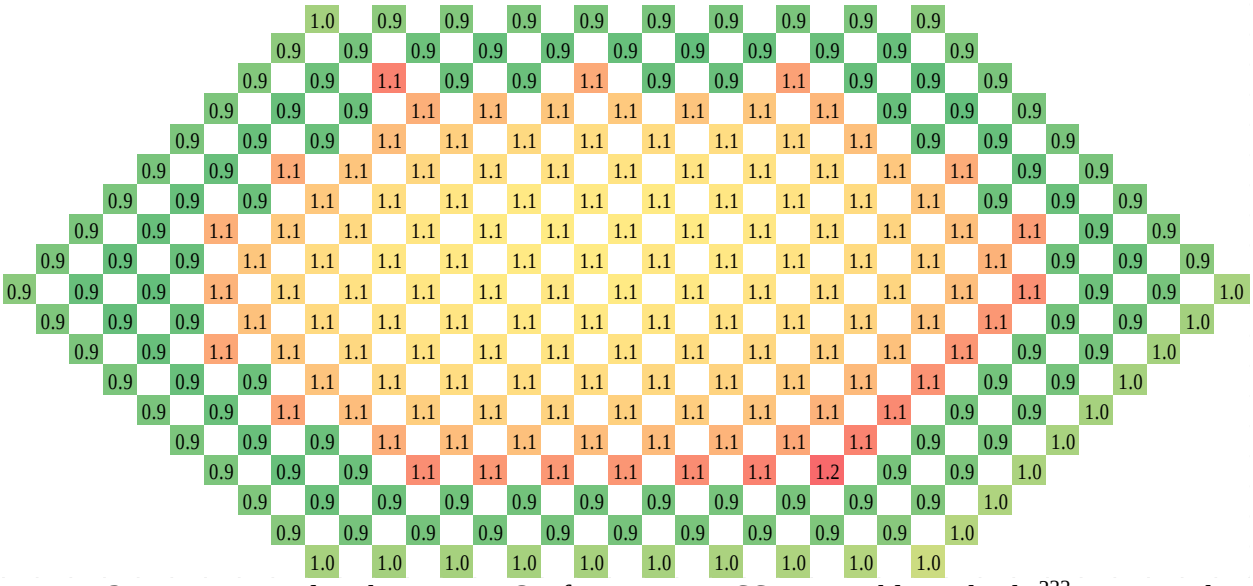

Figure 3.5. Pin power distribution at BOL for a RBWR-SSH assembly with Th-^{233}U pins in the center and DU-Pu pins along the periphery, assuming the water in the bypass region is boiling. The control blade is along the bottom and lower right faces.

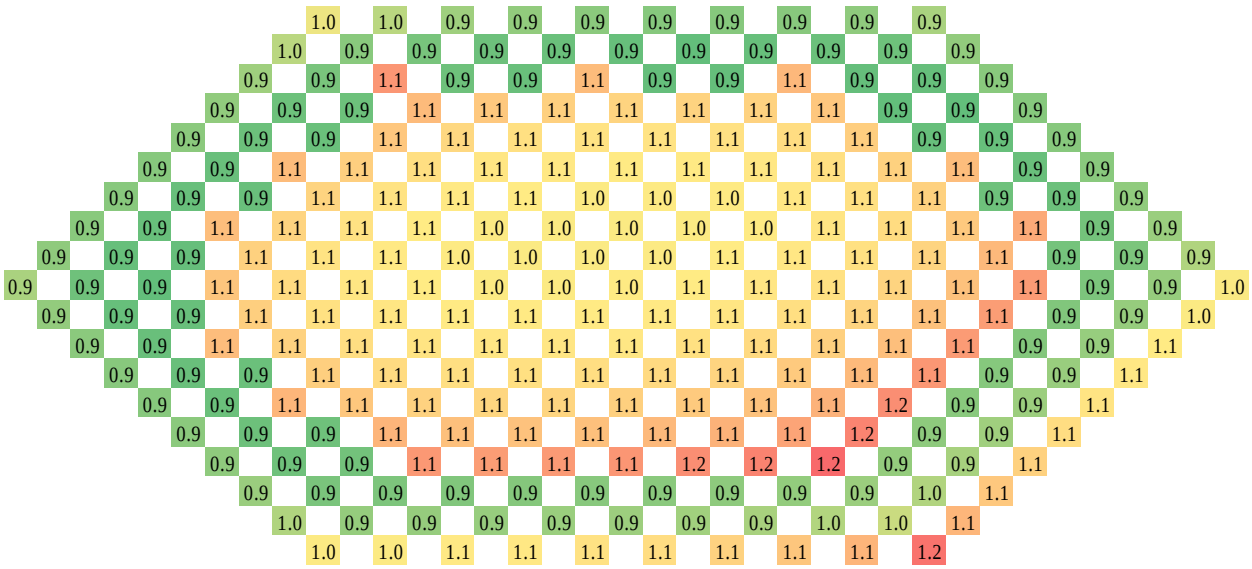

Figure 3.6. Pin power distribution at BOL for a RBWR-SSH assembly with Th-^{233}U pins in the center and DU-Pu pins along the periphery, assuming the water in the bypass region is liquid water. The control blade is along the bottom and lower right faces.

3.1.2.3. Final Enrichment Scheme

A graded enrichment scheme was created, in which the fuel around the periphery (especially near the control blade) was less enriched than the fuel at the center of the assembly. The enrichment scheme is shown in Figure 3.7, while the power distributions are shown in Figure 3.8 and Figure 3.9. The pin peaking power is less than or equal to 1.2 regardless of what assumption is made regarding the bypass region water density; in addition, the discharge burnup is 20 to 30% higher than using a uniformly enriched assembly.

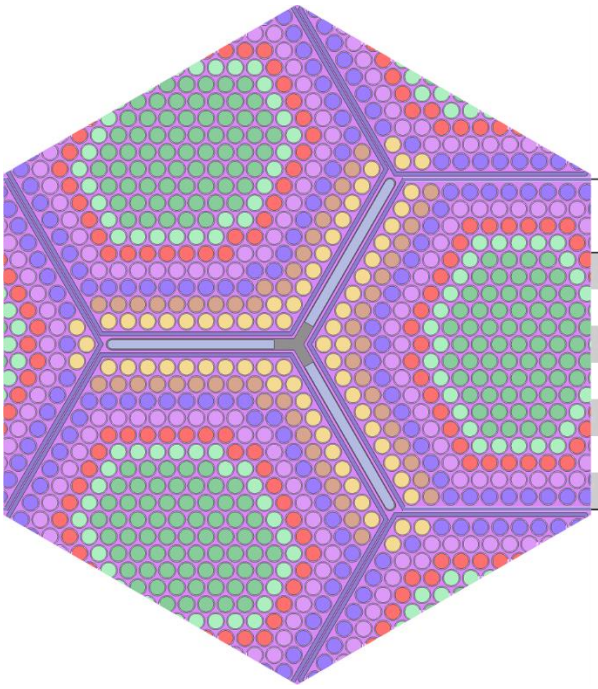

Enrichment color	# of pins	BOL group TRF moles per pin / average TRF moles per pin (%)
Tan	23	40.0%
Brown	19	60.0%
Blue	48	77.5%
Purple	44	100.0%
Red	38	115.0%
Light Green	32	120.0%
Dark Green	67	130.0%

Figure 3.7. 7-group enrichment scheme used with the RBWR-SS with 271 pins.

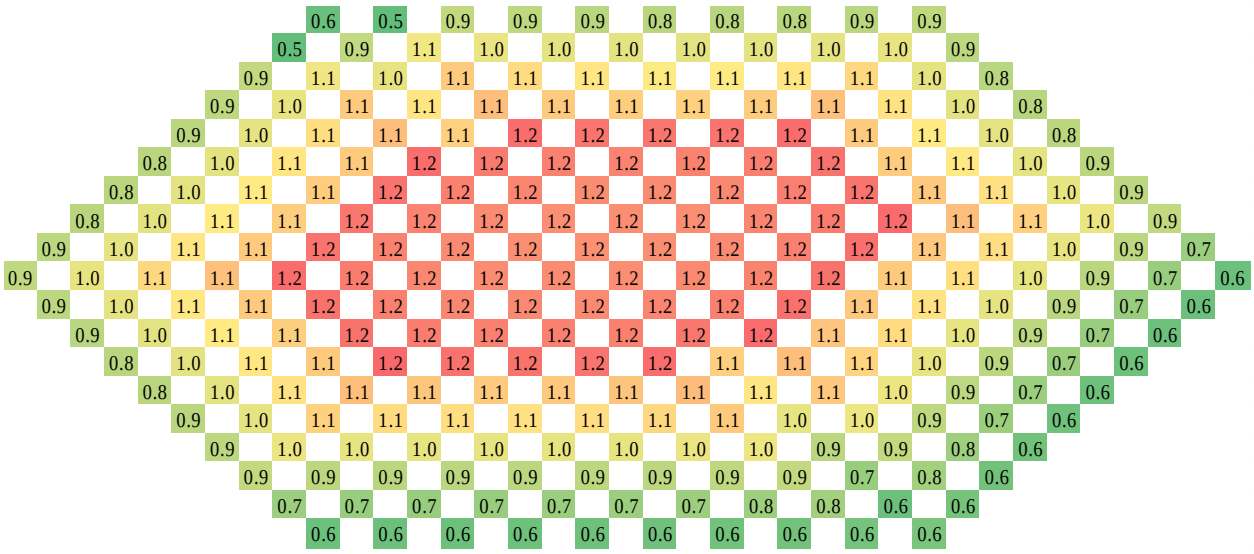

Figure 3.8. Pin power distribution at BOL for a RBWR-SSH assembly with 271 pins using the specified 7-group enrichment scheme, assuming the water in the bypass region is boiling. The control blade is along the bottom and lower right faces.

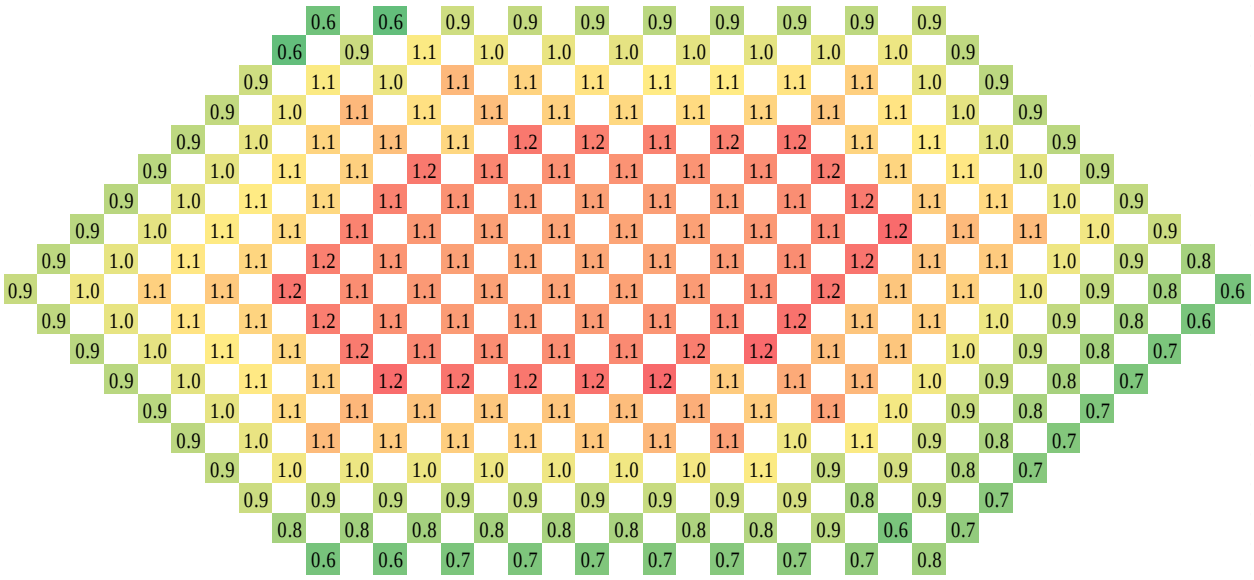

Figure 3.9. Pin power distribution at BOL for a RBWR-SSH assembly with 271 pins using the specified 7-group enrichment scheme, assuming the water in the bypass region is liquid density. The control blade is along the bottom and lower right faces.

3.2. Parametric Studies

MocDown was used (as documented in Section 2.5) to assess the effects of each of the design variables (Section 2.3) on the ability to meet the design constraints (Section 2.2) and the discharge burnup. The tradeoff studies have been published in detail in [50], and are summarized qualitatively in Table 3.3. The starting design for these parametric studies is shown in Table 3.2. These results were performed using the model for the RBWR-SSM using a single fuel pin model; however, they are valid for both the RBWR-SSM and the RBWR-SSH.

Table 3.2. Starting values for the self-sustaining RBWR tradeoff studies.

Parameter	Value
Seed length	300 cm
Upper blanket length	40 cm
Lower blanket length	40 cm
Clad thickness	0.04225 cm
Fuel pin radius	0.7075 cm
Fuel pin pitch	0.7990 cm
Pitch to diameter ratio	1.1293
Exit quality	28.5%
Number of pins per assembly	547
Atom fraction of DU in the seed makeup	28%
Full core power	3926 MW_{th}
Number of assemblies	720
Fuel residence time	3000 EFPD
Axial isotopic charge distribution	Uniform
Void fraction correlation	LPG

Table 3.3. Summary of the parametric tradeoff studies for the RBWR-SS. An increase in the variable noted in the left column results in the change noted by the arrows. The arrows in the heading indicate which change would help meet the associated constraints.

Variable	MCPR (↑)	Critical BU (↑)	VCR (↓)	SDM (↑)	ΔP (↓)
Coolant flow rate	↑	↓	↓		↑
Depletion time			↑	↓	
Seed length	↑	↓	↑	↑	↑
Outer blanket lengths		↑[1]	↑		↑
Internal blanket length[2]		↓	↓		
Makeup DU fraction			↑	↑	
Axial enrichment variation[3]	*[4]	*[4]		↑	↑
Pitch to diameter ratio (P/D)	↑	↓	↓	↑	↓
Number of pins per assembly[5]	↑		↓	↑	↑
Power[6]	↓	↓			↑

The coolant flow rate had a very strong effect on both the MCPR and the achievable burnup. Increasing the flow rate reduces the flow quality throughout the seed region, providing more margin against the critical heat flux; however, increasing the flow rate also softens the spectrum, which reduces the achievable burnup. The void coefficient is reduced, although the shutdown margin is not affected since there are slightly fewer voids to collapse and since the reactivity swing reduces too. It also increases the pressure drop due to increased friction losses. Since the MCPR was the most sensitive to the flow rate, the flow rate for a given design was set so that the MCPR constraint was barely met.

The depletion time was not a free design variable, as it was effectively set so that the core was critical. However, it was still useful to examine how increasing the depletion time affected the other variables. With increasing time, the void coefficient becomes more positive due to the buildup of higher actinides which tend to have a high fission threshold energy and have a sharp increase in η when the spectrum hardens, as noted in Sections 1.2.1 and 1.2.3.2. Similarly, the shutdown margin increases due to the reduction in the void collapse worth.

[1] The peak discharge burnup occurs with a blanket length between 20 cm and 30 cm.
[2] Increasing the blanket length was accomplished by replacing a section of the seed with blanket material, and thereby holding the total fuel length constant.
[3] An increase in axial enrichment variation was taken as moving TRF material from the bottom third of the seed to the top third.
[4] Any variation from uniform axial enrichment reduces the MCPR and the burnup.
[5] The P/D and the flow gap between the fuel lattice and the wall were held constant; the number of pins, pin diameter, and pitch were changed simultaneously.
[6] The coolant flow rate was increased so that quality remained constant.

The seed length affects every design constraint. Increasing the seed length reduces the achievable burnup and increases the pressure drop, but it also increases the MCPR by increasing the boiling length so that a lower mass flow rate could be used. If the MCPR were held constant, then increasing the seed length would have a net benefit to the achievable burnup. In addition, increasing the seed length reduces leakage, causing the void feedback to become more positive and increasing the shutdown margin.

Increasing the length of the blankets outside of the seed region has almost no effect on the MCPR, due to the low power produced in the blankets. They have a mixed effect on the achievable burnup: they capture leaking neutrons from the seed and improve breeding, but adding larger blankets increases the heavy metal mass so that the average discharge burnup is reduced. The optimal blanket size was found to be between 20 cm and 30 cm. Additionally, adding more length (no matter where it comes from) increases the pressure drop, although the lower blanket caused a much lower pressure difference than the upper blanket due to the two-phase flow multiplier for frictional losses.

Replacing some of the seed with a small internal blanket has a much different effect than enlarging the external blankets. The burnup is significantly reduced, due to more absorption occurring in the peak flux region. This also reduces the void coefficient, as expected from the RBWR-AC design concept. The shutdown margin is not significantly impacted; the reduction of the void coefficient and subsequent increase in the void collapse worth was counteracted by a reduction in the reactivity swing due to breeding in the blanket and a reduction in the Doppler coefficient since the seed enrichment was increased.

The amount of depleted uranium (DU) in the seed makeup stream had a negligibly small impact on the achievable burnup and the T/H characteristics, since it was also fertile fuel. However, since the plutonium which is bred from the DU tends to make the void feedback more positive, the DU feed fraction effectively allows the void coefficient to be fine-tuned while having very little impact on the other constraints. It was desired to have the peak core-averaged VCR very close to zero in order to help prevent two-phase oscillations (which are not covered in detail in this thesis) and to help provide more shutdown margin.

Previous studies [19] had showed a significant improvement in MCPR and burnup from moving some of the TRF from the bottom third of the seed to the top third of the seed. However, this previous study used only thorium as the fertile feed material, and had a much too strongly negative void coefficient [49]; the effects are significantly different when DU is added to the feed such that the void coefficient is small. It was found that with a nearly zero void coefficient, any deviation from a uniformly enriched seed penalized the MCPR and the discharge burnup somewhat. Moving fuel to the top of the seed benefits the pressure drop since it reduces the amount of two-phase boiling, and the shutdown margin is slightly increased since there are fewer voids to collapse.

The pitch to diameter ratio of the fuel has a huge effect on many of the constraints. Increasing the pitch to diameter ratio benefits the MCPR somewhat by reducing the coolant mass flux while keeping the exit quality the same, but it softens the spectrum which significantly reduces the burnup. The void coefficient is slightly reduced from the spectral softening while the void worth

is significantly increased. The reduced coolant mass flux provides large benefits to the pressure drop due to the increased flow area.

Increasing the number of pins per assembly allowed the fuel to be better "wetted"; that is, the ratio of the surface area to the volume of the fuel was increased. This provides a benefit to the MCPR, and slightly reduced the void coefficient. Additionally, the shutdown margin was improved, as the coolant area was reduced which reduced the coolant void worth. However, this increases the friction losses significantly.

The effects of changing the power was also investigated. Even though doing so would violate the objective of meeting the same power output as the ABWR and would significantly affect the economics of the design, reducing the power would allow nearly every constraint to be more easily met. Increasing the power reduces the MCPR due to the increased heat flux, while the achievable burnup reduces slightly due to the more parasitic absorption in the Pa-233 before it decays. The pressure drop increases due the increased mass flux necessary to keep the same quality. The void coefficient was relatively unaffected, as was the shutdown margin; however, it should be noted that while MocDown calculates the water densities, it does not calculate any fuel temperatures, as MCNP5 lacks any on-the-fly Doppler broadening. It is expected that with higher powers, the resulting temperature increase would reduce the shutdown margin.

In addition to the design variables, the effects of changing the thermal hydraulics assumptions were examined. Changing the MCPR correlation had no impact on the MocDown simulation, as the MCPR calculation is performed after-the-fact; however, using the H-CISE correlation predicts a much higher MCPR than the MFP-CISE correlations. This would permit a much lower flow rate to be used, which would extend the burnup significantly. Additionally, using the RELAP correlation rather than the LPG void fraction hardens the spectrum, as it predicts a higher void fraction for all qualities.

3.3. Full Core Performance of RBWR-SS vs. RBWR-AC

Earlier publications showed preliminary results which indicated that the RBWR-SSM could attain similar performance to the RBWR-AC while meeting the safety metrics, with a slight penalty in power due to the stringent pressure drop and MCPR requirements [49, 51, 52]; however, these studies had assumed that the reprocessing losses were negligible. After accounting for 1.2% reprocessing losses after each recycle (in accordance with [1]), the multiplication factor took a large penalty, and it would have been necessary to operate below 50% power with a pitch-to-diameter ratio of less than 1.08 in order to operate on a self-sustaining cycle. This is considered economically and mechanically infeasible.

In the full core simulation, the same shuffling scheme was used as in the Hitachi-designed RBWR-AC. A four-and-a-half batch scheme was used, with 156 assemblies in each of the first four batches and 96 assemblies in the last batch. The most burned half-batch was placed at the periphery of the core, with the fresh fuel loaded next to it, and the once-burned fuel placed in a ring inside of that. Half of the three-times-burned fuel was placed in a ring inside the once-burned fuel, while the remaining assemblies (the twice-burned batch and half of the three-times-burned batch) were arranged in a checkerboard pattern in the center of the core.

Since the axial assembly configuration was completely different, a new control rod pattern was defined. The control rods at the center of the core were more inserted at BOEC in order to control the power peaking; however, as the excess reactivity diminishes, the radial power profile becomes more peaked at EOC. Since the power is much more peaked for the RBWR-SSH compared to the RBWR-AC, in order to maintain cooling throughout the core, the loss coefficients for the orifices at the periphery of the core were doubled compared to the RBWR-AC values.

Even when using the same thermal-hydraulic assumptions as Hitachi, it does not appear possible to achieve sufficient shutdown margin while maintaining negative void feedback. However, the achievable discharge burnup is nearly the same. The optimized design of the RBWR-SSH is presented in Table 3.4, alongside similar metrics compared against the RBWR-AC and the Advanced Recycling Reactor (ARR), a CR=1.0 SFR [4] in Table 3.5. The axial power shape at BOC and EOC are shown in Figure 3.10 and Figure 3.11, while the 2-D radial power map is shown at BOC and EOC in Figure 3.12 and Figure 3.13. Figure 3.14 shows the excess reactivity as a function of burnup. The different components of the shutdown margin are shown at BOC in Table 3.6.

Although the shutdown margin of the RBWR-SSH is insufficient, it is expected that it could be improved if a multi-seed approach were adopted, since this would increase the average enrichment in the seed and thus reduce the Doppler coefficient. However, care must be taken to avoid the power spikes that are observed in the Hitachi-designed cores, which are discussed in Section 5.4. It may be more prudent to reduce the assembly size and increase the thickness of the control blades. Lastly, reducing the power should benefit the shutdown margin, as it would reduce the fuel temperature.

The harder spectrum of the ARR compared to the RBWRs allows it to operate with a much higher burnup. The RBWR-SSH and the RBWR-AC achieve very similar burnups; while the RBWR-SSH has a much lower linear heat generation rate (LHGR), the RBWR-AC successfully meets the shutdown margin and negative feedback constraints.

Table 3.4. Design parameters for the RBWR-SS, RBWR-AC, and the ARR. Design parameters for the RBWR-AC are from [7] while the ARR design information is from [4].

Parameter	**Units**	**RBWR-SSM**	**RBWR-SSH**	**RBWR-AC**	**ARR**
Coolant	-	light water	light water	light water	sodium
Fuel form	-	oxide	oxide	oxide	metal
Core thermal power	MW_{th}	1963	3926	3926	1000
Core electric power	MW_e	677	1356	1356	400
# of assemblies	#	720	720	720	151
Core HM mass (BOC)	T	360	154	140	16.7
Core TRF mass (BOC)	T	45.1	18.3	16.7	2.4
TRF/HM core avg at BOC	w/o	12.57%	11.93%	11.90%	14.60%
Seed TRF/HM at BOC	w/o	14.28%			
Core volume	m^3	84	40	32	3

Parameter	Units	RBWR-SSM	RBWR-SSH	RBWR-AC	ARR
Core flow rate	kg/s	3142.8	7464.5	7222	6138
Specific power	MW_e/t	1.9	9	10	24
Power density	W_{th}/cm^3	23	99	123	289
Upper blanket length	cm	25	20	7	-
Upper seed length	cm	300	114.3	28	101.6
Internal blanket length	cm	-	-	52	-
Lower seed length	cm	-	-	19.3	-
Lower blanket length	cm	20	28	28	-
Fuel pin OD	cm	0.7398	1.01	1.005	0.808
Fuel pin pitch	cm	0.799	1.14	1.135	0.889
Fuel pin P/D	-	1.08	1.13	1.13	1.1
Pins per assembly	-	547	271	271	271

Table 3.5. Performance metrics of the RBWR-SS compared against the RBWR-AC and the ARR.

Metric	Units	RBWR-SSM[7]	RBWR-SSH	RBWR-AC	ARR
Pressure Drop	MPa	0.17	0.27	0.14	
Outlet quality	%	39.9	34	35	-
Peak/average assembly power	-	1.25 (assumed)	1.4	1.2	1.7
Maximum LHGR	Wth/cm	37.0	84.2	472	389
MCPR	-	1.41	1.30	1.28	n/a
# of batches	#	4.5	4.5	4.5	3
Average discharge burnup	GWd/t	21.7	44	45	73
Peak discharge burnup	GWd/t	36	73	Not available	101
Fuel residence time	EFPD	2000	1758	1651	1222
Cycle length	EFPD	468	411	380	370
Cycle reactivity swing	%dk	0.2	1.3	1.5	-0.1[8]
VCR (BOC/EOC)	pcm/% void		-23/+9.4	-24	-
FTCR (BOC/EOC)	pcm/K		-4.6/-4.5	Not available	-2.4/-2.4

[7] All results for the RBWR-SSM are extrapolated from an assembly model, as the design was abandoned when it could not achieve half of the RBWR-AC's discharge burnup while operating at 50% power.
[8] A negative value in this context indicates that the reactivity increases over the cycle.

Power coefficient of reactivity (BOC/EOC)	pcm/MW_{th}	-0.48/-0.31	Not available	Not available
Shutdown margin	pcm	-582	Not available	Not available

Table 3.6. Components of the shutdown margin for the RBWR-SSH.

Metric	**Value [pcm]**
Excess reactivity	1264
Void collapse to 1.0 g/cc water	3784
Cooling to room temperature	3399
Control rod worth	-7865
Total shutdown margin	-582

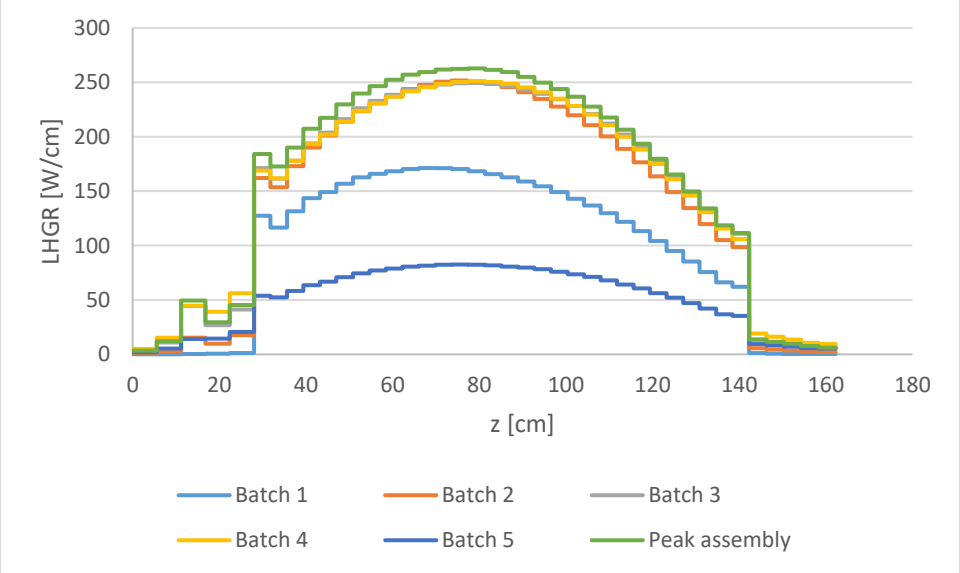

Figure 3.10. Batch-average LHGR profiles for the RBWR-SSH at BOC with a critical control rod configuration.

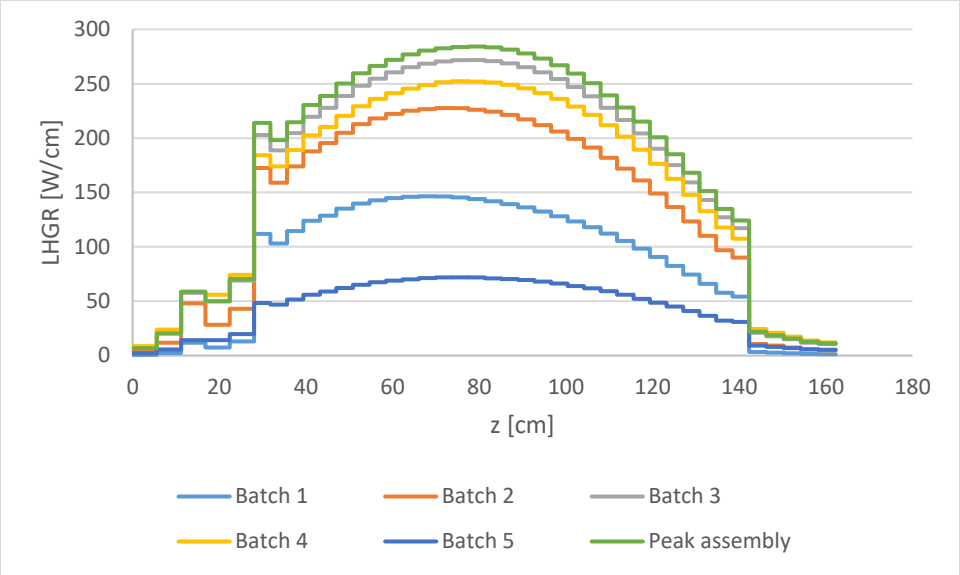

Figure 3.11. Batch-average LHGR profiles for the RBWR-SSH at EOC.

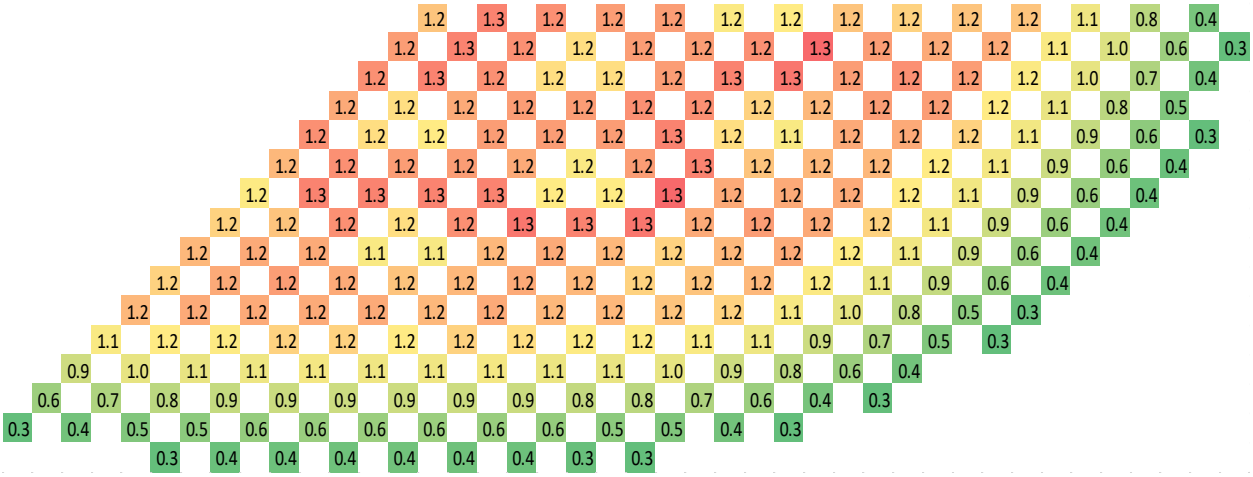

Figure 3.12. 2-D radial power map for the RBWR-SSH at BOC with a critical control rod configuration.

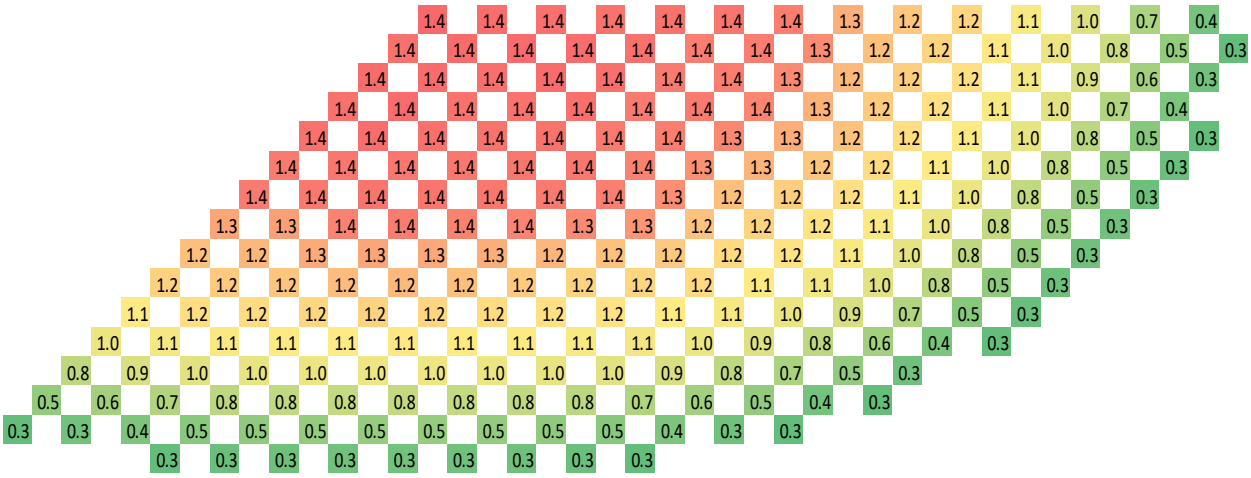

Figure 3.13. 2-D radial power map for the RBWR-SSH at EOC.

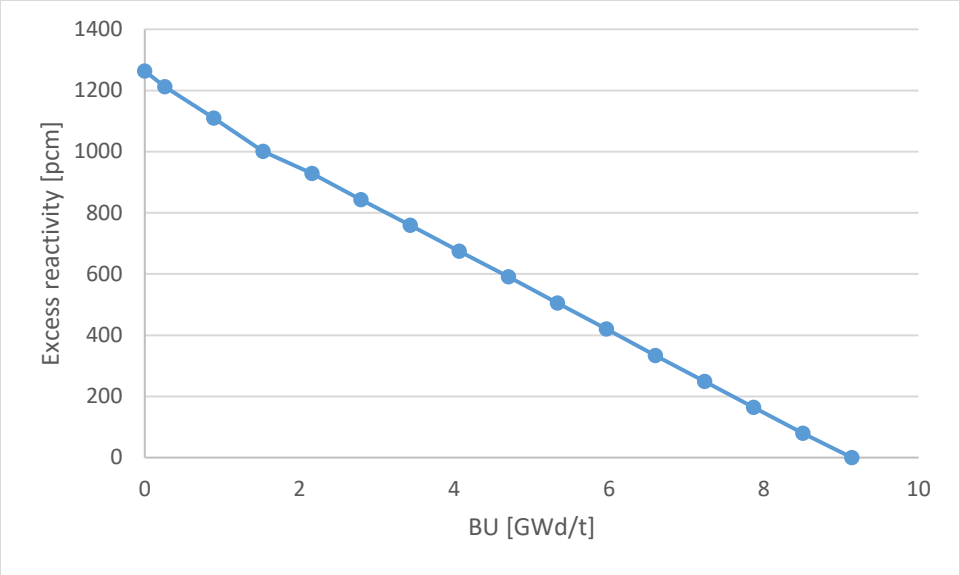

Figure 3.14. Excess reactivity vs. burnup for the RBWR-SSH.

3.4. Generalized Perturbation Theory uncertainty analysis

3.4.1. k_∞ Uncertainty due to Uncertainty in Nuclear Data

The uncertainty in k_∞ due to the cross sections of each of the isotopes present in the fresh fuel was assessed for fresh fuel and for average discharged fuel (45 GWd/t) for the RBWR-SSH. A modified version of Serpent 2.1.19 was used to generate sensitivity coefficients, which were collapsed with the cross section covariance matrices to calculate the uncertainty, as detailed in Section 2.8. An assembly unit cell was modeled using the specifications from Table 3.4, using the average water density distribution.

The k_∞ at BOL was calculated to be 1.05371 ± 1356 pcm, while at EOL, it was calculated to be 0.99800 ± 1389 pcm. Effectively all of the quoted uncertainties are due to the uncertainty from the nuclear data, as the statistical uncertainty from the Monte Carlo simulation contributed less than 1 pcm towards the final uncertainty. The decomposition due to reaction type and isotope is shown in Table 3.7 and Table 3.8 at BOL and EOL, respectively, while the uncertainty as a function of energy is shown in Figure 3.15 and Figure 3.16.

The uncertainty is dominated by the uncertainty in epithermal fissions in ^{233}U. Capture in ^{232}Th and inelastic scattering in ^{238}U are the next largest contributors; these are both most important in the fast energies. The thermal reactions contribute almost no uncertainty due to the relatively hard spectrum of the RBWR-SSH; additionally, the uncertainty changes very little over the cycle.

Table 3.7. Uncertainty of the multiplication factor measured in pcm at reference conditions due to uncertainty in each reaction type and isotope for the RBWR-SSH unit cell at BOL.

Isotope	(n,g)	Elastic	Fission	Inelastic	(n, 2n)	Cross-terms	Total
Am-241	33	2	4	2	0	6	34
Am-242m	6	0	20	0	0	n/a	21

Isotope	(n,g)	Elastic	Fission	Inelastic	(n, 2n)	Cross-terms	Total
Am-243	20	1	8	1	0	n/a	22
Cm-243	1	0	0	0	0	0	1
Cm-244	21	0	4	0	0	1	22
Cm-245	18	0	14	0	0	1	23
Cm-246	4	0	1	0	0	0	4
Cm-247	3	0	2	0	0	0	3
H-1	1	26	n/a	n/a	n/a	n/a	26
Np-237	29	0	4	1	0	n/a	29
O-16	183	56	n/a	7	0	3	191
Pu-238	38	4	5	0	0	9	39
Pu-239	85	1	90	18	0	40	131
Pu-240	46	1	21	18	0	7	54
Pu-241	42	1	29	1	0	n/a	51
Pu-242	41	1	4	1	0	n/a	41
Th-232	389	33	15	n/a	n/a	24	391
U-232	4	0	10	0	0	1	11
U-233	104	9	1166	17	1	114	1176
U-234	80	5	247	10	0	n/a	260
U-235	42	0	10	2	0	6	44
U-236	15	1	25	4	0	n/a	30
U-238	166	15	21	361	5	82	406
Total	499	72	1196	362	5	149	1356

Table 3.8. Uncertainty of the multiplication factor measured in pcm at reference conditions due to uncertainty in each reaction type and isotope for the RBWR-SSH unit cell at EOL.

Isotope	(n,g)	Elastic	Fission	Inelastic	(n, 2n)	Cross-terms	Total
Am-241	20	2	3	2	0	4	20
Am-242m	4	0	16	0	0	n/a	16
Am-243	17	0	9	1	0	n/a	19
Cm-243	1	0	1	0	0	0	1
Cm-244	22	0	5	0	0	1	22
Cm-245	17	0	15	0	0	1	22
Cm-246	3	0	1	0	0	0	4
Cm-247	2	0	2	0	0	0	3
H-1	2	36	n/a	n/a	n/a	n/a	36
Np-237	27	0	4	1	0	n/a	27
O-16	182	65	n/a	6	n/a	3	194
Pu-238	33	4	5	0	0	8	35
Pu-239	85	1	98	24	0	40	138
Pu-240	43	1	24	22	0	3	54
Pu-241	43	1	35	2	0	n/a	55
Pu-242	35	1	4	1	0	n/a	35

Isotope	(n,g)	Elastic	Fission	Inelastic	(n, 2n)	Cross-terms	Total
Sm-149	14	1	n/a	0	0	n/a	14
Sm-151	10	0	n/a	1	0	n/a	10
Th-232	375	30	16	n/a	n/a	19	377
U-232	4	0	11	0	n/a	1	12
U-233	94	8	1205	17	1	108	1213
U-234	73	4	270	10	0	n/a	279
U-235	41	0	10	2	0	7	43
U-236	12	1	27	5	0	n/a	30
U-238	149	11	21	375	4	55	408
Total	477	82	1240	377	4	129	1389

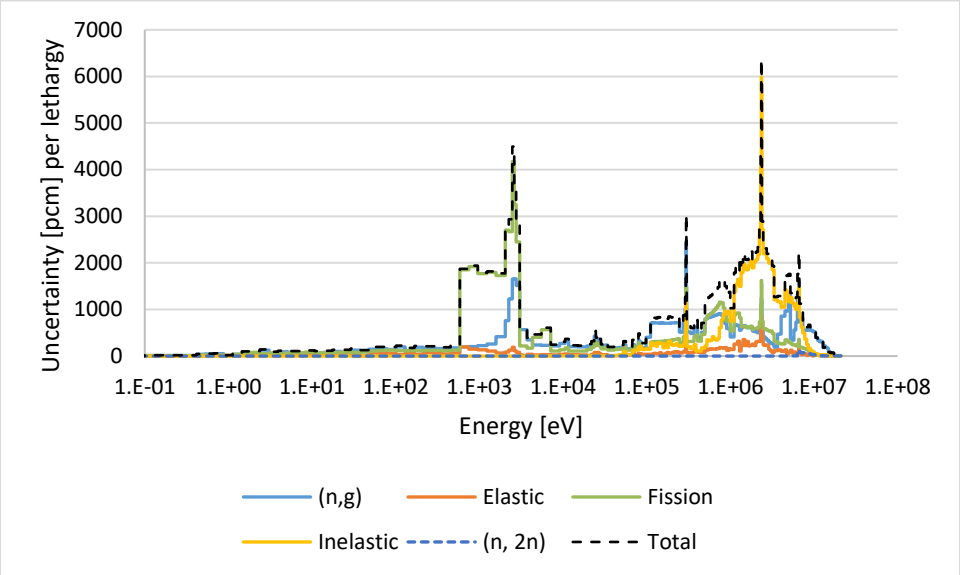

Figure 3.15. Group-wise uncertainty in k_∞ from the uncertainty due to each reaction for the RBWR-SSH unit cell at BOL.

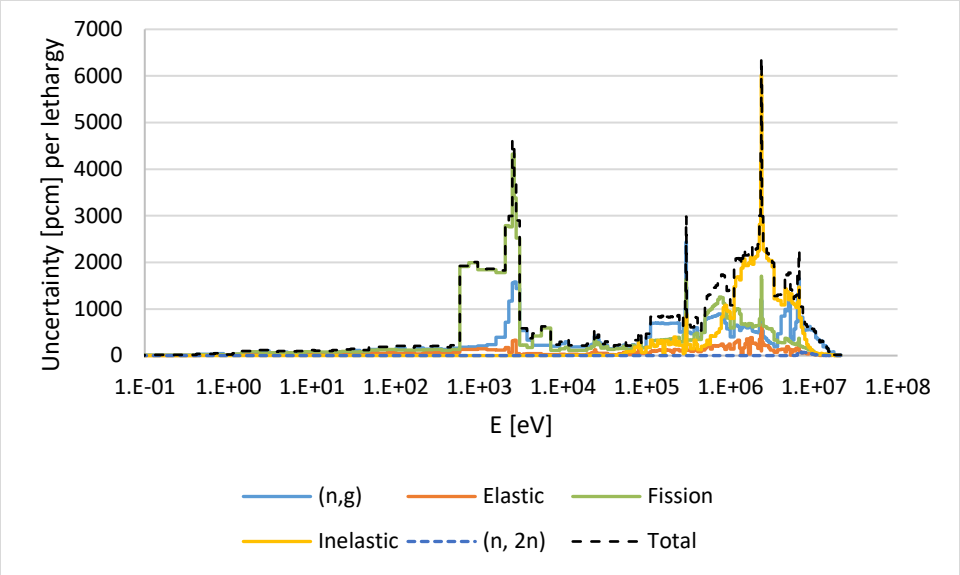

Figure 3.16. Group-wise uncertainty in k_∞ from the uncertainty due to each reaction for the RBWR-SSH unit cell at EOL.

3.4.2. Changes in Reactor State

In addition to the uncertainty in the multiplication factor, the uncertainty in the quantities which depend on k_∞ (including coolant void coefficient, coolant void collapse worth at nominal temperature, coolant void worth, and control rod worth) was also calculated and summarized in Table 3.13. In all cases, the statistical uncertainty is negligible. The uncertainty contribution from each isotope and reaction when the reactor is flooded is presented in Table 3.9 and Table 3.11, while the breakdown for when the reactor is voided is shown in Table 3.10 and Table 3.12. The uncertainty breakdown for each change in reactor state is shown in Table 3.14 through Table 3.21.

To elaborate further on the differences between the two sets of tables, Table 3.9 shows the uncertainty in the reactor in the flooded condition, while Table 3.15 shows the uncertainty associated with the transition between reference conditions to the flooded conditions. The uncertainties in the Reference Conditions referred to in Table 3.9 through Table 3.12 are the uncertainties which were presented in Section 3.4.1 – that is, using the average flow rate distribution. Since the uncertainty in the nuclear data is fixed between states, Table 3.14 through Table 3.21 effectively show the change in importance for each reaction between the reference and perturbed state, weighted by the uncertainty of each reaction.

For the cases in which the water density was perturbed, the change in the spectrum significantly affects the uncertainties. Since inelastic scattering is a threshold reaction, the sensitivity to it changes the most compared to other reactions. Similarly, the uncertainty in ^{232}Th capture increases as the spectrum hardens. The uncertainty due to ^{233}U fission is highest when the spectrum is the most epithermal, so both voiding the core and flooding it reduce the total uncertainty. The control rod worth has very low uncertainty relative to the other changes; even with rods inserted, the uncertainty in the ^{10}B (n,α) reaction is nearly negligible, and the uncertainty from ^{10}B is only greater than 1 pcm when the control rods are inserted.

Table 3.9. Uncertainty in pcm of the multiplication factor for the RBWR-SSH unit cell at BOL when it is flooded due to uncertainty in each isotope and reaction.

Isotope	(n,g)	Elastic	Fission	Inelastic	(n, 2n)	Cross-terms	Total	Ref. Cond.
Am-241	86	2	2	1	0	9	87	34
Am-242m	17	0	24	0	0	n/a	29	21
Am-243	30	1	5	0	0	n/a	31	22
Cm-243	1	0	0	0	0	0	1	1
Cm-244	30	0	2	0	0	1	30	22
Cm-245	12	0	21	0	0	3	24	23
Cm-246	3	0	1	0	0	0	3	4
Cm-247	2	0	3	0	0	1	4	3
H-1	10	21	n/a	n/a	n/a	n/a	23	26
Np-237	29	0	2	0	0	n/a	29	29
O-16	176	34	n/a	5	0	3	179	191
Pu-238	59	4	2	0	0	12	60	39
Pu-239	80	1	99	6	0	33	132	131
Pu-240	74	1	11	7	0	1	75	54
Pu-241	53	1	40	1	0	n/a	67	51
Pu-242	88	0	2	1	0	n/a	88	41
Th-232	205	35	10	n/a	n/a	5	209	391
U-232	3	0	7	0	0	2	8	11
U-233	83	2	552	6	1	51	561	1176
U-234	78	7	122	4	0	n/a	145	260
U-235	19	0	5	0	0	4	20	44
U-236	21	0	17	1	0	n/a	27	30
U-238	119	19	14	139	6	44	189	406
Total	371	57	577	139	6	77	707	1356
Ref. Cond.	499	72	1196	362	5	149		

Table 3.10. Uncertainty in pcm of the multiplication factor for the RBWR-SSH unit cell at BOL when it is voided due to uncertainty in each isotope and reaction.

Isotope	(n,g)	Elastic	Fission	Inelastic	(n, 2n)	Cross-terms	Total	Ref. Cond.
Am-241	13	0	4	3	0	1	14	34
Am-242m	4	0	33	0	0	n/a	34	21
Am-243	12	0	10	3	0	n/a	16	22
Cm-243	1	0	1	0	0	0	1	1
Cm-244	18	0	5	1	0	0	19	22
Cm-245	12	0	15	0	0	0	19	23
Cm-246	3	0	1	0	0	0	3	4
Cm-247	1	0	1	0	0	0	2	3
H-1	0	1	n/a	n/a	n/a	n/a	1	26

Isotope	(n,g)	Elastic	Fission	Inelastic	(n, 2n)	Cross-terms	Total	Ref. Cond.
Np-237	21	0	5	2	0	n/a	21	29
O-16	183	137	n/a	7	0	4	229	191
Pu-238	24	1	8	1	0	2	25	39
Pu-239	107	1	85	46	0	10	144	131
Pu-240	51	1	31	32	0	10	68	54
Pu-241	31	0	23	10	0	n/a	40	51
Pu-242	5	0	5	2	0	n/a	7	41
Th-232	557	19	17	n/a	n/a	49	560	391
U-232	4	0	7	0	0	0	8	11
U-233	171	2	579	42	1	32	606	1176
U-234	106	0	364	17	0	n/a	379	260
U-235	79	0	14	4	0	4	80	44
U-236	7	0	30	9	0	n/a	32	30
U-238	148	11	23	570	4	108	599	406
Total	655	139	693	574	4	123	1129	1356
Ref. Cond.	499	72	1196	362	5	149		

Table 3.11. Uncertainty in pcm of the multiplication factor for the RBWR-SSH unit cell at EOL when it is flooded due to uncertainty in each isotope and reaction.

Isotope	(n,g)	Elastic	Fission	Inelastic	(n, 2n)	Cross-terms	Total	Ref. Cond.
Am-241	53	1	2	1	0	3	54	20
Am-242m	7	0	17	0	0	n/a	19	16
Am-243	25	0	6	0	0	n/a	26	19
Cm-243	1	0	0	0	0	0	1	1
Cm-244	30	0	3	0	0	1	30	22
Cm-245	10	0	21	0	0	2	23	22
Cm-246	3	0	1	0	0	0	3	4
Cm-247	2	0	3	0	0	1	3	3
H-1	11	36	n/a	n/a	n/a	n/a	38	36
Np-237	25	0	2	0	0	n/a	25	27
O-16	176	36	n/a	5	n/a	3	180	194
Pu-238	45	4	2	0	0	10	46	35
Pu-239	69	0	110	8	0	24	133	138
Pu-240	62	1	12	9	0	1	64	54
Pu-241	51	1	48	1	0	n/a	69	55
Pu-242	79	0	2	1	0	n/a	79	35
Sm-149	78	1	n/a	0	0	n/a	78	14
Sm-151	15	0	n/a	0	0	n/a	15	10
Th-232	205	33	12	n/a	n/a	8	208	377
U-232	3	0	8	0	0	2	9	12

Isotope	(n,g)	Elastic	Fission	Inelastic	(n, 2n)	Cross-terms	Total	Ref. Cond.
U-233	75	3	592	6	1	58	599	1213
U-234	67	6	135	5	0	n/a	151	279
U-235	17	0	5	1	0	4	18	43
U-236	15	0	18	2	0	n/a	24	30
U-238	103	16	14	155	4	17	189	408
Total	354	64	620	156	4	67	737	1389
Ref. Cond.	477	82	1240	377	4	129		

Table 3.12. Uncertainty in pcm of the multiplication factor for the RBWR-SSH unit cell at EOL when it is voided due to uncertainty in each isotope and reaction.

Isotope	(n,g)	Elastic	Fission	Inelastic	(n, 2n)	Cross-terms	Total	Ref. Cond.
Am-241	10	1	4	2	0	1	11	20
Am-242m	3	0	26	0	0	n/a	26	16
Am-243	12	0	10	4	0	n/a	16	19
Cm-243	1	0	1	0	0	n/a	1	1
Cm-244	21	0	6	1	0	0	22	22
Cm-245	12	0	15	0	0	0	20	22
Cm-246	3	0	1	0	0	0	3	4
Cm-247	1	0	1	0	0	0	2	3
H-1	0	1	n/a	n/a	n/a	n/a	1	36
Np-237	20	0	5	2	0	n/a	21	27
O-16	181	149	n/a	7	n/a	3	235	194
Pu-238	24	0	8	1	0	1	26	35
Pu-239	111	1	92	49	0	12	152	138
Pu-240	52	1	32	34	0	4	70	54
Pu-241	35	1	28	14	0	n/a	47	55
Pu-242	5	1	5	2	0	n/a	8	35
Sm-149	9	0	n/a	1	0	n/a	9	14
Sm-151	10	0	n/a	1	0	n/a	10	10
Th-232	523	17	16	n/a	n/a	44	526	377
U-232	4	0	8	0	n/a	0	9	12
U-233	156	4	571	40	1	42	595	1213
U-234	105	1	375	18	0	n/a	389	279
U-235	77	0	15	4	0	7	79	43
U-236	7	1	31	9	0	n/a	33	30
U-238	138	10	22	534	4	100	561	408
Total	621	151	693	539	4	118	1092	1389
Ref. Cond.	477	82	1240	377	4	129		

Table 3.13. Uncertainty in the RBWR-SSH void coefficient, void collapse worth, void worth, and control rod worth due to uncertainty in the nuclear data.

	Void coefficient [pcm/% void]	Reactivity insertion from flooding the reactor [pcm]	Reactivity insertion from voiding the reactor [pcm]	Control rod worth [pcm]
BOL	-16.3 ± 8.4	4309 ± 734	2000 ± 861	-10581 ± 110
EOL	33.01 ± 7.2	651 ± 736	5121 ± 868	-11084 ± 103

Table 3.14. Uncertainty in the void coefficient in pcm/% void for the RBWR-SSH unit cell at BOL due to uncertainty in each isotope and reaction.

Isotope	(n,g)	Elastic	Fission	Inelastic	(n, 2n)	Cross-terms	Total
Am-241	0.6	0.2	0.0	0.0	0.0	0.3	0.7
Am-242m	0.1	0.0	0.2	0.0	0.0	n/a	0.2
Am-243	0.2	0.1	0.0	0.0	0.0	n/a	0.2
Cm-244	0.3	0.1	0.0	0.0	0.0	0.0	0.3
Cm-245	0.1	0.0	0.2	0.0	0.0	0.0	0.2
H-1	0.0	0.2	n/a	n/a	n/a	n/a	0.2
Np-237	0.2	0.0	0.0	0.0	0.0	n/a	0.2
O-16	0.1	0.1	n/a	0.0	0.0	0.0	0.2
Pu-238	0.4	0.1	0.0	0.0	0.0	0.1	0.4
Pu-239	0.8	0.1	0.7	0.4	0.0	0.2	1.2
Pu-240	0.4	0.3	0.2	0.4	0.0	0.4	0.8
Pu-241	0.5	0.1	0.3	0.2	0.0	n/a	0.6
Pu-242	0.7	0.0	0.0	0.0	0.0	n/a	0.7
Th-232	3.1	0.3	0.0	n/a	n/a	0.2	3.1
U-232	0.0	0.0	0.1	0.0	0.0	0.0	0.1
U-233	1.1	0.2	6.4	0.2	0.0	1.2	6.6
U-234	0.7	0.2	1.8	0.2	0.0	n/a	1.9
U-235	0.6	0.0	0.1	0.0	0.0	0.1	0.6
U-236	0.2	0.0	0.1	0.1	0.0	n/a	0.2
U-238	0.8	0.2	0.1	2.9	0.0	0.5	3.1
Total	3.8	0.7	6.7	3.0	0.0	1.4	8.4

Table 3.15. Uncertainty in the reactivity insertion in pcm from flooding the reactor for the RBWR-SSH at BOL due to uncertainty in each isotope and reaction.

Isotope	(n,g)	Elastic	Fission	Inelastic	(n, 2n)	Cross-terms	Total
Am-241	56	1	2	1	0	3	56
Am-242m	13	0	16	0	0	n/a	21
Am-243	11	0	3	1	0	n/a	12
Cm-243	0	0	0	0	0	0	1
Cm-244	14	0	2	0	0	0	14
Cm-245	7	0	14	0	0	2	16
Cm-246	2	0	0	0	0	0	2
Cm-247	1	0	2	0	0	1	2

Isotope	(n,g)	Elastic	Fission	Inelastic	(n, 2n)	Cross-terms	Total
H-1	9	5	n/a	n/a	n/a	n/a	10
Np-237	16	0	2	0	0	n/a	17
O-16	7	22	n/a	2	0	1	23
Pu-238	28	1	2	0	0	3	28
Pu-239	63	0	46	12	0	48	92
Pu-240	41	1	11	11	0	5	44
Pu-241	17	0	16	1	0	n/a	23
Pu-242	48	1	2	1	0	n/a	48
Th-232	196	12	5	n/a	n/a	14	197
U-232	2	0	5	0	0	1	6
U-233	65	7	632	11	0	72	640
U-234	31	1	125	6	0	n/a	129
U-235	24	0	6	1	0	3	25
U-236	6	0	10	3	0	n/a	12
U-238	58	9	7	222	1	38	233
Total	246	28	647	223	1	95	734

Table 3.16. Uncertainty in the reactivity insertion in pcm from voiding the reactor for the RBWR-SSH at BOL due to uncertainty in each isotope and reaction.

Isotope	(n,g)	Elastic	Fission	Inelastic	(n, 2n)	Cross-terms	Total
Am-241	32	2	1	2	0	6	33
Am-242m	5	0	21	0	0	n/a	22
Am-243	18	1	2	2	0	n/a	18
Cm-244	18	0	2	0	0	1	18
Cm-245	7	0	11	0	0	1	13
Cm-246	2	0	1	0	0	0	2
Cm-247	1	0	2	0	0	0	2
Cm-248	0	0	0	0	0	0	0
H-1	1	26	n/a	n/a	n/a	n/a	26
Np-237	17	0	2	1	0	n/a	17
O-16	1	82	n/a	1	0	0	82
Pu-238	32	4	4	0	0	8	34
Pu-239	56	1	87	30	0	37	113
Pu-240	37	1	17	15	0	2	43
Pu-241	39	1	28	10	0	n/a	49
Pu-242	39	1	1	1	0	n/a	39
Th-232	295	25	2	n/a	n/a	19	296
U-232	1	0	5	0	0	1	6
U-233	86	7	730	27	0	82	740
U-234	78	6	117	9	0	n/a	141
U-235	37	0	9	2	0	4	38
U-236	14	0	7	5	0	n/a	16

Isotope	(n,g)	Elastic	Fission	Inelastic	(n, 2n)	Cross-terms	Total
U-238	90	10	3	215	1	23	234
Total	347	90	746	219	1	95	861

Table 3.17. Uncertainty in the control rod worth in pcm for the RBWR-SSH at BOL due to uncertainty in each isotope and reaction.

Isotope	(n,g)	Elastic	Fission	Inelastic	(n, 2n)	Cross-terms	Total
Am-241	6	0	1	0	0	1	6
Am-242m	1	0	2	0	0	n/a	2
Am-243	3	0	1	0	0	n/a	3
B-10	10[9]	1	n/a	7	n/a	2	13
Cm-244	3	0	1	0	0	0	3
Cm-245	2	0	1	0	0	0	2
H-1	0	4	n/a	n/a	n/a	n/a	4
Np-237	4	0	1	0	0	n/a	4
O-16	0	10	n/a	1	0	0	10
Pu-238	5	1	1	0	0	1	5
Pu-239	8	0	7	4	0	3	12
Pu-240	6	1	3	3	0	2	7
Pu-241	6	0	3	0	0	n/a	6
Pu-242	8	0	1	0	0	n/a	8
Th-232	42	4	3	n/a	n/a	3	42
U-232	0	0	0	0	0	0	1
U-233	9	4	50	3	0	14	53
U-234	9	1	46	2	0	n/a	47
U-235	3	0	1	0	0	1	3
U-236	2	0	5	1	0	n/a	5
U-238	22	2	3	63	1	13	68
Total	52	12	68	63	1	20	110

Table 3.18. Uncertainty in the void coefficient in pcm/% void for the RBWR-SSH at EOL due to uncertainty in each isotope and reaction.

Isotope	(n,g)	Elastic	Fission	Inelastic	(n, 2n)	Cross-terms	Total
Am-241	0.3	0.6	0.0	0.1	0.0	0.3	0.8
Am-242m	0.0	0.0	0.2	0.0	0.0	n/a	0.2
Am-243	0.2	0.1	0.0	0.0	0.0	n/a	0.2
Cm-244	0.2	0.1	0.0	0.0	0.0	0.0	0.3
Cm-245	0.1	0.0	0.2	0.0	0.0	0.0	0.2
Cm-246	0.0	0.0	0.0	0.0	0.0	0.0	0.1
H-1	0.0	0.3	n/a	n/a	n/a	n/a	0.3
Np-237	0.2	0.0	0.0	0.0	0.0	n/a	0.2

[9] The (n,α) reaction is summarized here, as the ^{10}B (n,g) reaction is negligible.

Isotope	(n,g)	Elastic	Fission	Inelastic	(n, 2n)	Cross-terms	Total
O-16	0.2	0.5	n/a	0.2	n/a	0.1	0.5
Pu-238	0.4	0.4	0.0	0.0	0.0	0.2	0.6
Pu-239	0.7	0.1	0.8	0.2	0.0	0.3	1.1
Pu-240	0.4	0.3	0.2	0.1	0.0	0.1	0.6
Pu-241	0.5	0.1	0.4	0.1	0.0	n/a	0.6
Pu-242	0.5	0.1	0.0	0.1	0.0	n/a	0.5
Sm-149	0.3	0.2	n/a	0.1	0.0	n/a	0.3
Sm-151	0.1	0.0	n/a	0.0	0.0	n/a	0.1
Th-232	2.9	0.8	0.0	n/a	n/a	0.7	3.1
U-232	0.0	0.0	0.1	0.0	0.0	0.0	0.1
U-233	0.9	0.8	4.9	0.3	0.0	1.6	5.3
U-234	0.7	0.1	1.1	0.4	0.0	n/a	1.4
U-235	0.4	0.0	0.1	0.0	0.0	0.1	0.4
U-236	0.1	0.1	0.1	0.2	0.0	n/a	0.2
U-238	0.6	0.7	0.1	2.3	0.1	1.6	2.9
Total	3.4	1.7	5.1	2.3	0.1	2.4	7.2

Table 3.19. Uncertainty in the reactivity insertion in pcm from flooding the reactor for the RBWR-SSH at EOL due to uncertainty in each isotope and reaction.

Isotope	(n,g)	Elastic	Fission	Inelastic	(n, 2n)	Cross-terms	Total
Am-241	36	1	1	1	0	4	36
Am-242m	5	0	11	0	0	n/a	13
Am-243	9	1	3	1	0	n/a	10
Cm-243	0	0	0	0	0	0	1
Cm-244	15	1	2	0	0	0	16
Cm-245	7	0	13	0	0	2	15
Cm-246	2	0	0	0	0	0	2
Cm-247	1	0	2	0	0	1	2
H-1	10	1	n/a	n/a	n/a	n/a	10
Np-237	15	0	2	0	0	n/a	16
O-16	6	29	n/a	1	n/a	0	30
Pu-238	19	1	3	0	0	1	19
Pu-239	60	1	51	16	0	45	92
Pu-240	34	1	12	13	0	2	38
Pu-241	15	0	18	2	0	n/a	24
Pu-242	44	1	2	1	0	n/a	44
Sm-149	71	1	n/a	0	0	n/a	71
Sm-151	8	0	n/a	1	0	n/a	8
Th-232	184	10	4	n/a	n/a	12	185
U-232	2	0	6	0	0	1	7
U-233	62	5	637	12	0	59	643
U-234	31	2	135	6	0	n/a	138

Isotope	(n,g)	Elastic	Fission	Inelastic	(n, 2n)	Cross-terms	Total
U-235	25	0	6	1	0	3	26
U-236	4	1	10	3	0	n/a	12
U-238	55	8	7	220	0	41	231
Total	238	33	654	221	0	85	736

Table 3.20. Uncertainty in the reactivity insertion in pcm from voiding the reactor for the RBWR-SSH at EOL due to uncertainty in each isotope and reaction.

Isotope	(n,g)	Elastic	Fission	Inelastic	(n, 2n)	Cross-terms	Total
Am-241	19	2	1	2	0	4	19
Am-242m	3	0	16	0	0	n/a	16
Am-243	15	0	2	3	0	n/a	16
Cm-244	18	1	2	1	0	1	18
Cm-245	6	0	11	0	0	1	12
Cm-246	2	0	1	0	0	0	2
Cm-247	1	0	2	0	0	0	2
H-1	2	36	n/a	n/a	n/a	n/a	36
Np-237	14	0	1	1	0	n/a	14
O-16	2	84	n/a	1	n/a	0	84
Pu-238	28	4	4	0	0	8	30
Pu-239	55	1	93	27	0	37	117
Pu-240	33	1	18	13	0	4	40
Pu-241	39	1	34	13	0	n/a	54
Pu-242	33	1	1	1	0	n/a	33
Sm-149	13	2	n/a	0	0	n/a	13
Sm-151	9	0	n/a	0	0	n/a	9
Th-232	269	23	1	n/a	n/a	19	271
U-232	1	0	6	0	n/a	1	6
U-233	77	4	765	23	0	69	772
U-234	73	5	105	9	0	n/a	128
U-235	37	0	9	2	0	6	38
U-236	11	1	6	4	0	n/a	13
U-238	79	11	2	166	0	43	190
Total	317	95	779	171	0	92	868

Table 3.21. Uncertainty in the control rod worth in pcm for the RBWR-SSH at EOL due to uncertainty in each isotope and reaction.

Isotope	(n,g)	Elastic	Fission	Inelastic	(n, 2n)	Cross-terms	Total
Am-241	3	1	0	0	0	1	3
Am-242m	0	0	2	0	0	n/a	2
Am-243	2	0	1	0	0	n/a	3

Isotope	(n,g)	Elastic	Fission	Inelastic	(n, 2n)	Cross-terms	Total
B-10	11[10]	2	n/a	7	n/a	2	13
Cm-244	3	0	1	0	0	0	3
Cm-245	2	0	1	0	0	0	2
H-1	1	5	n/a	n/a	n/a	n/a	5
Np-237	3	0	1	0	0	n/a	3
O-16	1	11	n/a	1	n/a	0	11
Pu-238	4	3	1	0	0	2	6
Pu-239	9	0	8	3	0	3	13
Pu-240	5	1	3	2	0	1	6
Pu-241	6	1	3	1	0	n/a	7
Pu-242	6	0	1	0	0	n/a	6
Sm-149	2	1	n/a	0	0	n/a	3
Sm-151	1	0	n/a	1	0	n/a	2
Th-232	42	4	2	n/a	n/a	3	43
U-232	0	0	0	0	n/a	0	1
U-233	10	5	35	3	0	13	39
U-234	8	0	48	3	0	n/a	49
U-235	3	0	1	0	0	1	3
U-236	2	1	5	1	0	n/a	6
U-238	19	2	3	62	1	7	65
Total	50	14	60	62	1	15	103

3.4.3. Uncertainty in k_∞ due to Void Fraction Uncertainty

The uncertainty in k_∞ due to the uncertainty in the void fraction correlation was also calculated. The uncertainty corresponding to a superficial liquid velocity of 1.0 m/s in Table 4 of [44] was used. It should be noted that there is not much experimental data for such tight lattices, and that a 20% difference compared to the LPG correlation and other experimental data is observed [53]; therefore, to bound the uncertainty, the uncertainty in k_∞ assuming a constant 20% uncertainty in the void fraction was also assumed as a bounding case. The uncertainty is presented in Table 3.22, while Figure 3.17 shows the sensitivity coefficients and Figure 3.18 through Figure 3.21 show the water density covariance plots.

The uncertainty changes significantly with burnup. In the fresh fuel, increasing the water density in the seed causes the reactivity to increase, as it causes the leakage to decrease. The blankets have the opposite effect as thorium has effectively no chance of fissioning below its threshold energy. The enrichment of the fuel increases with burnup, so by the end of life, increasing the water density in the seed reduces the amount of fast fissions more significantly than the loss of leakage. Similarly, the sensitivity coefficient of the blanket becomes positive as ^{233}U is bred into the fuel.

[10] The (n,α) reaction is summarized here, as the ^{10}B (n,g) reaction is negligible.

Table 3.22. Uncertainty in k_∞ due to void fraction uncertainty for the RBWR-SSH.

Burnup	Uncertainty using [44] for α uncertainty [pcm]	Uncertainty assuming 20% α uncertainty [pcm]
BOL	252	610
EOL	161	418

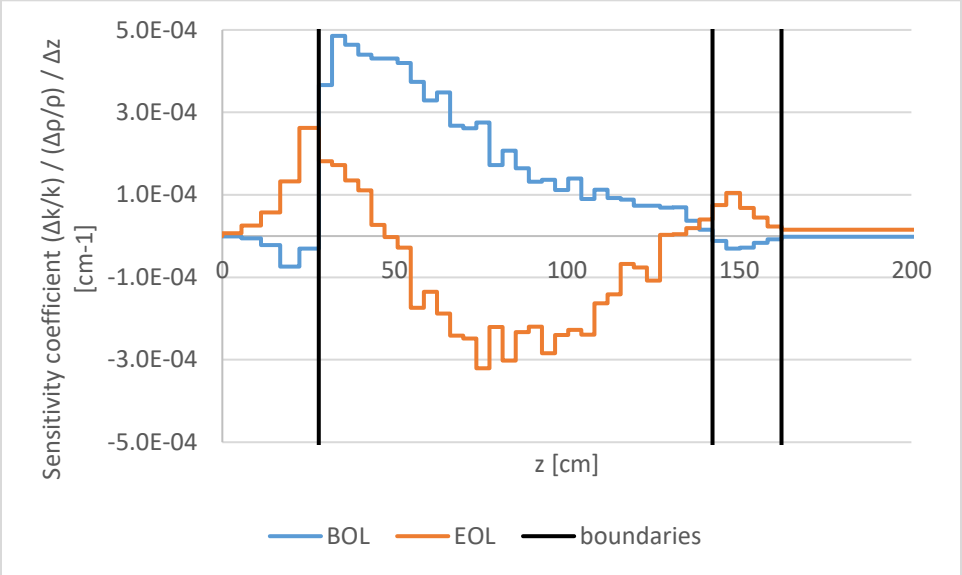

Figure 3.17. Sensitivity coefficients for the multiplication factor of the RBWR-SSH due to a relative change in water density.

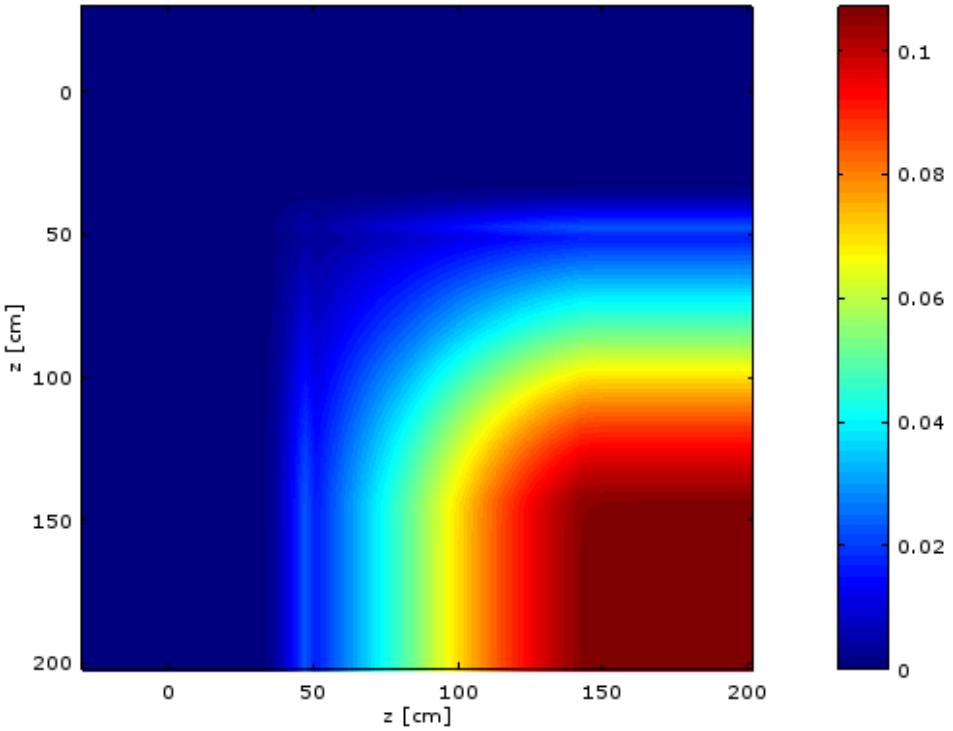

Figure 3.18. Relative water density covariance plot for the RBWR-SSH at BOL assuming void fraction uncertainty as specified in [44]. The x and y axes are the axial position in the fuel, where 0 is the bottom of the lower blanket.

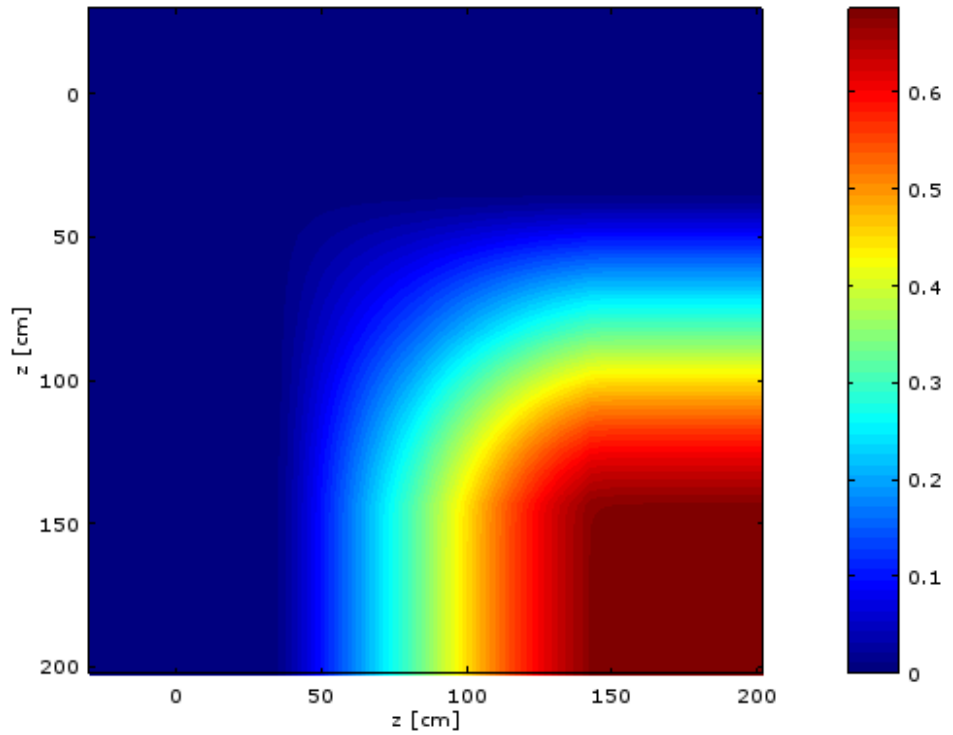

Figure 3.19. Relative water density covariance plot for the RBWR-SSH at BOL assuming 20% void fraction uncertainty.

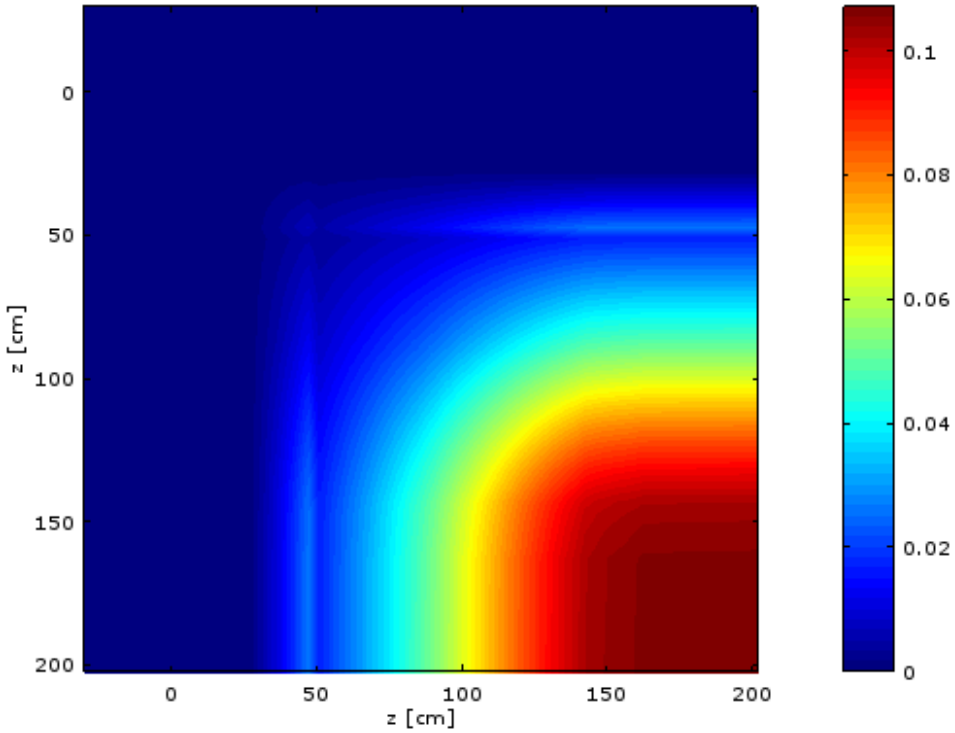

Figure 3.20. Relative water density covariance plot for the RBWR-SSH at EOL assuming void fraction uncertainty as specified in [44].

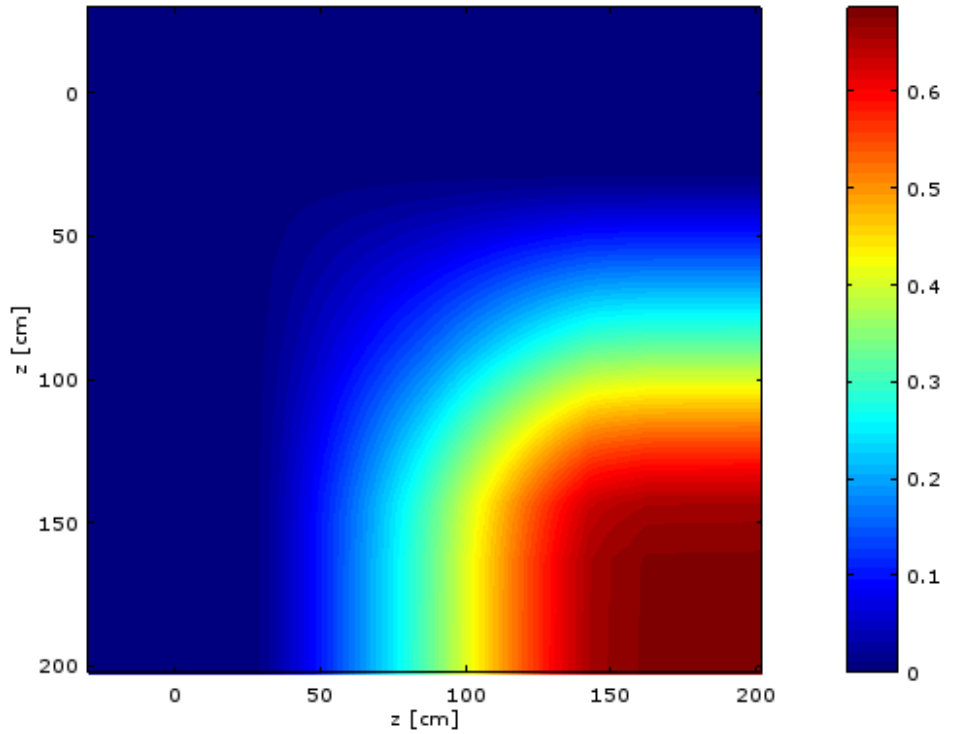

Figure 3.21. Relative water density covariance plot for the RBWR-SSH at EOL assuming 20% void fraction uncertainty.

3.5. Fuel cycle analysis

It was desired to assess the fuel cycle impacts of the RBWR-SSH as compared to the RBWR-AC and the ARR [4]. The methodology used by the recent DOE sponsored Fuel Cycle Evaluation and Screening (FCE&S) Campaign [1] is applied for part of this comparison, as described in Section 2.9.

3.5.1. General Fuel Cycle Characteristics

Figure 3.2 shows a schematic view of the RBWR-SSH fuel cycle, while Figure 3.22 shows the RBWR-AC and the ARR fuel cycles considered. These cores are designed to operate on a closed fuel cycle while being supplied no fissile fuel. Both the RBWR-AC and RBWR-SSH require a fertile blanket in order to breed enough fissile material within the reactor.

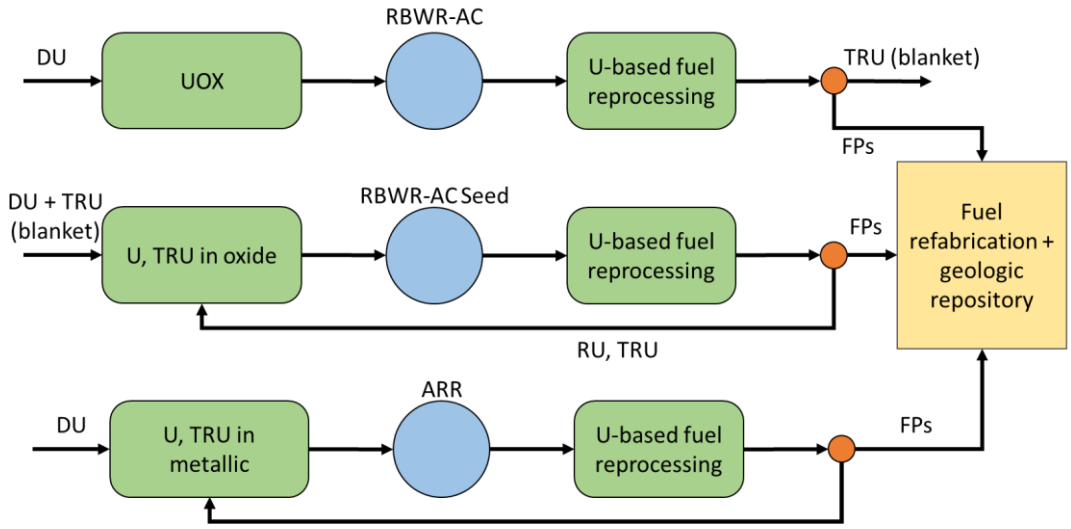

Figure 3.22. Schematic view of the RBWR-AC and the ARR fuel cycles.

Table 3.23 compares the performance characteristics of the different cores. The RBWR core has significantly smaller burnup and therefore features higher fuel reprocessing and fabrication capacity than the ARR. The capacity factor for the ARR was assumed to be 85% in accordance with the assumptions of [4].

Table 3.23. Performance characteristics of the RBWR-SSH, RBWR-AC, and ARR cores.

Parameters	**RBWR-SSH**	**RBWR-AC**	**ARR**
Thermal power, MW_{th}	3926	3926	1000
Electrical power, MW_e	1354	1354	400
Capacity factor, %	90	90	85
Average discharge burnup, GWD/t	44	45	73
Specific power, MW_{th}/t	25.2	27.3	59.7
Power density, W/cc	99.3	123	289
Peak LHGR, W/cm	84.2	472	389
Number of batches	4.5	4.5	3/3/4.5
Fuel inventory in core, t	154	144	16.7
Charge fuel mass per batch, t	34.7	33.9	4.8

Parameters	RBWR-SSH	RBWR-AC	ARR
Fuel residence time, EFFD	1758	1651	1110/1110/1665
Cycle length, EFPD	411	389	370
Burnup reactivity swing, %Δk/k	1.3	1.5	-0.1
Reprocessing capacity, kg/GWeYr	23882.0	23483.9	12500.0
Pu	1345.6	2717.7	1643.6
TRU	1503.3	2943.7	1711.3
Charge mass fraction, %			
- Th-232	58.3	-	-
- TRTh	5.5	-	-
- U-238	30.1	87.5	86.3
- TRU	6.2	12.5	13.7
Discharge mass fraction, %			
- Th-232	55.8	-	-
- TRTh	5.6	-	-
- U-238	28.0	82.9	78.5
- TRU	6.3	12.6	13.7
- FPs	4.2	4.6	7.8
Fuel mass at time of recycle, %			
- Th-232	55.8	-	-
- TRTh	5.6	-	-
- U-238	28.0	82.9	78.5
- TRU	6.3	12.5	13.7
- FPs	4.2	4.6	7.8

The discharged fuel composition after 5 years cooling is shown in Table 3.24; it is used for later fuel cycle analysis. In the more thermal systems, a larger fraction of the plutonium is composed of non-fissile isotopes.

Table 3.24. Discharged fuel composition of the RBWR-SSH, the RBWR-AC, and ARR after 5 years cooling. All values are given in weight percent.

Nuclide	RBWR-SSH	RBWR-AC	ARR
Th-232	58.24	0.00	0.00
Pa-231	0.03	0.00	0.00
U-232	0.02	0.00	0.00
U-233	3.59	0.00	0.00
U-234	1.46	0.03	0.03
U-235	0.42	0.09	0.30
U-236	0.38	0.03	0.39
U-238	29.29	86.72	84.43
Np-237	0.13	0.07	0.17
Pu-238	0.31	0.39	0.20
Pu-239	3.01	5.72	9.43
Pu-240	2.02	4.74	3.94
Pu-241	0.30	0.64	0.38
Pu-242	0.25	0.65	0.32
Am-241	0.29	0.54	0.25

Nuclide	RBWR-SSH	RBWR-AC	ARR
Am-242m	0.02	0.02	0.01
Am-243	0.11	0.19	0.08
Cm-244	0.07	0.13	0.06
Cm-245	0.03	0.04	0.01
Cm-246	0.02	0.02	0.01

3.5.2. Repository Analysis

The radioactivity, ingestion toxicity, and inhalation toxicity of the UNF and High Level Waste (HLW) was quantified at short term (10 years) and long term (100,000 years) after the fuel is discharged from the cores according to the methodology detailed in Section 2.9.

Figure 3.23 compares the radioactivity of the self-sustaining systems HLW at 10 years and 100,000 years after fuel discharge. Since fission products dominate the radioactivity, the differences are mainly due to the different thermal efficiencies between the different systems. The long-lived radioactivity is much higher for the thorium fuel cycles due to the much larger radioactivity coming from the ^{233}U decay daughters.

Figure 3.24 shows the inhalation toxicity at 10 years and 100,000 years. The short-term inhalation toxicity is driven by Pu and minor actinides; since the RBWR-SSH fuel is mostly thorium-based, it has less Pu and minor actinides than the RBWR-AC. The ARR reactor outperforms the RBWRs due to its significantly lower required reprocessing capacity. In the long term, the decay from ^{229}Th dominates the RBWR-SSH inhalation toxicity, while the DU-fueled reactors are dominated by long-lived Pu isotopes.

Figure 3.25 shows the ingestion toxicity of TRU the transmutation systems at 10 years and 100,000 years. At 10 years, fission products still dominate the ingestion toxicity, so burnup and thermal efficiency dictate the short-term ingestion toxicity. At 100,000 years, the buildup of ^{229}Th drives the ingestion toxicity much higher than that of the DU-fueled reactors.

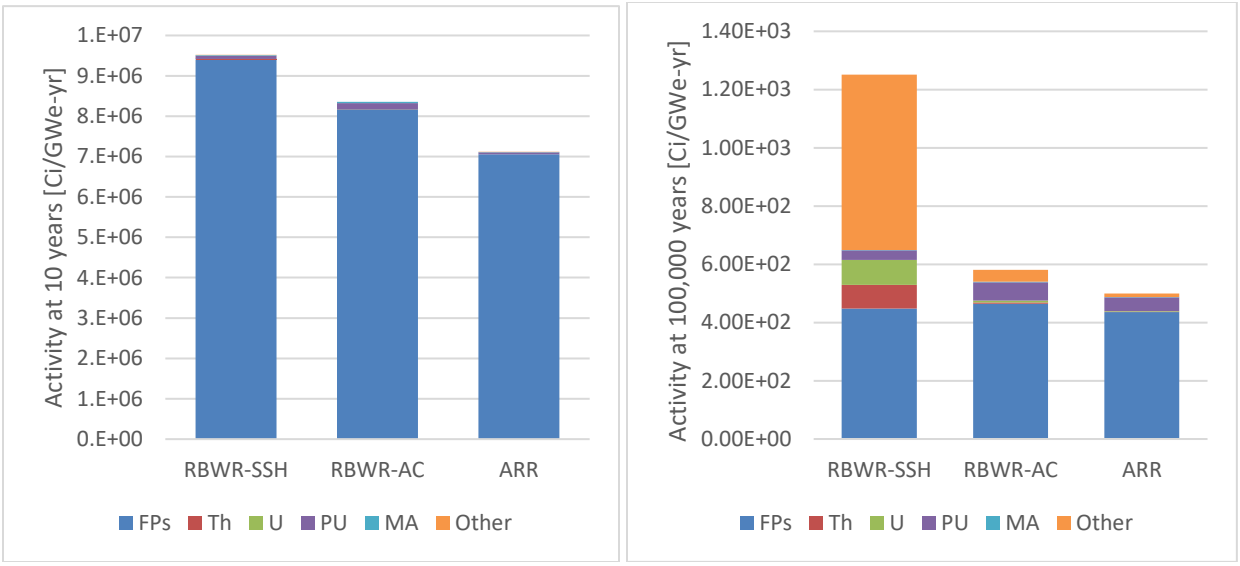

Figure 3.23. Radioactivity for the RBWR-SSH, RBWR-AC, and ARR at 10 years (left) and 100,000 years (right).

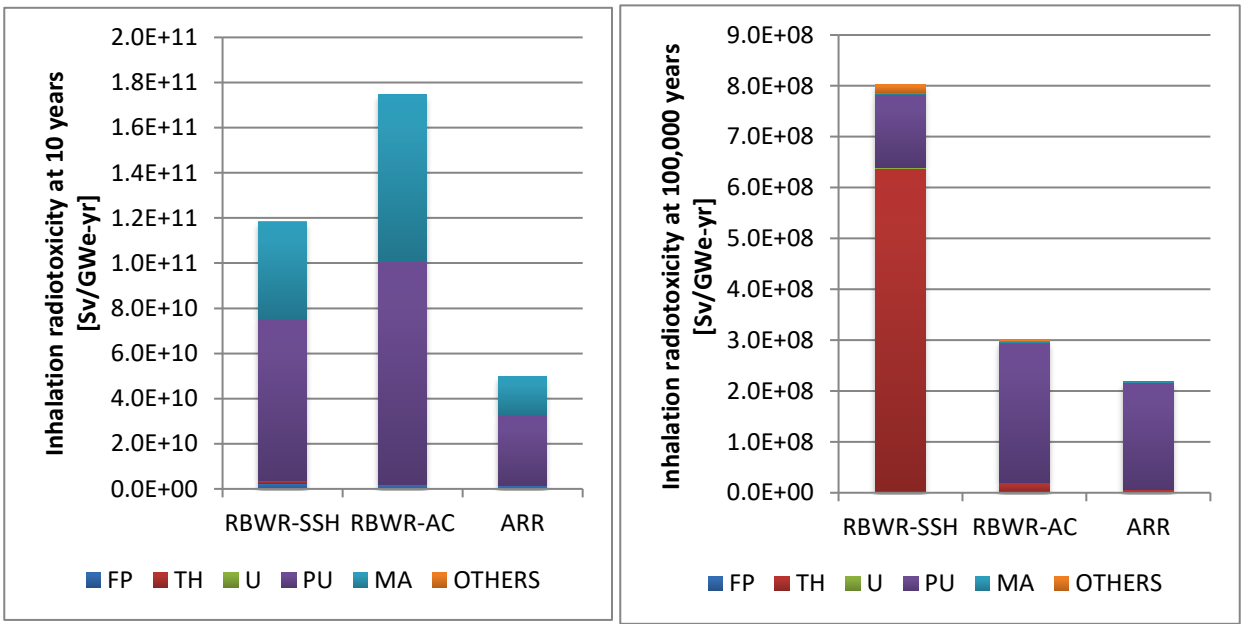

Figure 3.24. Inhalation toxicity of the waste stream from the RBWR-SSH, RBWR-AC, and ARR at 10 years (left) and 100,000 years (right).

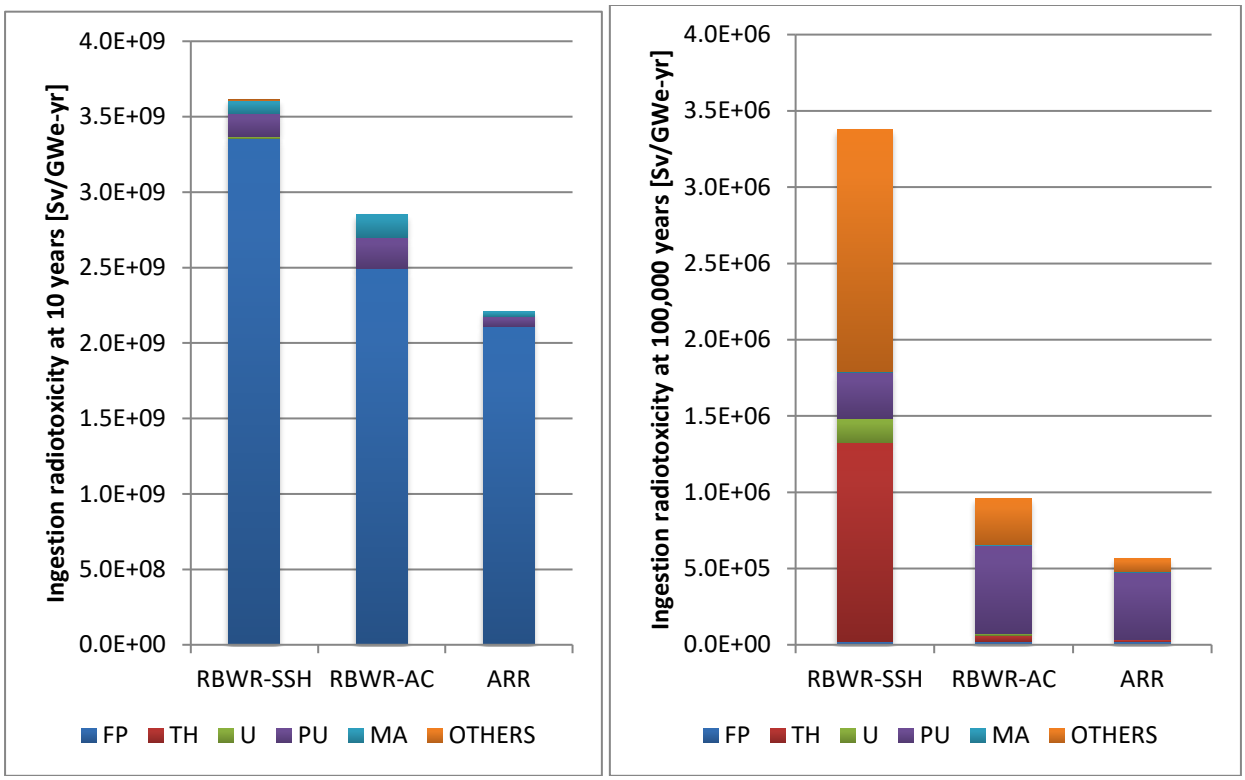

Figure 3.25 Ingestion toxicity of the waste stream from the RBWR-SSH, RBWR-AC, and ARR at 10 years (left) and 100,000 years (right).

3.5.3. Proliferation Resistance

The proliferation resistance is mainly evaluated based on the fissile plutonium fraction, specific decay heat of discharged plutonium, spontaneous fission neutron emission rate, plutonium inventory, ^{238}Pu/Pu ratio, and ^{232}U/^{233}U ratio, which are summarized for the self-sustaining reactors in Table 3.25. Pu-238, ^{240}Pu, and ^{242}Pu have high spontaneous neutron generation which significantly reduces the nuclear explosive yield. Pu-238 has a large decay heat that further complicates the design and maintenance of an explosive device [54]. It has been suggested [55] that it is not realistic to apply plutonium for weapon use when the fraction of ^{238}Pu is beyond 2% of the total plutonium; both RBWRs meet this metric, while the ARR has 1.4% ^{238}Pu/Pu. Similarly, ^{232}U poses a radiation hazard for anyone who would extract the uranium due to the 2.6 MeV gamma decay of its decay daughter, ^{208}Tl; just 1 ppm of ^{232}U/U poses a similar risk as reactor-grade Pu [56] although it would require 2.4% ^{232}U before the uranium would satisfy the IAEA standard for reduced physical protection requirements. Additionally, dilution with >80% ^{238}U or >70% ^{232}Th would make the material unattractive, although not to a sufficient degree that would reduce safeguards relative to existing levels [57].

Both epithermal spectrum reactors are significantly more proliferation resistant than the ARR, due to the accumulation of more non-fissile isotopes. The ARR has less than 2% ^{238}Pu/Pu, which is the threshold for weapons grade Pu; however, it still has sufficient ^{238}U for the material to be considered unattractive through dilution. The RBWR-SSH is the only one of the three which uses thorium, so it is the only one with any concern over ^{233}U. The addition of the DU into the feed stream is barely sufficient to reduce it to low-enriched uranium (12% ^{233}U or 20%

^{235}U), although it is expected that the removal of DU in order to keep the void feedback negative would change this; even without this, it has the lowest fraction of fissile material at reprocessing, and is unattractive for making weapons materials.

Table 3.25. Proliferation metrics for the RBWR-SSH, RBWR-AC, and ARR at reprocessing.

Metrics	RBWR-SSH	RBWR-AC	ARR
Fissile plutonium fraction at reprocessing, %	56%	52%	69%
^{238}Pu/Pu ratio at reprocessing, %	5.3%	3.2%	1.4%
Specific decay heat of plutonium at reprocessing, W/kg	33.9	22.0	11.2
Spontaneous fission neutrons per kg Pu at reprocessing, n/sec-kg	5.2E+05	5.3E+05	3.3E+05
Tot. plutonium reprocessed, tons/GWe-yr	1.35	2.72	1.64
Pu/^{238}U ratio at reprocessing	20.1%	14.0%	16.9%
^{232}U/^{233}U ratio at reprocessing, ppm	5093	-	-
Fissile U/U ratio at reprocessing, %	11.4%	-	-
Fissile U/Th ratio at reprocessing	6.9%	-	-
(Pu+fissile U)/(^{238}U+Th) ratio at reprocessing	11%	14%	17%

3.5.4. Fuel Cycle Costs

The fuel cycle costs for the transmuting reactors are compared in Figure 3.26, using the costs for activities specified in Table 2.4. The cost for these closed fuel cycle systems is largely dictated by the reprocessing and remote fabrication. The smaller reprocessing capacity for the ARR, due to its substantially higher average discharge burnup, reduces its fuel cycle cost compared with that of the RBWR systems. The RBWR-AC has slightly lower fuel cycle costs than the RBWR-SSH due to its lower discharge burnup.

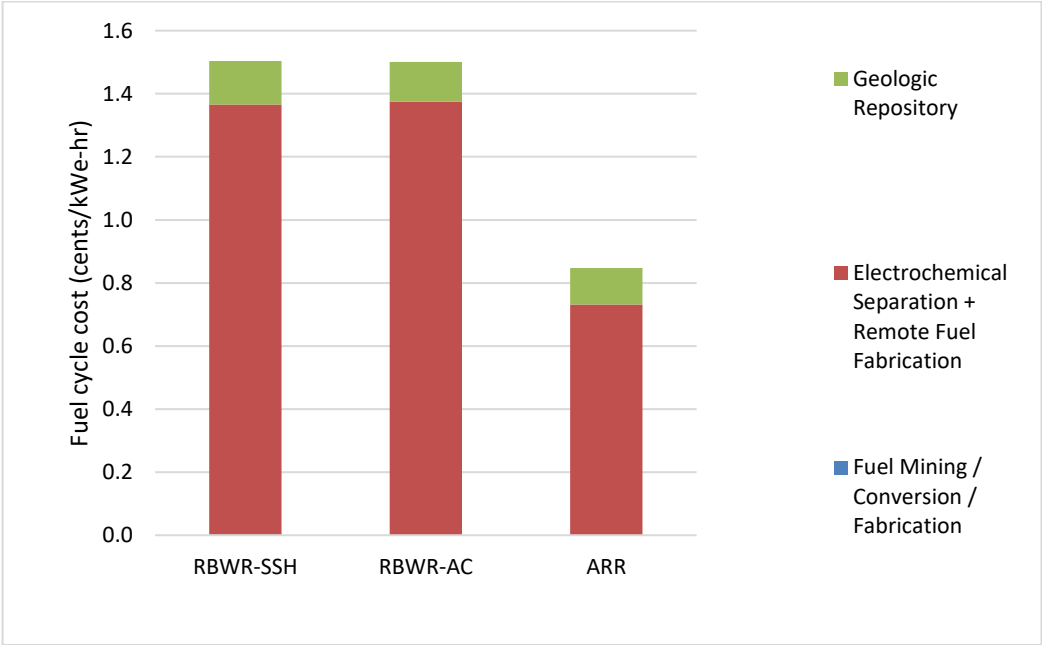

Figure 3.26. Fuel cycle costs of the RBWR-SSH compared against the RBWR-AC and the ARR.

3.5.5. Fuel Cycle Evaluation

Using the same methodology as the FCE&S campaign [1] which is summarized in Section 2.9.2, the performance of the RBWR-SSH system was compared against the performance of EG24 and EG28. EG24 and EG28 include all self-sustaining reactors which use natural uranium (EG24) or thorium (EG28) as the fertile feed material [1]. The mass flows were readjusted in order to use a uniform 33% thermal efficiency in both stages. The evaluation results are summarized in Table 3.26. The RBWR system can achieve very similar scores as the evaluation groups because most functions demonstrated by the ARR could be accomplished by the RBWRs. The RBWR-SSH performs in between EG24 and EG28, as they are all self-sufficient multirecycling systems and the RBWR-SSH uses a mix of thorium and DU feed. The economics of the TRU transmuting systems are not compared in Table 3.26.

Table 3.26. Fuel cycle evaluation metrics of the RBWR-SSH compared against existing evaluation groups.

	Metric	Value/Bin	Value/Bin	Value/Bin
		RBWR-SSH	EG24	EG28
Renormalization Factor		1.045	1.21	1.21
Nuclear Waste Management	Mass of SNF+HLW disposed, t/GWe-yr	1.29/A	1.34/A	1.58/A
	Activity of SNF+HLW (@100 years), MCi/GWe-yr	1.07/C	1.04/B	1.18/C
	Activity of SNF+HLW (@100,000 years), 10^{-4} MCi/GWe-Yr	12.5/C	6.1/B	30.3/D
	Mass of DU+RU+RTh disposed, t/GWe-yr	0.0/A	0.0/A	0.0/A
	Volume of LLW, m^3/GWe-yr	732.4/D	561.4/C	1168.7/D
Environmental Impact	Land use per energy generated, km^2/GWe-yr	0.08/A	0.08/A	0.09/A
	Water use per energy generated, ML/GWe-yr	23724/B	23717/B	23748/B
	Radiological exposure, Sv/GWe-yr	1.02/B	1.21/B	1.24/B
	Carbon emission - CO_2 released per energy generated, kt CO_2/GWe-yr	34.6/B	24.1/A	50.1/B
Resource Utilization	Natural Uranium required per energy generated, t/GWe-yr	0.1/A	1.4/A	0.0/A
	Natural Thorium required per energy generated, t/GWe-yr	0.8/A	0.0/A	1.7/A

3.6. Self-sustaining Thorium RBWR Conclusions

The RBWR-SS was designed to operate on a closed fuel cycle while only being supplied with fertile fuel. It was desired to use a single seed to alleviate some of the issues encountered with

the RBWR-AC. However, it was found that using the most conservative thermal-hydraulic correlations, it was not possible to sustain a self-sufficient fuel cycle without significant power downgrades. Even assuming the same thermal-hydraulic correlations as Hitachi used in the RBWR-AC, it was not possible to design the core to have sufficient shutdown margin while also having negative void feedback; using multiple seed regions may help with this, as it would reduce the Doppler coefficient while keeping the void coefficient negative. Alternatively, it is possible that reducing the assembly size while increasing the control blade thickness would provide the extra shutdown margin that is needed, although it will certainly incur a burnup penalty.

The spectrum of the RBWR-SSH remain similar to the RBWR-AC, although the physics are significantly different through the use of a single elongated seed and thorium as the primary fertile component of the fuel makeup. The RBWR-SSH and RBWR-AC designs can achieve a similar burnup, which is significantly smaller than that of the fast-spectrum ARR. The short-term radiotoxicity of the RBWR-SSH fuel is comparable to the RBWR-AC and ARR fuel since it is largely driven by fission products and Pu inventory; however, the long-lived decay daughters of ^{233}U increase the long-term radiotoxicity of the RBWR-SSH significantly relative to its uranium-fueled counterparts. The uncertainty in the RBWR-SSH multiplication factor was also assessed. The uncertainty from ^{232}Th capture and ^{233}U fission is very high, especially in the epithermal range. Future work may include performing a similar uncertainty analysis for the RBWR-AC and comparing the uncertainty.

4. RBWR-TR

The RBWR-TR is a low-conversion TRU-burning design based on the Hitachi RBWR-TB2 [7], [48]. The primary design objective for the RBWR-TR is to maximize the net TRU consumption rate while meeting the constraints in Section 2.2 in order to assure adequate safety margins. Since the external TRU feed is supplied from reprocessed used nuclear fuel from existing PWRs, maximizing the TRU consumption rate will effectively close the fuel cycle for an operating fleet of PWRs with a minimum number of RBWRs required. A related metric which is used throughout this chapter is the TRU fission efficiency, which is the fraction of fissions which occur in TRU isotopes.

Unlike in the RBWR-SS, the lattice in the RBWR-TR is not especially tight. Since its main objective is incinerating TRU, it benefits from reducing the conversion ratio; this leads it to have a relatively soft spectrum. However, the spectrum still needs to be significantly harder than a typical LWR in order to sustain criticality while retaining a negative void coefficient for an indefinite number of recycles. Nonetheless, the hydraulic diameter in the design space of interest was not sufficiently small to warrant using multiple void fraction correlations. Therefore, only one design for the RBWR-TR was created, and it was designed to meet the MCPR constraint with the most limiting correlation which was applicable. The M-CISE correlation [14] was used with an MCPR limit of 1.5, although the results are also reported using the H-CISE correlation.

Section 4.1 describes the models that were used, and additionally shows the results of a few modeling sensitivity studies. Section 4.2 documents the parametric studies that were performed. Section 4.3 presents the final RBWR-TR designs and compares their performance against that of the RBWR-TB2 and an analogous SFR. Section 4.4 calculates the uncertainty in several neutronics characteristics using generalized perturbation theory (GPT), and Section 4.4.1 analyses the fuel cycle of the RBWR-TR. Since the RBWR-TR benefits from using a more thermal spectrum, Section 4.6 briefly explores using a square lattice instead of a triangular lattice to achieve the same objective. Section 4.7 summarizes this chapter and draws general conclusions about the RBWR-TR design.

4.1. Assembly Model

Due to the time investment required to generate cross sections for the full core simulator, most of the design studies were performed on the assembly level using MocDown (Section 2.5) and extrapolating the performance to a full-core level.

The seed was axially split into 20 equally sized regions, while the upper and lower blankets were divided into 5 equally sized regions. A figure of the assembly unit cell model used for the equilibrium studies is shown in Figure 4.1; the fuel reprocessing scheme that was implemented in the equilibrium search is shown in Figure 4.2.

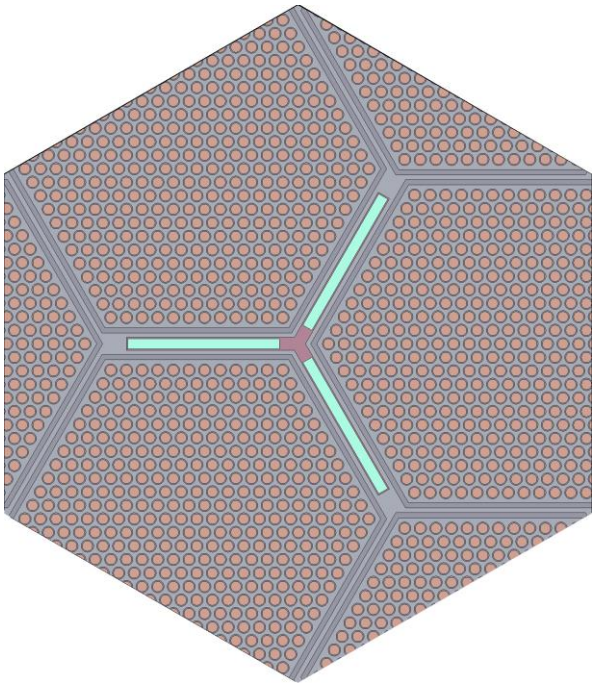

Figure 4.1. Fuel assembly slice of the RBWR-TR, as used in the equilibrium analysis.

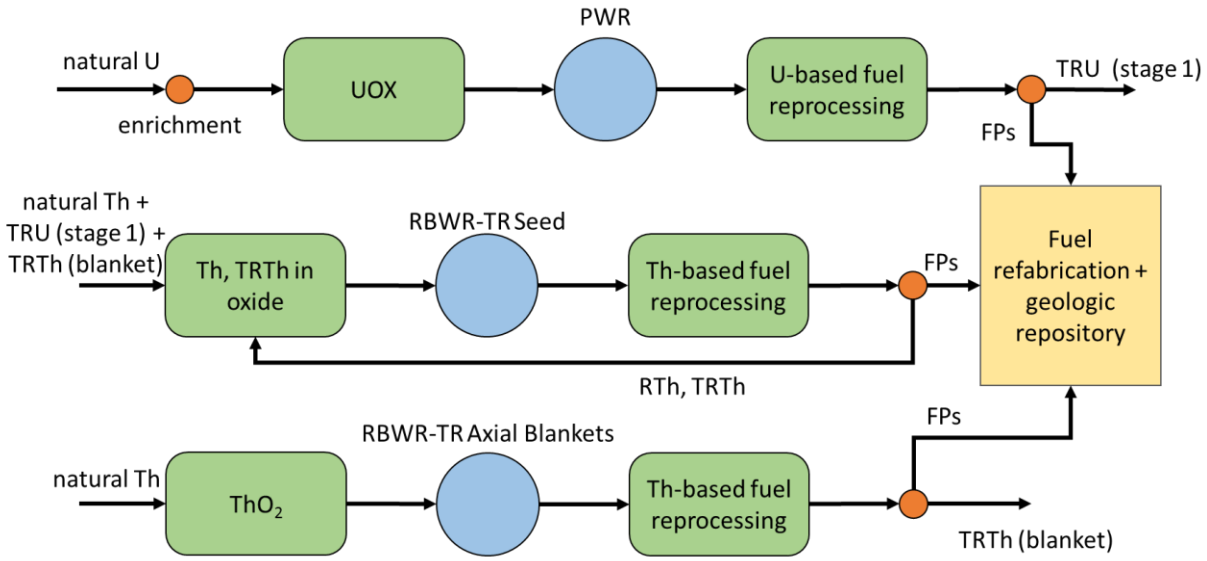

Figure 4.2. Fuel cycle scheme implemented in the equilibrium analysis.

4.1.1. Radial Enrichment Study

Since the spectrum of the RBWR-TR is much more thermal throughout the assembly than that of the RBWR-SS, the pin power peaking is less challenging. Additionally, since the objective is to maximize the TRU consumption rate, it is desired to keep the TRU near the assembly periphery where the spectrum is more thermal; therefore, a uniform enrichment was used. Although the pin peaking factor at BOL is 1.3, this was considered acceptable for the final design since it will even out with burnup and the margin against critical heat flux is high. The design parameters

used for this simulation are shown in Table 4.1. The pin power distribution assuming that the water in the bypass region is liquid density water is shown in Figure 4.3.

Table 4.1. Design parameters for the RBWR-TR assembly power peaking assessment.

Parameter	Units	Value
Assembly power	MW_{th}	5.453
Assembly HM mass (BOL)	kg	124.5
Avg TRF/HM at BOL	w/o	20.5
Seed TRF/HM at BOL	w/o	26.6
Avg TRU/HM at BOL	w/o	13.5
Seed TRU/HM at BOL	w/o	17.5
Assembly pitch	cm	19.77
Assembly coolant flow rate	kg/s	24.16
Upper blanket length	cm	15
Seed length	cm	100
Lower blanket length	cm	15
Fuel pin OD	cm	0.7048
Fuel pin pitch	cm	0.9444
Fuel pin P/D	-	1.34
Pins per assembly	-	397
Fraction of seed makeup which is TRU	a/o	4.05
Depletion time	EFPD	1185

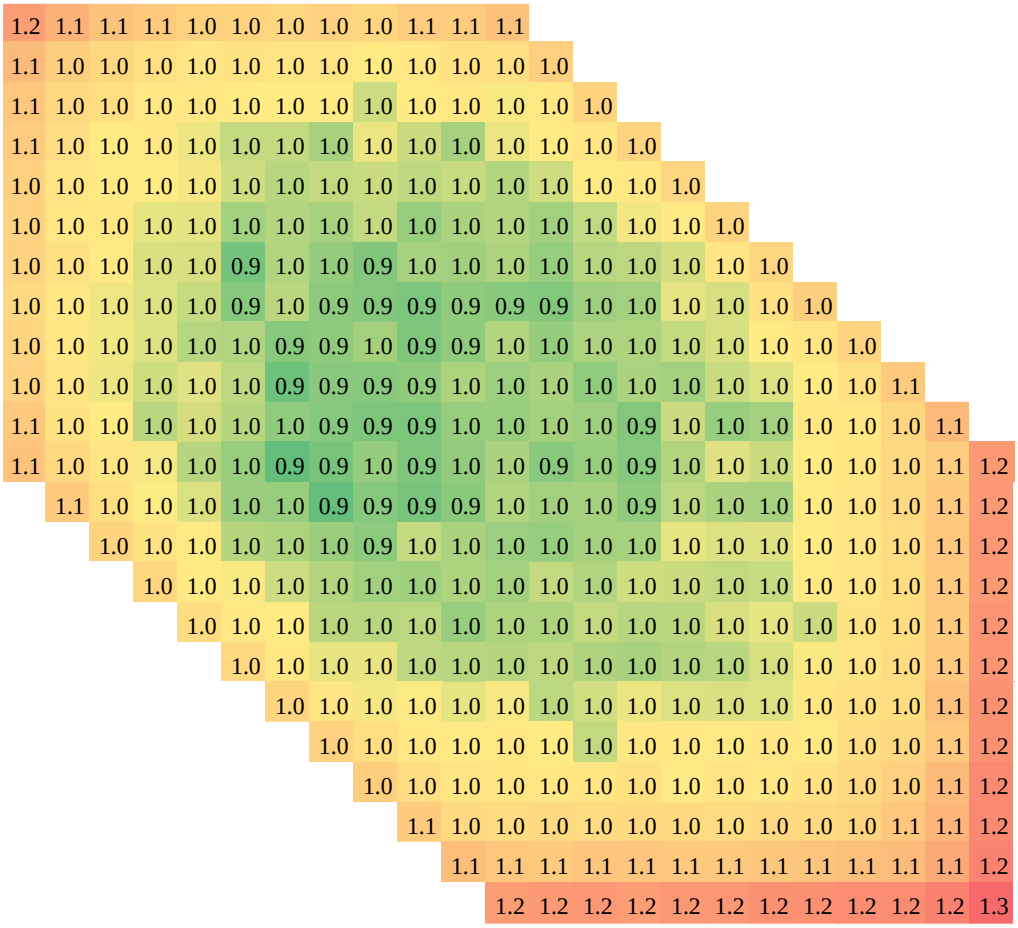

Figure 4.3. Pin power distribution for the RBWR-TR at BOL with uniform enrichment assuming the bypass region is inlet density water.

In order to assess the feasibility of segregating the fuel into separate Th-TRU pins and Th-U pins (as suggested in [22]), the same isotopic inventory was distributed into 218 Th-U pins and 179 Th-TRU pins; this distribution was chosen because the uniform enrichment had maintained a TRU fission efficiency of 45% averaged over the cycle, so 45% of the pins were Th-TRU pins. The enrichment scheme is shown in Figure 4.4, while the resulting pin power distribution is shown in Figure 4.5. However, this scheme produces a significantly more peaked power distribution than the uniform assembly, and it also reduces the TRU fission efficiency (from 46.0% to 38.5%). Although the power distribution could likely be accommodated with a graded enrichment scheme, since the minimum power of the Th-U pins is the average power of the entire assembly, no graded enrichment would offset the reduction in TRU fission efficiency, which is counterproductive to the mission of the RBWR-TR.

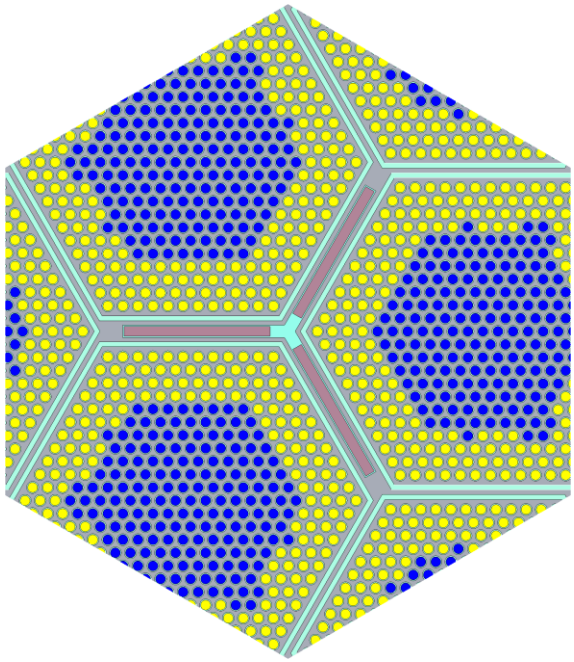

Figure 4.4. Enrichment scheme used for the segregated Th-U/Th-TRU pin study. The yellow pins are Th-U pins, with an enrichment of 16.6% (9.0% ^{233}U); the blue pins are Th-TRU pins, with an enrichment of 37.6% TRU (11.6% fissile).

1.3	1.2	1.2	1.1	1.1	1.1	1.1	1.1	1.1	1.1	1.1	1.2											
1.2	1.1	1.1	1.1	1.1	1.0	1.0	1.0	1.0	1.0	1.1	1.1	1.1										
1.2	1.1	1.1	1.1	1.0	1.0	1.0	1.0	1.0	1.0	1.0	1.0	1.1	1.1									
1.1	1.1	1.0	1.0	1.0	0.9	1.1	0.9	0.9	0.9	1.0	1.1	1.0	1.0	1.1								
1.1	1.1	1.0	1.0	1.0	1.0	0.9	0.9	0.9	1.0	0.9	0.9	1.0	1.0	1.0	1.1							
1.1	1.1	1.0	0.9	1.0	0.9	0.9	0.9	0.9	0.9	0.9	0.9	0.9	0.9	1.0	1.0	1.1						
1.1	1.0	1.0	1.0	1.0	0.9	0.8	0.8	0.8	0.8	0.8	0.8	0.9	0.9	0.9	1.0	1.0	1.1					
1.1	1.0	1.0	0.9	0.9	0.9	0.8	0.8	0.8	0.8	0.8	0.8	0.8	0.9	0.9	0.9	1.0	1.0	1.1				
1.1	1.0	1.0	0.9	1.0	0.9	0.8	0.8	0.8	0.8	0.8	0.8	0.8	0.8	0.9	0.9	1.1	1.0	1.1	1.1			
1.1	1.0	1.0	0.9	0.9	0.9	0.8	0.8	0.8	0.8	0.8	0.8	0.8	0.8	0.8	0.9	0.9	0.9	0.9	1.0	1.1	1.2	
1.1	1.1	1.0	1.0	0.9	0.9	0.8	0.8	0.8	0.8	0.8	0.8	0.8	0.8	0.8	0.8	0.8	0.9	1.0	1.0	1.1	1.1	1.2
1.2	1.1	1.0	1.1	0.9	0.9	0.8	0.8	0.8	0.8	0.8	0.8	0.8	0.8	0.8	0.8	0.8	0.9	0.9	1.1	1.0	1.1	1.2	1.3
	1.1	1.1	1.0	1.0	0.9	0.9	0.8	0.8	0.8	0.8	0.8	0.8	0.8	0.8	0.8	0.8	0.8	0.9	1.0	1.0	1.1	1.2	1.3
		1.1	1.1	1.0	0.9	0.9	0.9	0.8	0.8	0.8	0.8	0.8	0.8	0.8	0.8	0.8	0.9	0.9	1.0	1.0	1.1	1.2	1.3
			1.1	1.1	1.0	0.9	1.0	0.9	0.8	0.8	0.8	0.8	0.8	0.8	0.8	0.8	0.8	0.9	1.0	1.0	1.1	1.2	1.3
				1.1	1.0	1.0	0.9	0.9	0.9	0.8	0.8	0.8	0.8	0.8	0.8	0.8	0.9	0.9	1.0	1.0	1.1	1.2	1.3
					1.1	1.0	1.0	1.1	0.9	0.9	0.9	0.9	0.9	0.9	0.9	0.9	0.9	0.9	1.0	1.0	1.1	1.2	1.3
						1.1	1.1	1.0	0.9	1.0	0.9	0.9	0.9	0.9	0.9	0.9	0.9	0.9	1.0	1.0	1.1	1.2	1.3
							1.1	1.1	1.0	1.0	1.1	1.0	1.0	1.0	1.0	1.0	1.0	1.1	1.0	1.1	1.2	1.3	
								1.1	1.1	1.1	1.0	1.0	1.0	1.0	1.0	1.0	1.0	1.0	1.1	1.1	1.2	1.3	
									1.1	1.1	1.1	1.1	1.1	1.1	1.1	1.1	1.1	1.1	1.1	1.1	1.2	1.2	1.3
										1.2	1.2	1.2	1.2	1.2	1.1	1.2	1.2	1.2	1.2	1.2	1.3	1.3	
											1.3	1.3	1.3	1.3	1.3	1.3	1.3	1.3	1.3	1.3	1.4	1.4	

Figure 4.5, Pin power distribution for the RBWR-TR with segregated Th-U and Th-TRU pins at BOL assuming the bypass region is inlet density water.

4.2. Parametric Studies

MocDown was used (as documented in Section 2.5) to assess the effects of each of the design variables (Section 2.3) on the ability to meet the design constraints (Section 2.2) and the discharge burnup. The starting design for these tradeoff studies is shown in Table 4.2, and the results of the tradeoff studies are summarized qualitatively in Table 4.3.

Table 4.2. Starting design for the RBWR-TR tradeoff studies.

Parameter	Units	Value
Core thermal power	MW_{th}	3926
# of assemblies	#	720
# of batches	#	4
Core HM mass (BOEC)	t	87.7
Core TRU mass (BOEC)	t	12.9
TRU/HM core avg at BOEC	$^{w}/_{o}$	12.7%
TRU/HM seed avg at BOEC	$^{w}/_{o}$	16.5%
Total fuel length (seed + blanket)	cm	130.0
Seed length	cm	100.0
Number of seed regions	-	1
Fuel pin OD	cm	0.7048
Fuel pin pitch	cm	0.944
Fuel pin P/D	-	1.34
Coolant mass flow rate	kg/s/core	17395

Table 4.3. Summary of the parametric tradeoff studies for the RBWR-TR. An increase in the variable noted in the left column results in the change noted by the arrows. The arrows in the heading indicate which change would help meet the associated constraints.

Variable	TRU consumption rate (↑)	MCPR (↑)	Critical BU (↑)	VCR (↓)	SDM (↑)	ΔP (↓)
Coolant flow rate	↑	↑	↓	↓	↑	↑
Depletion time	↓		↑	↓	↑	
Seed length	↑	↑	↑	↑	↑	↑
Outer blanket lengths	↓		↑	↓	↓	↑
Internal blanket length[11]	↓		↓	↓		

[11] Increasing the blanket length was accomplished by replacing a section of the seed with blanket material, and thereby holding the total fuel length constant.

Variable	TRU consumption rate (↑)	MCPR (↑)	Critical BU (↑)	VCR (↓)	SDM (↑)	ΔP (↓)
Makeup TRU fraction	↑		↑	↑		
Pitch to diameter ratio (P/D)	↑	↑	↓	↓	↑	↓
Number of pins per assembly[12]		↑		↓	↑	↑
Power[13]	↑	↓	↓	↑		↑

Many of the variables have the same effect on the RBWR-TR as on the RBWR-SS (Section 3.2); for instance, the MCPR and pressure drop are completely independent of the neutronics of the designs, and exhibit the exact same trends. However, some variables exhibit reversed trends compared to the self-sustaining designs.

Notably, any effect which softened the spectrum also reduced the void coefficient. This is because many of the Pu isotopes, especially ^{239}Pu, have a much higher increase in η at high energies, as shown in Figure 1.4; at low energies, the slope is very gradual or even negative. Softening the spectrum shifts more of the fissions away from the fast region which causes the void coefficient to decrease. This effect is more prominent in the RBWR-TR than the RBWR-SS since the fraction of fissions from ^{239}Pu is much higher in the RBWR-TR.

Additionally, since a significant amount of the TRU which is fissioned is fed externally rather than bred within the reactor, the behavior of the reactor as a function of burnup is significantly different. As the depletion time increases in the RBWR-TR, there is more time for breeding ^{233}U in the fuel, which causes the TRU consumption rate to decrease and the void coefficient to decrease. Similarly, adding more external blankets increases the breeding of ^{233}U, reducing the fraction of fissions from the TRU and thus reducing the void coefficient. Increasing the power reduces the amount of breeding from the thorium since more of the ^{233}U is held up as ^{233}Pa, and it therefore increases the fraction of fissions from TRU and increases the void coefficient.

Increasing the TRU feed fraction affects the system much differently from increasing the DU feed. Both increase the void coefficient, but since the TRU feed contains a significant amount of fissile material, increasing the TRU feed fraction increases both the critical burnup and the reactivity swing. It additionally increases the TRU transmutation rate. As a whole, the reactivity swing of the RBWR-TR is much higher than that of the RBWR-SS, which poses an additional challenge for shutdown margin.

4.3. Full Core Performance vs. RBWR-TB2

The final optimized design for the RBWR-TR is shown in Table 4.4 and compared against the RBWR-TB2 and the CR=0.5 Advanced Burner Reactor [4], a comparable sodium fast reactor. Several ABR designs are shown in [4] with a variety of conversion ratios; the CR=0.5 is used here due to the fact that the RBWRs both maintain a conversion ratio of approximately 0.5.

[12] The P/D and the flow gap between the fuel lattice and the wall were held constant; the number of pins, pin diameter, and pitch were changed simultaneously.
[13] The coolant flow rate was increased so that quality remained constant.

Table 4.5 also shows the performance metrics of the selected reactors. It should be noted that the design and performance metrics of the RBWR-TB2 shown in these tables match the values shown in Reference [7], not necessarily the latest design information.

In the full core simulation, the same shuffling scheme was used as in the Hitachi-designed RBWR-TB2. Half of the most burned batch were placed in a ring around the periphery of the core, followed by the fresh fuel. The once-burned fuel came next, followed by the other half-batch of the most burned fuel. The twice-burned fuel was placed at the center of the core.

Since the conversion ratio was low, the power concentrated in the fresh fuel, and the control rods near the fresh fuel were fully inserted at BOC. The power peaking remained approximately constant throughout the cycle.

Unfortunately, it was not found possible to design a thorium-based burner to have sufficient shutdown margin while simultaneously maintaining negative void feedback. Using the TRU feed for void feedback control increased the reactivity swing too much for the shutdown margin to compensate. Table 4.6 shows the different components of the shutdown margin.

However, using a multi-seed approach as used in the RBWR-TB2 may help with the shutdown margin. Another assembly-level case was run with three 20-cm seeds separated by 30-cm internal blankets and capped with 5 cm blankets was simulated; the cycle length was held the same, and the TRU feed fraction was changed such that the reactor was critical. Two important changes were observed. First, the reactivity swing was reduced to 1% and became negative, since the inventory of ^{233}U increases at low burnups and communication between the seed sections increases with burnup; the evolution of the multiplication factor and the ^{233}U inventory is shown in Figure 4.11. Second, the reactivity insertion from cooling the core to room temperature was roughly half of that of the single-seed design, which was nearly invariant to any of the design variables. It should be noted that in the assembly level calculation, the change in fuel temperature is not captured, so this benefit may not remain through the full core calculations. The transmutation rate was reduced by nearly one third of the single seed value, as well. Additionally, the void coefficient was increased to +40.0 pcm/% void, so a multi-seed design would need a great deal of optimization, but these results are encouraging.

Similar to the self-sustaining designs, the significantly harder spectrum of the ABR allows it to achieve a longer burnup than its water-cooled counterparts. Additionally, since it could operate with positive void feedback, having a high TRU enrichment was not a large concern; the biggest challenge for the ABR is the reactivity swing. Although the CR=0.5 ABR was chosen for a comparison, fertile-free ABRs have been designed and meet basic safety requirements [4]. Despite having nearly double the coolant flow rate of the RBWR-TB2, the RBWR-TR achieves a similar discharge burnup. The high flow rate enables it to achieve a slightly higher transmutation rate than the RBWR-TB2, as well. The RBWR-TR has significantly higher margin against critical heat flux, although the pressure drop is much higher. The batch-averaged linear heat rate profiles at BOC and EOC are shown in Figure 4.6 and Figure 4.7, while Figure 4.8 and Figure 4.9 show the radial power map and Figure 4.10 shows the excess reactivity as a function of burnup.

Table 4.4. Design parameters for the RBWR-TR, RBWR-TB2, and the CR=0.5 ABR. Design parameters for the RBWR-TB2 are from [7] while the ABR design information is from [4].

Parameter	Units	RBWR-TR	RBWR-TB2	ABR (CR=0.5)
Core thermal power	MW_{th}	3926	3926	1000
Thermal efficiency	MW_e/MW_{th}	34.5%	34.5%	40.0%
Core electric power	MW_e	1354	1354	400
Fuel form	-	oxide	oxide	metal
Coolant	-	light water	light water	sodium
# of assemblies	#	720	720	144
# of batches	#	4	4	6
Core HM mass (BOEC)	t	86.3	76	9.5
Core TRU mass (BOEC)	t	12.9	24.8	3.1
TRU/HM core avg at BOEC	$^w/_o$	15.0%	43.7%	32.6%
TRU/HM seed avg at BOEC	$^w/_o$	19.5%	74.7%	32.6%
Specific power	MW_e/t	16	18	42
Core volume	m^3	32	25	3
Power density	W_{th}/cm^3	124	158	303
Upper blanket length	cm	15.0	2.0	-
Upper seed length	cm	100.0	22.4	101.6
Internal blanket length	cm	-	56.0	-
Lower seed length	cm	-	22.1	-
Lower blanket length	cm	15.0	-	-
Number of seed regions	-	1	2	1
Fuel pin OD	cm	0.724	0.72	0.623
Fuel pin pitch	cm	0.911	0.94	1.293
Fuel pin P/D	-	1.26	1.30	2.08
Coolant mass flow rate	kg/s/core	12343	6667	5599

Table 4.5. Performance metrics of the RBWR-TR compared against the RBWR-TB2 and the CR=0.5 ABR.

Parameter	Units	RBWR-TR	RBWR-TB2	ABR (CR=0.5)
Maximum LHGR	W_{th}/cm	234	472	327
MCPR (H-CISE)	-	1.87	1.28	n/a
MCPR (M-CISE)	-	1.50	-	n/a
Core pressure drop	MPa	0.2	0.06	Not available
Exit quality	%	17	36	n/a
Avg. discharge burnup	GWd/t	50.5	65	132
Peak discharge burnup	GWd/t	77.8	Not available	117
TRU consumption rate	kg/yr	688	564	174
TRU consumption rate	kg/GW_e-yr	508	404	434.5
TRU fission efficiency	%	49%	45%	46%
Fuel residence time	EFPD	1134	1256	1326

Cycle length	EFPD	283	314	221
Cycle reactivity swing	%dk	2.8%	2.5%	2.9%
HM reprocessing	t/GW_e-yr	21	16	6.5
VCR (BOEC/EOEC)	pcm/% void	-21/+3.7	-45/-43	n/a
FTCR (BOEC/EOEC)	pcm/K	-5.0/-3.6	Not available	-2.6/-2.8
Power coefficient of reactivity (BOC/EOC)	pcm/MW_{th}	-0.5/-0.3	Not available	Not available
Shutdown margin	pcm	-1337	Not available	Not available

Table 4.6. Components of the shutdown margin for the RBWR-TR.

Metric	**Value [pcm]**
Excess reactivity	2794
Void collapse to 1.0 g/cc water	2743
Cooling to room temperature	2588
Control rod worth	-6788
Total shutdown margin	-1337

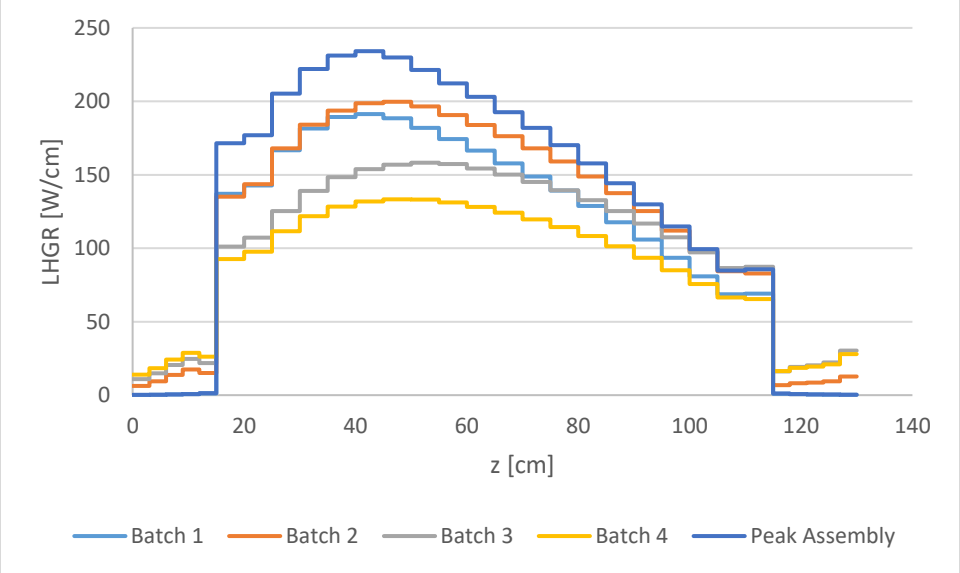

Figure 4.6. Batch-average LHGR profiles for the RBWR-TR core at BOC.

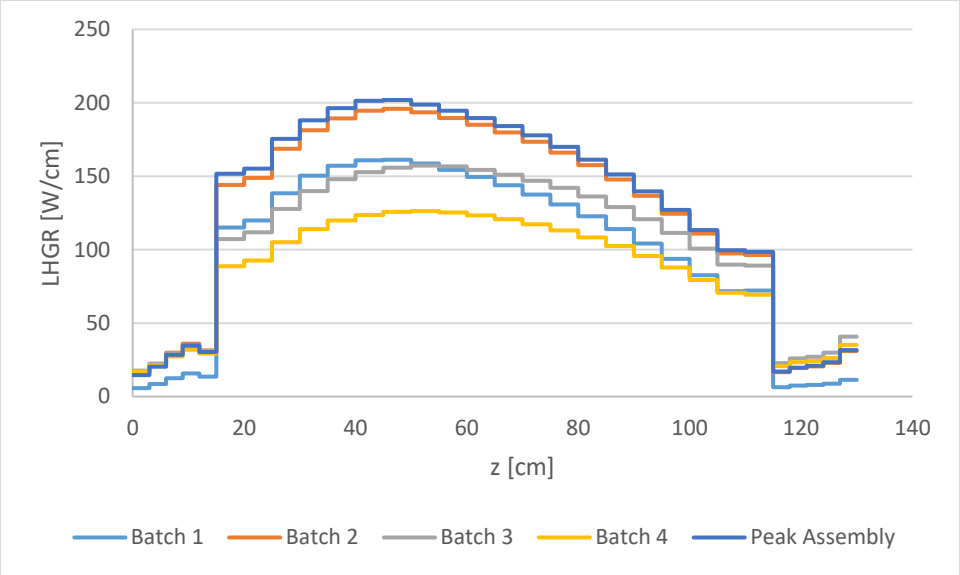

Figure 4.7. Batch-average LHGR profiles for the RBWR-TR core at EOC.

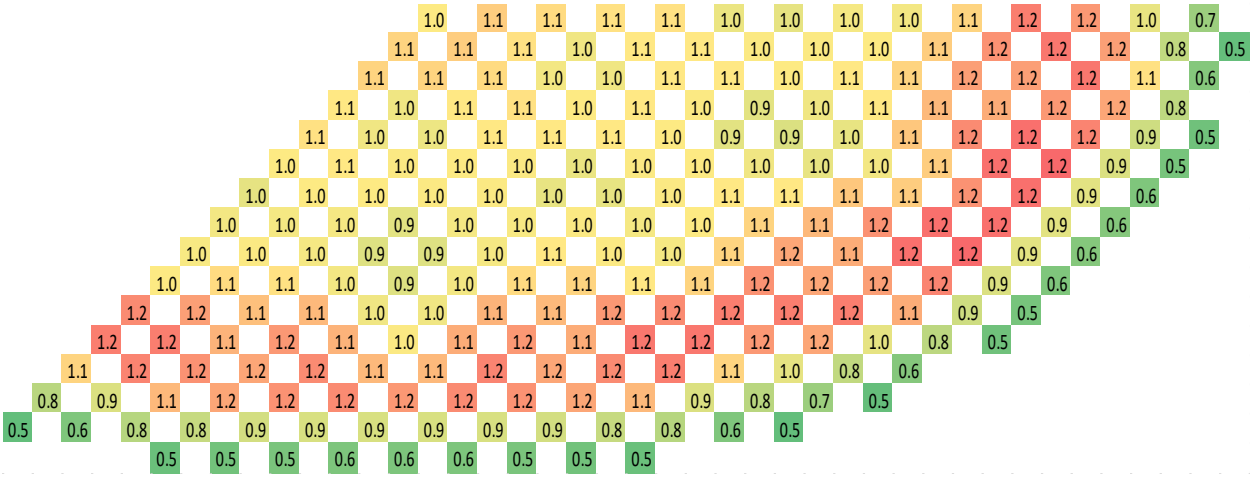

Figure 4.8. 2-D radial power map for the RBWR-TR at BOC.

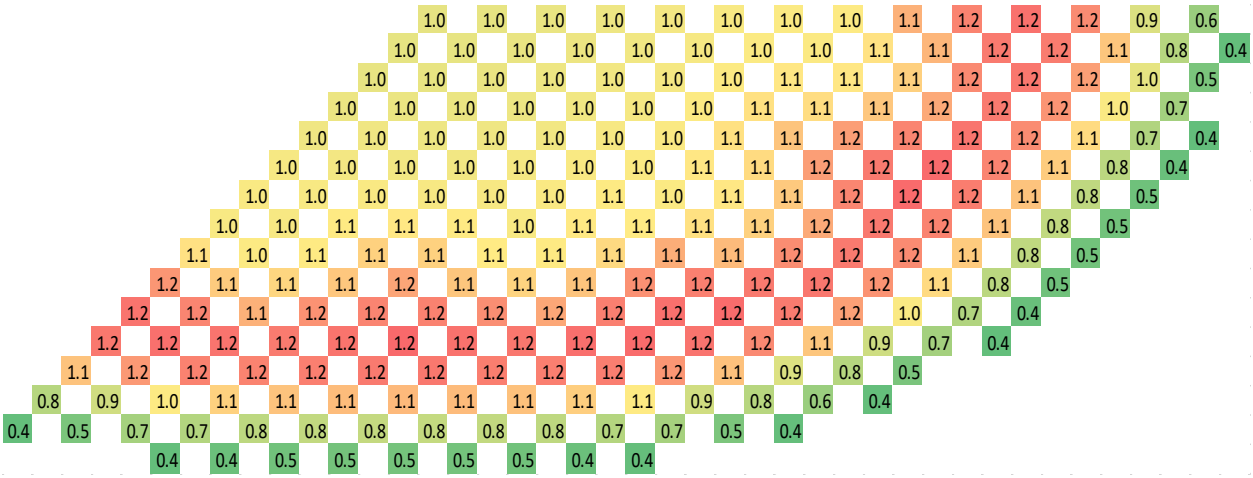

Figure 4.9. 2-D radial power map for the RBWR-TR at EOC.

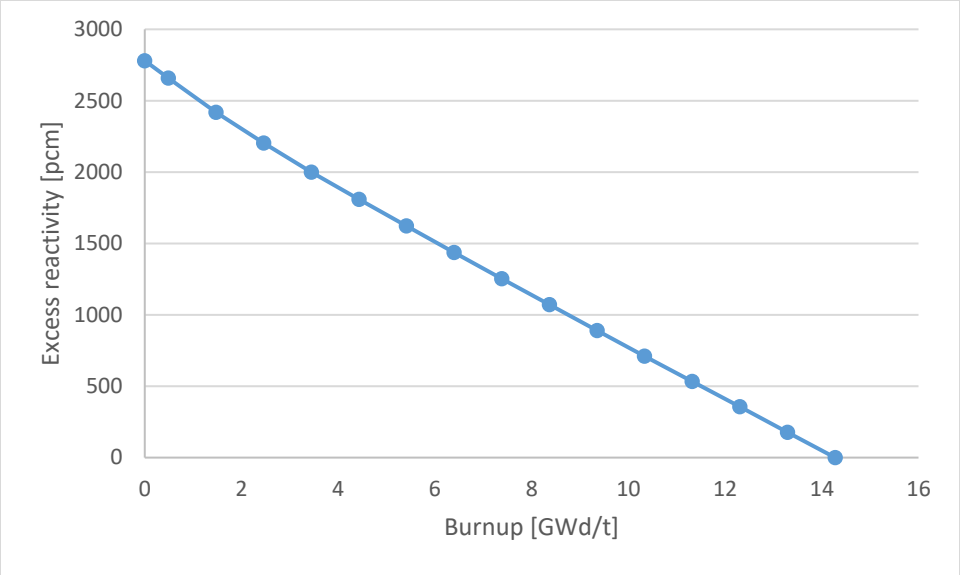

Figure 4.10. Excess reactivity vs. burnup for the RBWR-TR.

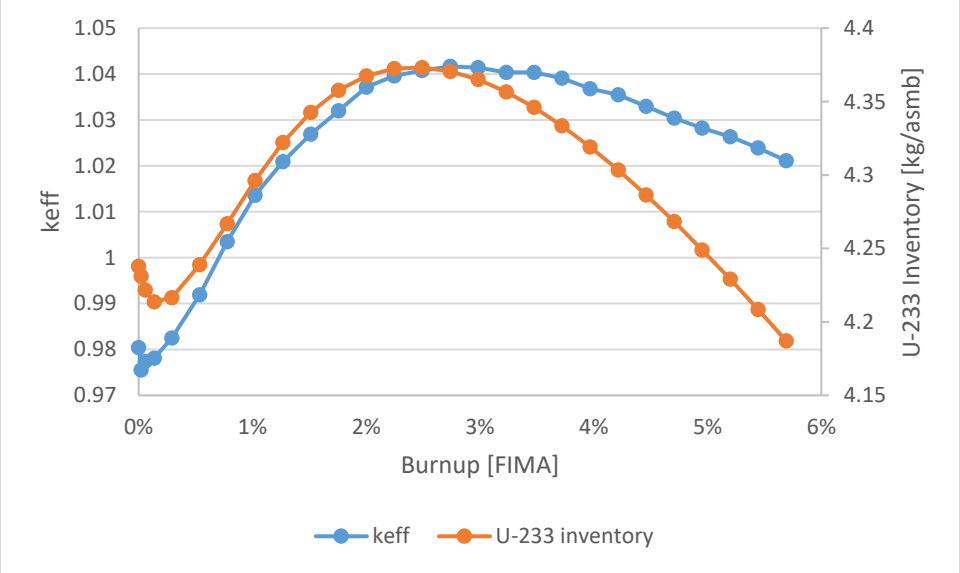

Figure 4.11. Radially infinite multiplication factor and ^{233}U inventory for a three-seed RBWR-TR variant based on an assembly model.

4.4. GPT Uncertainty Analysis

4.4.1. k_∞ Uncertainty due to Uncertainty in Nuclear Data

The uncertainty in k_∞ due to uncertainty in the cross sections of each of the isotopes present in the fresh fuel was assessed for fresh fuel and for average discharged fuel (50 GWd/t) for the RBWR-TR. A modified version of Serpent 2.1.19 was used to generate sensitivity coefficients, which were collapsed with the cross section covariance matrices to calculate the uncertainty, as detailed in Section 2.8. An assembly unit cell was modeled using the specifications from Table 4.4, using the average water density distribution.

The k_∞ at BOL was calculated to be 1.09561 ± 823 pcm, while at EOL, it was calculated to be 0.99296 ± 907 pcm. Effectively all of the quoted uncertainties are due to the uncertainty from the nuclear data, as the statistical uncertainty from the Monte Carlo simulation contributed less than 1 pcm towards the final uncertainty. The decomposition due to reaction type and isotope is shown in Table 4.7 and Table 4.8 at BOL and EOL, respectively, while the uncertainty as a function of energy is shown in Figure 4.12 and Figure 4.13.

At both BOL and EOL, by far the largest contribution to uncertainty are fissions in ^{233}U, followed by capture in ^{232}Th. The uncertainty due to fission undergoes a step change around 0.8 keV, since the uncertainty in the ^{233}U fission cross section also undergoes a step change at the same energy. The capture in ^{232}Th undergoes a similar increase in uncertainty around 2 keV and 0.1 MeV.

Table 4.7. Uncertainty of the multiplication factor measured in pcm at reference conditions due to uncertainty in each reaction type and isotope for the RBWR-TR unit cell at BOL.

Isotope	(n,g)	Elastic	Fission	Inelastic	(n, 2n)	Cross-terms	Total
Am-241	116	2	6	2	0	11	117
Am-242m	15	0	32	0	0	n/a	35
Am-243	94	2	29	2	0	n/a	98
Cm-243	2	0	1	0	0	0	2
Cm-244	102	4	16	1	0	5	104
Cm-245	72	0	90	1	0	9	115
Cm-246	18	0	5	0	0	1	19
Cm-247	11	0	11	0	0	3	16
Cm-248	1	0	1	0	0	1	2
H-1	5	40	n/a	n/a	n/a	n/a	40
Np-237	100	1	10	1	0	n/a	101
O-16	155	23	n/a	4	0	2	157
Pu-238	155	1	12	1	0	4	156
Pu-239	53	1	74	7	0	26	95
Pu-240	79	2	21	14	0	5	83
Pu-241	138	2	105	2	1	n/a	173
Pu-242	153	4	17	4	0	n/a	154
Th-232	329	39	17	n/a	n/a	21	333
U-232	4	0	10	0	0	3	11
U-233	66	2	588	6	1	40	594
U-234	77	6	166	6	0	n/a	183
U-235	29	0	7	1	0	6	31
U-236	20	0	23	2	0	n/a	31
Total	518	61	634	19	2	55	823

Table 4.8. Uncertainty of the multiplication factor measured in pcm at reference conditions due to uncertainty in each reaction type and isotope for the RBWR-TR unit cell at EOL.

Isotope	(n,g)	Elastic	Fission	Inelastic	(n, 2n)	Cross-terms	Total
Am-241	87	2	5	2	0	3	87
Am-242m	10	0	28	0	0	n/a	29
Am-243	91	1	31	2	0	n/a	96
Cm-243	2	0	2	0	0	0	3
Cm-244	111	4	21	1	0	6	113
Cm-245	75	0	109	1	0	10	133
Cm-246	18	0	6	0	0	1	19
Cm-247	12	0	13	0	0	4	18
Cm-248	1	0	1	0	0	1	2
H-1	9	44	n/a	n/a	n/a	n/a	45
Np-237	72	0	8	1	0	n/a	73
O-16	155	28	n/a	4	n/a	2	158
Pu-238	155	2	13	1	0	10	156
Pu-239	35	1	57	5	0	15	68
Pu-240	72	2	21	15	0	7	76
Pu-241	126	2	119	2	1	n/a	173
Pu-242	151	5	18	4	0	n/a	152
Sm-149	21	0	n/a	0	0	n/a	21
Sm-151	13	0	n/a	0	0	n/a	13
Th-232	337	40	20	n/a	n/a	18	341
U-232	4	0	12	0	0	2	13
U-233	67	4	695	7	1	66	701
U-234	76	5	194	6	0	n/a	208
U-235	30	0	9	1	0	6	32
U-236	18	0	27	3	0	n/a	33
Total	508	67	745	19	1	73	907

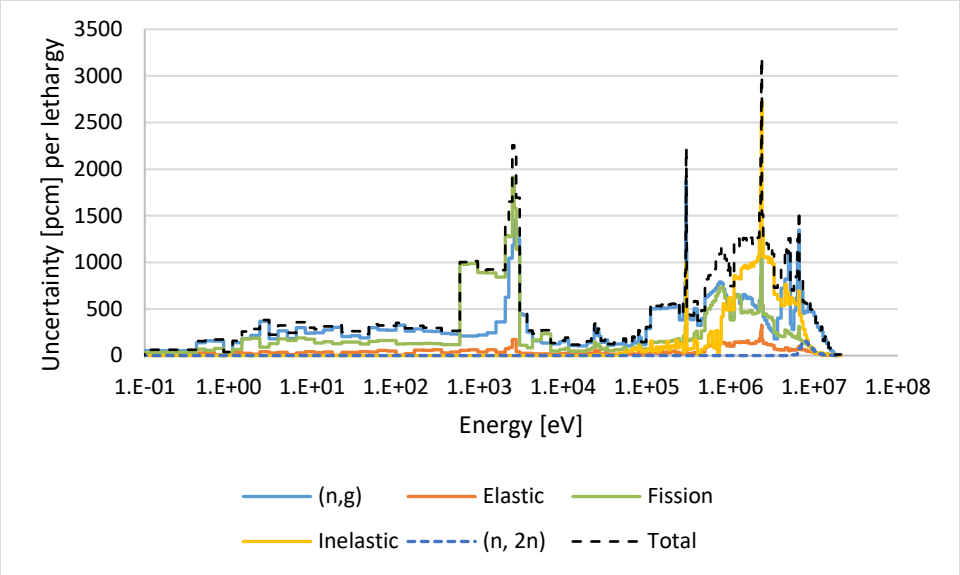

Figure 4.12. Group-wise uncertainty in k_∞ from the uncertainty due to each reaction for the RBWR-TR unit cell at BOL.

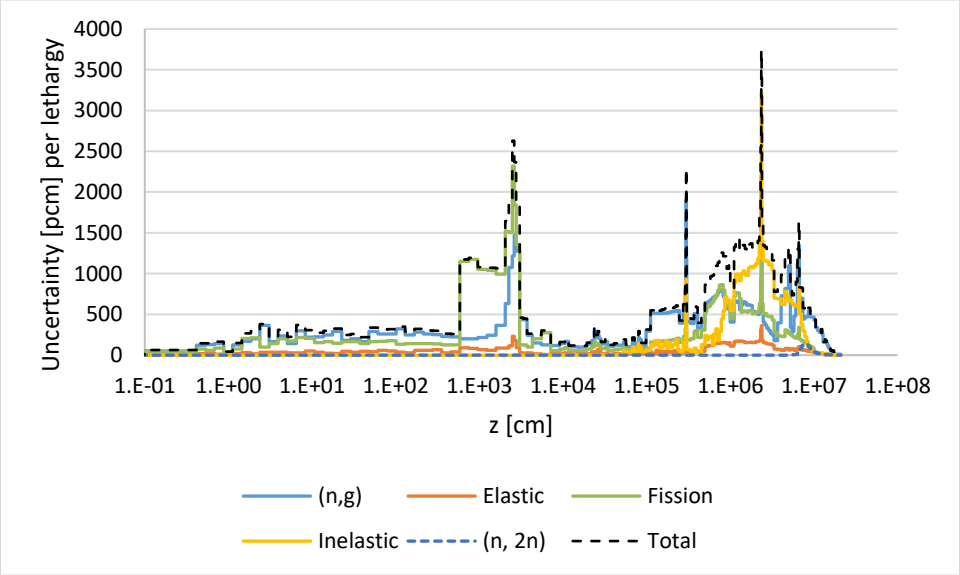

Figure 4.13. Group-wise uncertainty in k_∞ from the uncertainty due to each reaction for the RBWR- TR unit cell at EOL.

4.4.2. Changes in Reactor State

In addition to the uncertainty in the multiplication factor, the uncertainty in the quantities which depend on k_∞ (including coolant void coefficient, coolant void collapse worth at nominal temperature, coolant void worth, and control rod worth) was also calculated. The uncertainty in various reactor parameters are summarized in Table 4.13. In all cases, the statistical uncertainty is negligible. Note that these analyses were performed on the assembly level, so the spectrum is significantly more thermal and the values will not match the results in Section 4.3. The uncertainty contribution from each isotope and reaction when the reactor is flooded is presented in Table 4.9 and Table 4.11, while the breakdown for when the reactor is voided is shown in

Table 4.10 and Table 4.12. The uncertainty breakdown for each change in reactor state is shown in Table 4.14 through Table 4.21.

To elaborate further on the differences between the two sets of tables, Table 4.9 shows the uncertainty in the reactor in the flooded condition, while Table 4.15 shows the uncertainty associated with the transition between reference conditions to the flooded conditions. The uncertainties in the Reference Conditions referred to in Table 4.9 through Table 4.12 are the uncertainties which were presented in Section 3.4.1 – that is, using the average flow rate distribution. Since the uncertainty in the nuclear data is fixed between states, Table 4.14 through Table 4.21 effectively show the change in importance for each reaction between the reference and perturbed state, weighted by the uncertainty of each reaction.

For the changes to the water density, the spectrum changes cause significant changes in the uncertainty. The uncertainty from the epithermal ^{233}U fissions is very significant, as the uncertainty from ^{233}U fission decreases both when the reactor is flooded and when the reactor is voided. The uncertainty in ^{232}Th capture becomes dominant for very hard spectra. The control rod worth has very low uncertainty relative to the other changes; even with rods inserted, the uncertainty in the ^{10}B (n,α) reaction is nearly negligible, and the uncertainty from ^{10}B is only greater than 1 pcm when the control rods are inserted.

Table 4.9. Uncertainty in pcm of the multiplication factor for the RBWR-TR unit cell at BOL when it is flooded due to uncertainty in each isotope and reaction.

Isotope	(n,g)	Elastic	Fission	Inelastic	(n, 2n)	Cross-terms	Total	Ref. Cond.
Am-241	185	11	4	1	0	36	189	117
Am-242m	35	0	46	0	0	n/a	58	35
Am-243	95	1	19	1	0	n/a	97	98
Cm-243	1	0	1	0	0	0	2	2
Cm-244	96	5	11	0	0	5	97	104
Cm-245	49	0	129	0	0	20	139	115
Cm-246	15	0	4	0	0	1	15	19
Cm-247	9	0	11	0	0	5	15	16
Cm-248	1	0	1	0	0	1	2	2
H-1	19	32	n/a	n/a	n/a	n/a	37	40
Np-237	90	0	6	0	0	n/a	91	101
O-16	156	14	n/a	3	n/a	2	157	157
Pu-238	219	1	7	0	0	9	219	156
Pu-239	69	0	86	3	0	52	122	95
Pu-240	107	2	13	6	0	3	108	83
Pu-241	128	1	123	1	1	n/a	178	173
Pu-242	166	6	10	2	0	n/a	167	154
Th-232	191	33	12	n/a	n/a	8	195	333
U-232	3	0	8	0	0	3	9	11
U-233	60	3	326	3	1	42	334	594

U-234	68	5	95	2	0	n/a	117	183
U-235	16	0	5	0	0	4	17	31
U-236	21	0	15	1	0	n/a	26	31
Total	493	51	398	8	2	80	640	823
Ref. Cond.	518	61	634	19	2	55		

Table 4.10. Uncertainty in pcm of the multiplication factor for the RBWR-TR unit cell at BOL when it is voided due to uncertainty in each isotope and reaction.

Isotope	(n,g)	Elastic	Fission	Inelastic	(n, 2n)	Cross-terms	Total	Ref. Cond.
Am-241	28	1	10	7	0	1	31	117
Am-242m	7	0	49	1	0	n/a	50	35
Am-243	49	1	43	17	0	n/a	67	98
Cm-243	2	0	2	0	0	n/a	2	2
Cm-244	104	0	29	4	0	0	108	104
Cm-245	61	0	69	3	0	0	92	115
Cm-246	18	0	7	1	0	0	20	19
Cm-247	6	0	4	0	0	0	8	16
Cm-248	1	0	1	0	0	0	2	2
H-1	0	2	n/a	n/a	n/a	n/a	2	40
Np-237	70	0	20	7	0	n/a	73	101
O-16	152	144	n/a	5	n/a	3	209	157
Pu-238	96	1	33	4	0	4	101	156
Pu-239	76	1	60	40	0	10	105	95
Pu-240	84	1	46	60	0	13	114	83
Pu-241	91	1	60	45	1	n/a	118	173
Pu-242	31	1	30	13	0	n/a	45	154
Th-232	813	14	22	n/a	n/a	48	814	333
U-232	5	0	7	0	0	0	9	11
U-233	136	1	373	38	1	17	399	594
U-234	108	0	365	21	0	n/a	381	183
U-235	91	0	15	5	0	6	93	31
U-236	8	1	32	12	0	n/a	35	31
Total	881	144	544	100	1	54	1052	823
Ref. Cond.	518	61	634	19	2	55		

Table 4.11. Uncertainty in pcm of the multiplication factor for the RBWR-TR unit cell at EOL when it is flooded due to uncertainty in each isotope and reaction.

Isotope	(n,g)	Elastic	Fission	Inelastic	(n, 2n)	Cross-terms	Total	Ref. Cond.
Am-241	145	6	4	1	0	23	147	87
Am-242m	26	0	46	0	0	n/a	53	29
Am-243	92	1	20	1	0	n/a	94	96

Isotope	(n,g)	Elastic	Fission	Inelastic	(n, 2n)	Cross-terms	Total	Ref. Cond.
Cm-243	2	0	2	0	0	0	3	3
Cm-244	102	5	13	1	0	6	103	113
Cm-245	49	0	165	0	0	23	174	133
Cm-246	14	0	5	0	0	1	15	19
Cm-247	9	0	14	0	0	5	17	18
Cm-248	1	0	1	0	0	1	2	2
H-1	23	39	n/a	n/a	n/a	n/a	45	45
Np-237	66	0	5	0	0	n/a	66	73
O-16	156	17	n/a	3	n/a	2	157	158
Pu-238	209	1	8	0	0	5	209	156
Pu-239	49	0	73	2	0	45	99	68
Pu-240	98	2	13	6	0	2	99	76
Pu-241	115	2	144	2	1	n/a	185	173
Pu-242	162	6	11	2	0	n/a	163	152
Sm-149	88	0	n/a	0	0	n/a	88	21
Sm-151	18	0	n/a	0	0	n/a	18	13
Th-232	189	34	14	n/a	n/a	7	193	341
U-232	3	0	9	0	n/a	3	10	13
U-233	60	1	377	3	1	27	382	701
U-234	64	5	109	3	0	n/a	127	208
U-235	15	0	6	0	0	5	17	32
U-236	17	0	18	1	0	n/a	25	33
Total	420	55	426	9	1	54	603	907
Ref. Cond.	508	67	745	19	1	73		

Table 4.12. Uncertainty in pcm of the multiplication factor for the RBWR-TR unit cell at EOL when it is voided due to uncertainty in each isotope and reaction.

Isotope	(n,g)	Elastic	Fission	Inelastic	(n, 2n)	Cross-terms	Total	Ref. Cond.
Am-241	21	0	8	5	0	1	23	87
Am-242m	5	0	43	1	0	n/a	43	29
Am-243	50	2	46	18	0	n/a	70	96
Cm-243	2	0	2	0	0	0	3	3
Cm-244	124	1	37	6	0	0	130	113
Cm-245	66	0	84	3	0	0	107	133
Cm-246	19	0	8	1	0	0	21	19
Cm-247	7	0	5	0	0	0	9	18
Cm-248	1	0	1	0	0	1	2	2
H-1	0	2	n/a	n/a	n/a	n/a	2	45
Np-237	55	1	16	5	0	n/a	57	73
O-16	152	153	n/a	5	0	2	216	158

Pu-238	100	3	37	4	0	4	107	156
Pu-239	50	1	43	28	0	5	71	68
Pu-240	74	1	45	52	0	5	101	76
Pu-241	86	2	65	34	1	n/a	113	173
Pu-242	31	1	32	13	0	n/a	46	152
Sm-149	4	0	n/a	0	0	n/a	4	21
Sm-151	8	1	n/a	1	0	n/a	8	13
Th-232	814	15	25	n/a	n/a	53	817	341
U-232	6	0	10	0	n/a	0	11	13
U-233	138	2	482	38	1	33	504	701
U-234	112	1	421	23	0	n/a	436	208
U-235	99	0	18	6	0	7	101	32
U-236	8	0	38	13	0	n/a	41	33
Total	870	154	650	84	1	64	1102	907
Ref. Cond.	508	67	745	19	1	73		

Table 4.13. Uncertainty in the RBWR-TR unit cell void coefficient, void collapse worth, void worth, and control rod worth due to uncertainty in the nuclear data.

	Void coefficient [pcm/% void]	**Reactivity insertion from flooding the reactor [pcm]**	**Reactivity insertion from voiding the reactor [pcm]**	**Control rod worth [pcm]**
BOL	4.3 ± 9.1	1495 ± 362	5328 ± 843	-10536 ± 60
EOL	23.1 ± 10.1	198 ± 422	6873 ± 854	-12311 ± 65

Table 4.14. Uncertainty in the void coefficient in pcm/% void for the RBWR-TR unit cell at BOL due to uncertainty in each isotope and reaction.

Isotope	(n,g)	Elastic	Fission	Inelastic	(n, 2n)	Cross-terms	Total
Am-241	1.4	0.6	0.0	0.1	0.0	0.7	1.7
Am-242m	0.3	0.0	0.4	0.0	0.0	n/a	0.5
Am-243	0.4	0.1	0.2	0.1	0.0	n/a	0.5
Cm-244	0.7	0.2	0.1	0.1	0.0	0.0	0.8
Cm-245	0.7	0.0	1.1	0.0	0.0	0.2	1.4
Cm-246	0.1	0.1	0.1	0.0	0.0	0.0	0.2
Cm-247	0.1	0.0	0.1	0.0	0.0	0.0	0.1
Cm-248	0.0	0.1	0.0	0.0	0.0	0.0	0.1
H-1	0.1	0.2	n/a	n/a	n/a	n/a	0.2
Np-237	0.9	0.1	0.1	0.0	0.0	n/a	0.9
O-16	0.1	0.2	n/a	0.0	0.0	0.0	0.2
Pu-238	1.2	0.3	0.1	0.0	0.0	0.3	1.3
Pu-239	0.7	0.0	0.5	0.2	0.0	0.6	1.1
Pu-240	0.8	0.1	0.2	0.2	0.0	0.2	0.9
Pu-241	0.6	0.1	0.7	0.3	0.0	n/a	1.0
Pu-242	0.8	0.1	0.1	0.1	0.0	n/a	0.8

Isotope	(n,g)	Elastic	Fission	Inelastic	(n, 2n)	Cross-terms	Total
Th-232	3.9	0.4	0.1	n/a	n/a	0.4	3.9
U-232	0.1	0.0	0.1	0.0	0.0	0.0	0.1
U-233	0.8	0.2	7.0	0.3	0.0	1.4	7.2
U-234	0.4	0.1	2.0	0.1	0.0	n/a	2.0
U-235	0.4	0.0	0.1	0.0	0.0	0.1	0.4
U-236	0.1	0.0	0.1	0.1	0.0	n/a	0.2
Total	4.9	0.9	7.4	0.6	0.0	1.8	9.1

Table 4.15. Uncertainty in the reactivity insertion in pcm from flooding the reactor for the RBWR-TR unit cell at BOL due to uncertainty in each isotope and reaction.

Isotope	(n,g)	Elastic	Fission	Inelastic	(n, 2n)	Cross-terms	Total
Am-241	72	10	2	2	0	20	75
Am-242m	22	0	26	0	0	n/a	34
Am-243	6	2	10	1	0	n/a	12
Cm-243	1	0	1	0	0	0	1
Cm-244	22	1	6	0	0	1	23
Cm-245	30	0	55	0	0	12	64
Cm-246	5	0	2	0	0	0	5
Cm-247	4	0	4	0	0	1	6
Cm-248	0	0	0	0	0	0	1
H-1	14	8	n/a	n/a	n/a	n/a	16
Np-237	35	0	4	1	0	n/a	35
O-16	1	9	n/a	1	0	0	9
Pu-238	74	1	5	1	0	6	75
Pu-239	39	1	33	4	0	39	64
Pu-240	37	0	9	8	0	2	39
Pu-241	22	1	22	1	0	n/a	31
Pu-242	15	3	6	2	0	n/a	16
Th-232	143	10	5	n/a	n/a	11	144
U-232	1	0	3	0	0	0	4
U-233	24	2	279	3	0	25	281
U-234	16	1	71	3	0	n/a	73
U-235	14	0	3	1	0	2	15
U-236	1	0	8	1	0	n/a	8
Total	198	19	297	11	0	54	362

Table 4.16. Uncertainty in the reactivity insertion in pcm from voiding the reactor for the RBWR-TR unit cell at BOL due to uncertainty in each isotope and reaction.

Isotope	(n,g)	Elastic	Fission	Inelastic	(n, 2n)	Cross-terms	Total
Am-241	116	1	4	6	0	11	117
Am-242m	15	0	45	1	0	n/a	47
Am-243	91	1	15	15	0	n/a	94

Isotope	(n,g)	Elastic	Fission	Inelastic	(n, 2n)	Cross-terms	Total
Cm-243	1	0	1	0	0	0	1
Cm-244	107	4	15	3	0	5	109
Cm-245	25	0	92	3	0	9	96
Cm-246	16	0	5	1	0	1	17
Cm-247	6	0	11	0	0	3	13
Cm-248	1	0	1	0	0	1	2
H-1	5	38	n/a	n/a	n/a	n/a	38
Np-237	83	1	10	6	0	n/a	84
O-16	3	121	n/a	1	0	1	121
Pu-238	154	0	22	3	0	5	156
Pu-239	61	1	81	34	0	24	110
Pu-240	84	2	32	47	0	5	102
Pu-241	142	2	110	46	0	n/a	186
Pu-242	144	5	13	9	0	n/a	145
Th-232	578	33	5	n/a	n/a	15	579
U-232	3	0	7	0	0	3	8
U-233	103	1	368	33	0	27	385
U-234	102	7	200	16	0	n/a	225
U-235	63	0	12	4	0	6	64
U-236	20	1	13	10	0	n/a	25
Total	690	131	456	86	0	43	843

Table 4.17. Uncertainty in the control rod worth in pcm for the RBWR-TR unit cell at BOL due to uncertainty in each isotope and reaction.

Isotope	(n,g)	Elastic	Fission	Inelastic	(n, 2n)	Cross-terms	Total
Am-241	8	1	1	0	0	1	9
Am-242m	1	0	2	0	0	n/a	2
Am-243	7	2	4	1	0	n/a	8
B-10	8[14]	1	n/a	6	n/a	2	10
Cm-244	7	1	2	0	0	0	8
Cm-245	6	0	4	0	0	1	7
Cm-246	1	0	1	0	0	0	2
Cm-247	1	0	0	0	0	0	1
H-1	1	5	n/a	n/a	n/a	n/a	5
Np-237	8	1	2	0	0	n/a	8
O-16	0	12	n/a	0	0	0	12
Pa-231	n/a	n/a	n/a	n/a	n/a	n/a	0
Pu-238	11	3	2	0	0	3	12
Pu-239	4	1	3	1	0	2	5
Pu-240	5	1	2	4	0	2	7

[14] The (n,α) reaction is summarized here, as the ^{10}B (n,g) reaction is negligible.

Isotope	(n,g)	Elastic	Fission	Inelastic	(n, 2n)	Cross-terms	Total
Pu-241	10	1	3	1	0	n/a	10
Pu-242	11	1	2	1	0	n/a	11
Th-232	22	5	3	n/a	n/a	2	23
U-232	0	0	1	0	0	0	1
U-233	5	1	34	1	0	5	35
U-234	6	1	27	1	0	n/a	27
U-235	2	0	1	0	0	1	2
U-236	2	0	3	1	0	n/a	4
Total	35	15	45	7	0	7	60

Table 4.18. Uncertainty in the void coefficient in pcm/% void for the RBWR-TR unit cell at EOL due to uncertainty in each isotope and reaction.

Isotope	(n,g)	Elastic	Fission	Inelastic	(n, 2n)	Cross-terms	Total
Am-241	1.1	1.1	0.0	0.1	0.0	0.9	1.8
Am-242m	0.2	0.0	0.3	0.0	0.0	n/a	0.4
Am-243	0.4	0.1	0.2	0.2	0.0	n/a	0.5
Cm-244	0.8	0.2	0.2	0.1	0.0	0.0	0.9
Cm-245	0.6	0.0	1.4	0.0	0.0	0.2	1.5
Cm-246	0.1	0.1	0.1	0.0	0.0	0.0	0.2
Cm-247	0.1	0.0	0.1	0.0	0.0	0.1	0.2
Cm-248	0.0	0.0	0.0	0.0	0.0	0.0	0.0
H-1	0.1	0.2	n/a	n/a	n/a	n/a	0.2
Np-237	0.6	0.0	0.1	0.0	0.0	n/a	0.6
O-16	0.2	0.9	n/a	0.1	0.0	0.0	0.9
Pu-238	1.3	0.3	0.1	0.0	0.0	0.4	1.4
Pu-239	0.5	0.1	0.4	0.1	0.0	0.5	0.8
Pu-240	0.7	0.2	0.2	0.2	0.0	0.2	0.8
Pu-241	0.5	0.1	0.8	0.1	0.0	n/a	1.0
Pu-242	0.8	0.2	0.2	0.1	0.0	n/a	0.9
Sm-149	0.6	0.0	n/a	0.0	0.0	n/a	0.6
Sm-151	0.1	0.0	n/a	0.1	0.0	n/a	0.1
Th-232	3.9	0.4	0.1	n/a	n/a	0.1	3.9
U-232	0.1	0.0	0.1	0.0	0.0	0.0	0.1
U-233	0.7	0.4	8.2	0.2	0.0	1.1	8.3
U-234	0.4	0.2	2.1	0.2	0.0	n/a	2.2
U-235	0.5	0.0	0.1	0.0	0.0	0.1	0.5
U-236	0.1	0.1	0.1	0.0	0.0	n/a	0.1
Total	4.8	1.6	8.6	0.4	0.0	1.5	10.1

Table 4.19. Uncertainty in the reactivity insertion in pcm from flooding the reactor for the RBWR-TR unit cell at EOL due to uncertainty in each isotope and reaction.

Isotope	(n,g)	Elastic	Fission	Inelastic	(n, 2n)	Cross-terms	Total

Isotope	(n,g)	Elastic	Fission	Inelastic	(n, 2n)	Cross-terms	Total
Am-241	61	6	2	1	0	15	63
Am-242m	17	0	29	0	0	n/a	33
Am-243	6	1	11	2	0	n/a	12
Cm-243	1	0	1	0	0	0	2
Cm-244	26	2	8	1	0	1	27
Cm-245	34	0	76	0	0	14	84
Cm-246	6	0	2	0	0	0	6
Cm-247	4	0	5	0	0	2	7
Cm-248	0	0	0	0	0	0	1
H-1	14	5	n/a	n/a	n/a	n/a	15
Np-237	27	0	3	0	0	n/a	27
O-16	1	11	n/a	1	n/a	0	11
Pu-238	65	2	6	1	0	4	65
Pu-239	29	0	32	3	0	33	54
Pu-240	34	1	9	9	0	4	36
Pu-241	22	0	29	2	0	n/a	37
Pu-242	13	1	7	2	0	n/a	15
Sm-149	68	0	n/a	0	0	n/a	68
Sm-151	10	0	n/a	0	0	n/a	10
Th-232	154	11	6	n/a	n/a	13	155
U-232	2	0	4	0	0	0	5
U-233	25	4	339	3	0	43	343
U-234	17	1	84	3	0	n/a	86
U-235	15	0	4	1	0	3	16
U-236	1	1	9	2	0	n/a	9
Total	208	18	362	11	0	60	422

Table 4.20. Uncertainty in the reactivity insertion in pcm from voiding the reactor for the RBWR-TR unit cell at EOL due to uncertainty in each isotope and reaction.

Isotope	(n,g)	Elastic	Fission	Inelastic	(n, 2n)	Cross-terms	Total
Am-241	87	2	3	4	0	2	87
Am-242m	10	0	38	0	0	n/a	40
Am-243	88	2	17	16	0	n/a	91
Cm-243	1	0	2	0	0	0	2
Cm-244	121	5	19	5	0	6	123
Cm-245	24	0	112	3	0	10	115
Cm-246	17	0	5	1	0	1	17
Cm-247	6	0	13	0	0	4	15
Cm-248	1	0	1	0	0	1	2
H-1	9	42	n/a	n/a	n/a	n/a	43
Np-237	60	1	8	5	0	n/a	61
O-16	3	125	n/a	1	0	0	126

Isotope	(n,g)	Elastic	Fission	Inelastic	(n, 2n)	Cross-terms	Total
Pa-231	n/a	n/a	n/a	n/a	n/a	n/a	0
Pu-238	155	2	25	3	0	10	157
Pu-239	41	1	61	23	0	14	78
Pu-240	76	2	32	39	0	10	91
Pu-241	130	2	124	33	0	n/a	183
Pu-242	141	5	14	10	0	n/a	142
Sm-149	21	0	n/a	0	0	n/a	21
Sm-151	13	1	n/a	1	0	n/a	13
Th-232	570	34	6	n/a	n/a	26	572
U-232	3	0	9	0	0	2	10
U-233	106	3	398	32	0	37	415
U-234	103	6	228	18	0	n/a	251
U-235	69	0	14	5	0	6	71
U-236	17	1	14	10	0	n/a	25
Total	675	137	497	71	0	51	854

Table 4.21. Uncertainty in the control rod worth in pcm for the RBWR-TR unit cell at EOL due to uncertainty in each isotope and reaction.

Isotope	(n,g)	Elastic	Fission	Inelastic	(n, 2n)	Cross-terms	Total
Am-241	5	3	1	0	0	3	7
Am-242m	1	0	2	0	0	n/a	2
Am-243	6	0	4	1	0	n/a	7
B-10	8[15]	1	n/a	20	n/a	4	22
Cm-244	7	0	3	0	0	0	7
Cm-245	6	0	3	0	0	0	7
Cm-246	1	0	1	0	0	0	1
Cm-247	1	0	0	0	0	0	1
H-1	2	5	n/a	n/a	n/a	n/a	6
Np-237	6	0	1	0	0	n/a	6
O-16	1	10	n/a	0	n/a	0	10
Pu-238	9	1	2	0	0	2	9
Pu-239	3	0	2	0	0	1	3
Pu-240	4	1	2	1	0	1	5
Pu-241	7	1	3	1	0	n/a	7
Pu-242	9	3	3	1	0	n/a	10
Sm-149	3	1	n/a	0	0	n/a	3
Sm-151	1	0	n/a	0	0	n/a	1
Th-232	27	5	3	n/a	n/a	4	28
U-232	0	0	1	0	0	0	1
U-233	6	5	31	1	0	13	35

[15] The (n,α) reaction is summarized here, as the ^{10}B (n,g) reaction is negligible.

Isotope	(n,g)	Elastic	Fission	Inelastic	(n, 2n)	Cross-terms	Total
U-234	5	1	32	1	0	n/a	32
U-235	2	0	1	0	0	1	2
U-236	1	0	4	0	0	n/a	4
Total	35	14	46	2	0	14	65

4.4.3. Uncertainty in k_∞ due to Void Fraction Uncertainty

The uncertainty in k_∞ due to the uncertainty in the void fraction correlation was also calculated. The uncertainty corresponding to a superficial liquid velocity of 1.0 m/s in Table 4 of [44] was used. It should be noted that there is not much experimental data for such tight lattices, and that there is approximately a 10% difference compared to the limited experimental data [58]; therefore, to bound the uncertainty, the uncertainty in k_∞ assuming a constant 10% uncertainty in the void fraction was also assumed as a bounding case. The uncertainty is presented in Table 4.22, while Figure 4.14 shows the sensitivity coefficients. Figure 4.15 through Figure 4.18 show the water density covariance at each of the different conditions.

The trend in the sensitivity coefficient changes significantly over the length of the fuel. Near the periphery of the seed, the leakage is dominant; increasing the water density causes the leakage to reduce, which increases reactivity. In the center of the seed, the impact of softening the spectrum and reducing the fast fissions from non-fissile isotopes is dominant, which makes the sensitivity coefficient negative. The thorium in the fresh blankets has effectively no chance of fissioning below its threshold energy, so the reactivity similarly increases when the blanket water density is reduced. Conversely, the sensitivity coefficient of the blanket becomes positive as ^{233}U is bred into the fuel by the end of life. Since the sensitivity coefficient changes significantly over the seed, the uncertainty cancels out significantly.

Table 4.22. Uncertainty in k_∞ due to void fraction uncertainty for the RBWR-TR.

Burnup	**Uncertainty using** [44] **for α uncertainty [pcm]**	**Uncertainty assuming 10% for α uncertainty [pcm]**
BOL	24.2	38.1
EOL	56.4	65.7

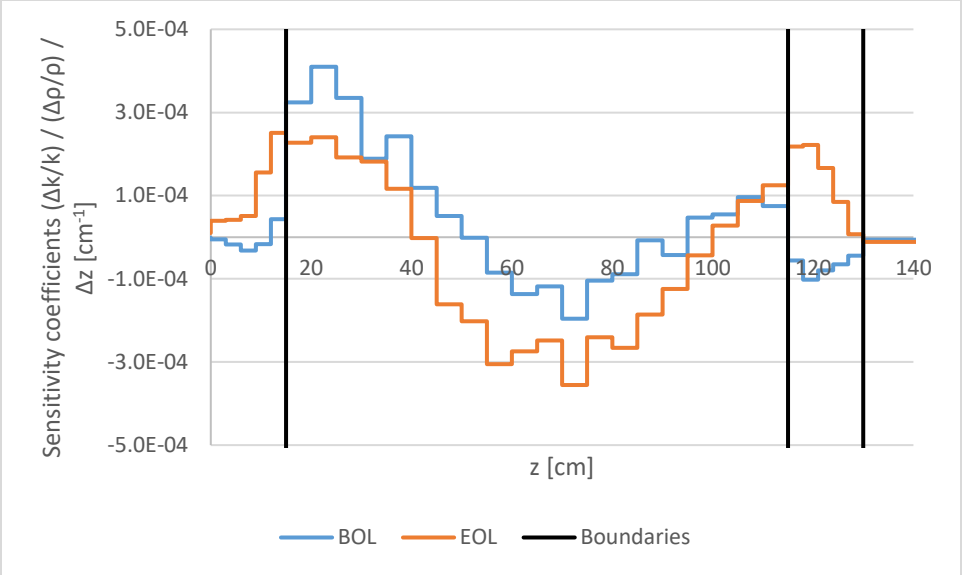

Figure 4.14. Sensitivity coefficients for the multiplication factor of the RBWR-TR due to a relative change in water density.

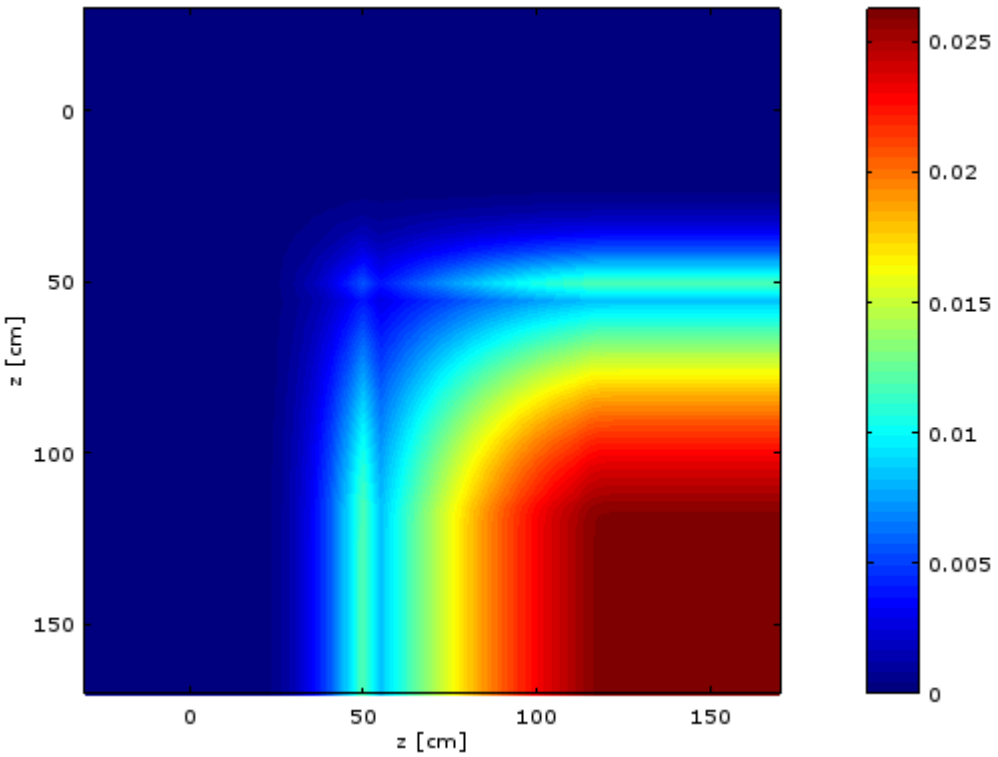

Figure 4.15. Relative water density covariance plot for the RBWR-TR at BOL assuming void fraction uncertainty as specified in [44]. The x and y axes are the axial position in the fuel, where 0 is the bottom of the lower blanket.

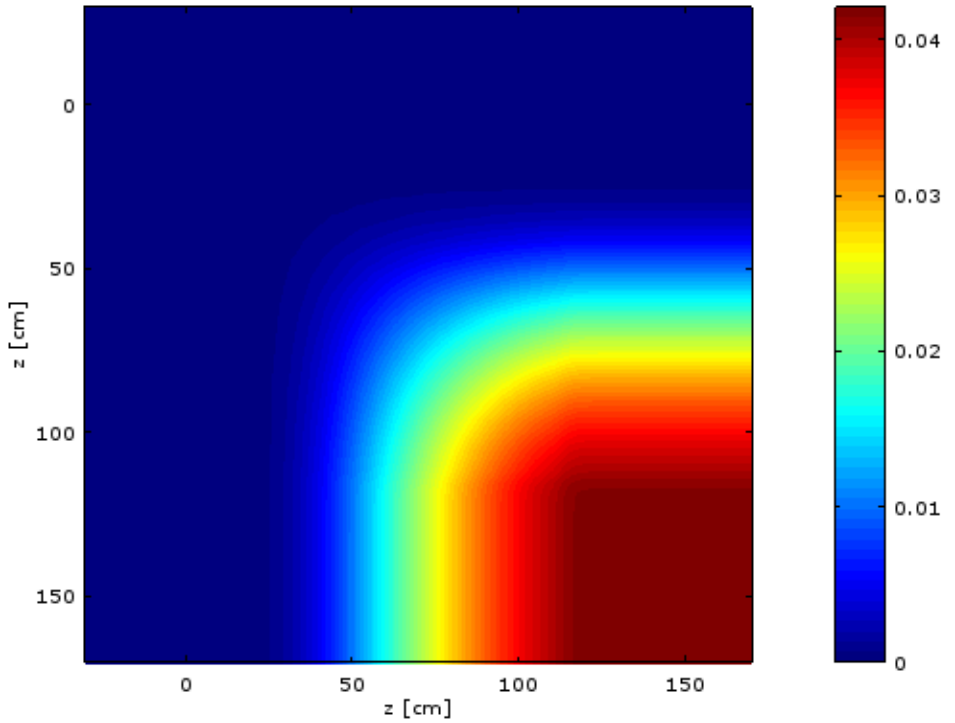

Figure 4.16. Relative water density covariance plot for the RBWR-TR at BOL assuming 10% void fraction uncertainty. The x and y axes are the axial position in the fuel, where 0 is the bottom of the lower blanket.

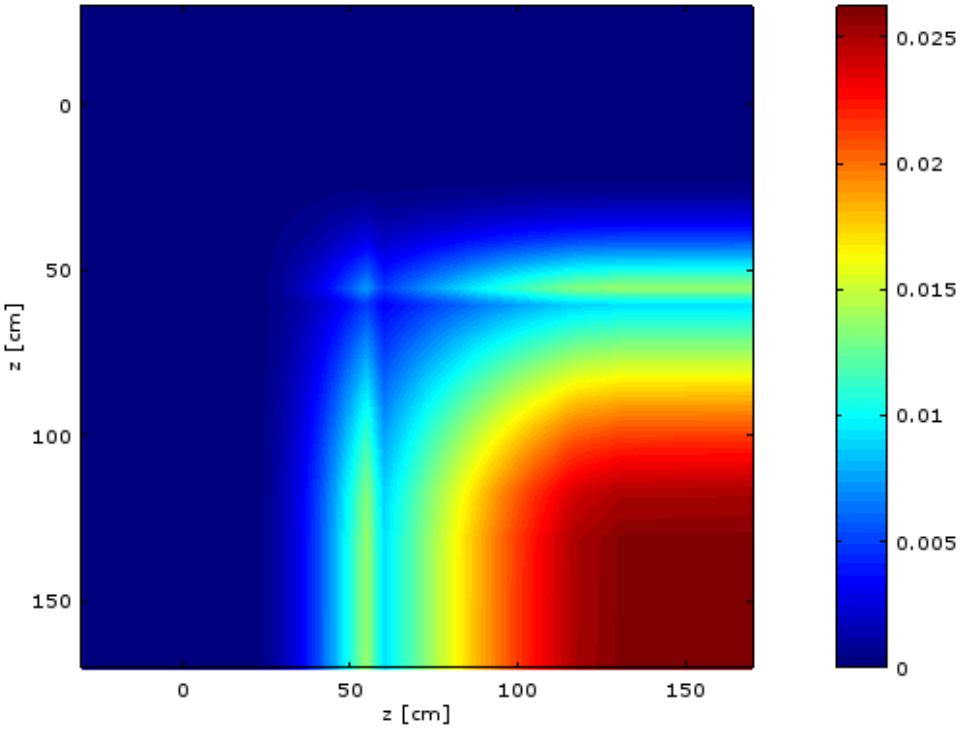

Figure 4.17. Relative water density covariance plot for the RBWR-TR at EOL assuming void fraction uncertainty as specified in [44]. The x and y axes are the axial position in the fuel, where 0 is the bottom of the lower blanket.

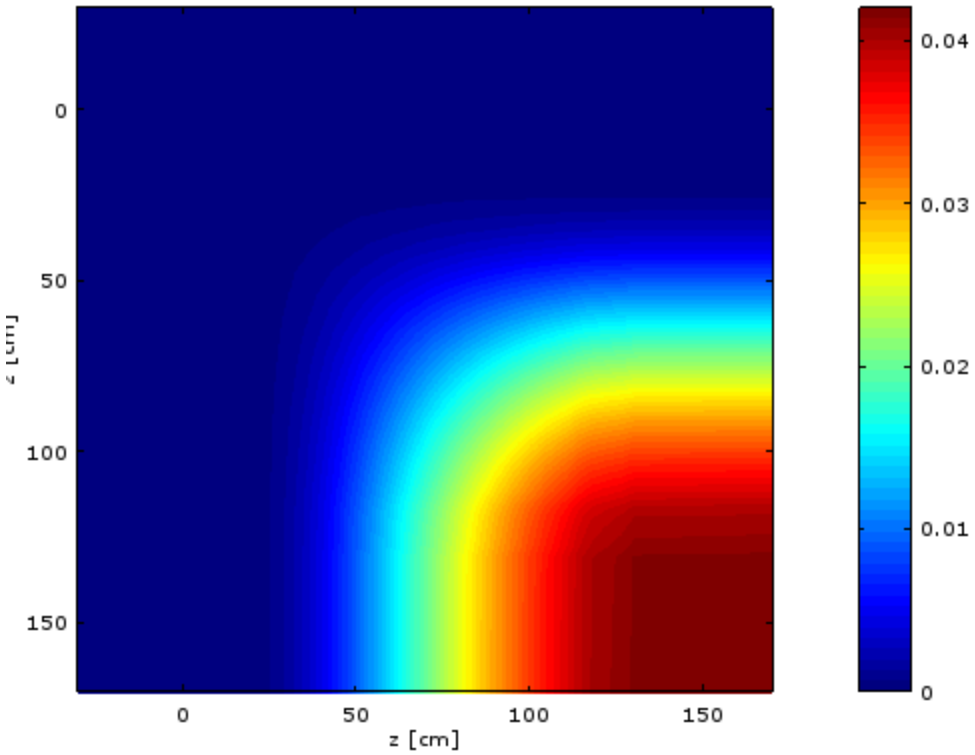

Figure 4.18. Relative water density covariance plot for the RBWR-TR at EOL assuming 10% void fraction uncertainty. The x and y axes are the axial position in the fuel, where 0 is the bottom of the lower blanket.

4.5. Fuel Cycle Analysis

It was desired to assess the fuel cycle impacts of the RBWR-TR as compared to the RBWR-TB2 and the CR=0.5 ABR. The CR=0.5 ABR was used as a comparison since the conversion ratio of the RBWR-TR and the RBWR-TB2 is roughly 0.5. The methodology used by the recent DOE sponsored Fuel Cycle Evaluation and Screening (FCE&S) Campaign [1] is applied for part of this comparison, as described in Section 2.9.

4.5.1. General Fuel Cycle Characteristics

Figure 4.2 shows a schematic view of the RBWR-TR fuel cycle, while Figure 4.19 shows the RBWR-TB2 and the ABR fuel cycles considered. All three reactors were designed to close the fuel cycle not only for themselves, but for a number of PWRs. The incineration of the enriched fuel in the PWR forms the first stage, while the incineration of the fuel in the multirecycling reactor forms the second stage. At equilibrium, the amount of TRU generated in the first stage equals the amount of TRU consumed in the second stage. The support ratio is the ratio of PWRs to second stage reactors necessary to maintain this balance. Rather than examining the impacts of just the second stage reactors, the impacts of the system (PWRs + second stage reactors) are considered.

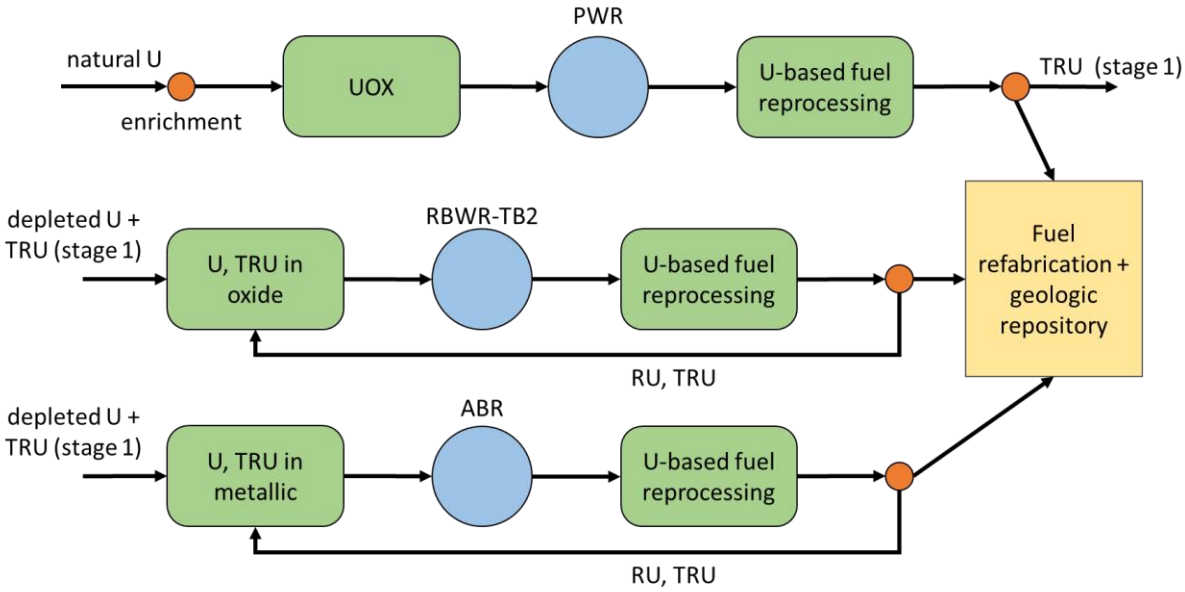

Figure 4.19. Schematic view of the RBWR-TB2 and the ABR fuel cycles.

Table 4.23 compares the performance characteristics of the different cores. The RBWR cores have significantly smaller burnup and therefore features higher fuel reprocessing and fabrication capacity than the ABR. The capacity factor for the ABR was assumed to be 85% in accordance with the assumptions of [4]. All three reactors assessed here have a conversion ratio of roughly 0.5.

Table 4.23. Performance characteristics of the RBWR-TR, RBWR-TB2, and CR=0.5 ABR cores.

Parameters	**RBWR-TR**	**RBWR-TB2**	**ABR**
Thermal power, MW_{th}	3926	3926	1000
Electric power, MW_e	1354	1354	400
Capacity Factor, %	90	90	85
Average discharge burnup, GWd/t	50.5	65.0	132
Specific power, MW_{th}/t	44.6	47.9	105.8
Power density, W/cc	124	158	303
Peak LHGR, W/cm	234	472	327
Number of batches	4	4	6
Fuel inventory in core, t	86.3	81.9	9.5
Fuel residence time, EFFD	1134	1355.6	1326
Cycle length per batch, EFPD	283	338.9	221
TRU transmutation rate, kg/GW_e-yr	517.7	533.6	458.7
TRU transmutation efficiency	52%	49%	46%
Power Fraction, %			
Stage 1 (PWR)	67.3	68.0	64.6
Stage 2	32.7	32.0	35.4
Support ratio	2.06	2.13	1.83

Parameters	RBWR-TR	RBWR-TB2	ABR
Reprocessing capacity, kg/GW_e-yr			
SNF from 1st stage	14748.4	14893.8	14154.8
SNF from 2nd stage	6833.6	5201.2	2446.7
Pu from 2nd stage	695.4	1230.4	591.0
TRU from 2nd stage	904.3	1433.0	651.5
Charge mass fraction, %			
- Th-232	77.1	0	0
- TRTh	7.2	0	0
- U238	0.0	69.2	66.7
- TRU	15.7	30.8	33.3
Discharge mass fraction, %			
- Th-232	74.6	0	0
- TRTh	7.3	0	0
- U238	0.0	65.7	59.0
- TRU	13.3	27.6	26.6
- FPs	4.8	6.7	14.4
Fuel mass at time of recycle, %			
- Th-232	74.6	0	0
- TRTh	7.4	0	0
- U238	0.0	65.8	59.0
- TRU	13.2	27.6	26.6
- FPs	4.8	6.7	14.4

The discharged fuel composition after 5 years cooling is shown in Table 4.24; it is used for later fuel cycle analysis. In the more thermal systems, a larger fraction of the plutonium is composed of non-fissile isotopes.

Table 4.24. Discharged fuel composition of the RBWR-TR, RBWR-TB2, and CR=0.5 ABR fuel after 5 years cooling. All values are given in weight percent.

Nuclide	RBWR-TR	RBWR-TB2	ABR
Th-232	78.50	0.0	0.0
Pa-231	0.04	0.0	0.0
U-232	0.03	0.0	0.0
U-233	4.19	0.0	0.0
U-234	2.17	0.14	0.17
U-235	0.75	0.09	0.04
U-236	0.61	0.04	0.07
U-238	0.00	70.19	68.17
Np-237	0.51	0.40	0.46
Pu-238	1.84	2.17	1.14
Pu-239	1.95	6.59	11.42
Pu-240	3.91	11.60	10.53

Nuclide	RBWR-TR	RBWR-TB2	ABR
Pu-241	1.01	1.56	1.42
Pu-242	2.00	3.45	3.19
Am-241	0.88	1.72	1.27
Am-242m	0.06	0.10	0.06
Am-243	0.68	0.91	1.07
Cm-244	0.61	0.68	0.66
Cm-245	0.26	0.22	0.21
Cm-246	0.16	0.12	0.11

4.5.2. Repository Analysis

The radioactivity, ingestion toxicity, and inhalation toxicity of the UNF and High Level Waste (HLW) was quantified at short term (10 years) and long term (100,000 years) after the fuel is discharged from the cores according to the methodology detailed in Section 2.9.

Figure 4.20 compares the radioactivity of the TRU burner systems HLW at 10 years and 100,000 years after fuel discharge. Since fission products dominate the radioactivity, the differences are mainly due to the different thermal efficiencies between the different systems.

Figure 4.21 shows the inhalation toxicity at 10 years and 100,000 years. The fuel discharged from the PWR has much lower Pu and MA contents than the fuel discharged from the second stage. As a result, the FPs, Pu and MA in the fuel discharged from the first stage contribute only few percent of the total inhalation toxicity of the 2-stage systems. Since the reprocessing capacity of the RBWR-TB2 is higher than that for the ABR system, the ABR features less inhalation toxicity at both 10 and 100,000 years. Additionally, the RBWR-TB2 features significantly more Pu-238, which contributes over 85% of the Pu inhalation radiotoxicity at 10 years; all of the Pu-238 has decayed away by 100,000 years, so the differences are smaller.

Figure 4.22 shows the ingestion toxicity of the TRU transmutation systems at 10 years and 100,000 years. At 10 years, fission products still dominate the ingestion toxicity, so there are no significant differences between the two systems. At 100,000 years, the decay daughters from Pu-238 (Po-210 and Pb-210) contribute significantly more ingestion toxicity for the RBWR-TB2 system waste than for the ABR.

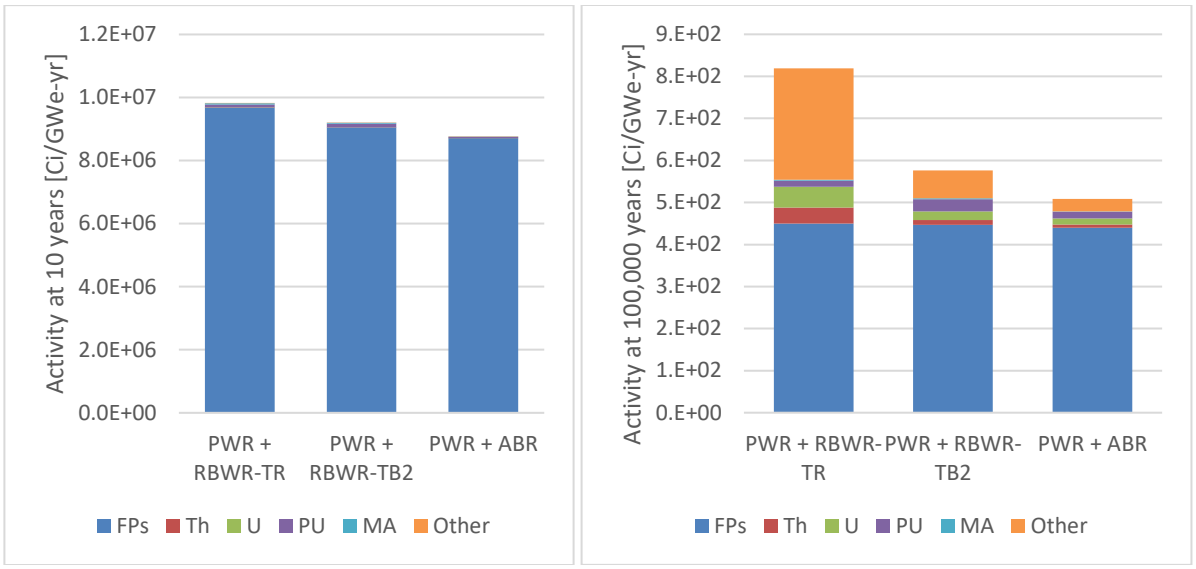

Figure 4.20. Radioactivity for the RBWR-TB2 and the ABR at 10 years (left) and 100,000 years (right).

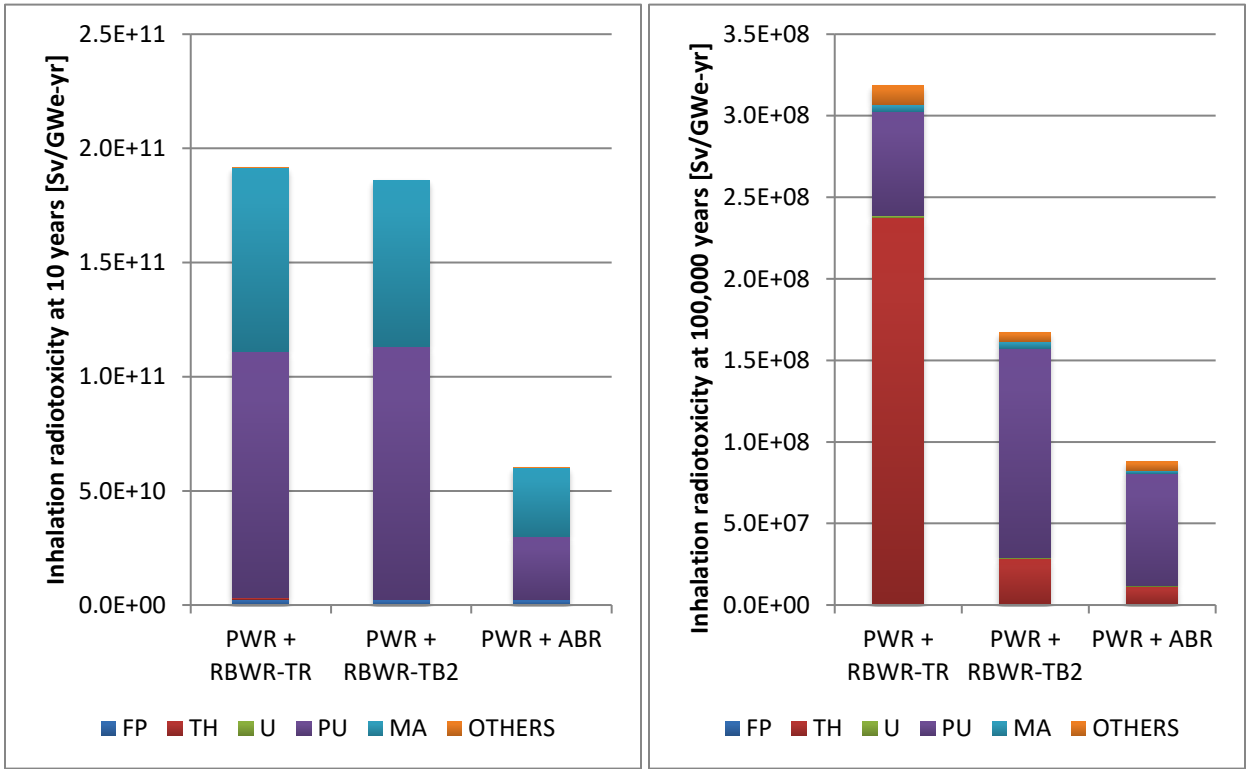

Figure 4.21. Inhalation toxicity of the waste stream from RBWR-TB2 and ABR at 10 years (left) and 100,000 years (right).

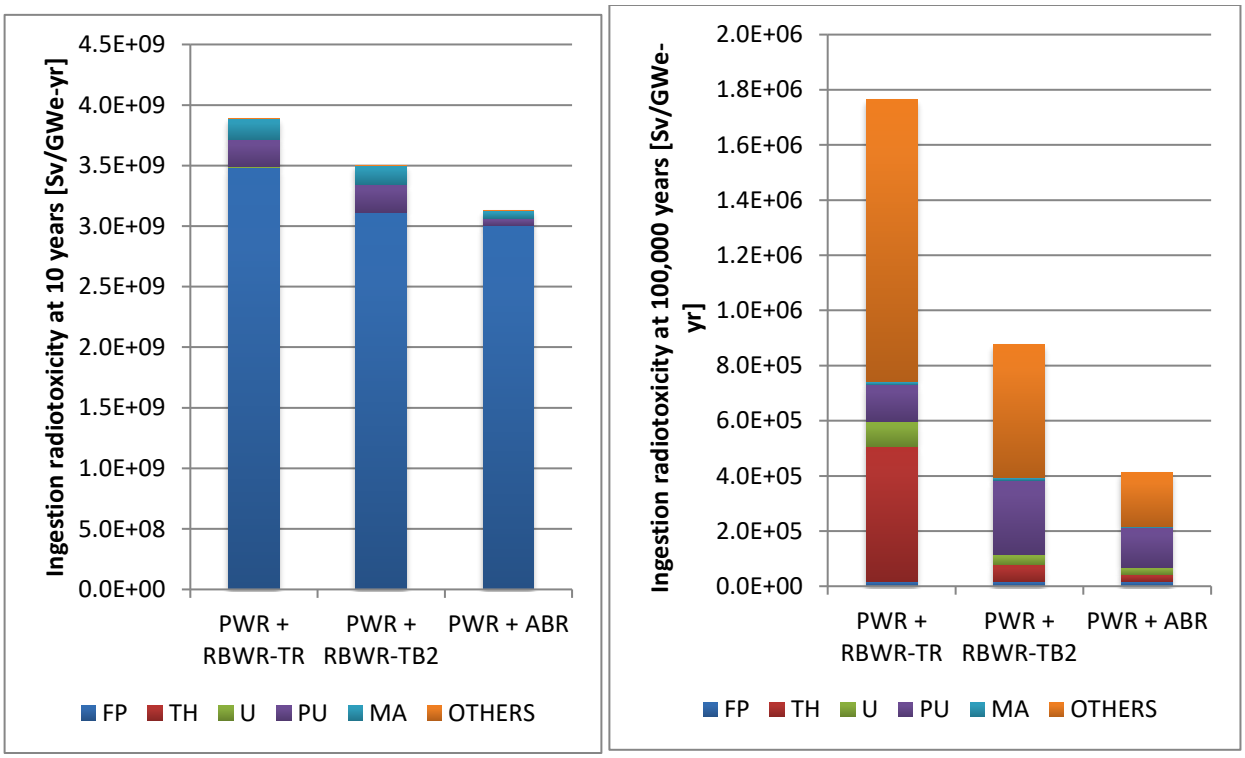

Figure 4.22. Ingestion toxicity of the waste stream from RBWR-TB2 and ABR at 10 years (left) and 100,000 years (right).

4.5.3. Proliferation Resistance

The proliferation resistance is evaluated by the fissile plutonium fraction, ^{238}Pu/Pu ratio, specific decay heat of discharged plutonium, spontaneous fission neutron emission rate, and the level of dilution of fissile isotopes by fertile isotopes, which are summarized for the TRU burners in Table 4.25. ^{238}Pu, ^{240}Pu, and ^{242}Pu have high spontaneous neutron generation which significantly reduces the nuclear explosive yield. ^{238}Pu has a large decay heat that further complicates the design and maintenance of an explosive device [54]. It has been suggested [55] that it is not realistic to apply plutonium for weapon use when the fraction of ^{238}Pu is beyond 2% of the total plutonium. All of the TRU transmuting cores meet this criterion.

Relative to the ABR, the RBWR-TB2 system has over twice the total Pu throughput per unit of electricity generated but this Pu has a smaller fissile fraction and more than twice the specific decay heat. The RBWR-TR uses less Pu than either of the other TRU burners, but it generates high-quality uranium. Nonetheless, since the discharged fuel is more than 70% Th, it is considered unattractive for weapons use [57].

Table 4.25. Proliferation resistance metrics of RBWR-TR, RBWR-TB2, and ABR.

Metrics	**RBWR-TR**	**RBWR-TB2**	**ABR**
Fissile plutonium fraction at reprocessing, %	28%	32%	46%
^{238}Pu/Pu ratio at reprocessing, %	17.2%	8.6%	4.1%
Specific decay heat of plutonium at reprocessing, W/kg	100.81	53.17	26.94
Spontaneous fission neutrons per kg Pu at	11.0E+05	8.7E+05	6.5E+05

Metrics	RBWR-TR	RBWR-TB2	ABR
reprocessing, n/sec-kg			
Tot. plutonium reprocessed, tons/GWe-yr	2.13	3.85	1.67
Pu/^{238}U ratio at reprocessing	-	36%	40.7%
Fissile U/U ratio at reprocessing, %	64%	-	-
Fissile U/Th ratio at reprocessing	6.3%	-	-
(Pu+fissile U)/(^{238}U+Th) ratio at reprocessing	20.0%	36%	40.7%

4.5.4. Fuel Cycle Costs

The fuel cycle costs for the transmuting reactors are compared in Figure 4.23. These costs include the cost of activities for both stages of the fuel cycle, which is based on the mass flow rates in the system. An example of the mass flow rates for the RBWR-TB2 is given in Table 4.26. The smaller reprocessing capacity for the ABR, due to its substantially higher average discharge burnup, reduces the fuel cycle cost of the PWR+ABR system compared with that of the PWR+RBWR-TB2 system. The larger fraction of power from stage 1 of the PWR+RBWR system partially compensates the effect of lower burnup of the RBWRs. The electro-chemical processing and fabrication of TRU-containing fuel are about five times more expensive than UREX processing and UOX fuel fabrication (Table 2.4).

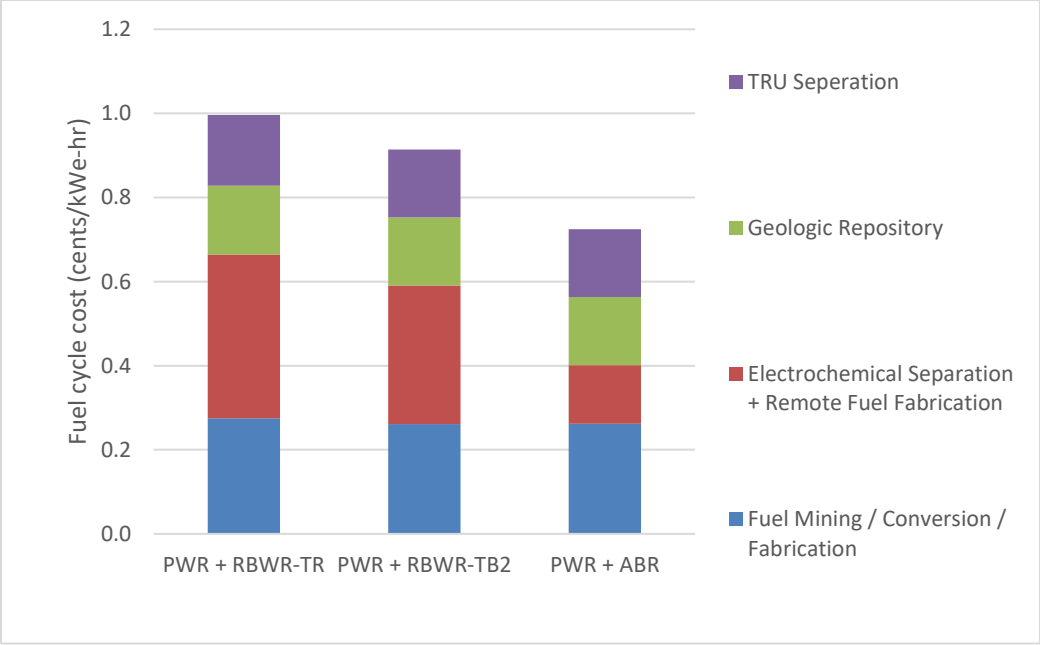

Figure 4.23. Fuel cycle costs for the RBWR-TR, RBWR-TB2 and the CR=0.5 ABR.

Table 4.26 Mass Flow Rate per 100 GWe-Yr for PWR+RBWR-TB2 system.

Stage	1			2			Sum[16]
Technology	Fuel	NPPT	Sep/WF	Fuel	NPPT	Sep/WF	

[16] Mass flow in metric ton required to produce 100.0 GWe-year from whole nuclear fleet was developed. The (-) and (+) signs indicate the feed to and production from each technology category, respectively
.

Stage		1			2			Sum[16]
Technology		Fuel	NPPT	Sep/WF	Fuel	NPPT	Sep/WF	
Electricity, GWe-yr		68.01			31.99			100.00
Feed or product of nuclear materials (metric ton)								
Natural resource	NU	-12,316.1						-12,316.1
Products from fuel or NPPT technology	DU	10,826.7				-18.0		10,808.7
	UOX	1,489.4	-1,489.4					0.0
	RU				341.8	-341.8		0.0
	TRU				160.4	-160.4		0.0
	DF		1,489.4	-1,489.4		520.1	-520.1	0.0
Products from Sep/WF technology	RU			1,395.6	-341.8		341.8	1,395.6
	TRU			17.1	-160.4		143.3	0.0
	FP			76.7			35.0	111.8

4.5.5. Fuel Cycle Evaluation

Using the same methodology as the FCE&S campaign [1] which is summarized in Section 2.9.2, the performance of the PWR+RBWR-TB2 system was assessed against the performance of EG32. EG32 is the evaluation group which represents two-stage systems which use enriched uranium in the first stage and a fast spectrum multirecycling reactor for the second stage [1]. The mass flows were readjusted in order to use a uniform 33% thermal efficiency in both stages. Table 4.27 summarizes the evaluation results of the RBWR-TB2 and the ABR two-stage fuel cycles. The RBWR system can achieve very similar scores as EG32 because most functions demonstrated by the ABR could be accomplished by the RBWRs. The economics of the TRU transmuting systems are not compared in Table 4.27.

Table 4.27. Evaluation of the RBWR-TB2 and ABR fuel cycle.

	Metric	Metric/Bin	Metric/Bin
		PWR+RBWR-TR	EG32
Renormalization Factor (stage 1)		1.014	1.07
Nuclear Waste Management	Mass of SNF+HLW disposed, t/GWe-yr	1.33/A	1.32/A
	Activity of SNF+HLW (@100 years), MCi/GWe-yr	1.10/C	1.08/C
	Activity of SNF+HLW (@100,000 years), 10^{-4} MCi/GWe-Yr	8.1/B	5.19/B
	Mass of DU+RU+RTh disposed, t/GWe-yr	122.8/E	127.15/E
	Volume of LLW, m^3/GWe-yr	692.3/D	579.27/C
Environmental Impact	Land use per energy generated, km^2/GWe-yr	0.14/B	0.13/B

	Metric	Metric/Bin	Metric/Bin
		PWR+RBWR-TR	EG32
	Water use per energy generated, ML/GWe-yr	23834/B	23838/B
	Radiological exposure, Sv/GWe-yr	1.03/B	1.13/B
	Carbon emission - CO_2 released per energy generated, kt CO_2/GWe-yr	47.1/B	41.6/B
Resource Utilization	Natural Uranium required per energy generated, t/GWe-yr	123.9/C	128.5/C
	Natural Thorium required per energy generated, t/GWe-yr	0.2/A	0.0/A

4.6. Square Lattice RBWR-TR

Since the RBWR-TR benefits significantly from a softer spectrum, it was decided to assess the feasibility of using a traditional square lattice to accomplish the same objective. It was desired to make a "retrofit" assembly for an ABWR – in other words, using the same cruciform control blades with no follower.

It was clear that it would be necessary to use multiple seeds, as the triangular lattice permitted much better wetting of the fuel, which significantly benefitted the MCPR. The Hench-Gillis CPR correlation [12] was used for the MCPR correlation with the square lattice; it was found that with a 14 x 14 assembly and a pitch-to-diameter ratio (P/D) of 1.2 (both of which are more favorable to the MCPR than a standard BWR), a boiling length of 2.4 m would be necessary to obtain an MCPR of 1.3, which is more than double the seed length of the RBWR-TR. This is due to the fact that there are roughly half of the fuel rods in a square lattice bundle as in the triangular lattice RBWR-TB2 and RBWR-TR bundles; the extra length is needed to reduce the average linear heat rate to manageable levels, but it poses a challenge for the void feedback and pressure drop constraints.

It was found that it would not be possible to simultaneously meet the pressure drop, MCPR, and void feedback constraints. A candidate design is presented in Table 4.28, and the results based off an assembly-level equilibrium analysis are shown in Table 4.29. The pressure drop is nearly an order of magnitude higher than the RBWR-TB2 pressure drop, since the flow rate is almost three times higher and the fuel length is almost doubled. Additionally, the void coefficient is large and positive. In order to meet the pressure drop constraint, either the pitch-to-diameter ratio would need to be increased; the fuel length would need to be reduced; or the mass flow rate would need to be reduced. Unfortunately, all of these changes negatively impact the MCPR, so it is not feasible to design a square-lattice thorium RBWR.

Table 4.28. Design characteristics of the square lattice thorium RBWR compared to the Hitachi designed RBWR-TB2.

Parameter	Square Lattice Thorium RBWR	RBWR-TB2
Core thermal power (MW_{th})	3926	3926
Thermal efficiency	34.5%	34.5%
# of assemblies	872	720
# of batches	4	4
Total fuel length (seed + blanket) (cm)	289.0	102.5
Total seed length (cm)	160.0	44.5
Number of seed regions	4	2
Fuel pin OD (cm)	0.764	0.72
Fuel pin pitch (cm)	0.917	0.94
Fuel pin P/D	1.20	1.30
Average assembly pitch (cm)	15.24	19.9
Assembly flat-to-flat (cm)	13.0	19.4
BOEC Core HM mass (t)	138.2	76
BOEC Core TRU mass (t)	22.8	24
TRU/HM seed avg for fresh fuel ($^{w}/_{o}$)	30.3%	75.2%
Specific power (MW_e/t)	9.8	18
Core volume (m^3)	58.7	25
Power density (W_{th}/cm^3)	66.9	158
Coolant mass flow rate (kt/hr)	63	24

Table 4.29. Performance characteristics of the square lattice thorium RBWR compared to the Hitachi-designed RBWR-TB2.

Parameter	Square lattice Thorium RBWR	RBWR-TB2
Maximum LHGR (W_{th}/cm)	225	472
MCPR	1.36	1.28
Core pressure drop (MPa)	0.575	0.06
Exit quality	22.6%	36%
Peak discharge burnup (GWd/t)	88.3	
Avg. discharge burnup (GWd/t)	33.7	65
TRU consumption rate (kg/yr)	719	564
TRU consumption rate (kg/GW_e-yr)	531	404
TRU fission efficiency	51.3%	45%
Fuel residence time (EFPD)	1200	1256
Cycle length (EFPD)	300	314
Cycle reactivity swing (%dk)	0.2%	2.5%
HM reprocessing (t/GW_e-yr)	31	16
VCR (BOEC/EOEC, pcm/% void)	+60 /+86	-40

4.7. Thorium RBWR Burner Conclusions

The RBWR-TR is a multirecycling thorium-fueled reactor designed to incinerate reprocessed fuel from existing PWRs. It was chosen to use thorium rather than depleted uranium in order to reduce void coefficient and use a single seed, in order to avoid many of the complications from using multiple seed regions. However, it was found that it was not possible to design the RBWR-TR such that both the shutdown margin and the negative void feedback constraints were met. This is due to the fact that the enrichment in the seed is much lower than that of the RBWR-TB2, which leads to a much more negative fuel temperature coefficient. Preliminary results using multiple seeds are promising, although the discharge burnup and the TRU consumption rate will likely be reduced.

Since the RBWR-TR benefits from using a softer spectrum, a design using a square lattice was also explored; however, since the number of fuel rods were approximately halved compared to the triangular lattice design, it was not possible to meet the MCPR constraint while simultaneously having negative void feedback and the pressure drop constraint.

An uncertainty analysis on the single-seed, triangular lattice design was performed using generalized perturbation theory, and the uncertainty in the multiplication factor was quantified. The fuel cycle impacts were also assessed. Although the decay daughters from ^{233}U are significantly more toxic in the long term than those resulting from the DU-Pu fuel cycle, the fuel cycle of the RBWR-TR falls into almost all of the same metric bins as an analogous DU-fueled burner reactor when using the same methodology as Fuel Cycle Evaluation and Screening study [1].

5. RBWR-TB2

In addition to the work with thorium-based designs as discussed in Chapters 3 and 4, additional analysis was performed for the depleted uranium-based RBWR-TB2. The work included in this chapter is an extension of the Hitachi-funded project entitled "Technical Evaluation of the Resource-Renewable BWR design by Hitachi" which was performed in Japanese fiscal year 2015. It is also to be used in an ongoing Hitachi-funded project which will be continued after this dissertation is submitted. As a part of this work, proprietary information was used; this proprietary information has been removed from this dissertation, and the results may not be entirely reproducible with the information provided.

For this assessment, no design optimizations or tradeoff studies were performed at UC Berkeley. Instead, Revision 4.2 of the RBWR-TB2 [59] was used; the core design is summarized in Section 5.1 based on what is available in the open literature [7]. The control rod worth of the RBWR-TB2 as a function of control rod position is presented in Section 5.2. Generalized perturbation theory (GPT) is applied in Section 5.3 in order to propagate the uncertainty in nuclear data to key performance parameters. Section 5.4 highlights problematic linear heat generation rate spiking in this system, and Section 5.5 concludes this chapter.

5.1. RBWR-TB2 Design Summary and Model Implementations

The RBWR-TB2 is a burner reactor (CR≈0.5) which features two fissile "seed" regions, separated by a large internal blanket. Unlike the RBWR-AC or the thorium designs, the RBWR-TB2 does not have a lower blanket below the lower seed [7]. The seed regions have high TRU enrichments, while the blankets are depleted uranium. The seed fuel is discretized into five separate radial enrichment zones. The fuel is in a standard oxide pellet, and the cladding is standard Zircaloy-2 that is used in most current BWRs. When the control rod is fully withdrawn, the top of the control blade lies at the bottom of the boron pins in the lower reflector, and the top of the follower lies at the top of the upper blanket; the control blade channel in the upper reflector is filled with water. When the control rod is inserted, the follower moves into the upper reflector.

The RBWR-TB2 features the nominal ABWR power level (3926 MW_{th}) and a core coolant flow rate of 24 kt/hr, which allows it to attain an exit void fraction above 80%. Hitachi reports a pressure drop of 0.11 MPa, an MCPR of 1.28 using the H-CISE correlation, and a maximum LHGR of 472 W/cm [7]. It can attain an average discharge burnup of 65 GWd/t with a TRU transmutation efficiency of 45% - that is, 45% of the of the fissions occur in transuranic isotopes [7].

The axial configuration of the fuel pins is shown in Figure 5.1, and a cross section of the assembly model as used in Serpent is shown in Figure 5.2. Within Serpent, the seed regions and the internal blanket were each divided into 8 equally sized slices, while the upper blanket was divided in two. The reflectors were divided according to the location of the boron absorbers. The water between the assemblies was assumed to be boiling with the same density as inside the assembly.

The fuel changes behavior significantly between BOL and EOL; therefore, all of the physics studies were performed at both BOL and EOL. The compositions at EOL were calculated using Serpent. The water densities were the same as University of Michigan used for the simulation of the RBWR-TB2 [60], while the fuel temperature was uniformly set to 900 K in the seeds and 600 K in the blankets.

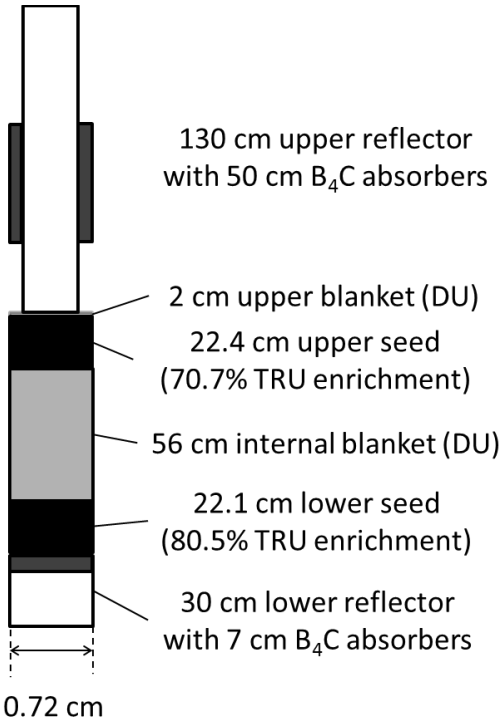

Figure 5.1. Axial configuration of the RBWR-TB2 core [59]. The black regions represent the seed, while the light grey regions are blankets and the dark grey are B_4C absorber material.

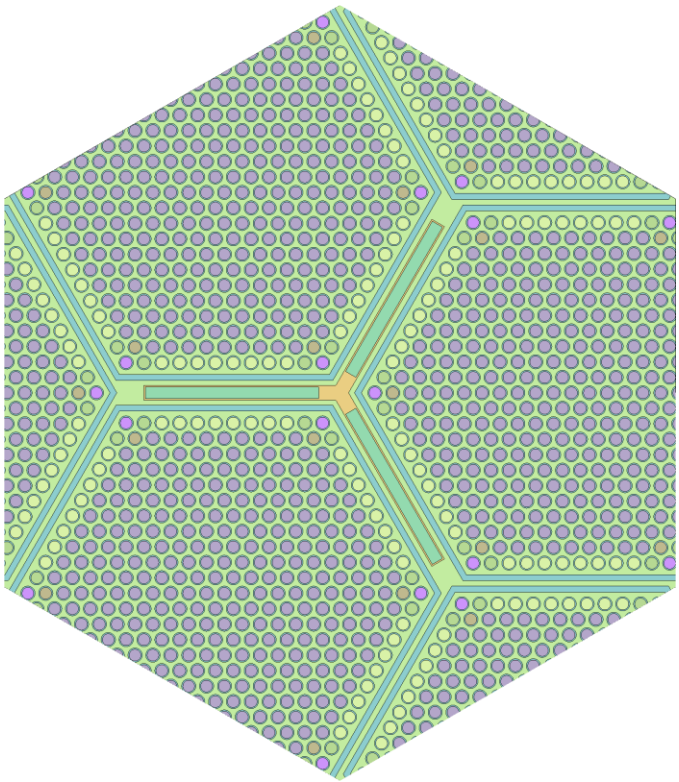

Figure 5.2. Fuel region. The five different pin colors denote different material compositions; one material was used per enrichment group per axial slice. The same binning was used for the blankets, although they have a uniform composition for fresh fuel.

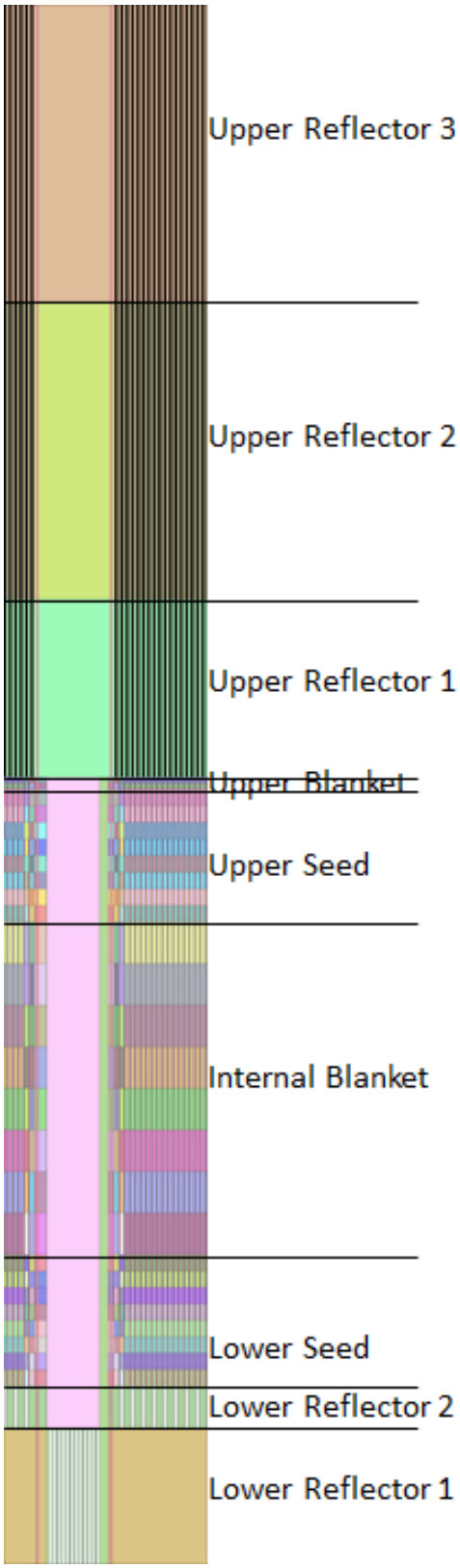

Figure 5.3. A x-z plot of the fuel assembly, cutting through the control blade and going from corner-to-corner of a fuel assembly.

5.2. Axial Control Rod Worth Study

In most reactors, the control rod worth forms an S-shaped curve, where the reactivity removal per length is smaller at the top and bottom of the core. However, in the dual-seed RBWR designs, the internal blanket will have very low worth for most of the core lifetime, which may result in very low control rod worth for most of the fuel length. Additionally, since the internal blanket composes most of the fuel length, the seeds may not have good neutronics communication with each other. If the control rod worth is much larger in one seed region than the other, this could be an indication that the seeds are effectively decoupled, and one seed region may be able to be critical independently of the other.

Therefore, it was decided to use Serpent 2 in order to calculate the control rod worth as a function of control rod position for the RBWR-TB2 unit cell. The coupled Serpent-OpenFOAM solver (Section 2.7) was used to ensure a self-consistent solution; a uniform 5 mm axial mesh was used to calculate the water densities and fuel temperatures. In addition to the control rod worth, the fraction of power generated at each seed was also calculated.

The reactivity worth of the control rods for the RBWR-TB2 is shown in Figure 5.4 and Figure 5.5, while the power generated in each seed is shown in Figure 5.6 and Figure 5.7. The most peaked power profiles are shown in Figure 5.8 and Figure 5.9. It is clear that even when the lower seed produces most of the power (as is the case at EOL), the control rod has very little worth until it reaches the upper seed.

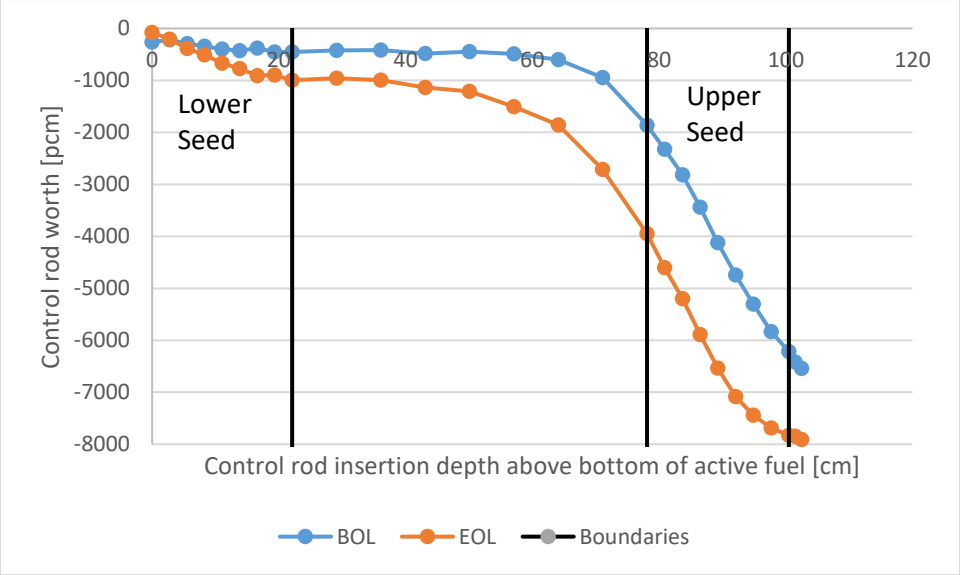

Figure 5.4. Control rod worth in the RBWR-TB2 unit cell.

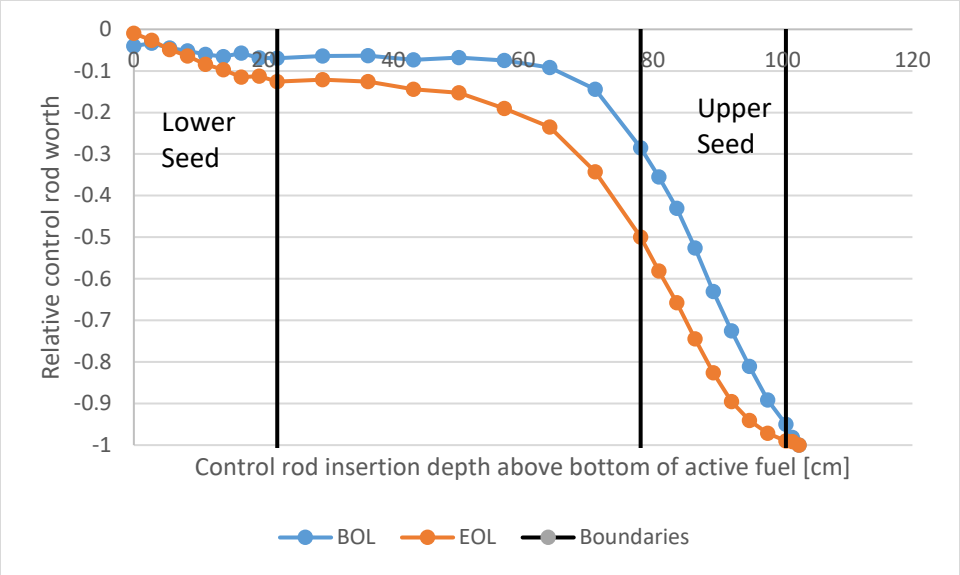

Figure 5.5. Relative control rod worth in the RBWR-TB2 unit cell.

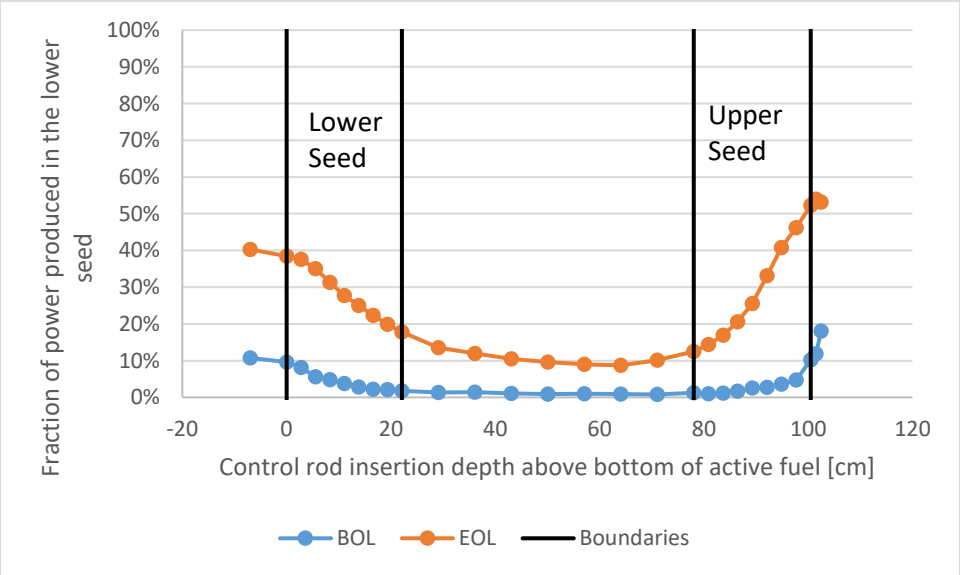

Figure 5.6. Fraction of assembly power generated in the lower seed as a function of control rod insertion in the RBWR-TB2 unit cell.

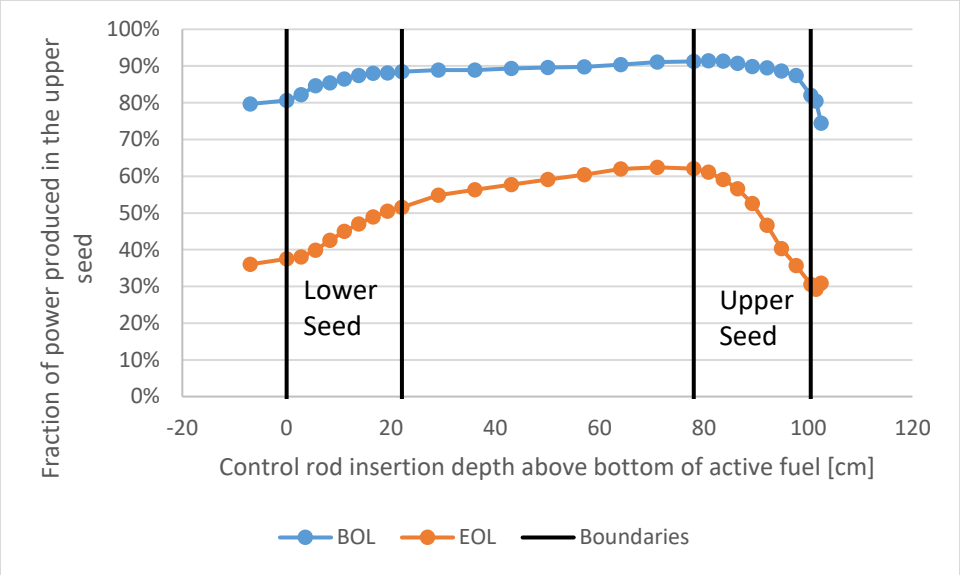

Figure 5.7. Fraction of assembly power generated in the upper seed as a function of control rod insertion in the RBWR-TB2 unit cell.

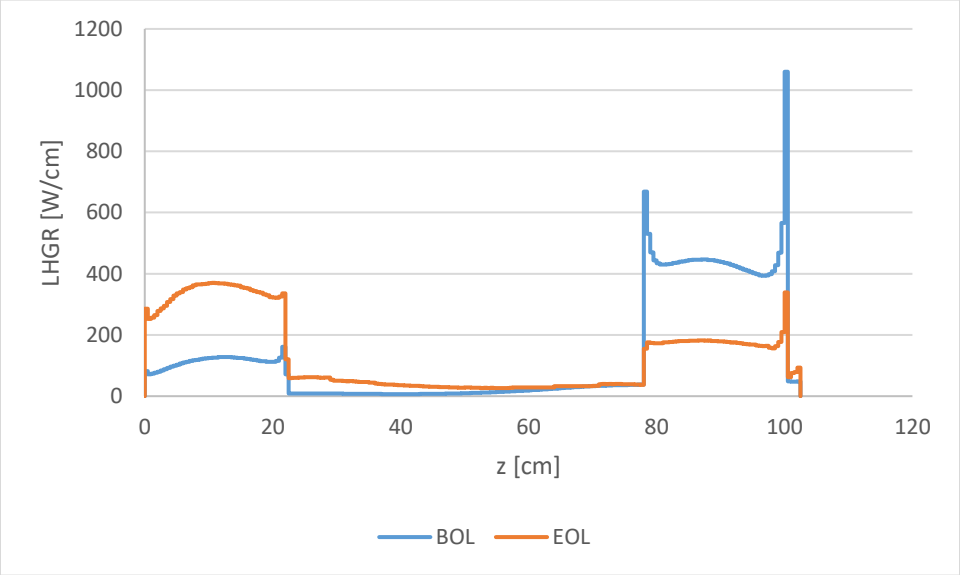

Figure 5.8. Linear heat generation rate profiles using a uniform 5 mm axial mesh for the most bottom-peaked power distributions in the RBWR-TB2 unit cell simulation. Both are when the control rods are fully inserted.

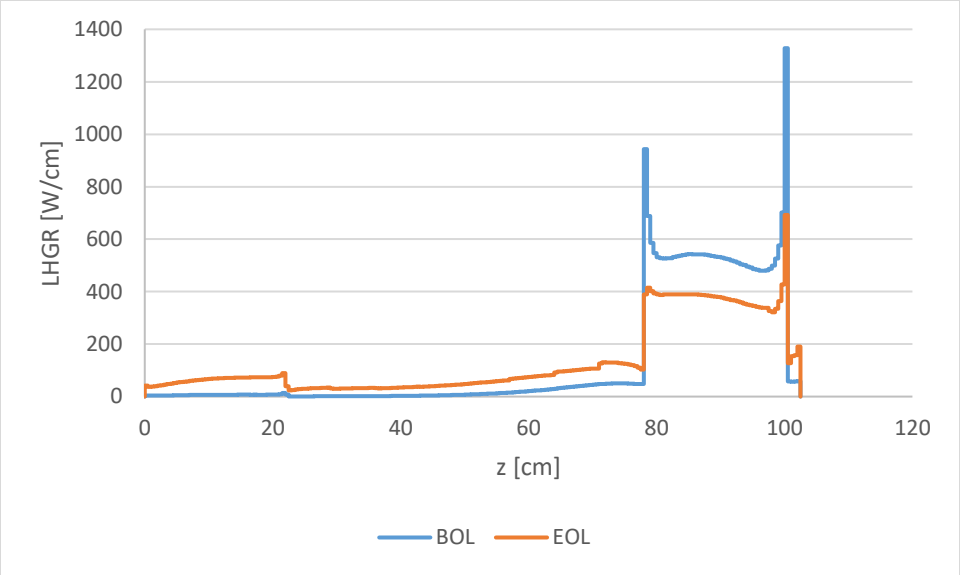

Figure 5.9. Linear heat generation rate profiles using a uniform 5 mm axial mesh for the most top-peaked power distributions in the RBWR-TB2 unit cell simulation. The BOL LHGR profile corresponds to a control rod insertion of 80.9 cm, while the EOL LHGR profile corresponds to a control rod insertion of 71.1 cm.

This study shows that the two seeds are nearly decoupled in the assembly level model. Since the vast majority of the control rod worth occurs when the control rods are inserted into the upper seed, this can cause issues with both power shaping and with transient response, although the latter is significantly mitigated by the short fuel length.

With the power spikes at the seed interfaces, the power shifts caused by inserting the control rods could be problematic, even if it were not already an issue in normal operating conditions (see Section 5.4).

5.3. GPT Uncertainty Analysis

It was desired to assess the uncertainty in the multiplication factor due to the propagation of uncertainty from the nuclear data. The methodology described in Section 2.8 was applied to the RBWR-TB2 assembly unit cell at BOL and EOL, as well as the RBWR test reactor full core at BOC. The uncertainty in k_{eff}, coolant void coefficient of reactivity, coolant total void worth, and control rod worth were assessed. In addition, the sensitivity of k_{eff} to water densities in each axial slice were quantified.

The same coolant densities were used as UM used for generating cross sections [60], since these densities were somewhat representative of what would be seen in the full core.

5.3.1. k_∞ Uncertainty Due to Uncertainty in Nuclear Data

The uncertainty in k_∞ due to the cross sections of each of the isotopes present in the fresh fuel was assessed for fresh fuel and for average discharged fuel (65 GWd/t). A modified version of Serpent 2.1.19 was used to generate sensitivity coefficients, which were collapsed with the cross section covariance matrices to calculate the uncertainty, as detailed in Section 2.8.

The k_∞ at BOL was calculated to be 1.06562 ± 471 pcm, while at EOL, it was calculated to be 0.97919 ± 515 pcm. Effectively all of the quoted uncertainties are due to the uncertainty from the nuclear data, as the statistical uncertainty from the Monte Carlo simulation contributed less than 1 pcm towards the final uncertainty. The decomposition due to reaction type and isotope is shown in Table 5.1 and Table 5.2.

The uncertainty is dominated primarily by capture, inelastic scattering, and fission. The uncertainty in inelastic scattering is almost entirely generated from U-238, which is the isotope which generates the most uncertainty. At EOL, most isotopes generate approximately the same amount of uncertainty as at BOL, except that the uncertainty from U-238 inelastic scattering is significantly increased; this is due to more power being generated in the blankets, which are abundant in U-238. In general, the isotopes which are the most abundant contribute the most uncertainty.

Table 5.1. Uncertainty of the multiplication factor measured in pcm at reference conditions due to uncertainty in each reaction type and isotope for the RBWR-TB2 unit cell at BOL.

Isotope\Rxn	(n,g)	Elastic	Fission	Inelastic	(n, 2n)	cross-terms	Sum
Am-241	105	10	18	11	0	2	108
Am-242m	13	0	37	1	0	n/a	39
Am-243	64	1	56	7	0	n/a	85
Cm-243	3	0	2	0	0	1	3
Cm-244	70	2	25	2	0	1	74
Cm-245	49	0	56	1	0	18	76
Cm-246	10	0	5	0	0	0	11
Cm-247	6	0	6	0	0	4	10
Cm-248	0	0	1	0	0	1	1
H-1	36	50	n/a	n/a	n/a	n/a	62
Np-237	56	0	11	2	0	n/a	57
O-16	146	27	n/a	5	0	2	148
Pu-238	120	1	21	3	0	2	122
Pu-239	102	5	131	46	1	73	188
Pu-240	135	11	68	110	1	26	189
Pu-241	105	2	94	7	2	n/a	141
Pu-242	103	5	40	18	1	n/a	112
U-235	3	0	5	0	0	9	10
U-238	84	48	12	163	3	76	204
Sum:	347	76	204	203	4	110	471

Table 5.2. Uncertainty of the multiplication factor measured in pcm at reference conditions due to uncertainty in each reaction type and isotope for the RBWR-TB2 unit cell at EOL.

Isotope	(n,g)	Elastic	Fission	Inelastic	(n, 2n)	Cross-terms	Total
Am-241	76	3	14	8	0	10	78
Am-242m	9	0	41	1	0	n/a	42
Am-243	64	1	52	6	0	n/a	83

Isotope	(n,g)	Elastic	Fission	Inelastic	(n, 2n)	Cross-terms	Total
Cm-243	2	0	2	0	0	0	3
Cm-244	75	2	28	2	0	4	80
Cm-245	48	0	63	1	0	3	79
Cm-246	9	0	5	0	0	1	10
Cm-247	6	0	7	0	0	1	10
Cm-248	0	0	1	0	0	1	1
H-1	15	71	n/a	n/a	n/a	n/a	72
Np-237	37	0	8	1	0	n/a	38
O-16	159	4	n/a	6	0	2	159
Pu-238	101	2	19	2	0	9	103
Pu-239	90	5	147	31	0	19	176
Pu-240	117	9	64	91	1	35	165
Pu-241	117	2	132	7	1	n/a	177
Pu-242	122	7	38	15	1	n/a	129
Sm-149	20	0	n/a	0	0	n/a	20
Sm-151	12	0	n/a	0	0	n/a	12
U-235	1	0	0	0	0	0	1
U-238	95	23	15	261	3	102	297
Total	339	76	234	279	3	110	515

The groupwise uncertainties were also calculated, and are shown in Figure 5.10 and Figure 5.11. It is clear that at EOL, fast fissions are more important than at BOL. Additionally, although the peak uncertainty per lethargy occurs above 0.1 MeV, the intermediate range has a consistently large uncertainty per lethargy.

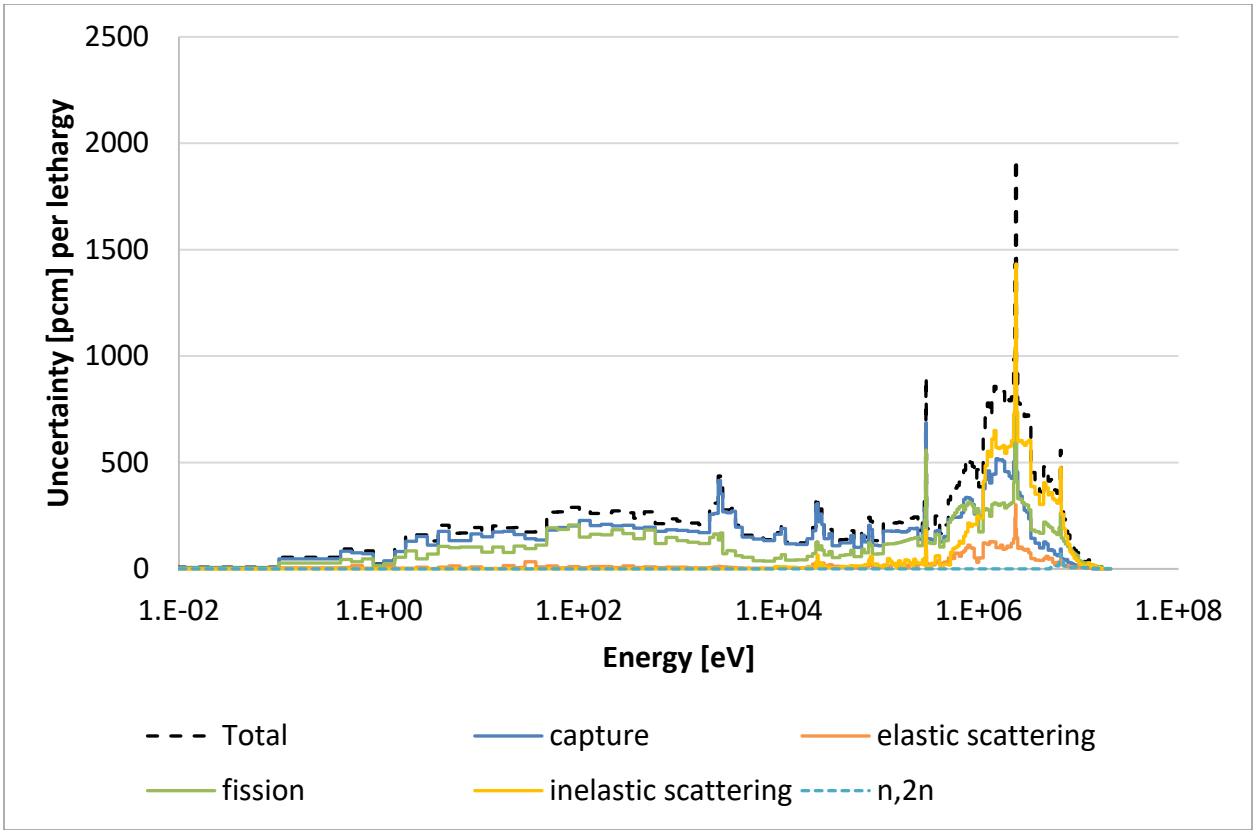

Figure 5.10. Group-wise uncertainty in k_∞ due to uncertainty in each reaction for the RBWR-TB2 unit cell at BOL.

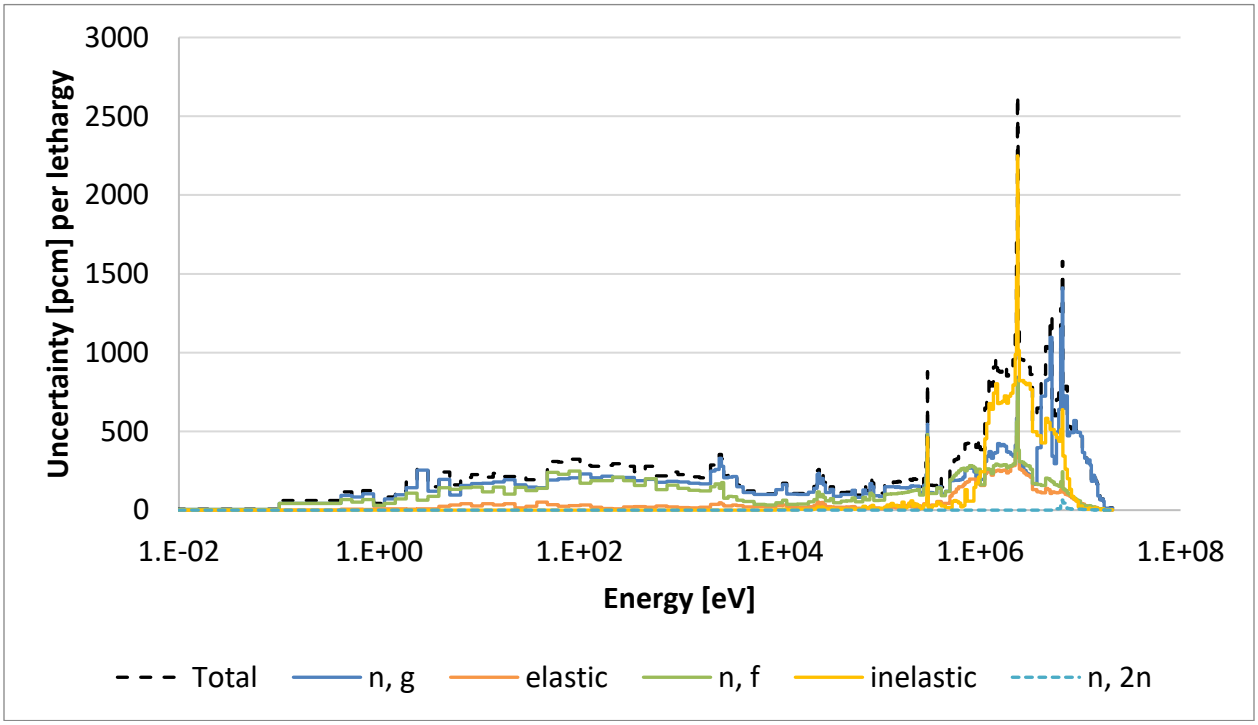

Figure 5.11. Group-wise uncertainty in k_∞ due to uncertainty in each reaction for the RBWR-TB2 unit cell at EOL.

5.3.2. Changes in Reactor State

In addition to the uncertainty in the multiplication factor, the uncertainty in the quantities which depend on k_∞ (including coolant void coefficient, coolant void worth, and control rod worth) was also calculated. The uncertainty in various reactor parameters are summarized in Table 5.7. In all cases, the statistical uncertainty is negligible. The uncertainty contribution from each isotope and reaction when the reactor is flooded and voided is presented in Table 5.3 through Table 5.6, while the breakdown for the change in state is shown in Table 5.8 through Table 5.15.

To elaborate further on the differences between the two sets of tables, Table 5.3 shows the uncertainty in the reactor in the flooded condition, while Table 5.9 shows the uncertainty associated with the transition between reference conditions to the flooded conditions. Since the uncertainty in the nuclear data is fixed between states, Table 5.8 through Table 5.15 effectively show the change in importance for each reaction, weighted by the uncertainty of each reaction.

For the changes to the water density, the spectrum changes significantly influence the uncertainty. Since inelastic scattering is a threshold reaction, the sensitivity to it changes the most compared to other reactions. However, the sensitivity to capture and fission reaction increases, and some higher actinides have relatively high uncertainty (especially ^{241}Am). The control rod worth has very low uncertainty relative to the other changes; even with rods inserted, the uncertainty in the ^{10}B (n,α) reaction is nearly negligible, and the uncertainty from ^{10}B is only greater than 1 pcm when the control rods are inserted.

It should also be noted that the void coefficient of the full core is significantly more negative than in the unit cell model, due to a softer spectrum; it is expected that the uncertainty in the void coefficient would decrease, due to the reduced importance of inelastic scattering with a softer spectrum. Nonetheless, it is expected that the uncertainty will remain on the same order of magnitude.

Table 5.3. Uncertainty in pcm of the multiplication factor due to uncertainty in each reaction in the RBWR-TB2 unit cell at BOL when it is flooded.

Isotope	(n,g)	Elastic	Fission	Inelastic	(n, 2n)	Cross-terms	Total	Ref. Cond.
Am-241	170	3	15	6	0	15	171	108
Am-242m	18	0	45	0	0	n/a	48	39
Am-243	82	1	47	3	0	n/a	94	85
Cm-243	3	0	3	0	0	0	4	3
Cm-244	78	3	21	1	0	5	81	74
Cm-245	44	0	83	1	0	7	94	76
Cm-246	10	0	4	0	0	1	11	11
Cm-247	7	0	9	0	0	2	11	10
Cm-248	1	0	1	0	0	1	1	1
H-1	30	60	n/a	n/a	n/a	n/a	67	62
Np-237	61	0	9	1	0	n/a	61	57
O-16	148	37	n/a	4	n/a	2	153	148

Isotope	(n,g)	Elastic	Fission	Inelastic	(n, 2n)	Cross-terms	Total	Ref. Cond.
Pu-238	153	3	16	1	0	16	154	122
Pu-239	95	6	156	19	1	39	188	188
Pu-240	130	11	52	45	1	29	151	189
Pu-241	137	1	133	5	2	n/a	191	141
Pu-242	139	9	33	9	1	n/a	144	112
U-235	2	0	4	0	0	2	5	10
U-238	55	25	6	36	2	41	82	204
Total	402	77	241	62	3	68	484	471
Ref. Cond.	347	76	204	203	4	110		

Table 5.4. Uncertainty in pcm of the multiplication factor due to uncertainty in each reaction in the RBWR-TB2 unit cell at BOL when it is voided.

Isotope	(n,g)	Elastic	Fission	Inelastic	(n, 2n)	Cross-terms	Total	Ref. Cond.
Am-241	36	2	24	23	0	6	49	108
Am-242m	5	0	52	2	0	n/a	53	39
Am-243	32	1	70	25	0	n/a	81	85
Cm-243	2	0	2	0	0	0	3	3
Cm-244	67	1	36	6	0	0	76	74
Cm-245	25	0	37	4	0	0	45	76
Cm-246	7	0	6	1	0	0	9	11
Cm-247	3	0	2	0	0	0	3	10
Cm-248	0	0	1	0	0	0	1	1
H-1	0	1	n/a	n/a	n/a	n/a	1	62
Np-237	26	0	17	6	0	n/a	32	57
O-16	142	80	n/a	6	n/a	2	163	148
Pu-238	69	2	36	8	0	8	79	122
Pu-239	95	8	123	143	1	46	216	188
Pu-240	191	13	109	267	1	83	356	189
Pu-241	84	2	57	35	1	n/a	108	141
Pu-242	33	7	56	37	1	n/a	75	112
U-235	6	0	2	1	0	1	7	10
U-238	82	57	16	557	1	248	618	204
Total	306	99	214	638	2	266	792	471
Ref. Cond.	347	76	204	203	4	110		

Table 5.5. Uncertainty in pcm of the multiplication factor due to uncertainty in each reaction in the RBWR-TB2 unit cell at EOL when it is flooded.

Isotope	(n,g)	Elastic	Fission	Inelastic	(n, 2n)	Cross-terms	Total	Ref. Cond.
Am-241	88	2	8	3	0	12	89	78

Isotope	(n,g)	Elastic	Fission	Inelastic	(n, 2n)	Cross-terms	Total	Ref. Cond.
Am-242m	11	0	34	0	0	0	36	42
Am-243	55	0	29	3	0	0	62	83
Cm-243	2	0	2	0	0	0	3	3
Cm-244	57	2	15	1	0	4	59	80
Cm-245	28	0	66	1	0	6	72	79
Cm-246	6	0	3	0	0	0	7	10
Cm-247	4	0	6	0	0	2	8	10
Cm-248	0	0	0	0	0	0	1	1
H-1	47	60	0	0	0	0	76	72
Np-237	28	0	4	0	0	0	28	38
O-16	168	8	0	5	0	2	168	159
Pu-238	92	1	10	1	0	3	93	103
Pu-239	131	2	192	14	0	123	264	176
Pu-240	96	5	33	40	1	18	111	165
Pu-241	106	1	161	3	1	0	193	177
Pu-242	120	6	20	7	0	0	122	129
Sm-149	52	0	0	0	0	0	52	20
Sm-151	22	0	0	0	0	0	22	12
U-235	1	0	1	0	0	0	1	1
U-238	120	13	15	152	5	39	199	297
Total	352	63	267	159	5	131	492	515
Ref. Cond.	339	76	234	279	3	110		

Table 5.6. Uncertainty in pcm the multiplication factor due to uncertainty in of each reaction in the RBWR-TB2 unit cell at EOL when it is voided.

Isotope	(n,g)	Elastic	Fission	Inelastic	(n, 2n)	Cross-terms	Total	Ref. Cond.
Am-241	28	2	21	18	0	5	39	78
Am-242m	6	1	66	2	0	0	66	42
Am-243	33	2	75	24	0	0	85	83
Cm-243	2	0	3	1	0	0	3	3
Cm-244	78	2	45	7	0	0	90	80
Cm-245	28	1	47	4	0	0	55	79
Cm-246	8	0	7	2	0	0	11	10
Cm-247	3	0	3	0	0	0	4	10
Cm-248	0	0	1	0	0	0	1	1
H-1	0	1	0	0	0	0	1	72
Np-237	19	0	13	4	0	0	24	38
O-16	142	87	0	7	0	3	167	159
Pu-238	69	3	40	8	0	12	80	103
Pu-239	84	1	115	104	0	6	176	176

Isotope	(n,g)	Elastic	Fission	Inelastic	(n, 2n)	Cross-terms	Total	Ref. Cond.
Pu-240	182	18	120	254	1	91	347	165
Pu-241	88	4	71	39	1	0	120	177
Pu-242	33	4	61	36	0	0	78	129
Sm-149	3	0	0	1	0	0	4	20
Sm-151	5	0	0	1	0	0	5	12
U-235	3	0	1	0	0	0	3	1
U-238	94	33	18	635	1	201	673	297
Total	303	95	230	694	2	221	827	515
Ref. Cond.	339	76	234	279	3	110		

Table 5.7. Uncertainty in the RBWR-TB2 unit cell void coefficient, void collapse worth, void worth, and control rod worth due to uncertainty in the nuclear data.

	Void coefficient [pcm/% void]	**Reactivity insertion from flooding the reactor [pcm]**	**Reactivity insertion from voiding the reactor [pcm]**	**Control rod worth [pcm]**
BOL	10.1 ± 5.7	-2819 ± 222.7	6213 ± 568.8	-6780 ± 51.5
EOL	-7.2 ± 4.5	1350 ± 228.1	5699 ± 563.1	-8028 ± 89.3

Table 5.8. Uncertainty in the void coefficient in pcm/% void for the RBWR-TB2 unit cell at BOL due to uncertainty in each isotope and reaction.

Isotope	(n,g)	Elastic	Fission	Inelastic	(n, 2n)	Cross-terms	Total
Am-241	1.4	0.1	0.1	0.1	0.0	0.1	1.4
Am-242m	0.2	0.0	0.4	0.0	0.0	n/a	0.5
Am-243	0.4	0.0	0.3	0.1	0.0	n/a	0.5
Cm-244	0.6	0.1	0.2	0.0	0.0	0.0	0.6
Cm-245	0.1	0.0	0.7	0.0	0.0	0.1	0.7
Cm-246	0.1	0.0	0.0	0.0	0.0	0.0	0.1
Cm-247	0.0	0.0	0.1	0.0	0.0	0.0	0.1
H-1	1.2	0.1	n/a	n/a	n/a	n/a	1.2
Np-237	0.4	0.0	0.1	0.0	0.0	n/a	0.4
O-16	0.0	0.3	n/a	0.0	0.0	0.0	0.3
Pu-238	1.4	0.1	0.2	0.0	0.0	0.1	1.4
Pu-239	0.8	0.1	1.2	0.8	0.0	0.5	1.7
Pu-240	1.0	0.1	0.5	1.5	0.0	0.5	1.9
Pu-241	0.9	0.0	1.1	0.1	0.0	n/a	1.4
Pu-242	0.8	0.1	0.2	0.2	0.0	n/a	0.8
U-238	0.3	0.3	0.1	3.8	0.0	1.4	4.0
Total	3.0	0.5	1.9	4.1	0.0	1.5	5.7

Table 5.9. Uncertainty in the reactivity insertion in pcm from flooding the reactor for the RBWR-TB2 unit cell at BOL due to uncertainty in each isotope and reaction.

Isotope	(n,g)	Elastic	Fission	Inelastic	(n, 2n)	Cross-terms	Total

Isotope	(n,g)	Elastic	Fission	Inelastic	(n, 2n)	Cross-terms	Total
Am-241	69	7	3	5	0	17	71
Am-242m	6	0	15	0	0	n/a	16
Am-243	20	1	9	4	0	n/a	22
Cm-243	1	0	1	0	0	0	2
Cm-244	27	1	5	1	0	2	27
Cm-245	7	0	34	1	0	3	35
Cm-246	3	0	1	0	0	0	3
Cm-247	1	0	3	0	0	1	4
Cm-248	0	0	0	0	0	0	0
H-1	7	10	n/a	n/a	n/a	n/a	12
Np-237	18	0	3	1	0	n/a	18
O-16	2	11	n/a	1	0	0	11
Pu-238	44	3	5	2	0	9	46
Pu-239	33	1	42	28	0	22	64
Pu-240	44	2	17	65	0	11	81
Pu-241	40	1	44	3	0	n/a	60
Pu-242	39	4	8	9	0	n/a	40
U-235	1	0	1	0	0	1	2
U-238	30	23	6	127	1	74	152
Total	124	28	75	146	1	80	223

Table 5.10. Uncertainty in the reactivity insertion from completely voiding the reactor in pcm for the RBWR-TB2 unit cell at BOL due to uncertainty in each isotope and reaction.

Isotope	(n,g)	Elastic	Fission	Inelastic	(n, 2n)	Cross-terms	Total
Am-241	104	9	6	13	0	23	108
Am-242m	12	0	39	1	0	n/a	41
Am-243	59	1	15	18	0	n/a	63
Cm-243	1	0	1	0	0	0	2
Cm-244	49	2	12	4	0	3	51
Cm-245	27	0	49	2	0	4	56
Cm-246	6	0	2	1	0	1	7
Cm-247	4	0	6	0	0	1	7
Cm-248	0	0	0	0	0	0	1
H-1	36	49	n/a	n/a	n/a	n/a	61
Np-237	40	0	6	4	0	n/a	41
O-16	4	106	n/a	1	0	1	106
Pu-238	108	1	17	5	0	5	109
Pu-239	69	3	128	100	0	47	182
Pu-240	95	5	57	162	0	29	198
Pu-241	100	2	92	37	1	n/a	141
Pu-242	94	6	16	20	0	n/a	98
U-235	5	0	5	0	0	3	8

Isotope	(n,g)	Elastic	Fission	Inelastic	(n, 2n)	Cross-terms	Total
U-238	64	13	4	397	2	89	412
Total	263	118	181	443	2	108	569

Table 5.11. Uncertainty in the control rod worth in pcm for the RBWR-TB2 unit cell at BOL due to uncertainty in each isotope and reaction.

Isotope	(n,g)	Elastic	Fission	Inelastic	(n, 2n)	Cross-terms	Total
Am-241	13	2	2	2	0	4	14
Am-242m	2	0	4	0	0	n/a	4
Am-243	6	1	6	1	0	n/a	9
B-10	5[17]	1	n/a	6	n/a	1	8
Cm-243	0	0	0	0	0	0	0
Cm-244	5	1	3	1	0	0	6
Cm-245	3	0	5	0	0	1	6
Cm-246	1	0	0	0	0	0	1
Cm-247	0	0	0	0	0	0	1
Cm-248	0	0	0	0	0	0	0
H-1	10	8	n/a	n/a	n/a	n/a	13
Np-237	5	0	1	0	0	n/a	5
O-16	0	6	n/a	1	0	0	6
Pu-238	13	1	2	0	0	2	14
Pu-239	8	1	9	8	0	5	15
Pu-240	8	1	7	16	0	2	19
Pu-241	9	1	7	1	0	n/a	12
Pu-242	9	2	5	3	0	n/a	11
U-235	1	0	2	0	0	1	2
U-238	21	2	1	21	1	9	31
Total	36	11	18	27	1	12	51

Table 5.12. Uncertainty in the void coefficient in pcm/% void for the RBWR-TB2 unit cell at EOL due to uncertainty in each isotope and reaction.

Isotope	(n,g)	Elastic	Fission	Inelastic	(n, 2n)	Cross-terms	Total
Am-241	0.7	0.1	0.1	0.1	0.0	0.2	0.7
Am-242m	0.1	0.0	0.3	0.0	0.0	n/a	0.3
Am-243	0.2	0.0	0.4	0.1	0.0	n/a	0.4
Cm-244	0.6	0.1	0.2	0.1	0.0	0.0	0.6
Cm-245	0.2	0.0	0.6	0.0	0.0	0.1	0.6
Cm-246	0.1	0.0	0.0	0.0	0.0	0.0	0.1
Cm-247	0.0	0.0	0.1	0.0	0.0	0.0	0.1
H-1	0.4	0.3	n/a	n/a	n/a	n/a	0.5
Np-237	0.2	0.0	0.1	0.0	0.0	n/a	0.2

[17] The (n,α) reaction is summarized here, as the ^{10}B (n,g) reaction is negligible.

Isotope	(n,g)	Elastic	Fission	Inelastic	(n, 2n)	Cross-terms	Total
O-16	0.2	0.1	n/a	0.0	0.0	0.0	0.2
Pu-238	0.7	0.1	0.2	0.0	0.0	0.0	0.7
Pu-239	1.0	0.0	1.2	0.5	0.0	1.0	1.9
Pu-240	0.9	0.2	0.6	1.1	0.0	0.6	1.7
Pu-241	0.6	0.0	1.0	0.1	0.0	n/a	1.2
Pu-242	0.6	0.1	0.3	0.2	0.0	n/a	0.7
Sm-149	0.4	0.0	n/a	0.0	0.0	n/a	0.4
Sm-151	0.2	0.0	n/a	0.0	0.0	n/a	0.2
U-238	0.4	0.4	0.0	2.6	0.0	1.3	3.0
Total	2.1	0.5	1.9	2.9	0.0	1.8	4.5

Table 5.13. Uncertainty in the reactivity insertion from flooding the reactor measured in pcm for the RBWR-TB2 unit cell at EOL due to uncertainty in each isotope and reaction.

Isotope	(n,g)	Elastic	Fission	Inelastic	(n, 2n)	Cross-terms	Total
Am-241	19	5	6	4	0	6	22
Am-242m	5	0	16	0	0	n/a	17
Am-243	11	1	24	3	0	n/a	26
Cm-243	1	0	1	0	0	0	1
Cm-244	26	1	13	1	0	1	29
Cm-245	21	0	22	1	0	3	30
Cm-246	3	0	2	0	0	0	4
Cm-247	2	0	2	0	0	0	3
Cm-248	0	0	0	0	0	0	0
H-1	32	11	n/a	n/a	n/a	n/a	34
Np-237	13	0	4	0	0	n/a	14
O-16	9	10	n/a	1	0	0	14
Pu-238	24	2	10	1	0	2	26
Pu-239	75	3	83	17	0	83	141
Pu-240	48	4	31	51	0	17	79
Pu-241	27	1	36	4	0	n/a	45
Pu-242	10	2	18	8	0	n/a	22
Sm-149	34	0	n/a	0	0	n/a	34
Sm-151	14	0	n/a	0	0	n/a	14
U-235	0	0	0	0	0	0	1
U-238	34	17	0	109	2	58	130
Total	121	23	105	123	2	103	228

Table 5.14. Uncertainty in the reactivity insertion from completely voiding the reactor measured in pcm for the RBWR-TB2 unit cell at EOL due to uncertainty in each isotope and reaction.

Isotope	(n,g)	Elastic	Fission	Inelastic	(n, 2n)	Cross-terms	Total
Am-241	76	3	7	11	0	10	77
Am-242m	9	1	50	2	0	n/a	51

Isotope	(n,g)	Elastic	Fission	Inelastic	(n, 2n)	Cross-terms	Total
Am-243	60	1	23	18	0	n/a	67
Cm-243	1	0	2	0	0	0	2
Cm-244	62	3	19	5	0	4	65
Cm-245	24	0	57	3	0	3	62
Cm-246	6	1	3	1	0	0	7
Cm-247	4	0	7	0	0	1	8
Cm-248	0	0	0	0	0	1	1
H-1	15	70	n/a	n/a	n/a	n/a	71
Np-237	27	0	6	3	0	n/a	28
O-16	17	89	n/a	1	0	0	91
Pu-238	91	4	22	5	0	10	95
Pu-239	76	5	149	75	0	32	186
Pu-240	107	11	72	167	0	56	219
Pu-241	116	2	133	43	0	n/a	182
Pu-242	114	7	23	21	0	n/a	118
Sm-149	20	0	n/a	1	0	n/a	20
Sm-151	11	0	n/a	1	0	n/a	12
U-235	2	0	0	0	0	0	2
U-238	65	16	3	377	2	95	395
Total	268	115	231	423	2	116	575

Table 5.15. Uncertainty in the control rod worth measured in pcm for the RBWR-TB2 unit cell at EOL due to uncertainty in each isotope and reaction.

Isotope	(n,g)	Elastic	Fission	Inelastic	(n, 2n)	Cross-terms	Total
Am-241	3	2	3	1	0	1	5
Am-242m	1	0	5	0	0	n/a	5
Am-243	0	1	11	1	0	n/a	11
B-10	5[18]	1	n/a	6	n/a	1	8
Cm-243	0	0	0	0	0	0	0
Cm-244	1	0	5	1	0	0	5
Cm-245	1	0	4	0	0	1	5
Cm-246	0	1	1	0	0	0	1
Cm-247	0	0	1	0	0	0	1
Cm-248	0	0	0	0	0	0	0
H-1	9	5	n/a	n/a	n/a	n/a	11
Np-237	2	0	2	0	0	n/a	3
O-16	5	26	n/a	0	0	0	26
Pu-238	2	1	4	0	0	1	5
Pu-239	18	2	19	3	0	20	33
Pu-240	8	4	10	8	0	7	17

[18] The (n,α) reaction is summarized here, as the ^{10}B (n,g) reaction is negligible.

Isotope	(n,g)	Elastic	Fission	Inelastic	(n, 2n)	Cross-terms	Total
Pu-241	5	1	9	2	0	n/a	11
Pu-242	7	3	8	2	0	n/a	11
Sm-149	5	0	n/a	0	0	n/a	5
Sm-151	3	0	n/a	0	0	n/a	3
U-235	0	0	0	0	0	0	0
U-238	31	6	2	60	1	25	72
Total	40	28	29	60	1	33	89

5.3.3. Uncertainty in k_∞ due to Uncertainty in the Void Fraction

The uncertainty due to the uncertainty in the void fraction correlation was also calculated. The uncertainty corresponding to a superficial liquid velocity of 1.0 m/s in Table 4 of [44] was used, as the superficial liquid velocity exceeded 1.0 at all points. It should be noted that there is not much experimental data for such tight lattices, and that a 10% difference is observed compared to the limited experimental data [58]; therefore, to bound the uncertainty, the uncertainty in k_∞ assuming a constant 10% uncertainty in the void fraction was also assumed as a bounding case. The uncertainty is presented in Table 5.16, while Figure 5.12 shows the sensitivity coefficients. Figure 5.13 through Figure 5.16 show the relative water density covariance at the different conditions.

For most of the seed sections, an increase in the water density corresponds to a reduction in k_∞, indicating positive local water density feedback. This is due to the significantly enhanced fast fission probability when the coolant voids. Within the internal blanket and in the reflectors, the sensitivity coefficient switches sign, as an increase in local density would result in more reflection back to the seed. At BOL, the sensitivity coefficient and covariance is nearly zero everywhere outside of the upper seed, since that is where the power is concentrated; however, at EOL, the power is more balanced between the seeds, and the magnitude of the sensitivity coefficient is large throughout the entire fuel. Since the sign switches many times in the fuel, the uncertainty from each section nearly cancels out, and the uncertainty due to uncertainty in the water density distribution is nearly zero at EOL.

Table 5.16. Uncertainty in k_∞ due to void fraction uncertainty for the RBWR-TB2.

Burnup	**Uncertainty using** [44] **for α uncertainty [pcm]**	**Uncertainty assuming 10% α uncertainty [pcm]**
BOL	86.6	119.0
EOL	0.8	33.6

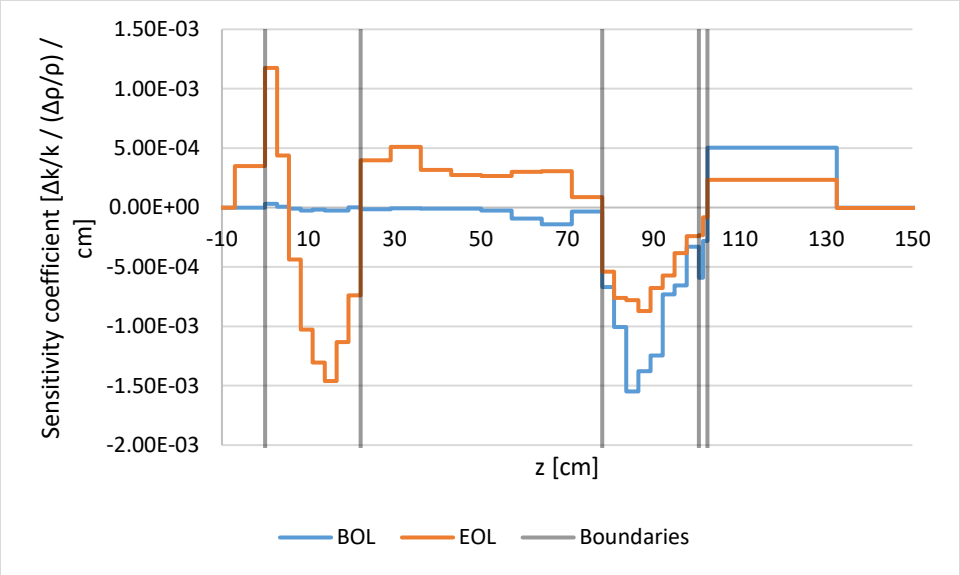

Figure 5.12. Sensitivity coefficients for the multiplication factor of the RBWR-TB2 due to a relative change in water density.

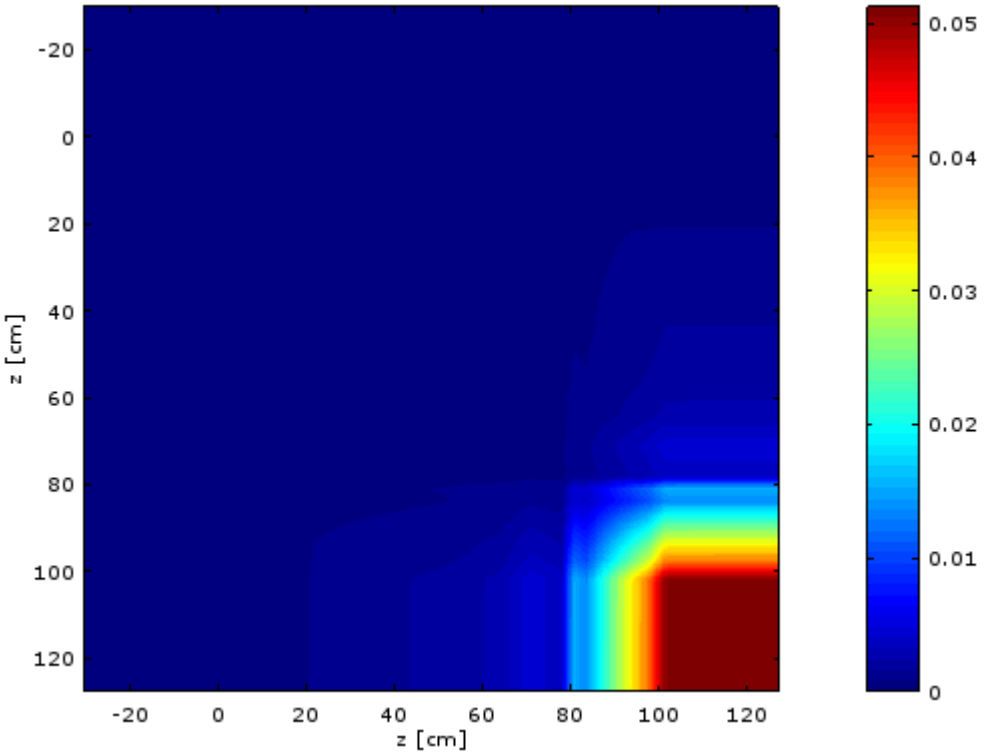

Figure 5.13. Relative water density covariance plot for the RBWR-TB2 at BOL assuming void fraction uncertainty as specified in [44].

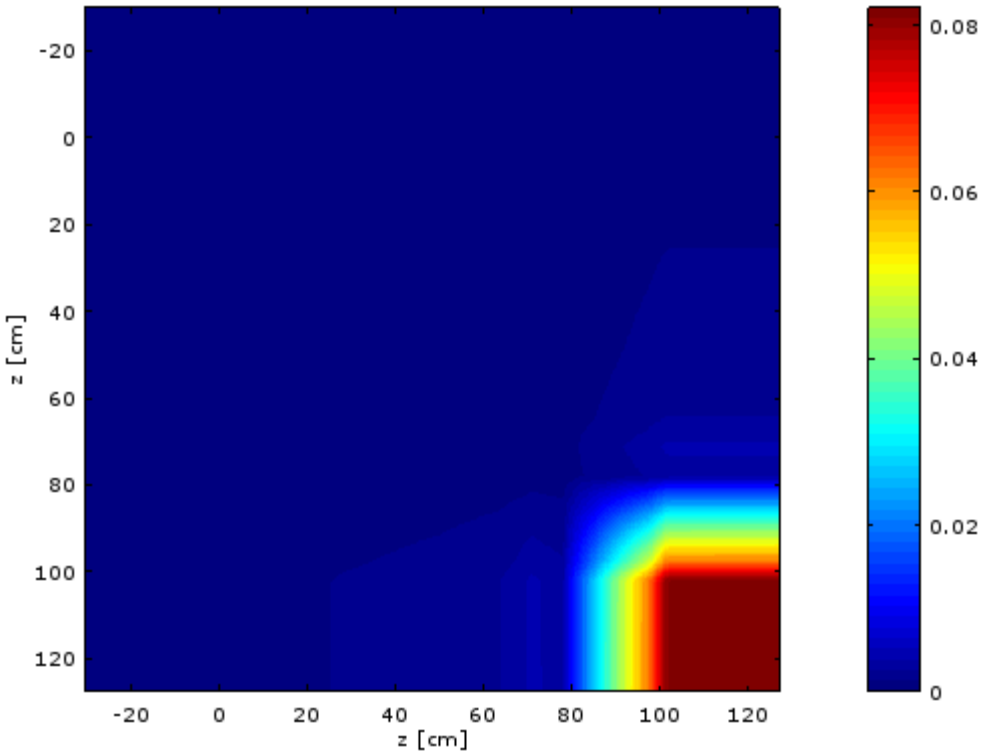

Figure 5.14. Relative water density covariance plot for the RBWR-TB2 at BOL assuming 10% void fraction uncertainty.

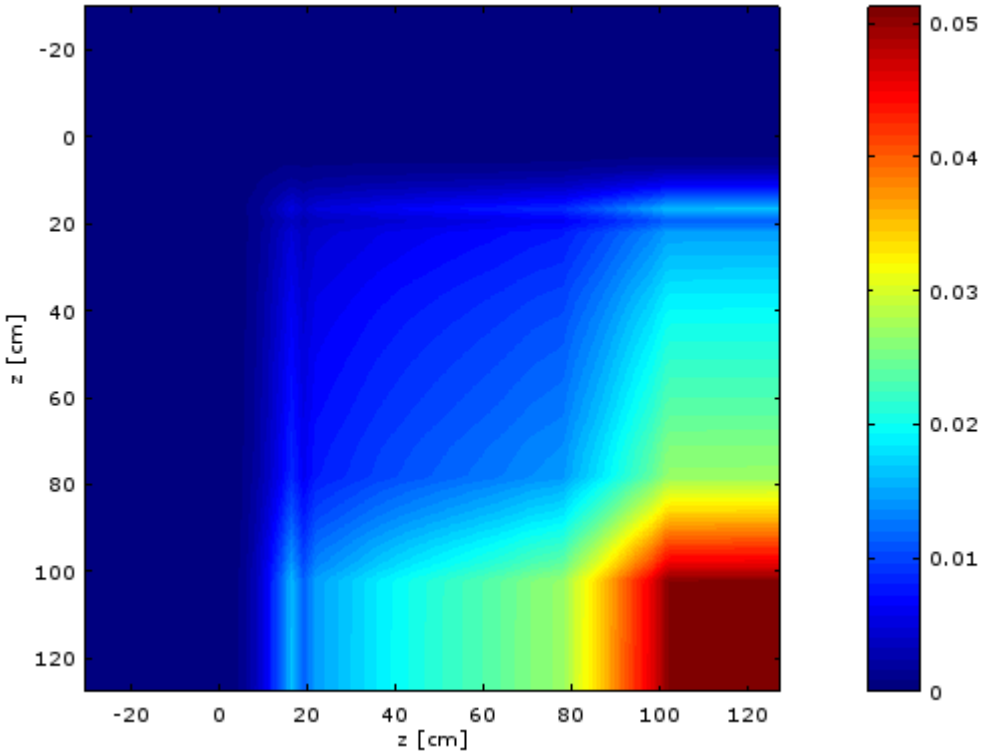

Figure 5.15. Relative water density covariance plot for the RBWR-TB2 at EOL assuming void fraction uncertainty as specified in [44].

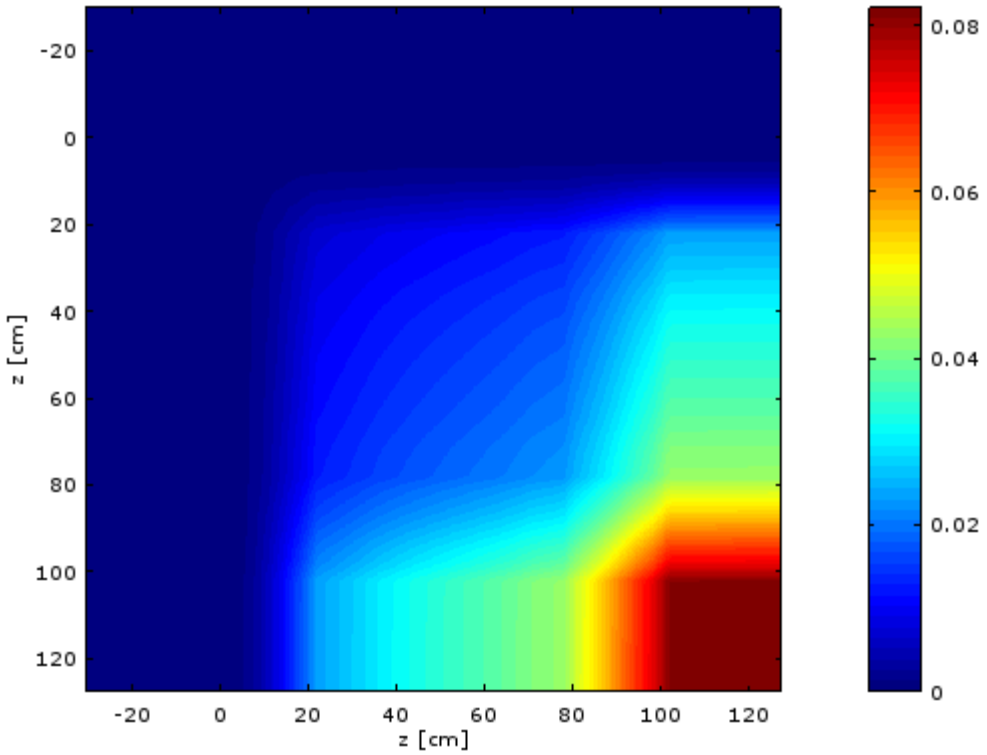

Figure 5.16. Relative water density covariance plot for the RBWR-TB2 at EOL assuming 10% void fraction uncertainty.

5.4. Fine Mesh Coupled Neutronics-T/H Analysis

Since the 1-D OpenFOAM/Serpent coupled code system does not use any finite differences (unlike PARCS/PATHS [32]), it is not required to have similarly sized cells near each other. Therefore, it was decided to use a very fine mesh where the power spikes near the seed interfaces for the RBWR-TB2 unit cell in order to determine the peak LHGR and the peak fuel temperatures in those locations.

The RBWR-TB2 unit cell was assessed at BOL and EOL. The top and bottom 1 mm of each of the seeds was split into 100 equally sized cells for the power density binning from Serpent and for the T/H calculation in OpenFOAM. The LHGR at BOL and EOL are shown in Figure 5.17 and Figure 5.18. The average fuel temperature is shown in Figure 5.19 and Figure 5.20, and the peak fuel temperature is shown in Figure 5.21 and Figure 5.22. Although the BOL results are far more peaked, the full core results tend to more closely resemble the EOL results.

It is found that the LHGR and, therefore, fuel temperature, spike at the seeds interface with the blankets or reflector. The largest spiking is located at the top of the upper seed. This spiking is due to the large flux of neutrons that slow down in the lower section of the upper reflector that are reflected back to the core. Since each bin is very small and Serpent uses a collision-based method to track reactions in each bin, the statistical uncertainty on each bin is somewhat high, which leads to some of the "fuzzing" seen in Figure 5.18, Figure 5.20, and Figure 5.22; this should not change the conclusions, though.

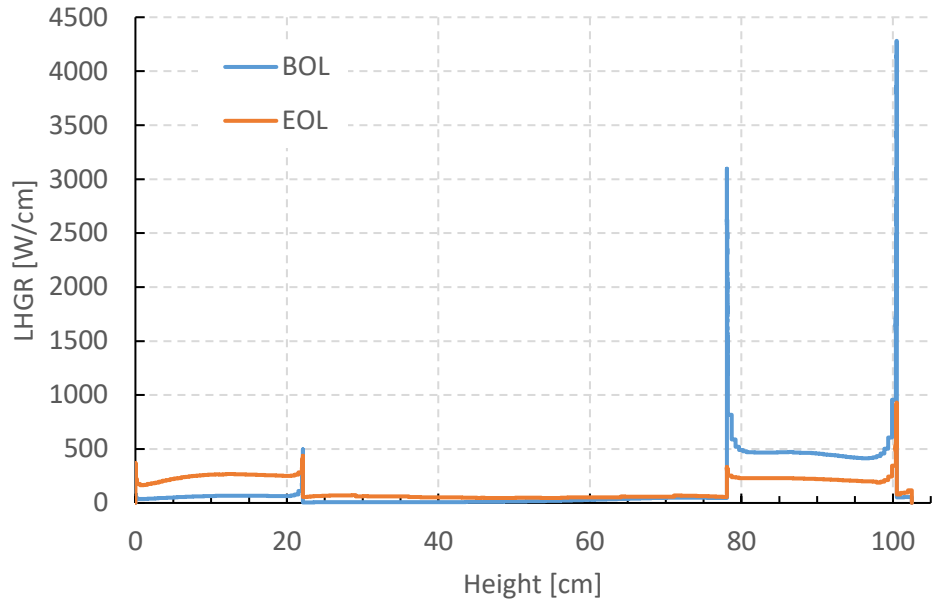

Figure 5.17. LHGR for the RBWR-TB2 unit cell at BOL and EOL.

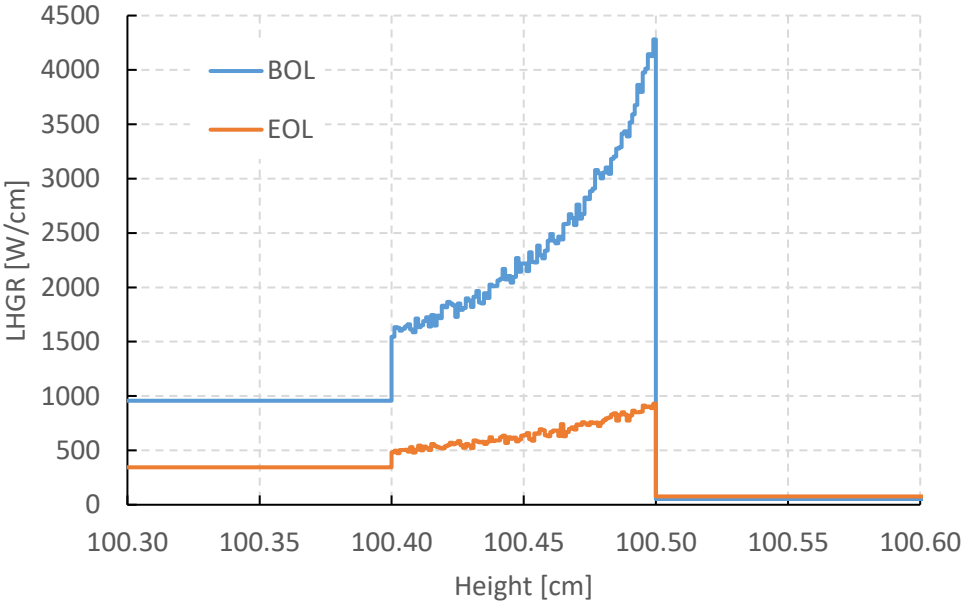

Figure 5.18. LHGR for the RBWR-TB2 at BOL and EOL, zoomed in at the upper blanket interface where both peak temperatures occurred.

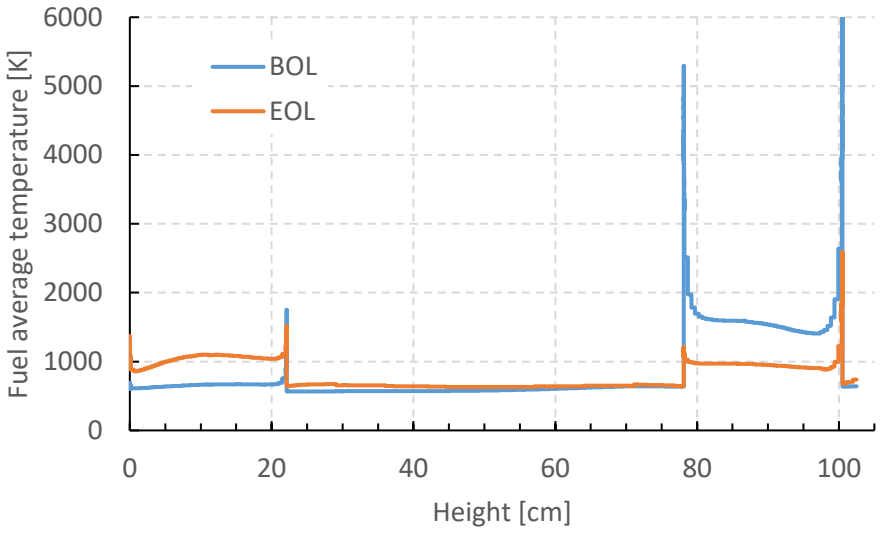

Figure 5.19. Average fuel temperature for the average RBWR-TB2 fuel pin at BOL and EOL.

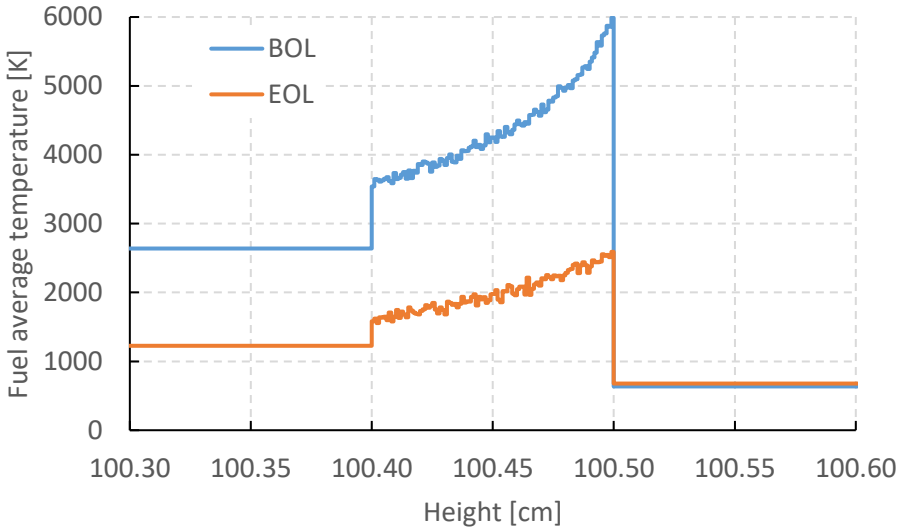

Figure 5.20. Average fuel temperature for the average RBWR-TB2 fuel pin at BOL and EOL, zoomed in to the interface with the upper blanket, where the peak temperature occurs.

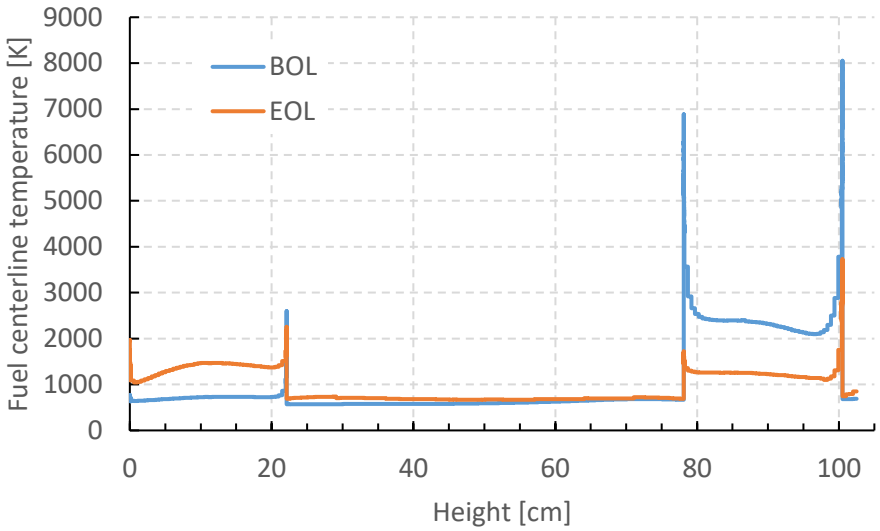

Figure 5.21. Centerline fuel temperature for the average RBWR-TB2 fuel pin at BOL and EOL.

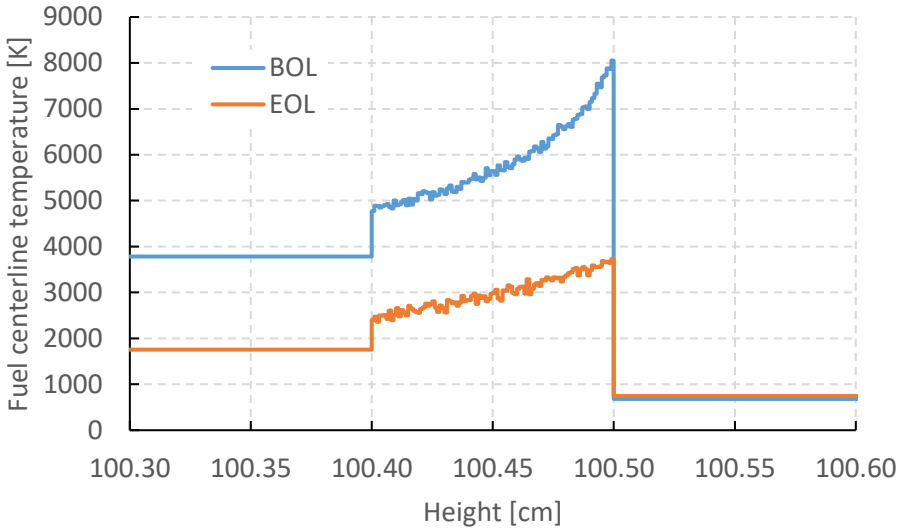

Figure 5.22. Centerline fuel temperature for the average RBWR-TB2 fuel pin at BOL and EOL, zoomed in to the upper blanket interface where the peak temperatures occur.

5.4.1. Estimation of Axial Conduction

The results above are not bounding, since axial conduction will reduce the peak temperatures. In order to approximately estimate the impact of axial conduction, a separate case was run at BOL with small change to the solver such that the $k_{fuel} \frac{d^2 T_{ave}}{dz^2}$ term was added to the power density (right hand side of the equation in Section 2.7.1), and iterated until it converged. Due to the very high magnitudes of the second derivative, the axial mesh was uniformly 0.5 mm to prevent negative power densities. Using the coarser mesh, the peak centerline fuel temperature was 4344.6 K; with the adjustments for axial heat conduction, the peak centerline temperature was

4223.1 K. While this is a very rough approximation of the effects of axial conductance, it is not expected that the fuel could avoid melting due to axial heat conduction.

5.4.2. Impact of Radial Peaking

It is expected that the peak power pin would experience a power that is 40% higher than the average power (assuming a 1.1 pin peaking factor, 5% overpower, and a 1.25 assembly peaking factor). Using the relations in Section 2 of Reference [40], the melting temperature of 66% Pu MOX is 2805 K. Using the BOL power distribution for the peak pin, 13.3 cm of the upper seed would be over 3000 K, and the peak temperature was over 10000 K.

The EOL power distribution is more favorable, and only 1 mm of the upper seed is above 3000 K, with a peak temperature of 4378 K. However, the lower seed temperature also peaks at 2915 K, indicating that there is no room for any power shift in either seed. Considering that the EOL power distribution is the most optimistic as it maximizes the power in the blankets and it still experiences some fuel melt, a design change will be necessary to avoid fuel melt.

5.4.3. Discussion of LHGR Spiking

In order to properly mitigate these LHGR spikes, it is important to know what are causing them. In order to assess the cause, the spectra of neutrons which cause fission which taken at different intervals within each seed in each simulation. The spectrum of neutrons inducing fission for the RBWR-TB2 at BOL over selected locations in the upper seed is shown in Figure 5.23, while the probability of a neutron being absorbed vs. energy and travel length in the fuel is shown in Figure 5.24.

Within the blanket regions, the thermal cross section is much lower than in the seed, since the fertile isotopes have a significantly smaller thermal cross section than the fissile isotopes, and there are relatively few fast neutrons being born from fission within the blankets. The neutrons in the reflector similarly slow down before being reflected back. At the interface with the seed, the abrupt change in composition causes an abrupt change in power, which exponentially attenuates as the thermal neutrons are absorbed in the seed.

In Figure 5.24, it shows that the biggest spike in absorption probability corresponds to the lowest energy ^{240}Pu resonance at 1 eV. Additionally, it shows that almost half of the thermal neutrons outside of the 0.3 eV ^{239}Pu resonance are absorbed after travelling 1 mm in fuel, while approximately 90% of the neutrons in peak are absorbed within 1 mm. Figure 5.23 shows that these 0.3 eV neutrons cause the largest spike within the top 10 μm of the seed, but that 1 mm away, this resonance is not as important. Since the LHGR and the fuel temperature are unacceptably high more than 1 mm away from the seed interface (as seen in Figure 5.18 and Figure 5.22), a similar phenomenon would occur in thorium-fueled design variants if they employed short seed sections with high average enrichments.

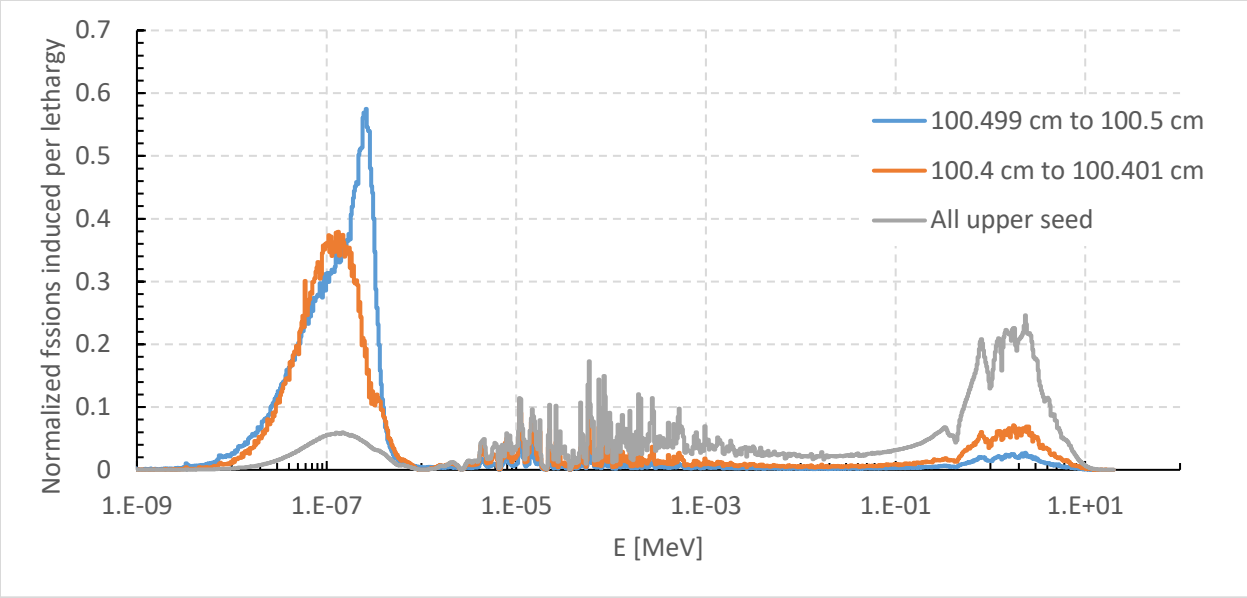

Figure 5.23. Spectrum in the upper seed for the RBWR-TB2 at BOL.

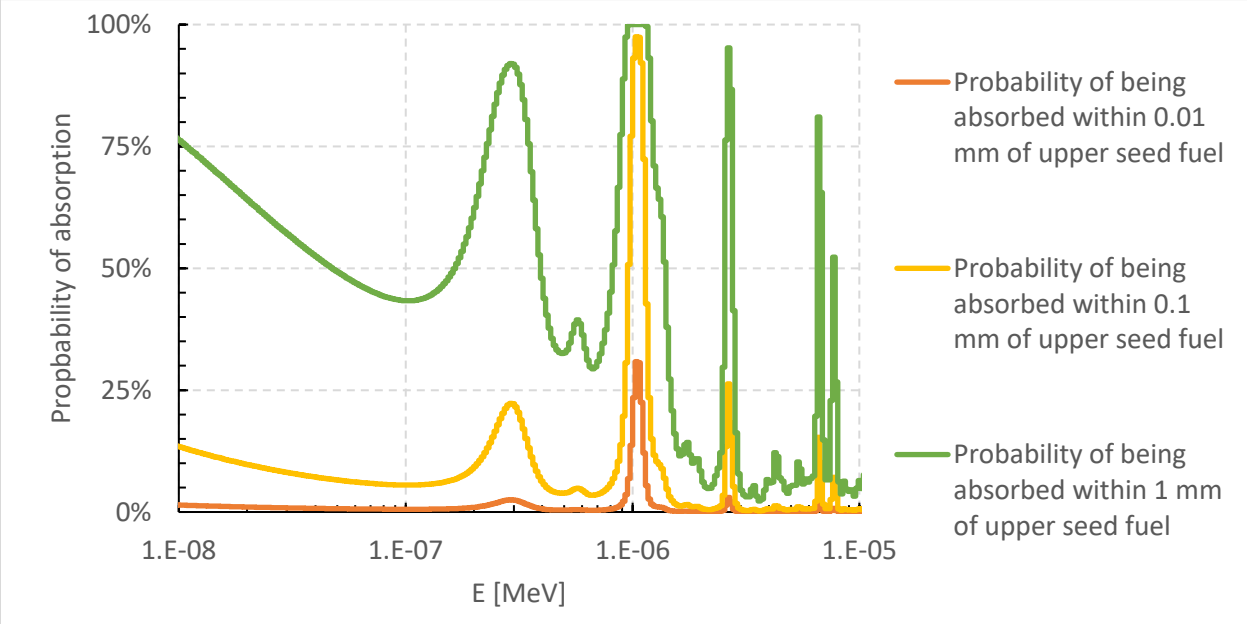

Figure 5.24. Probability of absorption in the RBWR-TB2 at BOL in the upper seed. The probabilities quoted are the probability of being absorbed after travelling the quoted distance; for example, a 1.03 eV neutron has a 31% chance of being absorbed within 0.01 mm of travel in the upper seed.

Since the peaks are caused by the leaking thermal flux from the reflectors, lengthening the blanket sections between the reflectors and the seed would help reduce the peaks with a minimal impact on k_{eff}. However, this will only help after burnup is accrued, since it relies on plutonium building up within the blankets; Figure 5.21 shows a similar peak at the interface with the internal blanket at BOL. A thermal absorber can be added to the seeds near the interfaces, but this will reduce the cycle length, and the RBWR-TB2 already has a cycle length shorter than a

year, which is unattractive. The most promising option is to smear the boundary between the seeds and the blankets by using a gradually changing enrichment; future work will assess the impact of this change on the void feedback, burnup, and TRU transmutation rate.

5.5. RBWR-TB2 Conclusions

The RBWR-TB2 unit cell was analyzed, and the uncertainty in many reactor parameters were found using GPT.

However, some issues were found with these two reactors. The control rods have relatively little impact on k_{eff} until they are nearly fully inserted, yet they have a large effect on the axial power profile and axial peaking factor. This is due to the weak coupling between the seeds. Finally, even in normal operation, the fuel experiences very sharp power and temperature spikes near the seed interfaces due to the sharply differing spectra in the seeds and the rest of the fuel assembly. It is expected that the fuel will melt unless design changes are implemented to mitigate these peaks.

6. Conclusions and Future Work

This dissertation examined the design and feasibility of Resource-renewable Boiling Water Reactors (RBWRs), especially focusing on thorium-based design variants. Assembly and core designs were developed, and their fuel cycle impacts (including the fuel cycle costs) were assessed. Additionally, the uncertainty in the multiplication factor due to nuclear data and thermal-hydraulic uncertainty was quantified.

The self-sustaining RBWR-SS was designed to maximize the attainable burnup while meeting the required safety constraints. It was able to achieve comparable performance to the Hitachi-designed RBWR-AC while avoiding some of the feasibility issues associated with using multiple high-enrichment seeds. However, it was found that if more conservative thermal hydraulic assumptions were adopted (i.e. using the LPG correlation for void fraction and the MFP-CISE correlation for critical power [26]), then a self-sustaining fuel cycle was not attainable. Additionally, a pure thorium design was not feasible, due to insufficient shutdown margin from the strongly negative coolant void feedback; in order to keep the void coefficient as close to zero as possible, between 30% and 50% of the feed consisted of depleted uranium. Unfortunately, it was found that it was not possible to keep the void coefficient negative while maintaining sufficient shutdown margin due to the large Doppler feedback from using a single elongated seed. The waste characteristics are mostly favorable; although the fuel is more radiotoxic than waste from an analogous SFR, it is still very good since it is a completely self-sufficient fuel cycle. Additionally, the uranium from the fuel is significantly denatured by the addition of the depleted uranium in the feed, but it is still not considered LEU.

The low-conversion RBWR-TR was designed to maximize the TRU consumption rate while sustaining a reasonable cycle length in addition to the required safety constraints. The spectrum of the RBWR-TR is significantly more thermal than the spectrum of the RBWR-SS design, but it is still an epithermal spectrum. Unfortunately, it was not found to be able to sustain sufficient shutdown margin while maintaining negative void feedback. Nonetheless, it is anticipated that a design which meets the constraints could be made if either a multi-seed approach is adopted or if the conversion ratio were increased. The repository impacts of the RBWR-TR were dominated by the TRU consumption rate; therefore, changing the conversion ratio would have significant impacts on this assessment. Since the RBWR-TR could reach approximately the same discharge burnup as the RBWR-TB2 with a much higher coolant flow rate and approximately the same transmutation efficiency, it is not expected that DU is significantly better than Th in the feed makeup; if sufficient shutdown margin can be obtained using multiple seeds, then thorium would likely be preferable since it has had significantly better thermal margins for transients.

As a whole, the thorium RBWRs feature significantly larger uncertainty than the Hitachi designs. The uncertainty in ^{233}U fission is very large in the intermediate spectrum, and the uncertainty from ^{232}Th increases significantly when the spectrum hardens. In general, the uncertainty was reduced when the spectrum softened. Additionally, the thorium RBWRs feature larger uncertainty due to the void fraction uncertainty; the multi-seed design of the Hitachi RBWRs helps mitigate the uncertainty since the k_{eff} sensitivity to local water density changes signs many times throughout the fuel, which leads the uncertainty to cancel out rather than build upon itself.

As part of a contract with Hitachi, further analysis was performed for the RBWR-TB2. Although the analysis for the RBWR-TB2 was performed at the assembly level rather than the full core, the analyses uncovered a few causes for concern. The use of two seeds which are nearly independent causes the control rod worth to be very low for most of the fuel length and then increase rapidly in the upper seed, which may pose problems for controlling the reactor.

Most importantly, it was shown that there is significant enough power spiking in the Hitachi-designed RBWRs to melt the fuel over small lengths. The neutron spectrum leaking back from the reflectors is much more thermal than the spectrum in the seeds, which leads to a sharp peak in the linear heat rate in the seed boundaries. Although the length of the fuel which is affected by the peak is small, it is a sharp enough peak to induce melting in the RBWR-TB2 fuel at all burnups, with an estimated peak temperature that is over 10,000 K. This issue can almost certainly be overcome with design changes, but any design change will penalize the core performance.

There is a lot of future work associated with the RBWR projects. As noted above, the current designs do not meet the shutdown margin constraint. It is expected that adopting a multi-seed approach (as used in the DU-fueled designs) would help by reducing the magnitude of the Doppler feedback. Alternatively, reducing the assembly size and increasing the control blade thickness would help, although this would reduce the burnup. Lastly, the power could be reduced, although this would significantly hurt the economics of the design.

Transient analysis should also be performed for the final designs. It is anticipated that the thorium design variants will perform at least as well as their uranium-fueled counterparts due to their lower linear heat rates. A full economic analysis (including capital costs and operation and maintenance costs) would also be beneficial to assess the levelized cost of electricity.

References

[1] R. Wigeland, T. Taiwo, H. Ludewig, M. Todosow, W. Halsey, J. Gehin, R. Jubin, J. Buelt, S. Stockinger, K. Jenni, and B. Oakley, "Nuclear Fuel Cycle Evaluation and Screening – Final Report," 2014.

[2] U.S. Energy Information Agency, "International Energy Outlook 2013," 2013.

[3] E. Greenspan, "A phased development of breed-and-burn reactors for enhanced nuclear energy sustainability," *Sustainability*, vol. 4, no. 10, pp. 2745–2764, 2012.

[4] E. A. Hoffman, W. S. Yang, and R. N. Hill, "Preliminary Core Design Studies for the Advanced Burner Reactor over a Wide Range of Conversion Ratios," 2006.

[5] A. E. Dubberley, K. Yoshida, C. E. Boardman, and T. Wu, "Superprism Oxide and Metal Fuel Core Designs," in *ICONE 8*, 2000.

[6] IAEA, "Status of advanced light water reactor designs 2004," 2004.

[7] T. Hino, M. Ohtsuka, R. Takeda, J. Miwa, and Y. Ishii, "Core Designs of RBWR (Resource-renewable BWR) for Recycling and Transmutation of Transuranium Elements - an Overview," in *ICAPP 2014*, 2014, pp. 1–8.

[8] GE Hitachi Nuclear Energy, "The ABWR Plant General Description." pp. A1–A2, 2007.

[9] EPRI, "Technical Evaluation of the Hitachi Resource- Renewable BWR (RBWR) Design Concept 2012," 2012.

[10] OECD NEA, "Java-based Nuclear Data Information System (JANIS) 4.0," 2013. [Online]. Available: https://www.oecd-nea.org/janis/.

[11] T. K. Kim, W. S. Yang, C. Grandy, and R. N. Hill, "Core design studies for a 1000 MWth Advanced Burner Reactor," *Ann. Nucl. Energy*, vol. 36, no. 3, pp. 331–336, 2009.

[12] N. Todreas and M. Kazimi, *Nuclear Reactor Systems*. 2012.

[13] J. G. Collier and J. R. Thome, *Convective Boiling and Condensation*. 1996.

[14] K. Shirvan, N. Andrews, and M. S. Kazimi, "Best Estimate Void Fraction and Critical Power Correlations for Tight Lattice BWR Bundles," in *Proceedings of ICAPP 2013*, 2013.

[15] J. J. Duderstadt and L. J. Hamilton, *Nuclear Reactor Analysis*. 1976.

[16] G. Zhang, M. Fratoni, J. Vujic, and E. Greenspan, "Compact Sodium-cooled Fast Reactor with Thorium Breed and Burn Blanket Guanheng," in *ANS Winter Meeting 2015*, 2015.

[17] F. Ganda, F. J. Arias, J. Vujic, and E. Greenspan, "Self-Sustaining Thorium Boiling Water Reactors," *Sustainability*, vol. 4, pp. 2472–2497, 2012.

[18] C. R. Varela, J. E. Seifried, J. L. Vujic, and E. Greenspan, “Sensitivity of Thorium-Fueled Reduced Moderation BWR Performance to Void Fraction Correlation,” in *Proceedings of the 2013 American Nuclear Society Annual Meeting*, 2013.

[19] G. Zhang, J. Seifried, J. Vujic, and E. Greenspan, “Variable Enrichment Thorium-Fueled Boiling Water Breeder Reactor,” in *Proceedings of the 2013 American Nuclear Society Annual Meeting*, 2013.

[20] B. A. Lindley, F. Franceschini, and G. T. Parks, “The closed thorium – transuranic fuel cycle in reduced-moderation PWRs and BWRs,” *Ann. Nucl. Energy*, vol. 63, pp. 241–254, 2014.

[21] B. A. Lindley, F. Franceschini, and G. T. Parks, “Transmutation, Burn-Up and Fuel Fabrication Trade-Offs in Reduced-Moderation Water Reactor Thorium Fuel Cycles,” in *Waste Management Symposia 2013*, 2013.

[22] B. A. Lindley, “The use of reduced-moderation light water reactors for transuranic isotope burning in thorium fuel,” University of Cambridge, 2014.

[23] B. R. Herman, “Cross section generation strategy for high conversion light water reactors,” Massachusetts Institute of Technology, 2011.

[24] A. Hall, Y. Xu, A. Ward, T. Downar, K. Shirvan, and M. Kazimi, “Advanced Neutronics Methods for Analysis of the RBWR-AC,” in *Proceedings of the 2013 American Nuclear Society Annual Meeting*.

[25] The RELAP5-3D Code Development Team, “RELAP5-3D © Code Manual Volume IV : Models and Correlations,” 2012.

[26] K. Shirvan, Y. Wu, and M. S. Kazimi, “Thermal Hydraulic Recommendation Update For the Resource Renewable BWR (RBWR),” 2014.

[27] J. E. Seifried, P. M. Gorman, J. L. Vujic, and E. Greenspan, “Accelerated equilibrium core composition search using a new MCNP-based simulator,” in *SNA + MC 2013*, 2013.

[28] X-5 Monte Carlo Team, “MCNP — A General Monte Carlo N-Particle Transport Code, Version 5.” 2005.

[29] A. G. Croff, “A User’s Manual for the ORIGEN2 Computer Code.” .

[30] A. Wysocki, Y. Xu, A. Manera, B. Collins, and T. Downar, “PATHS : PARCS Advanced Thermal Hydraulic Solver,” pp. 1–42, 2012.

[31] M. B. Chadwick, P. Oblozinsky, M. Herman, N. M. Greene, R. D. McKnight, D.L.Smith, P. G. Young, R. E. MacFarlane, G. M. Hale, S. C. Frankle, A. C. Kahler, T. Kawano, R. C. Little, D. G. Madland, P. Moller, R. D. Mosteller, P. R. Page, P. Talou, H. Trellue, M. C. White, W. B. Wilson, R. Arcilla, C. L. Dunford, S. F. Mughabghab, B. Pritychenko, D. Rochman, A. A. Sonzogni, C. R. Lubitz, T. H. Trumbull, J. P. Weinman, D. A. Brown, D.

E. Cullen, D. P. Heinrichs, D. P. McNabb, H. Derrien, M. E. Dunn, N. M. Larson, L. C. Leal, A. D. Carlson, R. C. Block, J. B. Briggs, E. T. Cheng, H. C. Huria, M. L. Zerkle, K. S. Kozier, A. Courcelle, V. Pronyaev, and S. C. van der Marck, "ENDF/B-VII.0: Next Generation Evaluated Nuclear Data Library for Nuclear Science and Technology," *Nucl. Data Sheets*, vol. 107, pp. 2931–3060, 2006.

[32] T. Downar, Y. Xu, V. Seker, and N. Hudson, "PARCS v3.0 U.S. NRC Core Neutronics Simulator User Manual." pp. 1–156, 2010.

[33] J. Leppanen, "Serpent – a Continuous-energy Monte Carlo Reactor Physics Burnup Calculation Code: User's Manual." 2015.

[34] M. Pusa and J. Leppänen, "Computing the Matrix Exponential in Burnup Calculations," *Nucl. Sci. Eng.*, no. 164, pp. 140–150, 2010.

[35] A. Ward, Y. Xu, and T. Downar, "GenPMAXS: Code for Generating the PARCS Cross Section Interface File PMAXS," no. October. 2013.

[36] C. J. Greenshields, "OpenFOAM – The Open Source CFD Toolbox User Guide." OpenFOAM Foundation Ltd, 2015.

[37] M. Aufiero, C. Fiorina, A. Laureau, P. Rubiolo, and V. Valtavirta, "Serpent – OpenFOAM Coupling in Transient Mode: Simulation of a Godiva Prompt Critical Burst," in *SNA+MC 2015*, 2015.

[38] W. Wagner, J. R. Cooper, A. Dittmann, J. Kijima, H. J. Kretzschmar, A. Kruse, R. Mares, K. Oguchi, H. Sato, I. Stocker, and O. Sifner, "The IAPWS Industrial Formulation 1997 for the Thermodynamic Properties of Water and Steam," *J. Eng. Gas Turbines Power*, vol. 122, no. 1, pp. 150–184, 2000.

[39] M. Murabayashi, S. Tanaka, and Y. Takahashi, "Thermal Conductivity and Heat Capacity of Zircaloy-2 , -4 and Unalloyed Zirconium," *J. Nucl. Sci. Technol.*, vol. 12, no. 10, pp. 661–662, 1975.

[40] S. G. Popov, J. J. Carbajo, V. K. Ivanov, and G. L. Yoder, "Thermophysical Properties of MOX and UO2 Fuels Including the Effects of Irradiation," 2000.

[41] M. Inoue, "Thermal conductivity of uranium-plutonium oxide fuel for fast reactors," *J. Nucl. Mater.*, vol. 282, pp. 186–195, 2000.

[42] M. Aufiero, A. Bidaud, M. Hursin, J. Leppänen, G. Palmiotti, S. Pelloni, and P. Rubiolo, "A collision history-based approach to sensitivity / perturbation calculations in the continuous energy Monte Carlo code SERPENT," *Ann. Nucl. Energy*, vol. 85, pp. 245–258, 2015.

[43] G. Palmiotti, "Uncertainty Analysis Contribution Tables Definition (unpublished)." .

[44] C. Clark, M. Griffiths, S. Chen, T. Hibiki, M. Ishii, and I. Kinoshita, "Experimental study

of void fraction in an 8 x 8 rod bundle at low pressure and low liquid flow conditions," *Int. J. Multiph. Flow*, vol. 62, pp. 87–100, 2014.

[45] D. E. Shropshire, K. A. Williams, E. A. Hoffman, J. D. Smith, D. J. Hebditch, J. J. Jacobson, J. D. Morton, A. M. Phillips, and J. P. Taylor, "Advanced Fuel Cycle Economic Analysis of Symbiotic Light-Water Reactor and Fast Burner Reactor Systems," 2009.

[46] K. Eckerman, J. Harrison, H.-G. Menzel, and C. H. Clement, "ICRP PUBLICATION 119: Compendium of Dose Coefficients based on ICRP Publication 60," *2012*.

[47] N. E. Stauff, T. K. Kim, and T. A. Taiwo, "Variations in nuclear waste management performance of various fuel-cycle options," *J. Nucl. Sci. Technol.*, vol. 52, no. 7--8, pp. 1058–1073, 2016.

[48] R. Takeda, J. Miwa, and K. Moriya, "BWRs for Long-Term Energy Supply and for Fissioning Almost All Transuraniums," in *GLOBAL 2007*, 2007.

[49] P. M. Gorman, G. Zhang, J. E. Seifried, C. R. Varela, J. L. Vujic, and E. Greenspan, "The fuel-self-sustaining RBWR-Th core concept and parametric studies," in *ICAPP 2014*, 2014.

[50] P. M. Gorman, J. L. Vujic, and E. Greenspan, "Trade-off studies for the fuel-self-sustaining RBWR-Th core," *Nucl. Technol.*, vol. 191, no. 3, pp. 282–294, 2015.

[51] P. Gorman, S. Bogetic, J. Hou, J. E. Seifried, G. Zhang, J. Vujic, and E. Greenspan, "Thorium Fuelled Resource-Renewable BWR (RBWR) Design Update," in *ANS Winter Meeting 2014*, 2014, vol. 111, pp. 299–303.

[52] P. Gorman, S. Bogetic, G. Zhang, M. Fratoni, J. Vujic, and E. Greenspan, "The fuel self-sufficient RBWR-SS core designs," in *GLOBAL 2015*, 2015.

[53] K. Shirvan, "Technical Report Reduced Moderated Boiling Water Reactor Thermal Hydraulics and Safety Assessment (unpublished)," 2015.

[54] Z. Xu, M. S. Kazimi, and M. J. Driscoll, "Impact of High Burnup on PWR Spent Fuel Characteristics," *Nucl. Sci. Eng.*, vol. 151, pp. 261–273, 2010.

[55] B. Pellaud, "Proliferation aspects of plutonium recycling," *J. Inst. Nucl. Mater. Manag.*, 2002.

[56] J. Kang and F. N. Von Hippel, "U-232 and the Proliferation- Resistance of U-233 in Spent Fuel," *Sci. Glob. Secur.*, vol. 9, pp. 1–32, 2001.

[57] C. G. Bathke, H. R. Trellue, B. B. Ebbinghaus, B. A. Collins, A. W. Prichard, and B. W. Smith, "An Assessment of the Attractiveness of Material Associated with Thorium Fuel Cycles," in *2014 ANS Winter Meeting*, 2014.

[58] K. Shirvan, "Technical Report Reduced Moderated Boiling Water Reactor Thermal

Hydraulics and Safety Assessment Phase II (unpublished),” 2016.

[59] Hitachi Ltd., “Resource-Renewable BWR for Effective Use of Transuranic Elements (RBWR-TB2/BDBA) Rev. 4.2,” 2016.

[60] T. Downar, V. Seker, and A. Hall, “Analysis of RBWR TB2 and RBWR Test Reactor Design with the SERPENT/PARCS/PATHS code system.” .

Appendix A. Single Assembly Comparison between Serpent and PARCS

In order to build confidence in the PARCS simulator, a benchmark comparison between Serpent and PARCS was performed. A single assembly was modelled in PARCS and compared against an assembly unit cell from Serpent. This comparison was performed for both the RBWR-SSH (Section A.1) and the RBWR-TR (Section A.2).

PARCS was not coupled to PATHS; the same water density and fuel temperature profiles were used in Serpent and in PARCS. For both models, the k_∞ versus burnup was compared, as was the linear heat generation rate distribution at different burnup points. In addition, the control rod worth, void collapse worth, and shutdown margin were assessed for fresh fuel.

A.1. RBWR-SSH Comparison

The k_∞ comparison is shown in Figure A.1, and it shows good agreement between Serpent and PARCS at low burnups. For fresh fuel, the difference in k_∞ is 15 pcm, which is less than the uncertainty in Serpent (which is 18 pcm). The difference between the two codes grows with burnup; with the average discharge burnup, PARCS underpredicts the multiplication factor by almost 250 pcm. This is likely due to the fact that the blanket power is underpredicted from moderate burnups (Figure A.2 through Figure A.4); in particular, the concave-up shape in the upper blanket power with higher burnups is not shown in PARCS. Table A.1 shows good agreement when the reactor changes state, indicating that the branching works appropriately, although it is anticipated that the error would increase when the burnup increases as well.

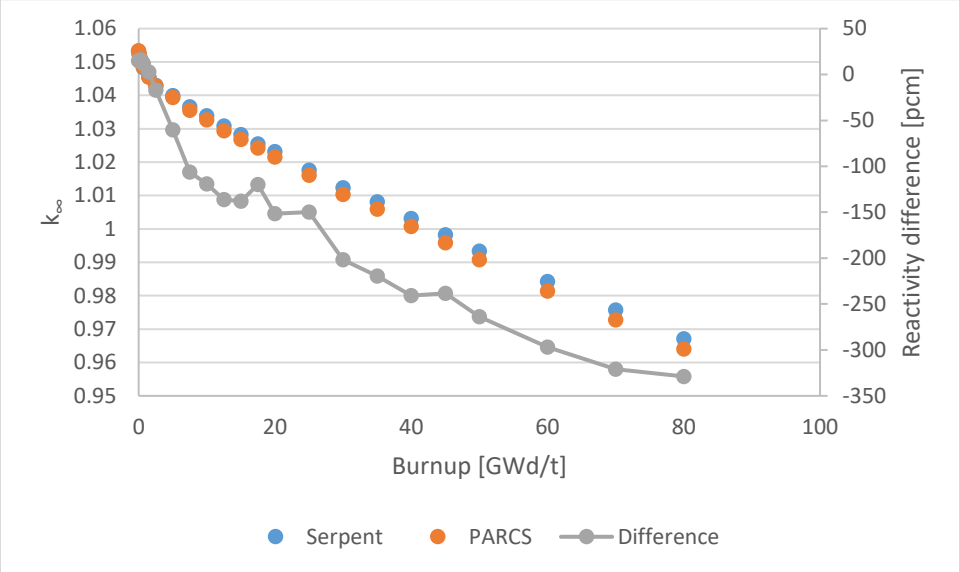

Figure A.1. Reactivity evolution for the RBWR-SSH unit cell in Serpent and PARCS.

Table A.1. Comparison between changes in state using Serpent and PARCS for the RBWR-SSH. All reactivity changes are given in pcm.

Parameter	Serpent	PARCS
CR worth	-10511	-10503
Flooding worth	4369	4339

Parameter	Serpent	PARCS
Cooling worth	3548	3572
CR worth (shut down conditions)	-8107	-8133

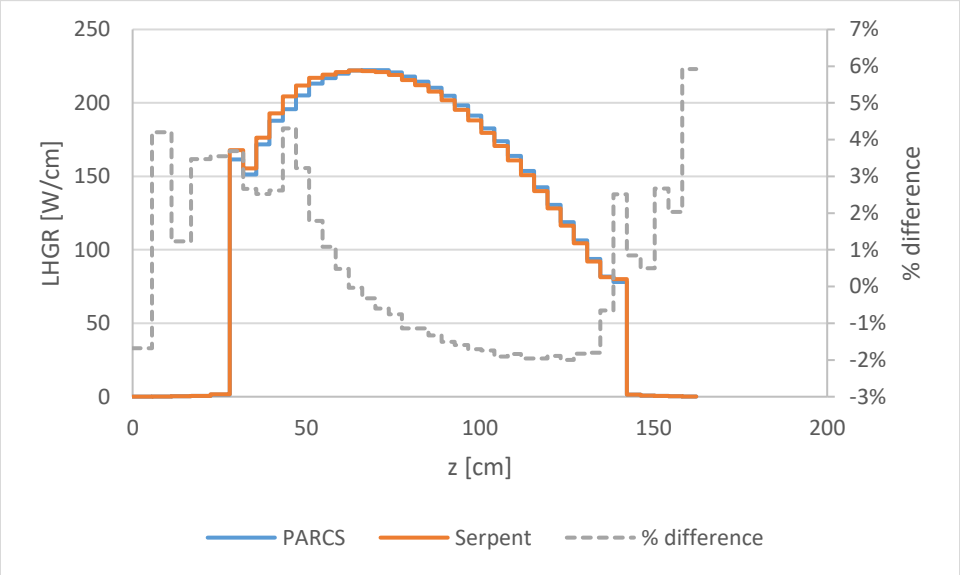

Figure A.2. Linear heat generation rate comparison for the RBWR-SSH unit cell as simulated in Serpent and PARCS with fresh fuel.

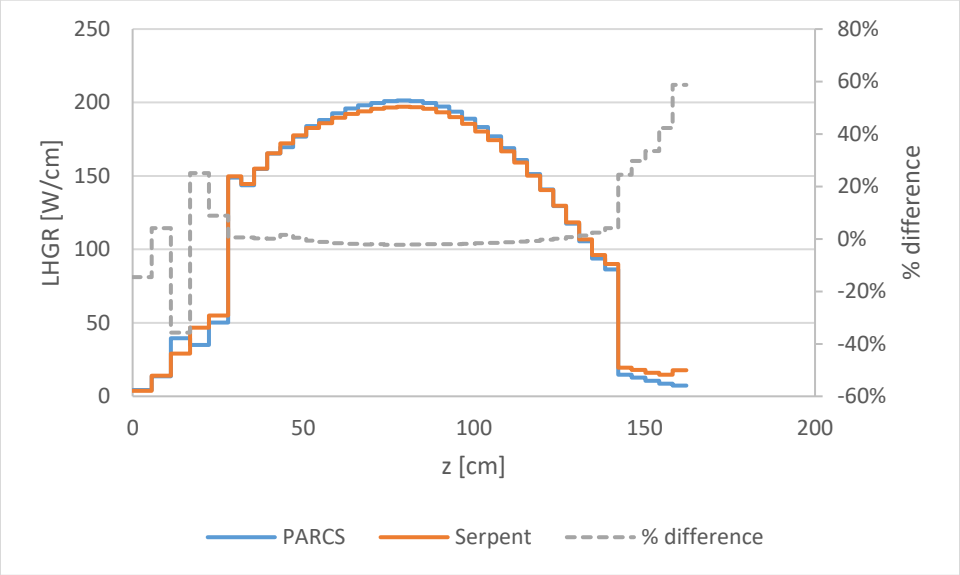

Figure A.3. Linear heat generation rate comparison for the RBWR-SSH unit cell as simulated in Serpent and PARCS with fuel depleted to 30.0 GWd/t.

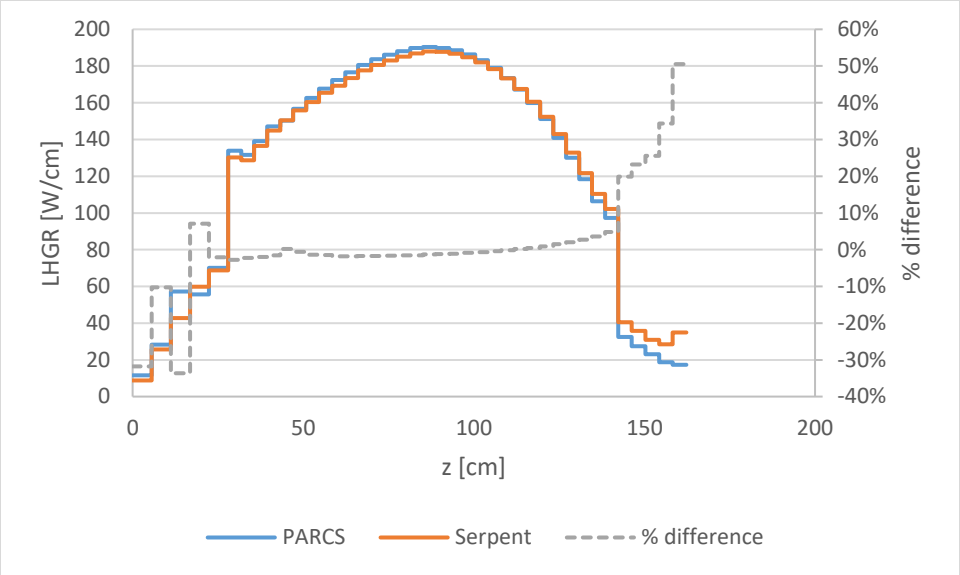

Figure A.4. Linear heat generation rate comparison for the RBWR-SSH unit cell as simulated in Serpent and PARCS with fuel depleted to 70 GWd/T.

A.2. RBWR-TR Comparison

The k_∞ comparison is shown in Figure A.5 shows acceptable agreement between Serpent and PARCS at low burnups. For fresh fuel, the difference in k_∞ is 32 pcm, which is slightly larger than the uncertainty in Serpent (which is 13 pcm). The difference between the two codes grows with burnup; with the average discharge burnup, PARCS underpredicts the multiplication factor by over 200 pcm. This is likely due to the fact that the blanket power is underpredicted from moderate burnups (Figure A.6 through Figure A.8); although the concave-up shape of the power is seen in PARCS (unlike in the RBWR-SSH), the largest amount of error is still seen in the top-most node. Table A.2 shows good agreement when the reactor changes state, indicating that the branching works appropriately, although it is anticipated that the error would increase when the burnup increases as well.

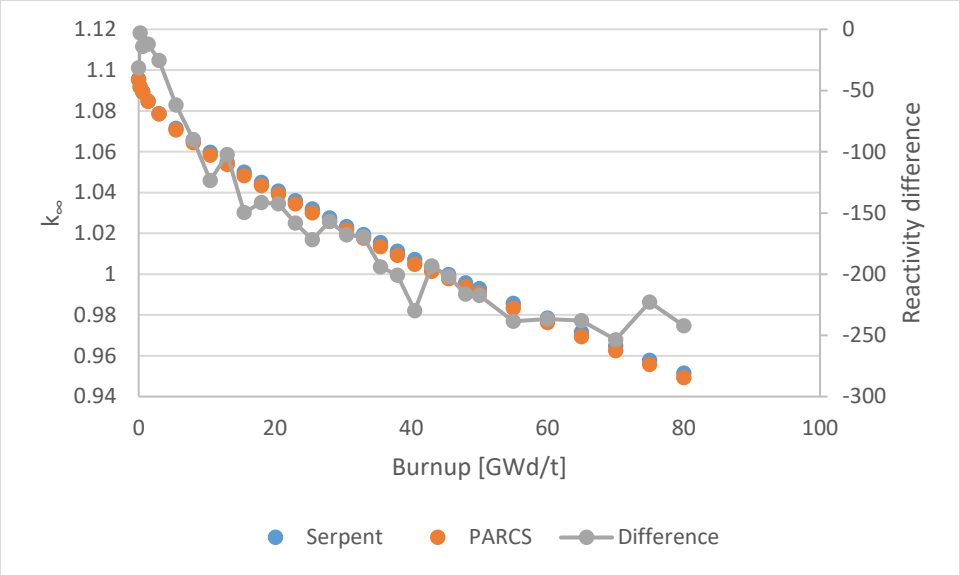

Figure A.5. Reactivity evolution for the RBWR-TR unit cell in Serpent and PARCS.

Table A.2. Comparison between changes in state using Serpent and PARCS for the RBWR-TR. All reactivity changes are given in pcm.

Parameter	Serpent	PARCS
CR worth	-10537	-10473
Flooding worth	1491	1427
Cooling worth	2571	2572
CR worth (shut down conditions)	-7302	-7268

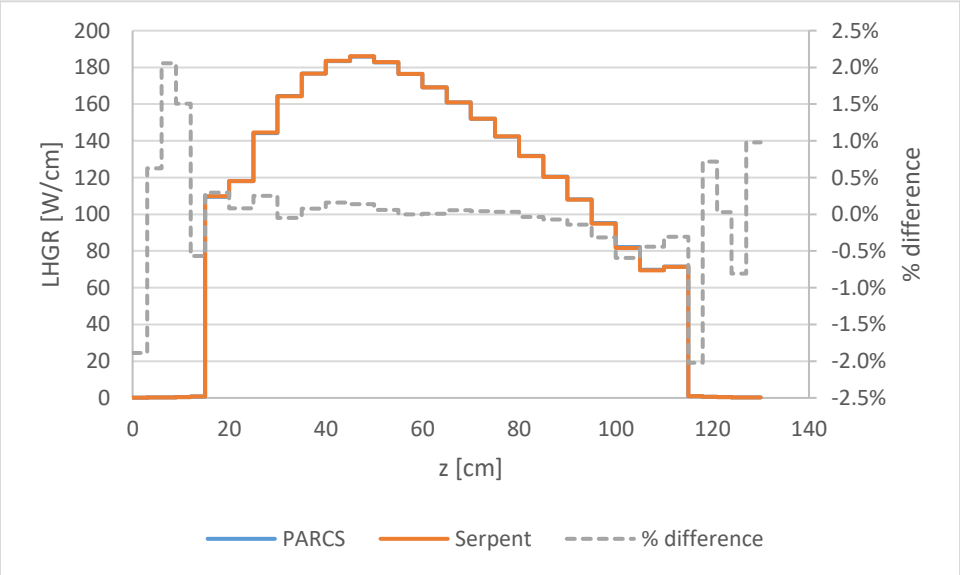

Figure A.6. Linear heat generation rate comparison for the RBWR-TR unit cell as simulated in Serpent and PARCS with fresh fuel.

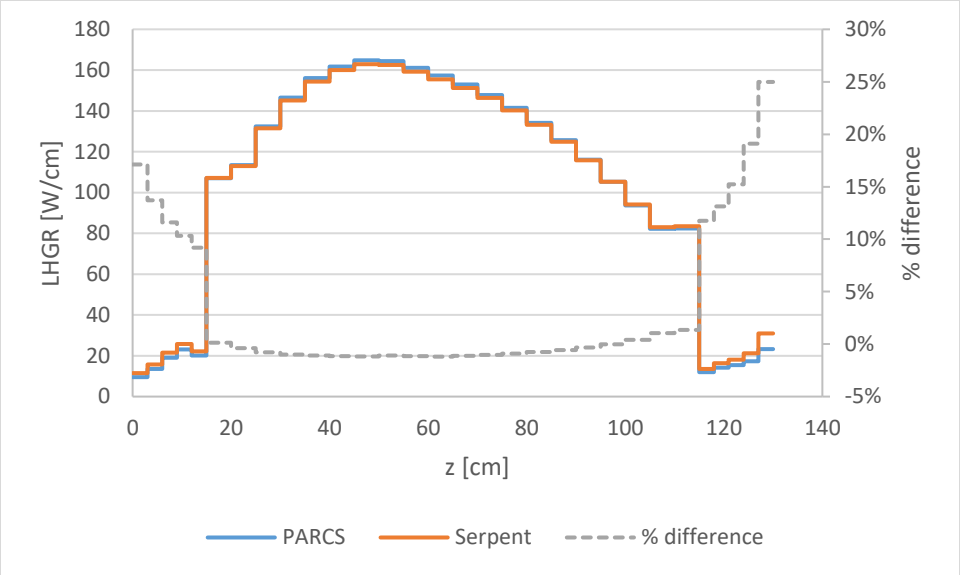

Figure A.7. Linear heat generation rate comparison for the RBWR-TR unit cell as simulated in Serpent and PARCS with fuel depleted to 25.5 GWd/t.

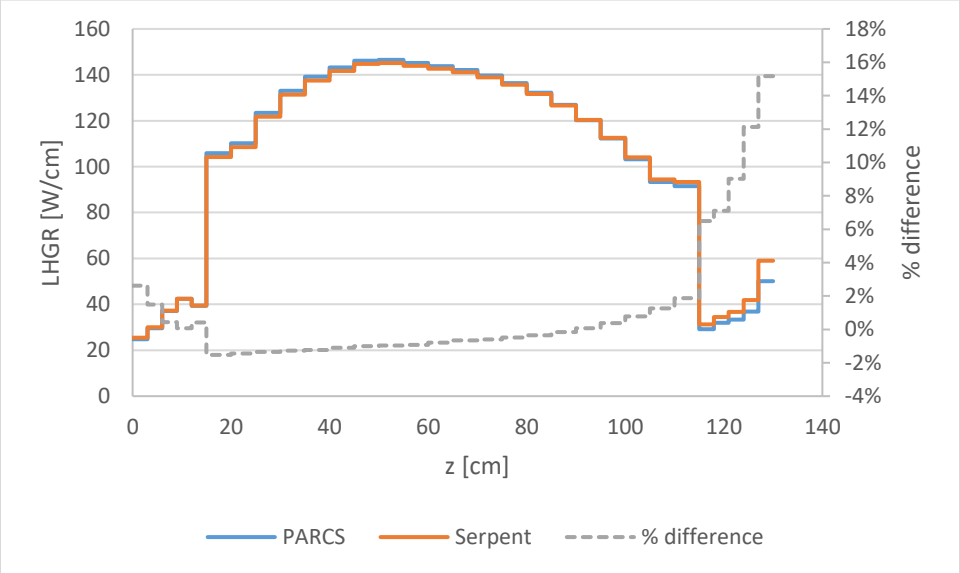

Figure A.8. Linear heat generation rate comparison for the RBWR-SSH unit cell as simulated in Serpent and PARCS with fuel depleted to 70 GWd/T.

Appendix B. Differences in the Assembly Unit Cell and the Full Core Performance

This appendix was added to help future students who may work on the RBWR projects. Many of the core performance metrics change significantly between the assembly unit cell model and the full core model. Most of these changes are driven by the addition of the leakage. Since the self-sustaining designs operate on a 4.5-batch scheme and the TRU-burning designs operate on a 4-batch scheme, the radial leakage affects the two cores differently. In the RBWR-SSH, the leakage from the fuel region varies from 2.7% to 3.7%, while in the RBWR-TR, the leakage from the fuel region varies from 4.5% to 5.5%. In both cases, the leakage reduced with burnup.

One of the biggest changes between the assembly model and the full core model is the void coefficient of reactivity. As the coolant voids, the leakage increases, which contributes negative feedback; the changes in the axial leakage are captured by the assembly models, but the changes in the radial leakage are not. Therefore, the void coefficient of the full core model is more negative than the assembly model. This also causes the reactivity insertion from collapsing the voids to be larger in the full core model: when the reactor is flooded, the radial leakage drops by 1 to 1.5%, which increases the reactivity insertion. The void coefficient for the different designs is summarized in Table B.1; the assembly void coefficients were calculated by interpolating the void coefficient as a function of burnup and averaging according to burnup.

Table B.1. Void coefficients for the RBWR-SSH and RBWR-TR calculated from the assembly model and the full core model. All results are in pcm/% void.

Reactor	Assembly	Full Core
RBWR-SSH (BOC)	-0.4	-23
RBWR-SSH (EOC)	+20	+9.4
RBWR-TR (BOC)	+19	-21
RBWR-TR (EOC)	+20	+3.7

The spectrum will also be softer in the full core model than in the assembly model, since the fast neutrons preferentially leak out due to their higher mean free path. This will additionally reduce the void coefficient in the RBWR-TR as softening the spectrum was found to reduce the void coefficient, but this is a second order effect.

For a similar reason, the power profile will be more bottom peaked in the full core model. The void fraction at the top of the core is higher, and thus the spectrum is harder and the mean free path is higher. More neutrons will leak from the top of the core, so the power will shift towards the bottom.

For the RBWR-SSH at full power conditions, the power tends to be concentrated at the center of the core (Figure 3.12 and Figure 3.13), while in the RBWR-TR, the power is concentrated in the fresh assemblies (Figure 4.8 and Figure 4.9). However, when the reactors are shut down, the effect of radial leakage to suppress the power of the assemblies around the edge of the core is diminished; nearly all of the power is concentrated in the fresh fuel, as it is the most reactive (Figure B.1 and Figure B.2). Even though there is no power when the reactor is shut down, this has two important implications for the shutdown margin: first, the void collapse worth is

weighted towards the value used for the fresh fuel, which is when it is highest; second, the central control rod has nearly no worth, since there is nearly no power produced in the center. Both of these reduce the available shutdown margin beyond what is indicated by averaging the results from the unit cell analysis.

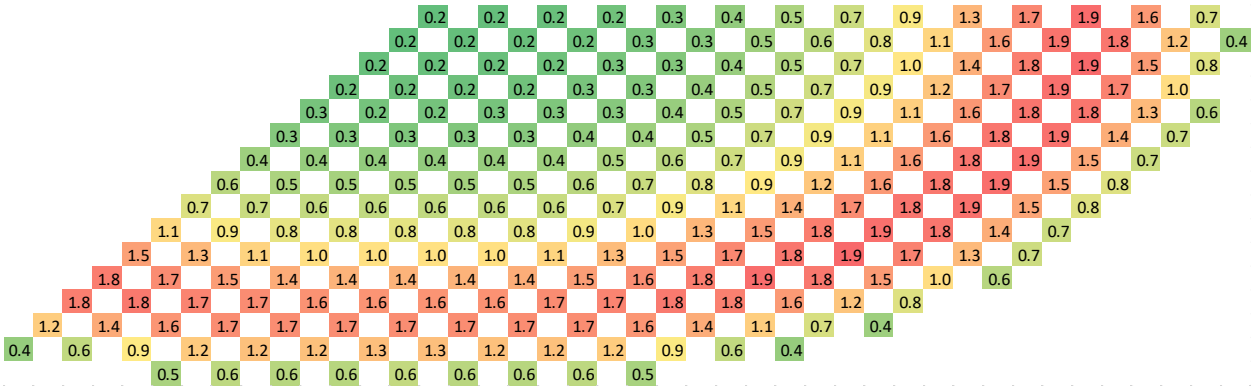

Figure B.1. Power map for the RBWR-SSH at BOC when the reactor is flooded and at room temperature. All control rods are inserted.

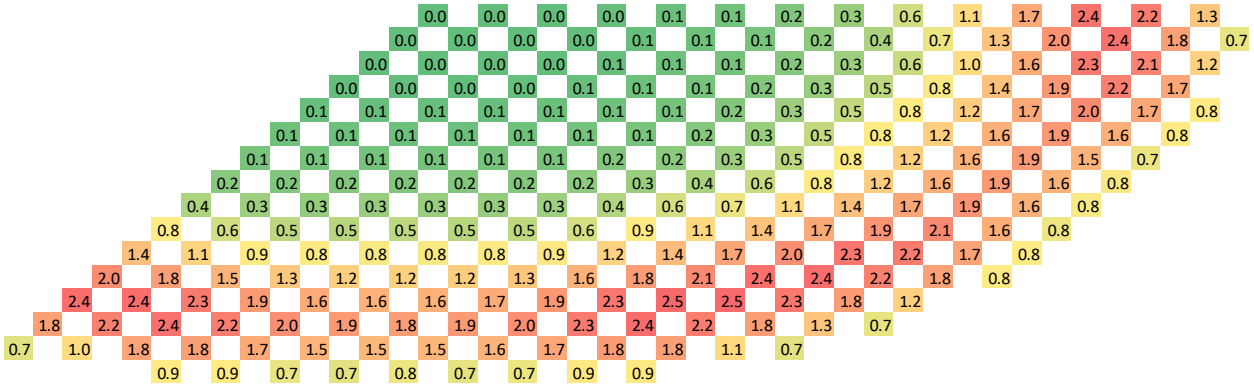

Figure B.2. Power map for the RBWR-TR at BOC when the reactor is flooded and at room temperature. All control rods are inserted.

Appendix C. Input File Listing

In order to assist future students, the input files used for the thorium RBWR analyses are available on the Savio cluster. They are all in a read-only format in the `/global/scratch/pgorman/dissertationInputs` folder; since the scratch directory is not suitable for a permanent repository, they are also available in a gzipped tar file located at `/global/home/users/pgorman/dissertationInputs.tar.gz`. The list of input files is given below.

```
RBWR-SSH:
total 20
drwxr-xr-x 2 pgorman ucb 4096 Dec 12 05:12 GenPMAXS
drwxr-xr-x 4 pgorman ucb 4096 Dec 12 04:50 MocDown
drwxr-xr-x 2 pgorman ucb 4096 Dec 12 05:13 PARCS
drwxr-xr-x 4 pgorman ucb 4096 Dec 12 04:52 SerpentXS
drwxr-xr-x 4 pgorman ucb 4096 Dec 12 04:35 Serpent_GPT

RBWR-SSH/GenPMAXS:
total 10240
-rw-r--r-- 1 pgorman ucb 247337 Dec 12 04:32 RBWR-SSH_901.inp
-rw-r--r-- 1 pgorman ucb 236560 Dec 12 04:32 RBWR-SSH_902.inp
-rw-r--r-- 1 pgorman ucb 244495 Dec 12 04:32 RBWR-SSH_903.inp
-rw-r--r-- 1 pgorman ucb 247292 Dec 12 04:32 RBWR-SSH_904.inp
-rw-r--r-- 1 pgorman ucb 247302 Dec 12 04:32 RBWR-SSH_905.inp
-rw-r--r-- 1 pgorman ucb 247306 Dec 12 04:32 RBWR-SSH_906.inp
-rw-r--r-- 1 pgorman ucb 247374 Dec 12 04:32 RBWR-SSH_907.inp
-rw-r--r-- 1 pgorman ucb 247375 Dec 12 04:32 RBWR-SSH_908.inp
-rw-r--r-- 1 pgorman ucb 247388 Dec 12 04:32 RBWR-SSH_909.inp
-rw-r--r-- 1 pgorman ucb 249784 Dec 12 04:32 RBWR-SSH_910.inp
-rw-r--r-- 1 pgorman ucb 249790 Dec 12 04:32 RBWR-SSH_911.inp
-rw-r--r-- 1 pgorman ucb 249790 Dec 12 04:32 RBWR-SSH_912.inp
-rw-r--r-- 1 pgorman ucb 249785 Dec 12 04:32 RBWR-SSH_913.inp
-rw-r--r-- 1 pgorman ucb 249793 Dec 12 04:32 RBWR-SSH_914.inp
-rw-r--r-- 1 pgorman ucb 249793 Dec 12 04:32 RBWR-SSH_915.inp
-rw-r--r-- 1 pgorman ucb 249791 Dec 12 04:32 RBWR-SSH_916.inp
-rw-r--r-- 1 pgorman ucb 249793 Dec 12 04:32 RBWR-SSH_917.inp
-rw-r--r-- 1 pgorman ucb 249793 Dec 12 04:32 RBWR-SSH_918.inp
-rw-r--r-- 1 pgorman ucb 249791 Dec 12 04:32 RBWR-SSH_919.inp
-rw-r--r-- 1 pgorman ucb 249791 Dec 12 04:32 RBWR-SSH_920.inp
-rw-r--r-- 1 pgorman ucb 249793 Dec 12 04:32 RBWR-SSH_921.inp
-rw-r--r-- 1 pgorman ucb 249787 Dec 12 04:32 RBWR-SSH_922.inp
-rw-r--r-- 1 pgorman ucb 249792 Dec 12 04:32 RBWR-SSH_923.inp
-rw-r--r-- 1 pgorman ucb 249793 Dec 12 04:32 RBWR-SSH_924.inp
-rw-r--r-- 1 pgorman ucb 249793 Dec 12 04:32 RBWR-SSH_925.inp
-rw-r--r-- 1 pgorman ucb 249793 Dec 12 04:32 RBWR-SSH_926.inp
-rw-r--r-- 1 pgorman ucb 249788 Dec 12 04:32 RBWR-SSH_927.inp
-rw-r--r-- 1 pgorman ucb 249785 Dec 12 04:32 RBWR-SSH_928.inp
-rw-r--r-- 1 pgorman ucb 249785 Dec 12 04:32 RBWR-SSH_929.inp
-rw-r--r-- 1 pgorman ucb 249781 Dec 12 04:32 RBWR-SSH_930.inp
-rw-r--r-- 1 pgorman ucb 249781 Dec 12 04:32 RBWR-SSH_931.inp
-rw-r--r-- 1 pgorman ucb 249777 Dec 12 04:32 RBWR-SSH_932.inp
-rw-r--r-- 1 pgorman ucb 249775 Dec 12 04:32 RBWR-SSH_933.inp
-rw-r--r-- 1 pgorman ucb 249769 Dec 12 04:32 RBWR-SSH_934.inp
-rw-r--r-- 1 pgorman ucb 249768 Dec 12 04:32 RBWR-SSH_935.inp
-rw-r--r-- 1 pgorman ucb 249766 Dec 12 04:32 RBWR-SSH_936.inp
```

```
-rw-r--r-- 1 pgorman ucb 249725 Dec 12 04:32 RBWR-SSH_937.inp
-rw-r--r-- 1 pgorman ucb 249722 Dec 12 04:32 RBWR-SSH_938.inp
-rw-r--r-- 1 pgorman ucb 249723 Dec 12 04:32 RBWR-SSH_939.inp
-rw-r--r-- 1 pgorman ucb 249722 Dec 12 04:32 RBWR-SSH_940.inp
-rw-r--r-- 1 pgorman ucb 249718 Dec 12 04:32 RBWR-SSH_941.inp
-rw-r--r-- 1 pgorman ucb 249778 Dec 12 04:32 RBWR-SSH_942.inp
-rwxr-x--- 1 pgorman ucb   1076 Dec 12 05:12 genp.sub
-rwxr-x--- 1 pgorman ucb    839 Dec 12 05:12 genp2.sub

RBWR-SSH/MocDown:
total 8
drwxr-xr-x 2 pgorman ucb 4096 Dec 12 04:50 equilibrium
drwxr-xr-x 2 pgorman ucb 4096 Dec 12 04:51 pinPowerTallies

RBWR-SSH/MocDown/equilibrium:
total 72
-rwxr-x--- 1 pgorman ucb   326 Dec 12 04:50 MocDown.sub
-rw-r--r-- 1 pgorman ucb 55120 Dec 12 04:50 denat
-rwxr-x--- 1 pgorman ucb  8424 Dec 12 04:50 mocdown.inp

RBWR-SSH/MocDown/pinPowerTallies:
total 2604
-rw-r--r-- 1 pgorman ucb 2662225 Dec 12 04:51 denat.i
-rwxr-x--- 1 pgorman ucb     403 Dec 12 04:51 mcnp.sub

RBWR-SSH/PARCS:
total 28
-rwxr-x--- 1 pgorman ucb  4552 Dec 12 04:33 Paths-SSH.inp
-rwxr-x--- 1 pgorman ucb 16223 Dec 12 04:33 RBWR-SSH.inp
-rwxr-x--- 1 pgorman ucb   570 Dec 12 05:13 parcs.sub

RBWR-SSH/SerpentXS:
total 8
drwxr-xr-x 2 pgorman ucb 4096 Dec 12 05:13 RadialReflector
drwxr-xr-x 2 pgorman ucb 4096 Dec 12 05:14 ReferenceHistory

RBWR-SSH/SerpentXS/RadialReflector:
total 36
-rwxr-x--- 1 pgorman ucb 29461 Dec 12 04:53 RadReflector_sss.inp
-rwxr-x--- 1 pgorman ucb   491 Dec 12 05:14 sss.sub

RBWR-SSH/SerpentXS/ReferenceHistory:
total 556
-rw-r--r-- 1 pgorman ucb    395 Dec 12 05:14 SerpentXS.sub
-rw-r--r-- 1 pgorman ucb 156675 Dec 12 04:34 branch_S2.inp
-rw-r--r-- 1 pgorman ucb 403250 Dec 12 04:34 geom_file

RBWR-SSH/Serpent_GPT:
total 8
drwxr-xr-x 9 pgorman ucb 4096 Dec 12 04:35 isotopicSensitivity
drwxr-xr-x 4 pgorman ucb 4096 Dec 12 04:49 voidSens

RBWR-SSH/Serpent_GPT/isotopicSensitivity:
total 28
drwxr-xr-x 2 pgorman ucb 4096 Dec 12 04:35 Cm
drwxr-xr-x 2 pgorman ucb 4096 Dec 12 04:35 LowZ
drwxr-xr-x 2 pgorman ucb 4096 Dec 12 04:35 NpAm
```

```
drwxr-xr-x 2 pgorman ucb 4096 Dec 12 04:35 Pu
drwxr-xr-x 2 pgorman ucb 4096 Dec 12 04:35 Th
drwxr-xr-x 2 pgorman ucb 4096 Dec 12 04:35 Th2
drwxr-xr-x 2 pgorman ucb 4096 Dec 12 04:35 UPu238Cm238

RBWR-SSH/Serpent_GPT/isotopicSensitivity/Cm:
total 1772
-rw-r--r-- 1 pgorman ucb  678204 Dec 12 04:35 S2_Ref
-rw-r--r-- 1 pgorman ucb 1121815 Dec 12 04:35 S2_Ref.out
-rw-r--r-- 1 pgorman ucb      11 Dec 12 04:35 S2_Ref.seed
-rw-r--r-- 1 pgorman ucb     419 Dec 12 04:35 SerpentGPT.sub
lrwxrwxrwx 1 pgorman ucb      72 Dec 12 04:35 sss2 ->
/global/scratch/pgorman/RBWR_FullCore/testCore/gpt/serpent2.1.19_Cm/sss2

RBWR-SSH/Serpent_GPT/isotopicSensitivity/LowZ:
total 2864
-rw-r--r-- 1 pgorman ucb  678204 Dec 12 04:35 S2_Ref
-rw-r--r-- 1 pgorman ucb 2243630 Dec 12 04:35 S2_Ref.out
-rw-r--r-- 1 pgorman ucb      11 Dec 12 04:35 S2_Ref.seed
-rw-r--r-- 1 pgorman ucb     421 Dec 12 04:35 SerpentGPT.sub

RBWR-SSH/Serpent_GPT/isotopicSensitivity/NpAm:
total 2556
-rw-r--r-- 1 pgorman ucb  678204 Dec 12 04:35 S2_Ref
-rw-r--r-- 1 pgorman ucb     421 Dec 12 04:35 SerpentGPT.sub
-rwxr-xr-x 1 pgorman ucb 1929787 Dec 12 04:35 sss2

RBWR-SSH/Serpent_GPT/isotopicSensitivity/Pu:
total 2572
-rw-r--r-- 1 pgorman ucb  678204 Dec 12 04:35 S2_Ref
-rw-r--r-- 1 pgorman ucb       0 Dec 12 04:35 S2_Ref.out
-rw-r--r-- 1 pgorman ucb      11 Dec 12 04:35 S2_Ref.seed
-rw-r--r-- 1 pgorman ucb     419 Dec 12 04:35 SerpentGPT.sub
-rw-r--r-- 1 pgorman ucb    7213 Dec 12 04:35 SerpentXS.log
-rw-r--r-- 1 pgorman ucb      80 Dec 12 04:35 SerpentXS.serr
-rwxr-xr-x 1 pgorman ucb 1929787 Dec 12 04:35 sss2

RBWR-SSH/Serpent_GPT/isotopicSensitivity/Th:
total 3656
-rw-r--r-- 1 pgorman ucb  678204 Dec 12 04:35 S2_Ref
-rw-r--r-- 1 pgorman ucb 1121815 Dec 12 04:35 S2_Ref.out
-rw-r--r-- 1 pgorman ucb      11 Dec 12 04:35 S2_Ref.seed
-rw-r--r-- 1 pgorman ucb     419 Dec 12 04:35 SerpentGPT.sub
-rwxr-xr-x 1 pgorman ucb 1929787 Dec 12 04:35 sss2

RBWR-SSH/Serpent_GPT/isotopicSensitivity/Th2:
total 3656
-rw-r--r-- 1 pgorman ucb  678204 Dec 12 04:35 S2_Ref
-rw-r--r-- 1 pgorman ucb 1121815 Dec 12 04:35 S2_Ref.out
-rw-r--r-- 1 pgorman ucb      11 Dec 12 04:35 S2_Ref.seed
-rw-r--r-- 1 pgorman ucb     420 Dec 12 04:35 SerpentGPT.sub
-rwxr-xr-x 1 pgorman ucb 1929787 Dec 12 04:35 sss2

RBWR-SSH/Serpent_GPT/isotopicSensitivity/UPu238Cm238:
total 3656
-rw-r--r-- 1 pgorman ucb  678204 Dec 12 04:35 S2_Ref
-rw-r--r-- 1 pgorman ucb 1121815 Dec 12 04:35 S2_Ref.out
```

```
-rw-r--r-- 1 pgorman ucb      11 Dec 12 04:35 S2_Ref.seed
-rw-r--r-- 1 pgorman ucb     421 Dec 12 04:35 SerpentGPT.sub
-rwxr-xr-x 1 pgorman ucb 1929787 Dec 12 04:35 sss2

RBWR-SSH/Serpent_GPT/voidSens:
total 36
drwxr-xr-x 2 pgorman ucb  4096 Dec 12 04:35 gpt
drwxr-xr-x 6 pgorman ucb 32768 Dec 12 05:18 ofCoupling

RBWR-SSH/Serpent_GPT/voidSens/gpt:
total 303524
-rw-r--r-- 1 pgorman ucb    668912 Dec 12 04:35 S2_Ref
-rw-r--r-- 1 pgorman ucb   1144566 Dec 12 04:35 S2_Ref.out
-rw-r--r-- 1 pgorman ucb        11 Dec 12 04:35 S2_Ref.seed
-rw-r--r-- 1 pgorman ucb     57953 Dec 12 04:35 S2_Ref_res.m
-rw-r--r-- 1 pgorman ucb 308841995 Dec 12 04:35 Serpent.log
-rw-r--r-- 1 pgorman ucb        98 Dec 12 04:35 Serpent.serr
-rwxr-x--- 1 pgorman ucb       380 Dec 12 04:35 Serpent.sub
-rw-r--r-- 1 pgorman ucb     57953 Dec 12 04:35 backup_res.m
lrwxrwxrwx 1 pgorman ucb        73 Dec 12 04:35 sss2 ->
/global/scratch/pgorman/RBWR_FullCore/testCore/gpt/serpent2.1.24_SSH/sss2

RBWR-SSH/Serpent_GPT/voidSens/ofCoupling:
total 3096
drwxr-xr-x 2 pgorman ucb   28672 Dec 12 05:18 0
drwxr-xr-x 3 pgorman ucb    4096 Dec 12 04:35 9
-rwxr-x--- 1 pgorman ucb   17309 Dec 12 04:35 OfSerpent.py
-rw-r--r-- 1 pgorman ucb  669808 Dec 12 04:35 S2_Ref
-rw-r--r-- 1 pgorman ucb  678063 Dec 12 04:35 S2_Ref.of
-rw-r--r-- 1 pgorman ucb 1160395 Dec 12 04:35 S2_Ref.of.out
-rw-r--r-- 1 pgorman ucb      11 Dec 12 04:35 S2_Ref.of.seed
-rw-r--r-- 1 pgorman ucb   34725 Dec 12 04:35 S2_Ref.of_res.m
-rw-r--r-- 1 pgorman ucb  539755 Dec 12 04:35 Serpent.log
drwxr-xr-x 3 pgorman ucb    4096 Dec 12 04:35 constant
-rw-r--r-- 1 pgorman ucb     425 Dec 12 04:35 of.sub
-rw-r--r-- 1 pgorman ucb    3135 Dec 12 04:35 openFoam.log
-rw-r--r-- 1 pgorman ucb     464 Dec 12 04:35 slurm.log
-rw-r--r-- 1 pgorman ucb       0 Dec 12 04:35 slurm.serr
drwxr-xr-x 2 pgorman ucb    4096 Dec 12 04:35 system

RBWR-SSH/Serpent_GPT/voidSens/ofCoupling/0:
total 48
-rw-r--r-- 1 pgorman ucb 1407 Dec 12 04:35 PuWeightFraction
-rw-r--r-- 1 pgorman ucb 1149 Dec 12 04:35 T
-rw-r--r-- 1 pgorman ucb 1159 Dec 12 04:35 Tcenterline
-rw-r--r-- 1 pgorman ucb 1153 Dec 12 04:35 Tnormalized
-rw-r--r-- 1 pgorman ucb 1123 Dec 12 04:35 effectiveKclad
-rw-r--r-- 1 pgorman ucb 1123 Dec 12 04:35 effectiveKfuel
-rw-r--r-- 1 pgorman ucb 1122 Dec 12 04:35 h
-rw-r--r-- 1 pgorman ucb 1120 Dec 12 04:35 linHeatRate
-rw-r--r-- 1 pgorman ucb 1151 Dec 12 04:35 rho
-rw-r--r-- 1 pgorman ucb 1154 Dec 12 04:35 rhok
-rw-r--r-- 1 pgorman ucb 1130 Dec 12 04:35 superficialLiquidFlux
-rw-r--r-- 1 pgorman ucb 1636 Dec 12 04:35 volPower

RBWR-SSH/Serpent_GPT/voidSens/ofCoupling/9:
total 56
```

```
-rw-r--r-- 1 pgorman ucb 1421 Dec 12 04:35 PuWeightFraction
-rw-r--r-- 1 pgorman ucb 1541 Dec 12 04:35 T
-rw-r--r-- 1 pgorman ucb 1549 Dec 12 04:35 Tcenterline
-rw-r--r-- 1 pgorman ucb 1533 Dec 12 04:35 Tclad
-rw-r--r-- 1 pgorman ucb 1586 Dec 12 04:35 Tnormalized
-rw-r--r-- 1 pgorman ucb 1671 Dec 12 04:35 h
-rw-r--r-- 1 pgorman ucb 1494 Dec 12 04:35 linHeatRate
-rw-r--r-- 1 pgorman ucb 1246 Dec 12 04:35 phil
-rw-r--r-- 1 pgorman ucb 1537 Dec 12 04:35 rho
-rw-r--r-- 1 pgorman ucb 1542 Dec 12 04:35 rhok
-rw-r--r-- 1 pgorman ucb 1524 Dec 12 04:35 superficialLiquidFlux
drwxr-xr-x 2 pgorman ucb 4096 Dec 12 04:35 uniform
-rw-r--r-- 1 pgorman ucb 1503 Dec 12 04:35 voidFrac
-rw-r--r-- 1 pgorman ucb 1528 Dec 12 04:35 volPower

RBWR-SSH/Serpent_GPT/voidSens/ofCoupling/9/uniform:
total 4
-rw-r--r-- 1 pgorman ucb 960 Dec 12 04:35 time

RBWR-SSH/Serpent_GPT/voidSens/ofCoupling/constant:
total 16
-rw-r--r-- 1 pgorman ucb 1005 Dec 12 04:35 G
-rw-r--r-- 1 pgorman ucb 1199 Dec 12 04:35 globalParameters
drwxr-xr-x 2 pgorman ucb 4096 Dec 12 04:35 polyMesh
-rw-r--r-- 1 pgorman ucb 1906 Dec 12 04:35 transportProperties

RBWR-SSH/Serpent_GPT/voidSens/ofCoupling/constant/polyMesh:
total 24
-rw-r--r-- 1 pgorman ucb 1250 Dec 12 04:35 boundary
-rw-r--r-- 1 pgorman ucb 4350 Dec 12 04:35 faces
-rw-r--r-- 1 pgorman ucb 1067 Dec 12 04:35 neighbour
-rw-r--r-- 1 pgorman ucb 1532 Dec 12 04:35 owner
-rw-r--r-- 1 pgorman ucb 3599 Dec 12 04:35 points

RBWR-SSH/Serpent_GPT/voidSens/ofCoupling/system:
total 20
-rw-r--r-- 1 pgorman ucb 3950 Dec 12 04:35 backup_blockMeshDict
-rw-r--r-- 1 pgorman ucb 2092 Dec 12 04:35 blockMeshDict
-rw-r--r-- 1 pgorman ucb 1208 Dec 12 04:35 controlDict
-rw-r--r-- 1 pgorman ucb 1475 Dec 12 04:35 fvSchemes
-rw-r--r-- 1 pgorman ucb 1196 Dec 12 04:35 fvSolution

RBWR-TR:
total 20
drwxr-xr-x 2 pgorman ucb 4096 Dec 12 05:15 GenPMAXS
drwxr-xr-x 5 pgorman ucb 4096 Dec 12 05:09 MocDown
drwxr-xr-x 2 pgorman ucb 4096 Dec 12 04:58 PARCS
drwxr-xr-x 4 pgorman ucb 4096 Dec 12 05:06 SerpentXS
drwxr-xr-x 4 pgorman ucb 4096 Dec 12 05:08 Serpent_GPT

RBWR-TR/GenPMAXS:
total 11592
-rw-r--r-- 1 pgorman ucb 354223 Dec 12 04:52 RBWR-TR_01.inp
-rw-r--r-- 1 pgorman ucb 354222 Dec 12 04:52 RBWR-TR_02.inp
-rw-r--r-- 1 pgorman ucb 354135 Dec 12 04:52 RBWR-TR_03.inp
-rw-r--r-- 1 pgorman ucb 354143 Dec 12 04:52 RBWR-TR_04.inp
-rw-r--r-- 1 pgorman ucb 354151 Dec 12 04:52 RBWR-TR_05.inp
```

```
-rw-r--r-- 1 pgorman ucb 354159 Dec 12 04:52 RBWR-TR_06.inp
-rw-r--r-- 1 pgorman ucb 354152 Dec 12 04:52 RBWR-TR_07.inp
-rw-r--r-- 1 pgorman ucb 354228 Dec 12 04:52 RBWR-TR_08.inp
-rw-r--r-- 1 pgorman ucb 354254 Dec 12 04:52 RBWR-TR_09.inp
-rw-r--r-- 1 pgorman ucb 357809 Dec 12 04:52 RBWR-TR_10.inp
-rw-r--r-- 1 pgorman ucb 357820 Dec 12 04:52 RBWR-TR_11.inp
-rw-r--r-- 1 pgorman ucb 357825 Dec 12 04:52 RBWR-TR_12.inp
-rw-r--r-- 1 pgorman ucb 357825 Dec 12 04:52 RBWR-TR_13.inp
-rw-r--r-- 1 pgorman ucb 357824 Dec 12 04:52 RBWR-TR_14.inp
-rw-r--r-- 1 pgorman ucb 357827 Dec 12 04:52 RBWR-TR_15.inp
-rw-r--r-- 1 pgorman ucb 357825 Dec 12 04:52 RBWR-TR_16.inp
-rw-r--r-- 1 pgorman ucb 357823 Dec 12 04:52 RBWR-TR_17.inp
-rw-r--r-- 1 pgorman ucb 357823 Dec 12 04:52 RBWR-TR_18.inp
-rw-r--r-- 1 pgorman ucb 357820 Dec 12 04:52 RBWR-TR_19.inp
-rw-r--r-- 1 pgorman ucb 357818 Dec 12 04:52 RBWR-TR_20.inp
-rw-r--r-- 1 pgorman ucb 357813 Dec 12 04:52 RBWR-TR_21.inp
-rw-r--r-- 1 pgorman ucb 357808 Dec 12 04:52 RBWR-TR_22.inp
-rw-r--r-- 1 pgorman ucb 357801 Dec 12 04:52 RBWR-TR_23.inp
-rw-r--r-- 1 pgorman ucb 357791 Dec 12 04:52 RBWR-TR_24.inp
-rw-r--r-- 1 pgorman ucb 357789 Dec 12 04:52 RBWR-TR_25.inp
-rw-r--r-- 1 pgorman ucb 357785 Dec 12 04:52 RBWR-TR_26.inp
-rw-r--r-- 1 pgorman ucb 357784 Dec 12 04:52 RBWR-TR_27.inp
-rw-r--r-- 1 pgorman ucb 357713 Dec 12 04:52 RBWR-TR_28.inp
-rw-r--r-- 1 pgorman ucb 357717 Dec 12 04:52 RBWR-TR_29.inp
-rw-r--r-- 1 pgorman ucb 357718 Dec 12 04:52 RBWR-TR_30.inp
-rw-r--r-- 1 pgorman ucb 357722 Dec 12 04:52 RBWR-TR_31.inp
-rw-r--r-- 1 pgorman ucb 357735 Dec 12 04:52 RBWR-TR_32.inp
-rw-r--r-- 1 pgorman ucb 357792 Dec 12 04:52 RBWR-TR_33.inp
-rwxr-x--- 1 pgorman ucb    771 Dec 12 04:52 RBWR-TR_RadRef.inp
-rwxr-x--- 1 pgorman ucb    897 Dec 12 05:15 genp.sub
-rwxr-x--- 1 pgorman ucb    746 Dec 12 05:15 genp2.sub

RBWR-TR/MocDown:
total 12
drwxr-xr-x 2 pgorman ucb 4096 Dec 12 05:10 equilibrium_singleSeed
drwxr-xr-x 2 pgorman ucb 4096 Dec 12 05:10 equilibrium_threeSeeds
drwxr-xr-x 2 pgorman ucb 4096 Dec 12 05:11 pinPeaking

RBWR-TR/MocDown/equilibrium_singleSeed:
total 56
-rwxr-x--- 1 pgorman ucb   294 Dec 12 05:10 MocDown.sub
-rwxr-x--- 1 pgorman ucb  8391 Dec 12 05:10 mocdown.inp
-rw-r--r-- 1 pgorman ucb 37784 Dec 12 05:10 tru

RBWR-TR/MocDown/equilibrium_threeSeeds:
total 56
-rwxr-x--- 1 pgorman ucb   323 Dec 12 05:10 MocDown.sub
-rwxr-x--- 1 pgorman ucb  8495 Dec 12 05:10 mocdown.inp
-rw-r--r-- 1 pgorman ucb 38014 Dec 12 05:10 tru

RBWR-TR/MocDown/pinPeaking:
total 548
-rwxr-x--- 1 pgorman ucb    398 Dec 12 05:11 mcnp.sub
-rw-r--r-- 1 pgorman ucb 553041 Dec 12 05:11 tru.i

RBWR-TR/PARCS:
total 32
```

```
-rwxr-x--- 1 pgorman ucb  4178 Dec 12 04:58 Paths.inp
-rwxr-x--- 1 pgorman ucb 18253 Dec 12 04:58 RBWR-TR.inp
-rwxr-x--- 1 pgorman ucb   576 Dec 12 04:58 parcs.sub

RBWR-TR/SerpentXS:
total 8
drwxr-xr-x 2 pgorman ucb 4096 Dec 12 05:06 RadialReflector
drwxr-xr-x 2 pgorman ucb 4096 Dec 12 05:16 ReferenceHistory

RBWR-TR/SerpentXS/RadialReflector:
total 24
-rw-r--r-- 1 pgorman ucb 20176 Dec 12 05:06 RadReflector_sss.inp
-rwxr-x--- 1 pgorman ucb   504 Dec 12 05:06 serpent.sub

RBWR-TR/SerpentXS/ReferenceHistory:
total 208
-rw-r--r-- 1 pgorman ucb    395 Dec 12 05:16 SerpentXS.sub
-rw-r--r-- 1 pgorman ucb  27077 Dec 12 05:03 branch_S2.inp
-rw-r--r-- 1 pgorman ucb 177171 Dec 12 05:02 geom_file

RBWR-TR/Serpent_GPT:
total 8
drwxr-xr-x 9 pgorman ucb 4096 Dec 12 05:08 isootopicSensitivity
drwxr-xr-x 4 pgorman ucb 4096 Dec 12 05:08 voidSens

RBWR-TR/Serpent_GPT/isootopicSensitivity:
total 28
drwxr-xr-x 2 pgorman ucb 4096 Dec 12 05:07 Cm
drwxr-xr-x 2 pgorman ucb 4096 Dec 12 05:07 LowZ
drwxr-xr-x 2 pgorman ucb 4096 Dec 12 05:07 NpAm
drwxr-xr-x 2 pgorman ucb 4096 Dec 12 05:07 Pu
drwxr-xr-x 2 pgorman ucb 4096 Dec 12 05:07 Th
drwxr-xr-x 2 pgorman ucb 4096 Dec 12 05:07 Th2
drwxr-xr-x 2 pgorman ucb 4096 Dec 12 05:07 UPu238Cm238

RBWR-TR/Serpent_GPT/isootopicSensitivity/Cm:
total 208
-rw-r--r-- 1 pgorman ucb 201327 Dec 12 05:07 S2_Ref
-rw-r--r-- 1 pgorman ucb    418 Dec 12 05:07 SerpentGPT.sub
lrwxrwxrwx 1 pgorman ucb     72 Dec 12 05:07 sss2 ->
/global/scratch/pgorman/RBWR_FullCore/testCore/gpt/serpent2.1.19_Cm/sss2

RBWR-TR/Serpent_GPT/isootopicSensitivity/LowZ:
total 2092
-rw-r--r-- 1 pgorman ucb  201327 Dec 12 05:07 S2_Ref
-rw-r--r-- 1 pgorman ucb     420 Dec 12 05:07 SerpentGPT.sub
-rwxr-xr-x 1 pgorman ucb 1929787 Dec 12 05:07 sss2

RBWR-TR/Serpent_GPT/isootopicSensitivity/NpAm:
total 2092
-rw-r--r-- 1 pgorman ucb  201327 Dec 12 05:07 S2_Ref
-rw-r--r-- 1 pgorman ucb     420 Dec 12 05:07 SerpentGPT.sub
-rwxr-xr-x 1 pgorman ucb 1929787 Dec 12 05:07 sss2

RBWR-TR/Serpent_GPT/isootopicSensitivity/Pu:
total 2092
-rw-r--r-- 1 pgorman ucb  201327 Dec 12 05:07 S2_Ref
```

```
-rw-r--r-- 1 pgorman ucb     418 Dec 12 05:07 SerpentGPT.sub
-rwxr-xr-x 1 pgorman ucb 1929787 Dec 12 05:07 sss2

RBWR-TR/Serpent_GPT/isootopicSensitivity/Th:
total 2092
-rw-r--r-- 1 pgorman ucb  201327 Dec 12 05:07 S2_Ref
-rw-r--r-- 1 pgorman ucb     418 Dec 12 05:07 SerpentGPT.sub
-rwxr-xr-x 1 pgorman ucb 1929787 Dec 12 05:07 sss2

RBWR-TR/Serpent_GPT/isootopicSensitivity/Th2:
total 2092
-rw-r--r-- 1 pgorman ucb  201327 Dec 12 05:07 S2_Ref
-rw-r--r-- 1 pgorman ucb     419 Dec 12 05:07 SerpentGPT.sub
-rwxr-xr-x 1 pgorman ucb 1929787 Dec 12 05:07 sss2

RBWR-TR/Serpent_GPT/isootopicSensitivity/UPu238Cm238:
total 2092
-rw-r--r-- 1 pgorman ucb  201327 Dec 12 05:07 S2_Ref
-rw-r--r-- 1 pgorman ucb     420 Dec 12 05:07 SerpentGPT.sub
-rwxr-xr-x 1 pgorman ucb 1929787 Dec 12 05:07 sss2

RBWR-TR/Serpent_GPT/voidSens:
total 8
drwxr-xr-x 2 pgorman ucb 4096 Dec 12 05:08 gpt
drwxr-xr-x 6 pgorman ucb 4096 Dec 12 05:19 ofCoupling

RBWR-TR/Serpent_GPT/voidSens/gpt:
total 264596
-rw-r--r-- 1 pgorman ucb    198485 Dec 12 05:08 S2_Ref
-rw-r--r-- 1 pgorman ucb    532067 Dec 12 05:08 S2_Ref.out
-rw-r--r-- 1 pgorman ucb        11 Dec 12 05:08 S2_Ref.seed
-rw-r--r-- 1 pgorman ucb     52237 Dec 12 05:08 S2_Ref_res.m
-rw-r--r-- 1 pgorman ucb 270084013 Dec 12 05:08 Serpent.log
-rw-r--r-- 1 pgorman ucb        98 Dec 12 05:08 Serpent.serr
-rwxr-x--- 1 pgorman ucb       379 Dec 12 05:08 Serpent.sub
-rw-r--r-- 1 pgorman ucb     50975 Dec 12 05:08 backup_res.m
lrwxrwxrwx 1 pgorman ucb        72 Dec 12 05:08 sss2 ->
/global/scratch/pgorman/RBWR_FullCore/testCore/gpt/serpent2.1.24_TR/sss2

RBWR-TR/Serpent_GPT/voidSens/ofCoupling:
total 1216
drwxr-xr-x 2 pgorman ucb   4096 Dec 12 05:19 0
drwxr-xr-x 3 pgorman ucb   4096 Dec 12 05:08 9
-rwxr-x--- 1 pgorman ucb  17307 Dec 12 05:08 OfSerpent.py
-rw-r--r-- 1 pgorman ucb 198264 Dec 12 05:08 S2_Ref
-rw-r--r-- 1 pgorman ucb 199938 Dec 12 05:08 S2_Ref.of
-rw-r--r-- 1 pgorman ucb 533516 Dec 12 05:08 S2_Ref.of.out
-rw-r--r-- 1 pgorman ucb     11 Dec 12 05:08 S2_Ref.of.seed
-rw-r--r-- 1 pgorman ucb  34678 Dec 12 05:08 S2_Ref.of_res.m
-rw-r--r-- 1 pgorman ucb 214884 Dec 12 05:08 Serpent.log
drwxr-xr-x 3 pgorman ucb   4096 Dec 12 05:08 constant
-rw-r--r-- 1 pgorman ucb    424 Dec 12 05:08 of.sub
-rw-r--r-- 1 pgorman ucb   3132 Dec 12 05:08 openFoam.log
-rw-r--r-- 1 pgorman ucb    464 Dec 12 05:08 slurm.log
-rw-r--r-- 1 pgorman ucb      0 Dec 12 05:08 slurm.serr
drwxr-xr-x 2 pgorman ucb   4096 Dec 12 05:08 system
```

```
RBWR-TR/Serpent_GPT/voidSens/ofCoupling/0:
total 48
-rw-r--r-- 1 pgorman ucb 1309 Dec 12 05:08 PuWeightFraction
-rw-r--r-- 1 pgorman ucb 1149 Dec 12 05:08 T
-rw-r--r-- 1 pgorman ucb 1159 Dec 12 05:08 Tcenterline
-rw-r--r-- 1 pgorman ucb 1153 Dec 12 05:08 Tnormalized
-rw-r--r-- 1 pgorman ucb 1123 Dec 12 05:08 effectiveKclad
-rw-r--r-- 1 pgorman ucb 1123 Dec 12 05:08 effectiveKfuel
-rw-r--r-- 1 pgorman ucb 1122 Dec 12 05:08 h
-rw-r--r-- 1 pgorman ucb 1120 Dec 12 05:08 linHeatRate
-rw-r--r-- 1 pgorman ucb 1151 Dec 12 05:08 rho
-rw-r--r-- 1 pgorman ucb 1154 Dec 12 05:08 rhok
-rw-r--r-- 1 pgorman ucb 1130 Dec 12 05:08 superficialLiquidFlux
-rw-r--r-- 1 pgorman ucb 1427 Dec 12 05:08 volPower

RBWR-TR/Serpent_GPT/voidSens/ofCoupling/9:
total 56
-rw-r--r-- 1 pgorman ucb 1323 Dec 12 05:08 PuWeightFraction
-rw-r--r-- 1 pgorman ucb 1465 Dec 12 05:08 T
-rw-r--r-- 1 pgorman ucb 1475 Dec 12 05:08 Tcenterline
-rw-r--r-- 1 pgorman ucb 1458 Dec 12 05:08 Tclad
-rw-r--r-- 1 pgorman ucb 1508 Dec 12 05:08 Tnormalized
-rw-r--r-- 1 pgorman ucb 1567 Dec 12 05:08 h
-rw-r--r-- 1 pgorman ucb 1419 Dec 12 05:08 linHeatRate
-rw-r--r-- 1 pgorman ucb 1240 Dec 12 05:08 phil
-rw-r--r-- 1 pgorman ucb 1472 Dec 12 05:08 rho
-rw-r--r-- 1 pgorman ucb 1468 Dec 12 05:08 rhok
-rw-r--r-- 1 pgorman ucb 1460 Dec 12 05:08 superficialLiquidFlux
drwxr-xr-x 2 pgorman ucb 4096 Dec 12 05:08 uniform
-rw-r--r-- 1 pgorman ucb 1418 Dec 12 05:08 voidFrac
-rw-r--r-- 1 pgorman ucb 1449 Dec 12 05:08 volPower

RBWR-TR/Serpent_GPT/voidSens/ofCoupling/9/uniform:
total 4
-rw-r--r-- 1 pgorman ucb 960 Dec 12 05:08 time

RBWR-TR/Serpent_GPT/voidSens/ofCoupling/constant:
total 16
-rw-r--r-- 1 pgorman ucb 1005 Dec 12 05:08 G
-rw-r--r-- 1 pgorman ucb 1199 Dec 12 05:08 globalParameters
drwxr-xr-x 2 pgorman ucb 4096 Dec 12 05:08 polyMesh
-rw-r--r-- 1 pgorman ucb 1919 Dec 12 05:08 transportProperties

RBWR-TR/Serpent_GPT/voidSens/ofCoupling/constant/polyMesh:
total 20
-rw-r--r-- 1 pgorman ucb 1250 Dec 12 05:08 boundary
-rw-r--r-- 1 pgorman ucb 3495 Dec 12 05:08 faces
-rw-r--r-- 1 pgorman ucb 1040 Dec 12 05:08 neighbour
-rw-r--r-- 1 pgorman ucb 1397 Dec 12 05:08 owner
-rw-r--r-- 1 pgorman ucb 2775 Dec 12 05:08 points

RBWR-TR/Serpent_GPT/voidSens/ofCoupling/system:
total 20
-rw-r--r-- 1 pgorman ucb 3950 Dec 12 05:08 backup_blockMeshDict
-rw-r--r-- 1 pgorman ucb 2154 Dec 12 05:08 blockMeshDict
-rw-r--r-- 1 pgorman ucb 1208 Dec 12 05:08 controlDict
-rw-r--r-- 1 pgorman ucb 1475 Dec 12 05:08 fvSchemes
```

```
-rw-r--r-- 1 pgorman ucb 1196 Dec 12 05:08 fvSolution
```

Appendix D. RBWR-TB2 Water Density Covariance Script

The following script was written in python3 in order to calculate the water density covariance for the RBWR-TB2. For other cores using the same relative uncertainty (either a constant 10% or specified by [44] using a superficial liquid velocity of 1.0 m/s) and using the same saturation conditions, the only input that needs to be changed is the list of void fractions ('`alphas`').

```
#! /usr/bin/env python3

import scipy.special
import random
import math

numberOfTrials = 10000

#Set seed value for reproducibility.
random.seed(a=1)

#Liquid and vapor water densities at 7.2 MPa.
rho_l = 0.736168 #g/cc
rho_v = 0.0376982 #g/cc

#Void fractions for the RBWR-TB2 - one per node.
alphas = [0, 0, 0, 0, 0, 0, 0, 0, 0.00226896, 0.0201292, 0.0261875,
0.0313803, 0.0359823, 0.04156, 0.0517961, 0.0659594, 0.113799, 0.0901649,
0.324511, 0.446774, 0.536602, 0.602206, 0.650846, 0.689226, 0.719617,
0.763313, 0.776136, 0.778799, 0.779215, 0.779397, 0.779462]

#Relative uncertainty
#For superficial liquid velocities that are relevant for the RBWRs, Clark et
al. have a relative uncertaity
#of 15% for void fractions below 0.4, and 7.9% otherwise.
relUncertainties = []
for z in range(len(alphas)):
    #if alphas[z] < 0.4:
    #    relUncertainties.append(0.15)
    #else:
    #    relUncertainties.append(0.079)
        relUncertainties.append(0.1)

#List of average water densities.
rhoMeans = []
for z in range(len(alphas)):
    rhoMeans.append((1-alphas[z])*rho_l + alphas[z]*rho_v)

rhoTrials = []
rhoDeviations = []
alphaTrials = []
for n in range(numberOfTrials):
    rhoTrials.append([])
    rhoDeviations.append([])
    alphaTrials.append([])
    #Need to use one random float per trial, not one random float per
node/perturbation.  Otherwise, we'd have
    #nonphysical trials where the water density decreases, etc.
```

```
    #Bounded between 0 and 1.
    randomFloat = random.random()
    for z in range(len(alphas)):
        #CDF of the normal distribution = 0.5 * [1 + erf((x-
mu)/(sig*sqrt(2)))]
        # where mu = mean value
        #       sig = standard deviation
        #Set CDF equal to random number and solve for x.
        alphaTrial = (scipy.special.erfinv(2*randomFloat-1) * math.sqrt(2) *
relUncertainties[z] + 1) * alphas[z]
        rhoTrials[-1].append((1-alphaTrial)*rho_l + alphaTrial*rho_v)
        rhoDeviations[-1].append((rhoTrials[-1][z] -
rhoMeans[z])/rhoMeans[z])
        alphaTrials[-1].append(alphaTrial)

#From trial values, calculate the relative covariance.
#covariances is the water density covariance matrix
#alphaCovariances is the void fraction covariance matrix (used for
debugging/verification)
covariances = []
alphaCovariances = []
for z1 in range(len(alphas)):
    covariances.append([])
    alphaCovariances.append([])
    for z2 in range(len(alphas)):
        covariances[-1].append(0)
        alphaCovariances[-1].append(0)

for z1 in range(len(alphas)):
    for z2 in range(len(alphas)):
        for n in range(numberOfTrials):
            #Relative covariance_j_k = (rho_j_i - rho_j_mean) * (rho_k_i -
rho_k_mean) / rho_j_mean / rho_k_mean
            #where i is an index for trial
            #and j,k are indices for different nodes
            covariances[z1][z2] += rhoDeviations[n][z1] *
rhoDeviations[n][z2] / numberOfTrials
            if alphas[z1] != 0 and alphas[z2] != 0:
                alphaCovariances[z1][z2] += (alphaTrials[n][z1] - alphas[z1])
* (alphaTrials[n][z2] - alphas[z2]) / numberOfTrials / alphas[z1] /
alphas[z2]

# For verification, I output both the water density and void fraction
covariance into comma-delimited files.
# I only used the tab-delimited covariance for the uncertainty calculation.
outText = 'zNumber'
outText2 = ''
outText3 = 'zNumber'
for z in range(len(alphas)):
    outText += ',z={}'.format(z)
    outText3 += ',z={}'.format(z)
for z1 in range(len(alphas)):
    outText += '\nz={}'.format(z1)
    outText3 += '\nz={}'.format(z1)
    if z1 != 0:
        outText2 += '\n'
    for z2 in range(len(alphas)):
```

```
        outText += ',{}'.format(covariances[z1][z2])
        outText2 += '{}\t'.format(covariances[z1][z2])
        outText3 += ',{}'.format(alphaCovariances[z1][z2])

fileName = "TB2_BOL_waterDensityCovariances_2.csv"
fileName2 = "TB2_BOL_waterDensityCovariances_tabs_2"
fileName3 = "TB2_BOL_alphaCovariances_2.csv"

f = open(fileName, 'w')
f.write(outText)
f.close()
f = open(fileName2, 'w')
f.write(outText2)
f.close()
f = open(fileName3, 'w')
f.write(outText3)
f.close()
```